Pure spin current transport and magnetic state manipulation in lateral spin valves

Dissertation
zur Erreichung des Grades
„Doktor der Naturwissenschaften“
am Fachbereich Physik, Mathematik und Informatik
der Johannes-Gutenberg Universität
in Mainz

von:
Alexander Pfeiffer
geboren in Gießen
Mainz, 2019

JOHANNES GUTENBERG
UNIVERSITÄT MAINZ

Datum der mündlichen Prüfung: 15.01.2020
1. Berichterstatter: In der elektronischen Version entfernt aufgrund datenschutzrechtlicher Bestimmungen.
2. Berichterstatter: In der elektronischen Version entfernt aufgrund datenschutzrechtlicher Bestimmungen.

Eidesstattliche Erklärung

Hiermit erkläre ich an Eides statt, dass ich meine Dissertation selbständig und ohne fremde Hilfe verfasst und keine anderen als die von mir angegebenen Quellen und Hilfsmittel zur Erstellung meiner Dissertation verwendet habe. Die Arbeit ist in vorliegender oder ähnlicher Form bei keiner anderen Prüfungsbehörde zur Erlangung eines Doktorgrades eingereicht worden.

Mainz, den 29.10.2019

Alexander Pfeiffer

Abstract

Lateral spin valves are model systems that are well-suited for the study of pure spin current transport across interfaces. Furthermore, these systems allow for an efficient manipulation of magnetic states, e.g. a magnetic vortex, due to the intrinsic reduction of accompanying Oersted fields and Joule heating at the position where the magnetization is manipulated. This makes lateral spin valves attractive also for future device concepts such as data storage devices.

In the first part of this thesis, the field and pure spin current induced switching of a magnetic disc, acting as a detector electrode, is studied and discussed. By a judicious choice of the applied field direction and the amplitude and polarity of the applied current pulses in the injector, the switching behaviour of the magnetic disc can be measured as a function of the resulting absorbed spin current. Although nominally round and therefore without expected in-plane shape anisotropy, it is observed that small variations in the shape and randomly distributed imperfections can strongly affect the device behaviour. Suitable field sweep directions are identified, which allow for a study of the switching from a magnetic mono-domain state to a magnetic vortex state and from the vortex state to the opposite mono-domain state. Although most of the changes in the magnetic switching occur due to Joule heating, the spin transfer torque from the pure spin current also contributes to the switching, which is detectable thanks to our optimized device geometry which allows for synchronous current pulses from two injector electrodes.

The second part of the thesis tackles the fundamental properties of pure spin current transport across metallic interfaces.
In a first work, Pt-Py-Cu multi terminal spin valves have been fabricated, which allow to compare the temperature dependence of the spin current generated by two different spin current generation and detection methods. As the first method, the conventional electric spin injection is exploited where current injection and detection are based on two parallel ferromagnetic wires, bridged by a Cu conduit. As a second method, a spin to charge interconversion is used and either spin currents are generated by the spin Hall effect and detected by conventional non-local detection or spin currents are generated by conventional spin current injection and detected by the inverse spin Hall effect. Differences in the temperature dependences of these two detection methods are found, which means that the temperature dependence of the signals is not only governed by the spin transport and spin injection as previously claimed.

In a second work and motivated by previous results, again Pt-Py-Cu lateral spin valves, yet with an optimized device geometry, are studied which allow for a comparison of the conventional non-local signal, the spin absorption signal and the inverse spin Hall effect signal for varying temperatures. Depending on the fabricated induced quality of the relevant interfaces for the different samples, significant differences in the signals, i.e. either a very large spin absorption and a low spin Hall effect signal or no significant absorption but a very large spin Hall effect signal are determined. These large differences cannot be attributed to structural variations visible with conventional imaging and are also not reflected in the very similar electrical charge transport properties of the devices. Rather details of the interfaces are accessed via a special scanning electron microscope technique for buried interface imaging, revealing important details of the interfaces which explain the spin transport results.

By additional measurements of CoFe-Cu lateral spin valves with varying fabrication methods for both the CoFe wires and the Cu bridge, the reliability and reproducibility of the previous measurements are confirmed in a different system. While samples with high quality interfaces are expected to show no differences in the temperature behaviour of the conventional non-local and the spin absorption signal, a significantly stronger decrease of the spin absorption signal with increasing temperatures for samples with low quality interfaces is observed.

The last part of the thesis is about the fabrication of Co_2MnSi based lateral spin valves. Although no spin signal has been seen for these samples, the fabrication for samples based on thin films has been significantly improved and opens a route to potentially produce lateral spin valves with high spin signals based on the findings and improvements.

Kurzfassung

Laterale Spinventile sind hervorragend geeignete Modellsysteme zur Untersuchung von Spinströmen, die durch Grenzflächen fließen. Weiterhin bieten laterale Spinventile die Möglichkeit zur effizienten Manipulation magnetischer Zustände, zum Beispiel eines magnetischen Vortexzustands, dadurch dass sie intrinsisch unerwünschte Oersted-Feldern und Joulesche Wärme dort reduzieren, wo die Magnetisierung verändert wird. Diese Eigenschaften machen laterale Spinventile interessant für künftige potentielle Anwendungen wie zum Beispiel zur Datenspeicherung.

Der erste Teil der Arbeit beschäftigt sich mit dem strom- und feldinduzierten magnetischen Schalten einer Scheibe. Durch geeignete Wahl der Ausrichtung des externen Magnetfeldes sowie Amplitude und Polarität der angelegten Strompulse kann das magnetische Schaltverhalten der Scheibe als Funktion des Spinstroms vermessen werden. Obwohl keine Anisotropie in der Scheibenebene erwartet wird, ist das Schaltverhalten der Scheibe doch wesentlich durch kleine Abweichungen von der Form und durch zufällig verteilte Störstellen bestimmt. Durch geschickte Wahl der Richtung des äußeren Feldes lassen sich in der Probe zwei Schaltvorgänge messen: Zunächst das Schalten von einem Zustand homogener Magnetisierung zu einem Vortexzustand, anschließend von diesem Vortexzustand weiter zu einem Zustand homogener Magnetisierung, der dem Anfangszustand entgegengerichtet ist. Obgleich das Schaltverhalten wesentlich durch Joulesche Wärme bestimmt wird, lässt sich auch das vom Spinstrom übertragene Drehmoment auf die Scheibe experimentell nachweisen, was ohne unsere optimierte Geometrie nicht möglich gewesen wäre.

Im zweiten Teil der Arbeit geht um die fundamentalen Eigenschaften von reinen Spinströmen, die durch metallische Grenzflächen fließen.
Zuerst werden laterale Spinventile aus Pt-Py-Cu hergestellt. Diese erlauben einen Vergleich der Temperaturabhängigkeit von Spinströmen, die auf zwei verschiedene Arten erzeugt und detektiert werden. Bei der ersten Methode wird gewöhnliche Spininjektion verwendet. Als zweite Methode dient der Spin-Hall-Effekt. Entweder werden durch diesen Effekt Spinströme erzeugt, die über gewöhnliche Spindetektion nachgewiesen werden, oder es werden Spinströme mittels gewöhnlicher Spininjektion erzeugt und über den inversen Spin-Hall-Effekt nachgewiesen. Es zeigen sich deutliche Unterschiede im Temperaturverhalten zwischen beiden Detektionsmethoden, womit klar ist, dass die Temperaturabhängigkeit solcher Signale nicht nur vom Spintransport und von der Injektionsmethode, sondern auch von der Detektionsmethode abhängt.

Diese Ergebnisse motivieren eine zweite Arbeit, bei der erneut Pt-Py-Cu basierte Spinventile vermessen werden. Mittels dieser Proben lassen sich u.a. das Spinabsorptionssignal und der inverse Spin-Hall-Effekt temperaturabhängig vermessen. Abhängig von der Qualität der Grenzflächen ergeben sich zwei mögliche Szenarien: In diesen Proben misst man entweder einen großen Spin-Hall-Effekt und vernachlässigbare Spinabsorption oder umgekehrt eine hohe Spinabsorption, aber dafür nur einen geringen Spin-Hall-Effekt. Diese beiden grundlegend verschiedenen Messergebnisse, die letztendlich auf unterschiedliche Fabrikationsmethoden zurückzuführen sind, lassen sich weder durch konventionelle Elektronenmikroskopie beobachten noch auf die elektrischen Ladungstransporteigenschaften der Grenzflächen zurückführen. Stattdessen kann man mithilfe einer speziellen, auf Rasterelektronenmikroskopie basierenden Methode die verdeckten Grenzflächen direkt analysieren. Diese Analyse zeigt die Strukturen der Grenzflächen, die die gemessenen Spintransport-Ergebnisse erklären.

Die Reproduzierbarkeit dieser Ergebnisse lässt sich mithilfe zusätzlicher Messungen von auf CoFe-Cu basierten Spinventilen bestätigen. In diesen Proben werden sowohl die CoFe-Nanodrähte als auch die Kupferbrücke mithilfe verschiedener Fabrikationsmethoden hergestellt. Während Proben mit hoher Grenzflächenqualität keine Unterschiede im Temperaturverhalten von gewöhnlichem Spininjektions- und Spinabsorptionssignal aufweisen, zeigen sich erhebliche Unterschiede zwischen beiden Signalen für Proben mit geringer Grenzflächenqualität.

Im letzten Teil der Arbeit geht um die Fabrikation von auf Co_2MnSi basierenden lateralen Spinventilen. Es konnte zwar kein Spinsignal nachgewiesen werden, dennoch wurden erhebliche Fortschritte in der Fabrikation von lateralen Spinventilen, die aus dünnen Filmen hergestellt werden, erzielt.

Contents

Introduction

In the field of spintronics, coined after the words "spin" and "electronics", researchers try to exploit the spin degree of freedom of the electron to provide functionality such as manipulating magnetization. One of the first and most important discoveries in the field of spintronics was the giant magnetoresistance (GMR) effect by Albert Fert and Peter Grünberg in 1988, for which both were awarded the novel prize in 2005 [1, 2]. As a result of the GMR effect, the electric resistance of a multi layer system of alternating ferromagnetic and non-magnetic layers depends on the relative alignment of the magnetization of the ferromagnetic layers, which can be explained by different scattering probabilities of the conduction electrons at the nonmagnetic and ferromagnetic interfaces.

Over the next few years, Stuart Parkin, working at the IBM Almaden Research Center, built data storage devices exploiting the GMR effect for magnetic read-heads and in the year 1997, IBM commercialized a hard disk drive with 16.8 Gigabytes. This results in an increase of the data storage by a factor of 1000 compared to previous commercialized data storage devices [3]. Nowadays, hard disk drives (HDDs) with a storage of 3 Terrabytes are available, making things such as cloud computing and high quality video streaming possible.

However, such devices also face challenges, in particular the relatively slow information reading and writing times (which are typically of the order of a few milliseconds) and the relatively high energy consumption of a few Watts per Gigabyte. Even more problematic is the low robustness of such devices due to the mechanically moving parts, calling for new ideas and improvements. Motivated by this, Stuart Parkin et al. came up with the idea to use the magnetization in a magnetic nanowire, which depending on the orientation represents either a logic "1" or a logic "0" [4]. The information is separated by magnetic domain walls (DWs), which can be shifted within the magnetic nanowire via spin polarized currents and thus the magnetization is shifted to the position where it is read-out, making macroscopic mechanically moving parts redundant.

For spin transfer torque driven DW motion, however, high critical current densities are required [5, 6]. Recent research has investigated new methods of DW motion based on spin orbit torques, which have the potential for much more efficient manipulation [7–9]. However, also in spin orbit torque based devices, relatively large currents are required to switch a magnetic state, resulting in relatively large Joule heating and Oersted fields which is disadvantageous - in particular they also lead to undesired changes in the magnetic state of the device.

In addition to spin polarized currents, there is also the possibility to exploit pure spin currents to manipulate magnetization, in particular in a lateral spin valve geometry. In the simplest case this geometry is based on two ferromagnetic (FM) sub-micron electrodes, which are spatially separated but connected via a nonmagnetic (NM) spin current conduit with low spin orbit coupling [10, 11]. A spin polarized charge current with the spin current orientation depending on the magnetization of FM_1 flows across the FM_1/NM interface. Thus a spin accumulation is generated in the NM which is transported towards FM_2 where it can be detected as a non-local voltage and can exploited to e.g. switch a magnetic state [12] or displace a magnetic domain wall [13–15]. Since charge current injection and voltage detection are spatially separated, accompanying effects such as Joule heating, Oersted fields and capacitive effects are reduced in the manipulated magnetization region. One prominent example for a non-local spin signal based logic device with built-in memory has been proposed in 2010 [16]. Additionally, the lateral spin valve geometry opens a route for e.g. new magnetic read-heads for higher data storage devices [17, 18].

The goal of this thesis is to study both the fundamental properties of pure spin current transport across metallic interfaces in lateral spin valves and to check the suitability of the geometry for possible applications, e.g. the efficient and reproducible manipulation of a magnetic state by pure spin currents. In order to study the former, in particular different fabrication methods are used and their influence on the resulting interfaces and the spin signals is investigated. For possible applications, the magnetic switching of a very small disc via pure spin currents is investigated via a well-suited optimized geometry. Also, routes to producing lateral spin valves with high spin-signals are investigated via the employment of highly spin polarized materials in combination with promising spin conduit materials.

The thesis is divided into seven chapters as follows:

Chapter 1 provides the theoretical background for the understanding of magnetism on a nanometer length scale and discusses, in particular, the different contributions to the Landau free energy such as Heisenberg exchange energy, Zeeman energy, stray field energy and anisotropy energies. The fundamental equation of motion, the Landau-Lifshitz-Gilbert equation is motivated and exploited in order to describe the influence of external fields and spin currents on magnetic domain walls. After this, contributions such as intrinsic band structure effects, spin skew scattering and side jump contributions to the anomalous Hall effect and the spin Hall effect are presented and explained, the latter playing a key role in the experimental work of the thesis. An introduction to the lateral spin valve geometry and the non-local signal follows, the latter of which is based on a shift in the chemical potential of the different interfaces for the different spin states. The chapter ends with a derivation of the non-local signal based on a $1d$-diffusion model and a study of the spin transfer torque acting on non-collinear magnetization, which is intensively studied in the experimental part of the thesis.

Chapter 2 concerns the fabrication of lateral spin valves including the employed methods such as electron beam lithography, ultrahigh vacuum thin film deposition and ion beam etching. Furthermore, experimental techniques such as atomic force microscopy, X-ray reflectivity and the measurement of the non-local voltage via lock-in amplification are presented and explained, together with a presentation of the used experimental setup.

Chapter 3 presents an optimized lateral spin valve geometry, which allows for the study of the pure spin current assisted magnetic switching of a nanostructure. In particular the manipulation of the magnetization of a 160 nm diameter Py disc is demonstrated, with the disc acting as the detector. By a judicious choice of the applied external field direction and the amplitude and polarity of the applied current pulses, the switching behaviour of the magnetic disc can be measured as a function of the resulting absorbed spin current. Although a large portion of the changes of the switching fields can be attributed to Joule heating, the spin transfer torque arising from the pure spin current also contributes to the switching. Thanks to the optimized geometry which allows for the synchronous application of current pulses from two injectors, it is possible to observe and to determine the spin transfer torque contribution.

Chapter 4 describes the differences in the temperature dependence of the spin current generated by two different spin current generation and detection methods. As the first method, both conventional electric spin injection and detection are used, based on two ferromagnetic wires bridged by a nonmagnetic spin current conduit. As the second method, a spin current is either generated by the spin Hall effect and detected by conventional spin current detection or a spin current is generated by conventional spin injection and detected by the inverse spin Hall effect. A pioneered kinked geometry with the heavy metal electrode patterned perpendicular to the ferromagnetic wire allows one to link the detected signals with the magnetization orientation of the probed ferromagnetic wire. Differences in the temperature behaviour of the signals based on the different detection methods are seen, indicating that the temperature dependence is not only governed by the spin current transport and spin injection mechanism as previously claimed.

Chapter 5 compares the conventional non-local signal, the spin absorption signal and the (inverse) spin Hall effect signal in lateral spin valves based on different fabrication recipes for the patterning of the spin current conduit. Depending on the used fabrication recipe, either a large (inverse) spin Hall effect signal and low spin absorption is observed, or vice versa. Also the temperature dependencies of the different signals for samples based on the different recipes differ considerably. These large, counter-intuitive differences are not apparent from conventional imaging and are not reflected in the very similar charge transport properties of the devices. Rather a special technique for buried interface imaging is used, which provides a link between the transport results and the fabrication method depended quality of the interfaces. The results are confirmed by additional measurements in a different system which provide an estimation of the contribution of intrinsic parameters to the spin absorption which can be compared to interface contributions such as spin transparency and spin memory loss, which have been often disregarded in the literature.

Chapter 6 describes the fabrication of lateral spin valves from prior grown metallic films, which is challenging compared to lift-off based samples but is required for the study of materials with high intrinsic spin polarization such as Heusler materials due to the need for high temperature annealing of the films. Although no spin signal has been detected, significant progress in the fabrication procedure, in particular concerning the homogeneity of the etching and the removal of the residual resist, is achieved.

Chapter 7 sums up the main experimental results and provides an outlook for further possible experiments based on the lateral spin valve geometry.

Chapter I

Theoretical Background

This part of the thesis covers the basic theory behind the experimental work in order to provide a theoretical context for the experimental results.

Firstly, the appearance of magnetism is explained based on the quantum mechanical properties of bound electrons in atoms. However, in solids, electrons form electronic bands and here a different description is required. In the Stoner model the bands are shifted energetically for different spin orientations, resulting in a net macroscopic magnetization.

The next step will be to describe the dynamics of magnetism, based on the Landau-Lifshitz-Gilbert-equation (LLG). A semi-classical motivation will be used to deduce this fundamental equation of motion. After the derivation of the LLG-equation, the different energy contributions are studied to determine the effective magnetic fields which drive the magnetisation dynamics. One important example of the application of the LLG-equation is to describe the time evolution of a magnetic domain wall driven by effective fields, which will also play an important role in the experimental part of the thesis.

Thirdly, the-LLG equation is extended to include the effect of spin polarized currents via the so-called adiabatic and non-adiabatic spin transfer torque.

In the fourth part, the various Hall effects including the anomalous-Hall effect and the spin Hall effect are described, which play a vital role in the experiments.

In the fifth part of this chapter, a theoretical description of the generation, transport and detection of pure spin currents in (metallic) lateral spin valves is given, together with the derivation of the electric non-local signal as a function of the electrode separation. Additionally, spin currents generated by heat and the spin dependent Seebeck effect are shortly discussed.

The chapter ends with a discussion for a non-collinear magnetization orientations which gives rise to the spin transfer torque. The spin transfer torque in a lateral spin valve will play a vital role in the experimental results since it allows for an efficient manipulation of a magnetic state in such a device.

1.1. Microscopic Origins Of Magnetism

1.1.1. Atomic magnetism

Usually, magnetism is based on electrons; elementary particles which can be described by their electric charge $-e$, by their mass m_e and by their spin s. While the first two properties can be explained in terms of classical mechanics and electrodynamics, the electron spin s is a purely quantum mechanical property [19]. In a classical model of an atom, an electron moving around the atomic nucleus can be understood as a circular current. Its magnetic moment $\vec{\mu}$ is given by

$$\vec{\mu} = \frac{-e}{2m_e}\vec{L}, \tag{1.1}$$

with $\vec{L}$ as the angular momentum of the electron. The corresponding quantum mechanical description for the classical angular momentum vector is given by the following commutator relations and quantization rules

$$[\hat{L}_i, \hat{L}_j] = i\hbar\epsilon_{ijk}\hat{L}_k \tag{1.2}$$

$$[\hat{L}_i, \hat{L}^2] = 0 \tag{1.3}$$

$$\hat{L}^2|lm_l> = \hbar^2 l(l+1)|lm_l> \tag{1.4}$$

$$\hat{L}_z|lm> = \hbar m_l|lm_l> \tag{1.5}$$

$[\hat{A}, \hat{B}] = \hat{A}\cdot\hat{B} - \hat{B}\cdot\hat{A}$ is the commutator while $\hat{A}$ and $\hat{B}$ are operators. $\hat{L}^2 = \hat{L}_x^2 + \hat{L}_y^2 + \hat{L}_z^2$ is the squared angular momentum operator. $\hat{L}_z$ is the component of the angular momentum operator in the z-direction, which is assumed to be the quantization axis. Since $\hat{L}^2$ and $\hat{L}_z$ commutate, the operators have a same basis and $|lm_l>$ are the eigenvectors of this basis. $l = 0, 1, 2, ..., n-1$ is named the azimuthal quantum number, $n = 1, 2, ..$ the principal quantum number and $m_l = -l, -l+1, ..., l$ is known as magnetic quantum number. $\hbar = h/2\pi$ =1.05·10^{-34} J/s is the reduced Plank constant.

Similar to the (orbital) angular momentum, the spin angular momentum of the electron can be defined although it is emphasized here again that the spin angular momentum is a purely quantum entity without any classical analogy [20, 21]. One can write [22]

$$\hat{S}^2|s> = \hbar^2 s(s+1)|s>= \qquad |\hat{S}_Z|s>= m_s\cdot\hbar \qquad \text{with } s = \frac{1}{2} \text{ and } m_s = \pm\frac{1}{2}. \tag{1.6}$$

Electrons with $m_s = +1/2$ are named spin-up, electrons with $m_s = -1/2$ are named spin-down electrons. For a further description, the total magnetic moment operator $\hat{\mu}_{\text{tot}}$ is defined as follows

$$\hat{\mu}_{\text{tot}} = \hat{\mu}_{\text{orb}} + \hat{\mu}_{\text{spin}} = \frac{-e}{2m_e}\left(\hat{L} + g_e\hat{S}\right), \tag{1.7}$$

with g_e the Landé g-factor, which is close to 2 for electrons [19]. The interaction between these two angular momenta is called the spin-orbit-interaction (SOI). In a simple picture it can be understood as the interaction of the spin magnetic moment with the magnetic field in the rest frame of the electron, which itself is generated by the orbital motion of the electron in the electric field of the atom arising due to the positive charges of the nucleus. As a direct result of the SOI, the eigenvalues of neither $\hat{L}$ nor $\hat{S}$ are conserved. Instead, the total angular momentum operator $\hat{J}$ is defined as

$$\hat{J} = \hat{L} + \hat{S}. \tag{1.8}$$

A schematic illustration of the two magnetic moments is shown in Figure 1.1.

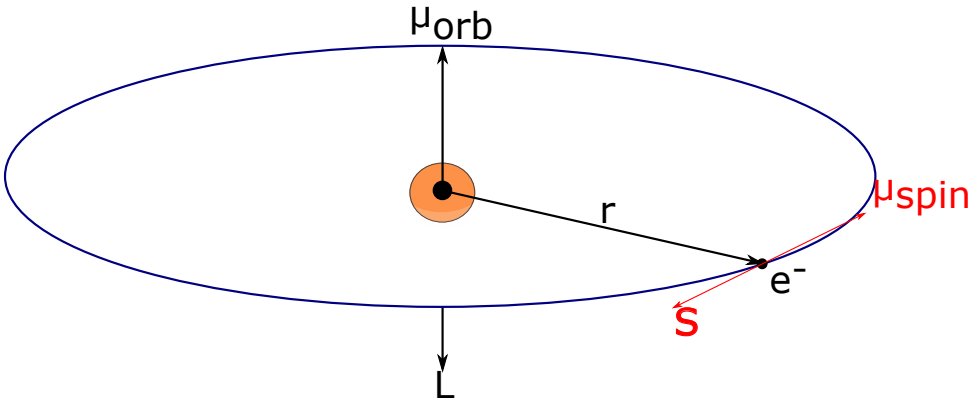

Fig. 1.1. Schematic illustration of a classical model of an atom with a nucleus and an electron orbiting around the nucleus with the distance r. The electron has two different angular momenta. The classical orbital angular momentum, which is antiparallel to the magnetic moment μ_{orb} and the pure quantum mechanical spin S which is antiparallel to the spin magnetic moment μ_{spin}.

1.1.2. Magnetism in itinerant electron systems: Stoner-model

Up to now, only the spin orbit interaction in a single atom has been studied. However magnetism in a solid arises not from a single atom, but rather is a many particle phenomenon. Compared to atoms, where electrons occupy different atomic orbitals which are localized around the nucleus, electrons in solids form electronic bands [23]. These electronic bands are generated as a result of the overlapping of the atomic orbitals of the atoms within the solid [24]. This holds especially for electrons sitting in outer shells, while electrons localized in inner-shells tend to be bound close to the nucleus. Electrons occupy states up to the Fermi energy, which is for metallic systems located within one or more of the electronic bands.

Electrons present in the bands at the Fermi energy are mobile and can be shared among several atoms. Thus these electrons are called itinerant electrons and lead to an electric conductivity in metals [23]. Hence these contributing electron bands are named conduction bands. In the case of simple $3d$ itinerant ferromagnetic elements such as Fe, Co and Ni the conduction band originates from the $3d$ and the $4s$ orbitals. As a consequence, the charge carriers in these metals are hybridized $3d$-$4s$ electrons.

A model for the ferromagnetism of these materials has been proposed by Stoner, which is based on a free-electron approximation [25]. In this model, the spin polarized bands of spin-up and spin-down electrons are spontaneously shifted in energy and as a consequence, one spin polarisation is energetically preferred for electrons in the vicinity of the Fermi energy. The split of the energy bands occurs if the Stoner-criterion is fulfilled, which reads [26]

$$I \cdot N_{\downarrow,\uparrow}(E_F) > 1 \tag{1.9}$$

with I as the Stoner exchange parameter and $N_{\downarrow,\uparrow}(E_F)$ as the density of states per atom for each spin state at the Fermi energy E_F. The density of states of a simple, itinerant ferromagnetic system with two spin-polarized sub-bands with the energy gap ΔE is shown schematically in Figure 1.2. In the situation as drawn, more spin-down electrons than spin-up electrons are present, resulting in a net magnetization $\vec{M}$, which is antiparallel to the spin-down electrons. Since in this example the majority band is completely filled up, these ferromagnets are named strong ferromagnets (such as Ni or Co) while ferromagnets with less filled majority bands such as Fe are named weak ferromagnets [27].

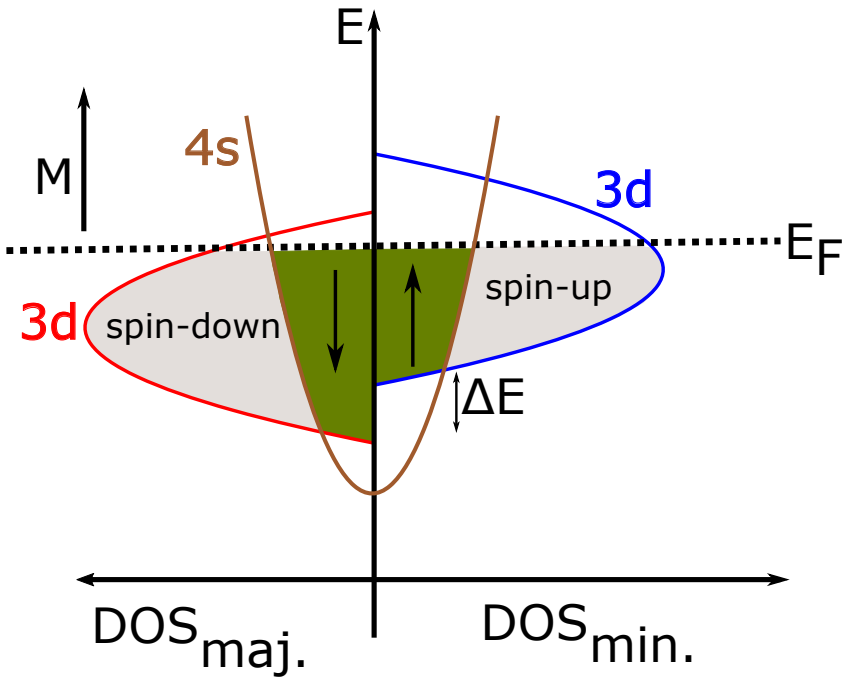

Fig. 1.2. Schematic illustration of the simplified density of states of a strong $3d$ itinerant ferromagnetic system such as Ni or Co. Since more spin-down than spin-up electrons are present, a net magnetization $\vec{M}$ antiparallel to the spin-down electrons is found.

1.2. Landau-Lifshitz-Gilbert Equation

In the year 1935, L. D. Landau and E. M. Lifshitz published an equation which describes the time evolution of an arbitrary magnetic solid [28], based on the Heisenberg model of ferromagnetism. In this section, this equation is derived by the aid of the Heisenberg equation of motion in a semi-classical continuum limit, following the derivation from [29].

The quantum mechanical Heisenberg equation of motion reads:

$$\frac{d}{dt}(\hat{A}_H) = \frac{i}{\hbar}[\hat{H}_H, \hat{A}_H] + (\partial_t \hat{A}_S)_H. \tag{1.10}$$

If the operator $\hat{A}_S$ does not have an explicit time dependence in the Schrödinger picture, the second term on the right hand side vanishes. If for the first consideration a single spin $\hat{S}$ is chosen, one obtains:

$$\frac{d\hat{S}_j}{dt} = \frac{i}{\hbar}[H, \hat{S}_j] = \frac{i}{\hbar}\left(\sum_k \frac{\partial \hat{H}}{\partial S_k}[\hat{S}_k, \hat{S}_j] + \mathcal{O}(\hbar^2)\right), \tag{1.11}$$

where $\mathcal{O}(\hbar^2)$ denotes a function containing terms of the order $\hbar^2$. In the following, the Einstein summation convention is used. By the aid of the fundamental commutation relation for the angular momentum and therefore for the spin

$$[\hat{S}_k, \hat{S}_j] = -i\hbar\epsilon_{jkl}\hat{S}_l, \tag{1.12}$$

one finds

$$\frac{d\hat{S}_j}{dt} = \frac{\partial \hat{H}}{\partial \hat{S}_k}\epsilon_{jkl}\hat{S}_l + \mathcal{O}(\hbar) \tag{1.13}$$

for the j-th component of the spin $\hat{S}$. Via a semi-classical approximation, the single spins $\hat{S}$ which are discrete in amplitude and orientation, can be approximated by the continuous vector field of the

magnetization $\vec{M}$, providing the characteristic length scale over which the magnetization changes its direction is large compared to the distance between the spins. Furthermore, in the limit $\hbar \to 0$, one can write

$$\frac{d\vec{M}}{dt} = -\gamma \vec{M} \times \vec{H}_{\text{eff}}, \tag{1.14}$$

where $\gamma = g \cdot \mu_O \cdot \mu_B/\hbar$ denotes the gyromagnetic ratio and $\mu_0 = 4 \cdot \pi \cdot 10^{-7} N/A^2$ the vacuum permeability. The effective field $\vec{H}_{\text{eff}}$ can be determined by

$$\vec{H}_{\text{eff}} = \frac{1}{\gamma} \left\langle \frac{1}{\mu_0} \frac{\partial \hat{H}}{\partial S} \right\rangle = -\frac{1}{\mu_0} \frac{dE}{d\vec{m}_s}, \tag{1.15}$$

where E is the energy of the system and $\vec{m}_s = -g\mu_B \vec{S}\hbar$ the magnetic moment of the spin (which is now treated as a simple vector). In the continuum limit, Equation 1.15 simplifies to

$$\vec{H}_{\text{eff}} = -\frac{1}{\mu_0} \frac{\delta E}{\delta M}, \tag{1.16}$$

with δ as the variational derivative defined as

$$\frac{\delta E[\vec{M}(\vec{r})]}{\delta \vec{M}(\vec{r}_0)} = \lim_{\varepsilon \to 0} \frac{1}{\varepsilon} \begin{pmatrix} E[\vec{M}(\vec{r})] + \varepsilon \vec{e}_x \delta^3(\vec{r} - \vec{r}_0) - E[\vec{M}(\vec{r})] \\ E[\vec{M}(\vec{r})] + \varepsilon \vec{e}_y \delta^3(\vec{r} - \vec{r}_0) - E[\vec{M}(\vec{r})] \\ E[\vec{M}(\vec{r})] + \varepsilon \vec{e}_z \delta^3(\vec{r} - \vec{r}_0) - E[\vec{M}(\vec{r})] \end{pmatrix}. \tag{1.17}$$

Equation 1.14 describes a precessional motion of the magnetization $\vec{M}$ along the effective field $\vec{H}_{\text{eff}}$. By a simple calculation

$$\frac{dE}{dt} = \int dV \left(-\mu_0 \vec{H}_{\text{eff}}\right) \cdot \left(-\gamma \vec{M} \times \vec{H}_{\text{eff}}\right) = 0 \tag{1.18}$$

one finds that there is no energy dissipation due to this motion and therefore, it is not possible for the magnetization to reach the energy minimum, which is in the simplest case parallel to an external field due to the Zeeman energy (see Section 1.3.1 for more details). To solve this problem, Gilbert [30] added a phenomenological damping term to Equation 1.14 proportional to $\vec{M} \times d\vec{M}/dt$. This leads to

$$\frac{d\vec{M}}{dt} = -\gamma \left(\vec{M} \times \vec{H}_{\text{eff}}\right) + \frac{\alpha}{M_s} \vec{M} \times \frac{d\vec{M}}{dt}, \tag{1.19}$$

with $\alpha \ll 1$ as the Gilbert damping constant and $M_s = |\vec{M}|$ as the saturation magnetization.

As desired, Equation 1.19 keeps the saturation magnetization M_s constant

$$\frac{d}{dt} M_s^2 = \frac{d}{dt} |\vec{M}|^2 = 2\vec{M} \frac{d\vec{M}}{dt} = 2\vec{M} \cdot \left(-\gamma \vec{M} \times \vec{H}_{\text{eff}} + \frac{\alpha}{M_s} \vec{M} \times \frac{d\vec{M}}{dt}\right) = 0. \tag{1.20}$$

Equation 1.19 is written in an implicit form with $d\vec{M}/dt$ appearing on both sides. To transform it to an explicit form, where the time derivative only appears at the left hand side, one uses the Grassmann identity $\vec{a} \times (\vec{b} \times \vec{c}) = (\vec{a} \cdot \vec{c}) \cdot \vec{b} - (\vec{a} \cdot \vec{b}) \cdot \vec{c}$, takes the vector product with $\vec{M}$ on both sides and gets

$$\vec{M} \times \frac{d\vec{M}}{dt} = -\gamma \vec{M} \times \left(\vec{M} \times \vec{H}_{\text{eff}}\right) + \frac{\alpha}{M_s} \left[\left(\vec{M} \cdot \frac{d\vec{M}}{dt}\right) \cdot \vec{M} - \vec{M} \cdot \vec{M} \frac{d\vec{M}}{dt}\right]. \tag{1.21}$$

Since $\vec{M} \cdot d\vec{M}/dt = 1/2 \cdot d/dt(M_s^2) = 0$ and $\vec{M} \cdot \vec{M} = |M|^2 = M_s^2$, one finds

$$\vec{M} \times \frac{d\vec{M}}{dt} = -\gamma \vec{M} \times \left(\vec{M} \times \vec{H}_{\text{eff}}\right) - \alpha M_s \cdot \frac{d\vec{M}}{dt}. \tag{1.22}$$

The right hand side of Equation 1.22 is inserted in Equation 1.19 and one obtains

$$\frac{d\vec{M}}{dt} = -(\gamma\vec{M} \times \vec{H}_{\text{eff}}) + \frac{\alpha}{M_s}\left[-\gamma\vec{M} \times (\vec{M} \times \vec{H}_{\text{eff}}) - \frac{\alpha}{M_s}\frac{d\vec{M}}{dt}\right], \tag{1.23}$$

$$\frac{d\vec{M}}{dt} = -\gamma\left(\vec{M} \times \vec{H}_{\text{eff}}\right) - \frac{\alpha}{M_s}\gamma\vec{M} \times (\vec{M} \times \vec{H}_{\text{eff}}) - \alpha^2\frac{d\vec{M}}{dt}. \tag{1.24}$$

The time derivative is moved from the right hand side to the left hand side, one factors out $(1+\alpha^2)$ and one gains the explicit Landau-Lifshitz-equation:

$$\frac{d\vec{M}}{dt}(1+\alpha^2) = -\gamma\vec{M} \times \vec{H}_{\text{eff}} - \gamma\frac{\alpha}{M_s}\vec{M} \times \left(\vec{M} \times \vec{H}_{\text{eff}}\right) \tag{1.25}$$

$$\Longrightarrow \frac{d\vec{M}}{dt} = -\gamma'\vec{M} \times \vec{H}_{\text{eff}} - \gamma'\frac{\alpha}{M_s}\vec{M} \times \left(\vec{M} \times \vec{H}_{\text{eff}}\right). \tag{1.26}$$

In the last step, an effective gyromagnetic ratio $\gamma' = \gamma/(1+\alpha^2)$ is introduced. Equation 1.26 consists of two terms. The first term on the right hand side describes a precessional motion of the magnetization $\vec{M}$ around the effective magnetic field $\vec{H}_{\text{eff}}$. The second term leads to a damped motion, which results in the magnetization $\vec{M}$ being parallel with the effective field $\vec{H}_{\text{eff}}$. The last step to check is the energy dissipation which is expected to be negative. Both sides of Equation 1.19 are multiplied with the cross product of $\vec{M}$. One obtains

$$\vec{M} \times \frac{d\vec{M}}{dt} = -\gamma\vec{M} \times \left(\vec{M} \times \vec{H}_{\text{eff}}\right) + \frac{\alpha}{M_s}\vec{M} \times \left(\vec{M} \times \frac{d\vec{M}}{dt}\right) \tag{1.27}$$

with the help of the already former used Grassman identity, one finds as before in Equation 1.22

$$\vec{M} \times \frac{d\vec{M}}{dt} = -\gamma\left[\left(\vec{M} \cdot \vec{H}_{\text{eff}}\right) \cdot \vec{M} - M_s^2\vec{H}_{\text{eff}}\right] - \alpha M_s \cdot \frac{d\vec{M}}{dt}. \tag{1.28}$$

If Equation 1.28 is solved for $\vec{H}_{\text{eff}}$, one obtains

$$\vec{H}_{\text{eff}} = \frac{1}{\gamma M_s^2}\vec{M} \times \frac{d\vec{M}}{dt} + \frac{\alpha}{\gamma M_s}\frac{d\vec{M}}{dt} + \frac{1}{M_s^2}\left(\vec{M} \cdot \vec{H}_{\text{eff}}\right) \cdot \vec{M} \tag{1.29}$$

by the aid of Equation 1.29, it is possible to calculate the energy dissipation:

$$\frac{dE}{dt} = \int dV \frac{\delta E}{\delta M}\frac{d\vec{M}}{dt}, \tag{1.30}$$

$$\frac{dE}{dt} = -\mu_0 \int dV \vec{H}_{\text{eff}} \cdot \frac{d\vec{M}}{dt} \tag{1.31}$$

where Equation 1.16 has been used to exchange $\delta E/\delta M$ by the effective field $\vec{H}_{\text{eff}}$. By using the expression determined in Equation 1.29, one obtains

$$\frac{dE}{dt} = -\mu_0 \int dV \left(\frac{1}{\gamma M_s^2}\vec{M} \times \frac{d\vec{M}}{dt} + \frac{\alpha}{\gamma M_s}\frac{d\vec{M}}{dt} + \frac{1}{M_s^2}\left(\vec{M} \cdot \vec{H}_{\text{eff}}\right) \cdot \vec{M}\right) \cdot \frac{d\vec{M}}{dt}. \tag{1.32}$$

The first term $\propto (\vec{M} \times d\vec{M}/dt) \cdot d\vec{M}/dt$ vanishes due to the attributes of the vector product and the scalar product. The last term $\propto \vec{M} \cdot d\vec{M}/dt = 1/2 \cdot d/dt(M_s^2)$ vanishes since M_s is constant. This yields

$$\frac{dE}{dt} = -\frac{\mu_0\alpha}{\gamma M_s}\int dV \left(\frac{d\vec{M}}{dt}\right)^2 < 0. \tag{1.33}$$

In the static case $d\vec{M}/dt$ vanishes and the energy minimum is reached, while in the dynamic case the energy dissipation is always negative. If the total motion of the magnetization for the two scenarios is sketched as calculated in Equation 1.14 and Equation 1.26, a picture as follows is found:

In Figure 1.3a) the precessional motion of the magnetization $\vec{M}$ around the effective magnetic field $\vec{H}_{\text{eff}}$ without any damping is drawn. As a result of the lacking damping, $\vec{M}$ can never reach its energy minimum being parallel to $\vec{H}_{\text{eff}}$, in contrast for the situation drawn in Figure 1.3b). As a result of the introduced damping term, the magnetization follows a spiral curve, reaching the energy minimum once the magnetization $\vec{M}$ is parallel to the effective field $\vec{H}_{\text{eff}}$.

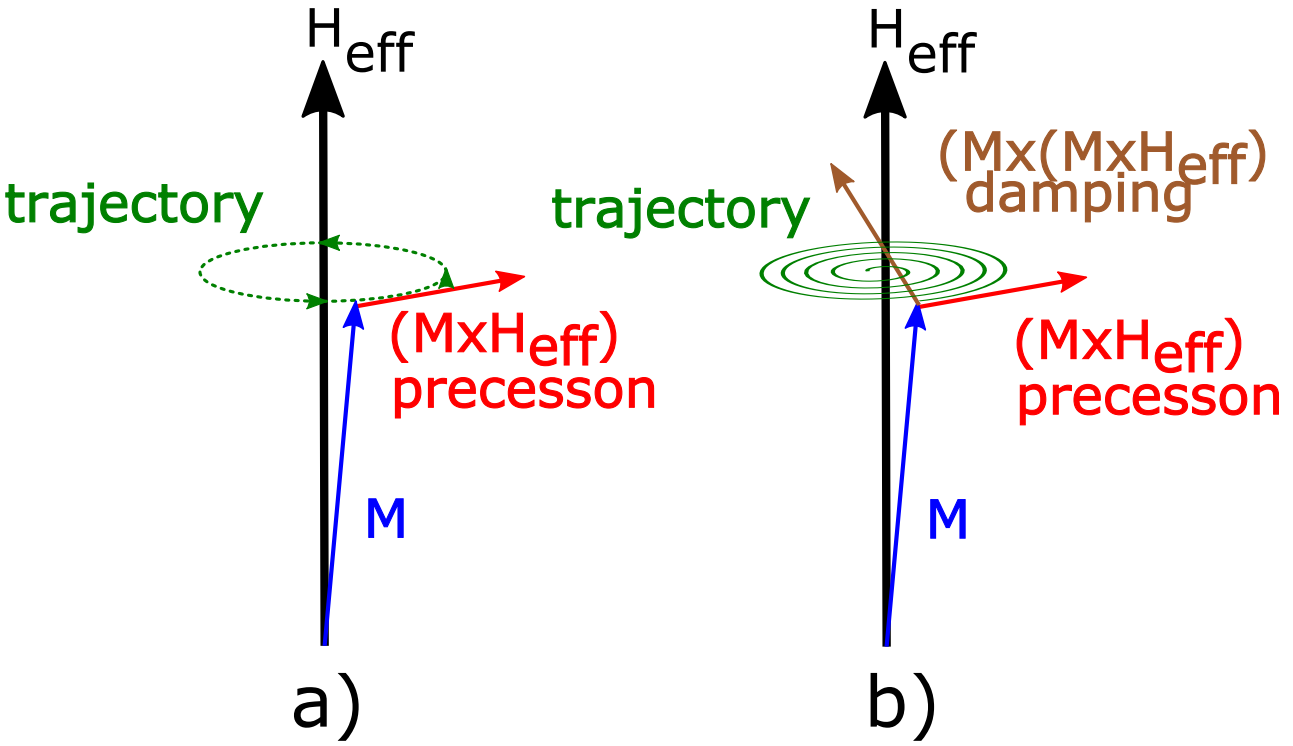

Fig. 1.3. Schematic time evolution of the magnetization $\vec{M}$.
a) Without any damping, the magnetization $\vec{M}$ precesses around the the effective field $\vec{H}_{\text{eff}}$, never reaching its energy minimum.
b) With an included damping term, the magnetization $\vec{M}$ follows a spiral trajectory until it reaches the energy minimum being parallel to the effective field $\vec{H}_{\text{eff}}$.

1.3. Contributions To The Landau Free Energy

To solve Equation 1.26 and to calculate the evolution of the magnetization $\vec{M}$ in time, a determination of the effective field $\vec{H}_{\text{eff}}$ is required. This effective field can be determined from different energy contributions to the Landau free energy, as described in the following subsections.

1.3.1. Zeeman energy

Zeeman energy is the energy contribution to the Landau free energy due to the presence of an external magnetic field $\vec{H}_{\text{ext}}$. The magnetization $\vec{M}$ favours being aligned with this external field and therefore the term is given by

$$E_Z = -\mu_0 \int dV \vec{H}_{\text{ext}} \cdot \vec{M} \tag{1.34}$$

The corresponding effective field is simply

$$H_Z = H_{\text{ext}} \tag{1.35}$$

1.3.2. Exchange energy

The exchange energy favours a parallel alignment of spins and can only be explained using quantum mechanics. For the calculation, an interaction between neighbouring spin is assumed and a Heisenberg type of interaction [31] is used. One can write the exchange energy E_{ex} as

$$E_{\text{ex}} = -J \sum_{<i,j>} \vec{S}_i \cdot \vec{S}_j, \tag{1.36}$$

with the sum being taken over all neighbouring spins and J being the exchange constant. The convention is used that each summand is only taken once. Equation 1.36 can be written as follows:

$$E_{\text{ex}} = -J \sum_i \sum_{NN} \vec{S}_i \vec{S}_{NN} = -J|\vec{S}|^2 \sum_i \sum_{NN} \cos(\phi_{i,NN}) \tag{1.37}$$

NN are the nearest neighbours of the i-th spin and $\phi_{i,NN}$ is the angle between the i-th spin and the corresponding next neighbour. By introducing the magnetization $\vec{M}$, one obtains

$$\left(\vec{M}(\vec{r}_i + \vec{r}_{NN}) - \vec{M}(\vec{r}_i)\right)^2 = 2M_s^2 - 2M_s^2 \cos\phi_{i,NN} \tag{1.38}$$

with $\vec{r}_{NN}$ as the distance vector between neighbouring spins. Equation 1.38 is inserted into the Heisenberg model Equation 1.37. The term $2M_s^2$ is neglected since it is constant and only energy differences are considered. One obtains

$$E_{\text{ex}} = \frac{JS^2}{2M_s^2} \sum_i \sum_{NN} \left(M(\vec{r}_i + \vec{r}_{NN}) - \vec{M}(\vec{r}_i)\right)^2. \tag{1.39}$$

In the continuum limit, the length scale of the magnetization changes is large compared to the distance between two spins, leading to small angles between neighbouring spins. Therefore, the magnetisation can be expanded in a Taylor expansion up to the first order which yields

$$E_{\text{ex}} = \frac{JS^2}{2M_s^2} \sum_i \sum_{NN} \left((\vec{r}_{NN}\vec{\nabla})\ \vec{M}(\vec{r}_i)\right)^2. \tag{1.40}$$

In the case of a simple cubic lattice with lattice parameter a, each spin has six nearest neighbours with the distance vectors $\vec{r}_{NN}$ as follows: $\vec{r}_{c,1} = (a,0,0)$, $\vec{r}_{c,2} = (-a,0,0)$, $\vec{r}_{c,3} = (0,a,0)$, $\vec{r}_{c,4} = (0,-a,0)$, $\vec{r}_{c,5} = (0,0,a)$ and $\vec{r}_{c,6} = (0,0,-a)$.
For a body-centred cubic lattice, one finds for each spin eight neighbours with the following distance vectors: $\vec{r}_{bcc,1} = (a/2,a/2,a/2)$, $\vec{r}_{bcc,2} = (-a/2,a/2,a/2)$, $\vec{r}_{bcc,3} = (a/2,-a/2,a/2)$, $\vec{r}_{bcc,4} = (a/2,a/2,-a/2)$, $\vec{r}_{bcc,5} = (-a/2,-a/2,a/2)$, $\vec{r}_{bcc,6} = (-a/2,a/2,-a/2)$ $\vec{r}_{bcc,7} = (a/2,-a/2,-a/2)$ and $\vec{r}_{bcc,8} = (-a/2,-a/2,-a/2)$.
In the third case of a face-centred cubic lattice, each spin has twelve neighbours with the distance vectors $\vec{r}_{fcc,1} = (0,a/2,a/2)$, $\vec{r}_{fcc,2} = (0,-a/2,a/2)$, $\vec{r}_{fcc,3} = (0,a/2,-a/2)$, $\vec{r}_{fcc,4} = (0,-a/2,-a/2)$, $\vec{r}_{fcc,5} = (a/2,0,a/2)$, $\vec{r}_{fcc,6} = (-a/2,0,a/2)$,$\vec{r}_{fcc,}(a/2,0,-a/2)$, $\vec{r}_{fcc,8} = (-a/2,0,-a/2)$, $\vec{r}_{fcc9} = (a/2,a/2,0)$, $\vec{r}_{fcc,10} = (-a/2,a/2,0)$,$\vec{r}_{fcc,11} = (a/2,-a/2,0)$ and $\vec{r}_{fcc,12} = (-a/2,-a/2,0)$.
For all three cubic lattice types, one finds for the exchange energy E_{ex}

$$E_{\text{ex}} = \frac{JS}{2M_s^2} \sum_i \left(2a^2 \left[\left(\frac{\partial\vec{M}}{\partial x}\right)^2 + \left(\frac{\partial\vec{M}}{\partial y}\right)^2 + \left(\frac{\partial\vec{M}}{\partial z}\right)^2\right]\right). \tag{1.41}$$

With the introduction of the spin density c_s/a^3 with c_s the number of spins per unit cell (1 for a simple cubic lattice, 2 for a body centred cubic lattice and 4 for a face centred cubic lattice) one finds

$$E_{\text{ex}} = \frac{JS}{M_s^2 a^2} \int dV \; \frac{c_s}{a^3} \left(\left[\left(\frac{\partial \vec{M}}{\partial x} \right)^2 + \left(\frac{\partial \vec{M}}{\partial y} \right)^2 + \left(\frac{\partial \vec{M}}{\partial z} \right)^2 \right] \right) \tag{1.42}$$

which is simplified by the introduction of the exchange constant $A = JS/a$ as follows:

$$E_{\text{ex}} = \frac{A}{M_s^2} \int dV \; \left(\left(\frac{\partial \vec{M}}{\partial x} \right)^2 + \left(\frac{\partial \vec{M}}{\partial y} \right)^2 + \left(\frac{\partial \vec{M}}{\partial z} \right)^2 \right). \tag{1.43}$$

The exchange field $\vec{H}_{\text{ex}}(\vec{r})$ can now be determined and one finds

$$\vec{H}_{\text{ex}}(\vec{r}) = -\frac{1}{\mu_0} \frac{\delta E_E}{\delta \vec{M}(\vec{r})}, \tag{1.44}$$

$$\vec{H}_{\text{ex}}(\vec{r}) = -\frac{2A}{\mu_0 M_s} \int dV' \; \left(\frac{\partial \vec{M}(\vec{r})}{\partial x'} \frac{\partial \delta^3(\vec{r}\,' - \vec{r})}{\partial x'} + \frac{\partial \vec{M}(\vec{r})}{\partial y'} \frac{\partial \delta^3(\vec{r}\,' - \vec{r})}{\partial y'} + \frac{\partial \vec{M}(\vec{r})}{\partial z'} \frac{\partial \delta^3(\vec{r}\,' - \vec{r})}{\partial z'} \right). \tag{1.45}$$

By integration by parts, one determines $\vec{H}_{\text{ex}}(\vec{r})$ to be

$$\vec{H}_{\text{ex}}(\vec{r}) = \frac{2A}{\mu_0 M_s^2} \int dV' \; \left(\frac{\partial^2 \vec{M}(\vec{r})}{\partial^2 x'^2} \delta^3(\vec{r}\,' - \vec{r}) + \frac{\partial^2 \vec{M}(\vec{r})}{\partial^2 y'^2} \delta^3(\vec{r}\,' - \vec{r}) + \frac{\partial^2 \vec{M}(\vec{r})}{\partial^2 z'^2} \delta^3(\vec{r}\,' - \vec{r}) \right), \tag{1.46}$$

$$\vec{H}_{\text{ex}}(\vec{r}) = \frac{2A}{\mu_0 M_s^2} \left(\frac{\partial^2 \vec{M}(\vec{r})}{\partial x^2} + \frac{\partial^2 \vec{M}(\vec{r})}{\partial y^2} + \frac{\partial^2 \vec{M}(\vec{r})}{\partial z^2} \right), \tag{1.47}$$

$$\vec{H}_{\text{ex}}(\vec{r}) = \frac{2A}{\mu_0 M_s^2} \vec{\nabla}^2 \vec{M}. \tag{1.48}$$

The boundary terms in the integration by parts vanish due to the Dirac-δ function which is localized at the position $\vec{r}$.

1.3.3. Stray field energy

In contrast to the Zeeman energy E_Z, which describes the energy of the magnetization in the presence of an external magnetic field, the demagnetization or stray field energy deals with the energy contribution of the long-distance dipolar interaction of the magnetic moments with each other.

Beginning with Ampère's law [32] one can write:

$$\vec{\nabla} \times \vec{H}_{\text{dip}} = \vec{j}_{\text{eff}} + \frac{\partial \vec{D}}{\partial t}, \tag{1.49}$$

with $\vec{j}_{\text{ext}}$ as the current density and $\vec{D}$ as the electric displacement field. In the absence of any applied currents and any external fields, Equation 1.49 simplifies to

$$\vec{\nabla} \times \vec{H}_{\text{dip}} = 0, \tag{1.50}$$

which means that $\vec{H}_{\text{dip}}$ is a conservative vector field and can be written by the aid of a scalar potential Φ_{dip}. Together with Gauss's law for the magnetic flux density $\vec{B}$ this yields

$$\vec{H}_{\text{dip}} = -\vec{\nabla} \left(\Phi_{\text{dip}} \right) \tag{1.51}$$

$$\vec{\nabla} \cdot \vec{B} = 0 \text{ and } \vec{B} = \mu_0 (\vec{H} + \vec{M}) \tag{1.52}$$

$$\Longrightarrow \triangle \Phi_{\text{dip}} = \vec{\nabla} \left(\vec{\nabla} \left(\Phi_{\text{dip}} \right) \right) = -\vec{\nabla} \left(\vec{H}_{dip} \right) = \vec{\nabla} \left(\vec{M} \right). \tag{1.53}$$

Φ_{dip} fulfils the Poisson equation for which the solution can be found in many textbooks on classical field theory, e.g. [32] and one finds

$$\Phi_{\text{dip}}(\vec{r}) = \frac{1}{4\pi}\int dV' \ \frac{1}{|\vec{r}-\vec{r}\,'|}\ \left(-\vec{\nabla}'(\vec{M}(\vec{r}))\right) + \frac{1}{4\pi}\int d\vec{S}\,' \ \frac{1}{|\vec{r}-\vec{r}\,'|}\ \vec{M}(\vec{r}). \tag{1.54}$$

The first integral integrates over the volume V of the sample and is the solution of the Possion equation. The second integral accounts for the boundaries, i.e. the surface of the sample S with $\vec{S}\,' = S'\vec{n}(\vec{r})$ as the component normal to the surface. With Equation 1.53 it is possible able to determine the stray field $\vec{H}_{\text{dip}}$ and one obtains

$$H_{\text{dip}}(\vec{r}) = -\vec{\nabla}\left(\frac{1}{4\pi}\int dV' \ \frac{1}{|\vec{r}-\vec{r}\,'|}\ \left(-\vec{\nabla}'(\vec{M}(\vec{r}))\right) + \frac{1}{4\pi}\int d\vec{S}\,' \ \frac{1}{|\vec{r}-\vec{r}\,'|}\ \vec{M}(\vec{r})\right). \tag{1.55}$$

The stray field energy E_{dip} is given as the scalar product of $\vec{M}$ and $\vec{H}_{\text{dip}}$. This yields

$$E_{\text{dip}} = -\frac{\mu_0}{2}\int dV \ \vec{M}(\vec{r})\cdot\vec{H}_{\text{dip}}(\vec{r}),$$

with the factor $1/2$ due to the double integration over the volume V

$$E_{\text{dip}} = \frac{\mu_0}{8\pi}\int dV \ \vec{M}(\vec{r})\ \vec{\nabla}\left(\int dV' \ \frac{1}{|\vec{r}-\vec{r}\,'|}\ \left(-\vec{\nabla}'(\vec{M}(\vec{r}))\right) + \int d\vec{S}\,' \ \frac{1}{|\vec{r}-\vec{r}\,'|}\ \vec{M}(\vec{r})\right). \tag{1.56}$$

By changing the integration order and reordering the two integrals, one obtains

$$E_{\text{dip}} = \frac{\mu_0}{8\pi}\int dV' \ \left(-\vec{\nabla}'\left(\vec{M}(\vec{r})\right) + d\vec{S}\,' \ \vec{M}(\vec{r})\right)\int dV \ \vec{M}(\vec{r})\ \vec{\nabla}\left(\frac{1}{|\vec{r}-\vec{r}\,'|}\right). \tag{1.57}$$

With the aid of the Gauss's theorem, one can write

$$\int d\vec{S} \ \frac{1}{|\vec{r}-\vec{r}\,'|}\ \vec{M}(\vec{r}) = \int dV \ \vec{\nabla}\left(\frac{1}{|\vec{r}-\vec{r}\,'|}\ \vec{M}(\vec{r})\right), \tag{1.58}$$

$$\int d\vec{S} \ \frac{1}{|\vec{r}-\vec{r}\,'|}\ \vec{M}(\vec{r}) = \int dV \ \frac{1}{|\vec{r}-\vec{r}\,'|}\ \vec{\nabla}\left(\vec{M}(\vec{r})\right) + \int dV \ \vec{M}(\vec{r})\ \vec{\nabla}\left(\frac{1}{|\vec{r}-\vec{r}\,'|}\right), \tag{1.59}$$

$$\Longrightarrow \int dV \ \vec{M}(\vec{r})\vec{\nabla}\left(\frac{1}{|\vec{r}-\vec{r}\,'|}\right) = \int d\vec{S} \ \frac{1}{|\vec{r}-\vec{r}\,'|}\ \vec{M}(\vec{r}) - \int dV \ \frac{1}{|\vec{r}-\vec{r}\,'|}\ \vec{\nabla}\left(\vec{M}(\vec{r})\right). \tag{1.60}$$

If Equation 1.60 is inserted in the last integral of Equation 1.57, one finds

$$E_{\text{dip}} = \frac{\mu_0}{8\pi}\int dV \ \left(-\vec{\nabla}\left(\vec{M}(\vec{r})\right) + d\vec{S}\vec{M}(\vec{r})\right)\int dV' \ \frac{1}{|\vec{r}-\vec{r}\,'|}\left(-\vec{\nabla}\left(\vec{M}(\vec{r})\right) + d\vec{S}\vec{M}(\vec{r})\right). \tag{1.61}$$

By introducing $\rho_V(\vec{r}) = -\vec{\nabla}\left(\vec{M}(\vec{r})\right)$ as the volume charges and $\sigma_S(\vec{r}) = \vec{M}(\vec{r})\cdot\vec{n}(\vec{r})$ as the surface charges, Equation 1.61 can be written in its standard form which reads:

$$E_{\text{dip}} = \frac{\mu_0}{8\pi}\left(\int dV \ \rho_V(\vec{r}) + \int d\vec{S} \ \sigma_S(\vec{r})\right)\left(\left(\int dV' \ \rho_V(\vec{r}\,') + \int d\vec{S}\,' \ \sigma_S(\vec{r}\,')\right)\frac{1}{|\vec{r}-\vec{r}\,'|}\right). \tag{1.62}$$

By Gauss's theorem, it is additionally possible to rewrite Equation 1.56

$$E_{\text{dip}} = \frac{\mu_0}{8\pi}\int dV \ \vec{M}(\vec{r})\ \vec{\nabla}\left(\int dV' \ \frac{1}{|\vec{r}-\vec{r}\,'|}\ \left(-\vec{\nabla}'(\vec{M}(\vec{r}))\right) + \int d\vec{S}\,' \ \frac{1}{|\vec{r}-\vec{r}\,'|}\ \vec{M}(\vec{r})\right) \tag{1.63}$$

which yields

$$E_{\text{dip}} = \frac{\mu_0}{8\pi} \int dV \int dV' \; \vec{M}(\vec{r}) \; \vec{\nabla} \left(\vec{M}(\vec{r}) \; \vec{\nabla}\,' \left(\frac{1}{\sqrt{(\vec{r}-\vec{r}\,')^2}} \right) \right), \tag{1.64}$$

$$E_{\text{dip}} = \frac{\mu_0}{8\pi} \int dV \int dV' \; \vec{M}(\vec{r}) \vec{\nabla} \left(\frac{\vec{M}(\vec{r})(\vec{r}-\vec{r}\,')}{\sqrt[3]{(\vec{r}-\vec{r}\,')^2}} \right), \tag{1.65}$$

$$E_{\text{dip}} = \frac{\mu_0}{8\pi} \int dV \int dV' \left(\frac{\vec{M}(\vec{r}) \cdot \vec{M}(\vec{r})}{\sqrt[3]{(\vec{r}-\vec{r}\,')^2}} - 3\frac{(\vec{M}(\vec{r})(\vec{r}-\vec{r}\,')) \cdot (\vec{M}(\vec{r})(\vec{r}-\vec{r}\,'))}{\sqrt[5]{(\vec{r}-\vec{r}\,')^2}} \right), \tag{1.66}$$

which is the energy of a field of magnetic dipoles with dipole density $\vec{M}(\vec{r})$ at position $\vec{r}$.

1.3.4. Anisotropy energies

Up to now in this section, the Heisenberg model, introduced in Equation 1.36, has been used to describe ferromagnetism. Since in the Heisenberg model the energy only depends on the relative orientation of the spins and is therefore anisotropic, it is insufficient to describe real ferromagnetism in real crystals. In real systems it is found that the energy of the system depends on the orientation of the spins with respect to the crystallographic directions leading to so-called "easy" and "hard" magnetic axes [33]. This anisotropy is based on the interaction of the crystalline ordered electronic orbitals and the spin moments, i.e. spin orbit coupling. Depending on the crystal symmetries, different symmetries are found for the anisotropies and the anisotropy is larger, the lower the symmetry of the crystal [34, 35].

The calculation is started with the anisotropy energy and follows [36]. One can write

$$E_{\text{ani}} = \int dV \epsilon_{\text{ani}}, \tag{1.67}$$

with ϵ_{ani} as the anisotropy energy density. Compared to the large exchange energy, anisotropy energies are small and allow for a series expansion. One obtains for ϵ_{ani}

$$\epsilon_{\text{ani}} = \epsilon_0 + \sum_{i,j} K_{i,j}\alpha_i\alpha_j + \sum_{i,j,k,l} K_{i,j,k,l}\alpha_i\alpha_j\alpha_k\alpha_l + ... + . \tag{1.68}$$

The first term in the sum is neglected since only energy differences are relevant. The constants K_i are temperature dependent anisotropy constants and α_i are the direction cosines to the z-axis. Due to the time inversion symmetry of the magnetization, only even terms in the magnetization will occur. In the simplest case of uniaxial anisotropy, for which the energy depends on the angle θ to a single axis (e.g. the stacking axis of the hexagonally closed packed planes for cobalt [37]) one finds

$$\epsilon_{\text{ani}}^{ua} = K_1 \sin^2\theta + K_2 \sin^4(\theta), \tag{1.69}$$

with θ as the angle between the stacking axis and the magnetization direction. Neglecting the forth order for a moment and assuming K_1 is positive, the uniaxial energy density becomes minimal for the magnetization being parallel to the stacking axis, i.e. the z-axis. In the case of a negative K_1, the hard axis is found to be parallel to the z-axis and therefore a preferred magnetization orientation in the xy-plane.

In a cubic system such as iron or nickel, the cubic anisotropy can be determined up to the 6-th order with the phenomenological ansatz as follows:
As for the case of uniaxial anisotropy, only even terms will occur due to the time reversal symmetry of the magnetization and therefore the anisotropy will be a function of M_x^2, M_y^2 and M_z^2. Due to the 90° rotation and the consequent four fold symmetry, the exchange of components, e.g. M_x^2 with M_y^2, keeps the anisotropy constant. There are therefore up to the 6-th order six linearly independent terms:

M_s^2,M_s^4,Ms^6, $M_x^2M_y^2M_z^2$, $M_x^2M_y^2$, $M_x^2M_z^2$ and $M_y^2M_z^2$ where the first three terms will be neglected since they are constant. Ordering these terms according to their power in M_i leads to

$$\epsilon_{\text{ani}}^{c} = K_1(M_x^2M_y^2 + M_x^2M_y^2 + M_y^2M_z^2) + K_2M_x^2M_y^2M_z^2 + ... + . \tag{1.70}$$

To give some numbers for the anisotropy constants, cubic Fe and cubic Ni have K_1 equal to $4.8{\cdot}10^4\text{J/m}^3$ and $-5.7 \cdot 10^3\text{J/m}^3$ respectively, while hexagonal Co has K_1 equal to $5.0 \cdot 10^5\text{J/m}^3$. In low symmetry permanent magnets like $Nd_2Fe_{14}B$ and $SmCo_5$, K_1 is determined to be $5 \cdot 10^6\text{J/m}^3$ and $1.7 \cdot 10^7\text{J/m}^3$ respectively [37].

After treating the relevant contributions to the Landau free energy, it is possible to solve the Landau Lifshitz Gilbert Equation 1.26 in order to determine the time evolution of the magnetization.

1.4. Magnetic Domain Walls

In this section, magnetic domain walls will be discussed, important singularities which can dramatically influence spin structure dynamics such as reversal modes of magnetic states in the magnetization field. Weiss was the first to propose the idea that a ferromagnet contains small areas, termed domains, in which the local magnetization reaches the saturation magnetization [38, 39].

These domains are separated by domain walls. By the introduction of the concepts of domains and domain walls, Weiss could additionally explain why some magnetic samples require much lower magnetic fields to be completely magnetized, than those what would be expected based on saturation magnetization, but where the magnetization direction differ from one domain to the next, resulting in a lower total magnetization for the system as a whole. In these samples, the magnetic moments within the domains are ordered at room temperature, but without any applied field, the domains may not be aligned. An external field shrinks the unfavoured domains that are not aligned with the field and increases the size of the aligned domains.

If two neighbouring domains show opposite magnetization, one calls the domain wall between the two domains a 180° domain wall, while for perpendicular magnetized domains, the domain wall is a 90° one. The size and form of a domain wall is mainly determined by the counter play of the exchange energy and the stray field energy. The short range exchange energy favours a parallel alignment of the spins and therefore wide walls are preferred while the long range dipolar stray field energy becomes minimal for a flux closure magnetization pattern with narrow walls.

In a simple picture, the magnetization can be modelled as a one-dimensional spin chain. In such a spin chain, there are two main ways to rotate the magnetization by 180°. In Figure 1.4, these two 180° domain walls are shown schematically [40]. In a Bloch wall, which is the most common 180° domain wall, the magnetization rotates in a plane parallel to the domain wall plane.

In a Néel wall, the magnetization rotates in a plane perpendicular to the domain wall plane, leading to an out-of-plane component. Néel walls are preferred in very thin magnetic films.

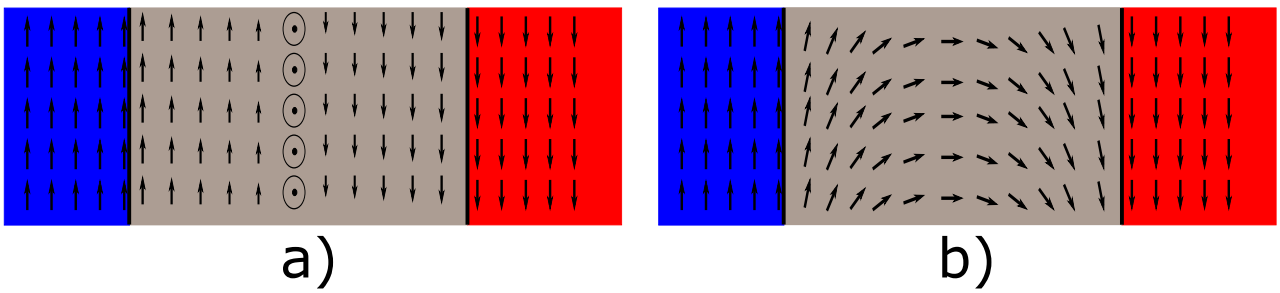

Fig. 1.4. Schematics of two 180° domain walls.
a) Bloch domain wall, in which the magnetization rotates parallel to the wall plane.
b) Néel domain wall with the magnetization rotating in a plane perpendicular to the wall plane.

In the next step, the domain wall width for a one-dimensional spin chain is determined by finding the energy minimum of exchange energy and anisotropy energy. One can write for the exchange energy E_{ex}

$$E_{\mathrm{ex}} = -2J \cdot S^2 \cos\phi. \tag{1.71}$$

As before, small angles between two neighboured spins are assumed and the $\cos\phi$ is developed in its Taylor expansion which yields

$$E_{\mathrm{ex}} = -2J \cdot S^2 \left(1 - \frac{\phi^2}{2}\right). \tag{1.72}$$

By neglecting the constant term $-2J \cdot S^2$ one obtains for the energy difference ΔE_{ex}

$$\Delta E_{\mathrm{ex}} = J \cdot S^2 \phi^2. \tag{1.73}$$

Changing to a system with $2n$ spins and defining a macroscopic angle $\phi_* = n \cdot \phi$ yields

$$\Delta E_{\mathrm{ex}}^n = 1 \cdot J \cdot S^2 \cdot \phi_*^2 = n^2 \cdot J \cdot S^2 \cdot \phi^2. \tag{1.74}$$

Considering a simple cubic lattice with side length a, one finds for the exchange energy density Δe_{ex} and for the anisotropy energy density Δe_{ani}

$$\Delta e_{\mathrm{ex}} = \frac{\Delta E_{\mathrm{ex}}}{A} = \frac{\pi^2 J_{\mathrm{ex}} S^2}{na^2} \tag{1.75}$$

$$\Delta e_{\mathrm{ani}} = \frac{\Delta E_{\mathrm{ani}}}{A} = \frac{Kna}{2} \tag{1.76}$$

where A is the area of the sample. Calculating the energy minimum of the total energy E_{tot} with respect to n yields

$$\begin{aligned} \frac{\partial}{\partial n}\left(\frac{E_{\mathrm{tot}}}{A}\right) &= -\frac{\pi^2 \cdot J \cdot S^2}{n^2 \cdot a^2} + \frac{K \cdot a}{2} \stackrel{!}{=} 0 \\ \Longrightarrow n^2 a^2 &= \frac{2a\pi^2 J S^2}{K}. \end{aligned} \tag{1.77}$$

By defining the thickness $\lambda = n \cdot a$ of the domain wall, one obtains

$$\lambda \propto \sqrt{\frac{J}{K}}. \tag{1.78}$$

This result can be explained as follows. The exchange energy E_{ex}, characterized by the exchange constant J favours small angles between neighboured spins, resulting in wide domain walls. On the other hand, the anisotropy energy E_{ani}, represented by the anisotropy constant K, favours the magnetization being parallel to the easy axis. For the anisotropy, it is therefore energetically favoured to quickly rotate the magnetization to reduce the contributions parallel to the hard axes, which results in narrow domain walls being preferred.

Up to now, only simple Bloch and Néel walls have been considered, where the magnetization is independent of the position along the wall. This is different when two-dimensional magnetic nanowires are considered [41]. In these model systems, which will play a vital role in understanding the experimental results, the drive to reduce surface charges leads to the easy axis being parallel to the wire axis. As before, two areas with opposite magnetization direction are separated by a domain wall. If the magnetization in the neighbouring domains points towards each other, it is called a head-to-head domain wall and otherwise it is named a tail-to-tail domain wall [42].

As before, there are two principal types of domain walls, the transverse wall and the vortex wall. For two-dimensional systems the type of wall that is energetically favoured crucially depends on the wire thickness t and the wire width w, as well as on the anisotropy and material parameters [43–46].

A simple, but useful model to describe which domain wall is favoured is presented in [43]. By assuming that the difference in the stray field energy of the two different types of domain wall is effectively the stray field of the transverse component of the transverse wall, the stray field energy differences ΔE_{dip} are calculated to be

$$\Delta E_{\mathrm{dip}} \propto -\frac{1}{8}\mu_0 M_s^2 t^2 w, \tag{1.79}$$

with M_s as the saturation magnetization, t the thickness and w the width of the nanowire. For the differences in the exchange energies, which are mainly given by the vortex core of the vortex domain wall, the energy difference is approximated as:

$$\Delta E_{\mathrm{ex}} \propto 2\pi t J \ln\left(\frac{r_{\mathrm{max}}}{r_{\mathrm{max}}}\right), \tag{1.80}$$

with J the exchange constant, r_{max} the outer radius of the vortex and r_{min} as the inner radius of the vortex. While the outer radius r_{max} is assumed to be $w/2$ as the half width of the strip, the inner radius r_{min} is given by the vortex core radius. To determine which domain wall is favoured as a function of thickness t and width w, the sum of the two energy differences is set to be zero and one finds

$$\Delta E_{\mathrm{ex}} + \Delta E_{\mathrm{dip}} \equiv 0 \Longrightarrow w \cdot t = const. \tag{1.81}$$

The small logarithmic dependence, present in Equation 1.80, is here neglected which results in a hyperbolic phase diagram as shown for the example of domain walls in Py (NiFe) rings in Figure 1.5.

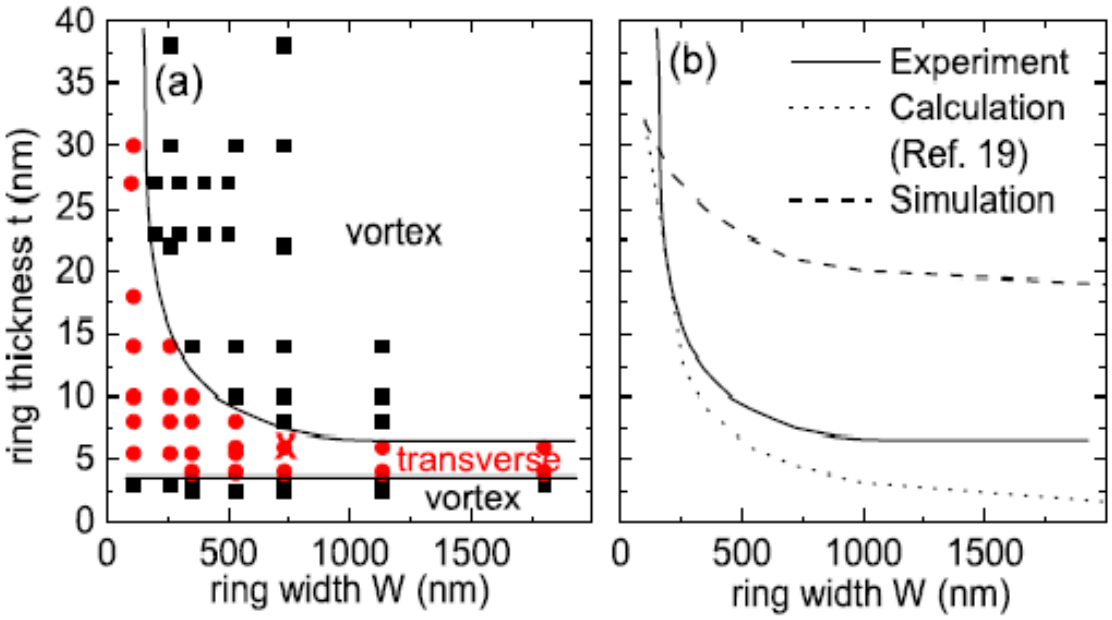

Fig. 1.5. Phase diagram for thicknesses and widths of Py rings. Reproduced from [45], with the permission of AIP Publishing. The interplay between the exchange energy E_{ex} and the stray field energy E_{dip} leads to a hyperbolic phase boundary with the vortex wall energetically favoured for wide and thick nanostructures and the transverse wall favoured for thin and narrow nanostructures.

Additionally both domain wall types can be realized in the same nanowire as either the local or global energy minimum [47]. In Figure 1.6, the transverse (TDW) and the vortex wall (VDW) in case of a head-to-head domain wall are shown with the two domains pointing towards each other.

TDW are energetically favoured for thin and narrow nanostructures [45]. In the case of the transverse wall, the magnetization rotates in the plane of the nanowire.

VDW are energetically preferred for wide and thick nanostructures. In the case of a vortex wall, the magnetization curls around the vortex core which points out of the nanowire plane.

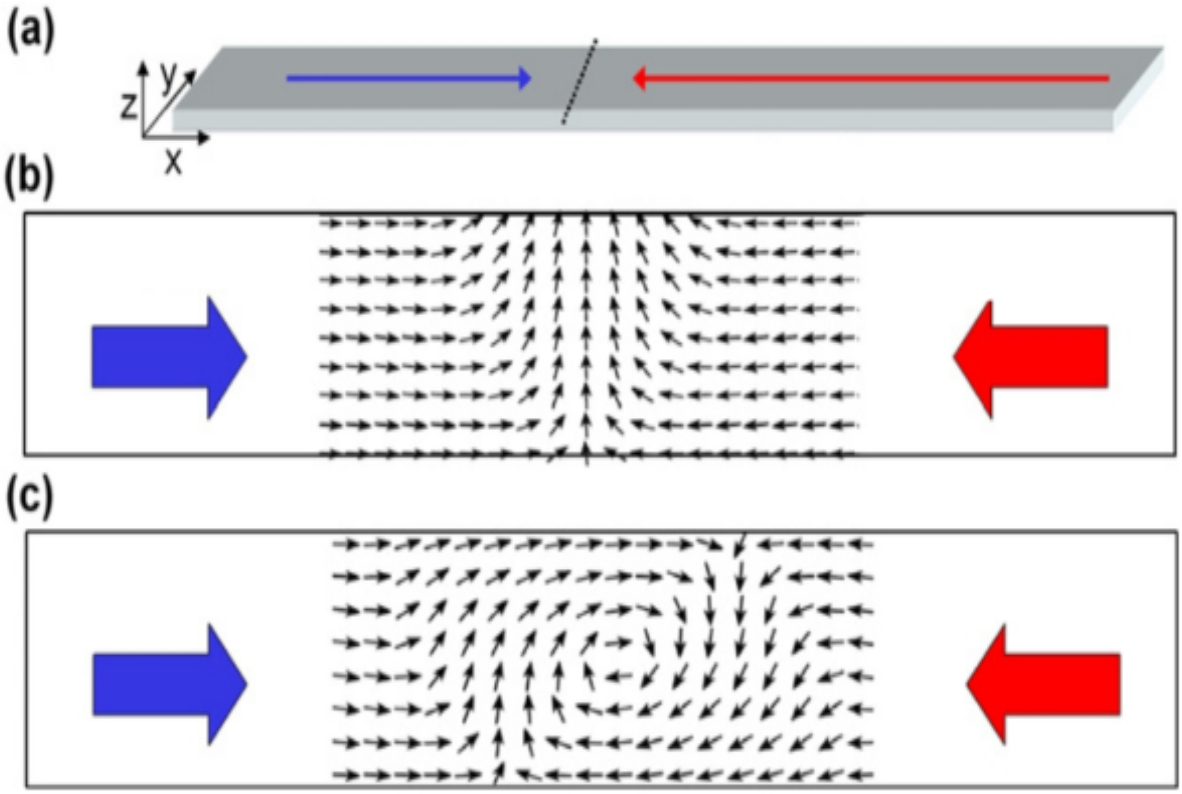

Fig. 1.6. Schematics of the two domain walls appearing in magnetic nanowires. Reproduced from [41] with the permission of IOP Publishing.
a) Schematic of a magnetic nanowire with the easy axis along the x-direction and the nanowire lying in the xy-plane. The two shown domains are separated by a head-to-head domain wall.
b) Schematic of a transverse wall with the magnetization rotating in the xy-plane.
c) Schematic of a vortex wall. The magnetization rotates around the vortex core which points out of the nanowire plane along the z-direction.

It is possible to move magnetic domain walls by applying external magnetic fields. To understand the effect of the precession and the damping term on the domain wall, the LLG-equation (Equation 1.19) is considered:

$$\frac{d\vec{m}}{dt} = \gamma_0 \vec{H}_{\text{eff}} \times \vec{m} + \alpha \vec{m} \times \dot{\vec{m}}. \tag{1.82}$$

A simple explanation is shown schematically in Figure 1.7. Two magnetic domains, pointing in either the $+x$-direction or $-x$-direction are separated by a head-to-head domain wall pointing in the $+y$-direction. An external magnetic field is applied along the $+x$-direction. If this information is inserted in the LLG-equation, one finds:

$$\frac{d\vec{m}}{dt} = \gamma_0 (\underbrace{\vec{H}_{\text{ext}}}_{+x} + \vec{H}_{\text{sf}}) \times \underbrace{\vec{m}}_{+y} + \alpha \underbrace{\vec{m}}_{+y} \times \underbrace{\dot{\vec{m}}}_{+z}. \tag{1.83}$$

The direction of $\dot{\vec{m}}$ on the right hand side is given by the precession and the resulting out-of-plane component along the $+z$-direction. The external field leads to a damping motion into the external field

along the $+x$-direction and a precessional motion out-of-plane along the $+z$-direction. This precessional motion causes a magnetic stray field pointing in the $-z$-direction, which leads to a damping torque into the $-z$-direction to reduce this stray field. The precessional motion of the magnetization around this stray field points in the $+x$-direction caused by the vector product rules. In equilibrium, the precession due to the applied external field and the damping due to the stray field cancel out, leading to an effective motion in the $+x$-direction. The domain wall therefore moves parallel to the applied field and will be destroyed at the end of the nanowire, resulting in a homogeneously magnetized wire aligned with the applied external field. It should be mentioned that this simple analysis is not the whole picture but rather depends on the amplitude of the magnetic field and the type of domain wall [48]. However, this simple example shows that the direction of the domain wall motion is consistent with our expectations, which is parallel to the applied field.

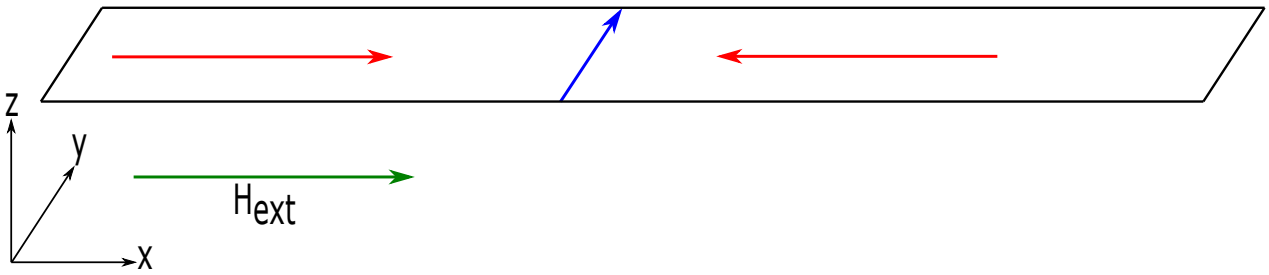

Fig. 1.7. Schematic of a magnetic nanowire with two domains pointing in the $+x$-direction and $-x$-direction which are separated by a head-to-head domain wall with magnetization pointing in the $+y$-direction. An external magnetic field is applied along the $+x$-direction. The analysis based on the LLG-equation leads to domain wall motion parallel to the applied external field.

Of particular interest in terms of the fundamental physics as well as possible employment for devices [4] is to move and manipulate magnetic domain walls by electric currents instead of external fields [49–54].
In terms of devices, field induced motion of such in-plane domain walls by in-plane fields would lead to data storage loss since different domain wall types, e.g. head-to-head and tail-to-tail domain walls, move in different directions and annihilate [55]. Secondly, field induced motion does not scale favourable on downsizing. The required magnetic field to move a domain wall stays constant which means the applied current in a strip line to generate the field increases with decreasing lateral dimensions [56].

In terms of fundamental physics, of interest is the microscopic origin of the current induced domain wall motion as well as the new arising torques acting on the magnetization. The motivation for the modified Landau-Lifshitz-Gilbert-equation, which includes the current induced domain wall motion terms, is given in the next section.

1.5. Current-Induced Magnetization Dynamics: Spin Transfer Torque

In normal, nonmagnetic metals, the spins of the itinerant electrons are randomly distributed and therefore the electric charge current is unpolarized. This is different for ferromagnetic materials, since here the itinerant ($4s$-electrons in case of Ni, Fe, Co) with their spin being antiparallel to the magnetization ($3d$-electrons) are scattered less than electrons that are parallel aligned with their spin to the magnetization.

As a consequence of the lower scattering probability, the antiparallel oriented electrons contribute more to the electric charge current, which results in a spin-polarized charge current.

In this section, which follows [57] the interaction of these spin polarized currents with a magnetic domain wall is motivated under the assumptions as follows:

- The dynamics of $\vec{m}$, given by the itinerant $4s$-electrons and described by the Bloch equation, is much faster than the dynamics of $\vec{M}$ given by the $3d$-electrons and described by the LLG-equation. Due to the different time scales, one can treat $\vec{m}$ and $\vec{M}$ separately.
- A Heisenberg type magnetic exchange interaction exists between the itinerant $4s$-electrons and the $3d$-electrons, which can be written as [58]:

$$\hat{H}_{sd} = -J_{ex} \underbrace{\vec{s}}_{4s} \underbrace{\cdot \vec{S}}_{3d}. \tag{1.84}$$

As a result of the so-called sd-interaction, the magnetization $\vec{M}$ leads to a polarisation of $\vec{m}$ as previously explained. Reciprocally, the polarized $4s$-electrons exert a torque onto the magnetization $\vec{M}$ due to the sd-exchange interaction.

Starting with the continuity relation for $\vec{s}$ yields:

$$\frac{\partial \vec{s}}{dt} + \vec{\nabla} \cdot \mathbf{J} = \frac{1}{i\hbar} \left[\vec{s}, \hat{H}_{sd}\right] - \Gamma_s(\vec{s}). \tag{1.85}$$

$\Gamma_s(\vec{s})$ represents a spin drain due to scattering and $\mathbf{J}$ is the current density tensor. The calculation of the commutator $[\vec{s}, \hat{H}_{sd}]$ yields

$$\frac{1}{i\hbar} [\vec{s}, H_{sd}] = -\frac{1}{\tau_{ex} M_s} \left(\vec{m} \times \vec{M}\right) \tag{1.86}$$

with $\tau_{\mathrm{ex}} = \hbar / S J_{ex}$ as the exchange time. By assuming $\vec{m}(\vec{r}, t) = <\vec{s}>$ and considering the continuity equation again, one finds

$$\frac{\partial \vec{m}(\vec{r}, t)}{\partial t} + \vec{\nabla} \cdot \mathbf{J} = -\frac{1}{\tau_{ex} M_s} \left(\vec{m} \times \vec{M}\right) - <\Gamma> . \tag{1.87}$$

Equation 1.87 is called a semi-classical Bloch transport equation where $<\Gamma>$ is a time averaged spin drain. The next step is to separate the spin density $\vec{m}$ into a part $\vec{m}_0$ parallel to the magnetization $\vec{M}$ and one part $\delta\vec{m}$ perpendicular to $\vec{M}$. By doing this analogously for $\mathbf{J}$, one finds

$$\begin{aligned} \vec{m}(\vec{r}, t) &= \vec{m}_0(\vec{r}, t) + \delta\vec{m}(\vec{r}, t) \\ \mathbf{J}(\vec{r}, t) &= \mathbf{J}_0(\vec{r}, t) + \delta\mathbf{J}(\vec{r}, t) = -\frac{\mu_B P}{e} \vec{j}_e \otimes \frac{\vec{M}(\vec{r}, t)}{M_s} + \delta\mathbf{J}(\vec{r}, t). \end{aligned} \tag{1.88}$$

$\vec{m}_0(\vec{r}, t)$ does not play any role for the dynamics due to the vector product and can be suppressed in the further calculation.
$\vec{j}_e \otimes \vec{M}(\vec{r}, t)$ describes the Cartesian product of the charge current density $\vec{j}_e$ and the magnetization $\vec{M}(\vec{r}, t)$ while $P = (N_\uparrow - N_\downarrow)/(N_\uparrow + N_\downarrow)$ is the spin polarization of the $3d$-electrons.

In order to solve Equation 1.87, only a linear response of $\delta\vec{m}$ on $\vec{j}_e$ and on $\partial\vec{M}/dt$ is considered and possible time derivatives $\partial\delta m/\partial t$ of $\delta\vec{m}$ are neglected. Additionally $<\Gamma>$ is substituted with $\delta\vec{m}(\vec{r}, t)/\tau_{\mathrm{sf}}$ with τ_{sf} the average time between two spin flip events. By considering a semi-classical Boltzmann equation for the current density tensor $\mathbf{J}$, one obtains

$$\delta\mathbf{J} = -D_0 \nabla \delta\vec{m} \tag{1.89}$$

with D_0 as the diffusion constant. By introducing the assumptions in Equation 1.87, one finds

$$D_0 \Delta \delta\vec{m} = \frac{1}{\tau_{\mathrm{ex}} M_s} \left(\delta\vec{m} \times \vec{M}\right) - \frac{\delta\vec{m}}{\tau_{\mathrm{sf}}} = \frac{\mu_0}{M_s} \frac{\partial \vec{M}}{\partial t} - \frac{\mu_B P}{e M_s} \left(\vec{j}_e \cdot \vec{\nabla}\right) \vec{M}. \tag{1.90}$$

It is noticeable that $\delta\vec{m}$ depends on the time derivative as well as on the spatial derivative of $\vec{M}$. Assuming wide domain walls, $\delta\vec{m}$ will change slowly due to a slow variation of $\vec{M}$. As before, second order derivations of $\delta\vec{m}$ are neglected which yields

$$\delta\vec{m} = \frac{\tau_{\mathrm{ex}}}{1+\left(\frac{\tau_{\mathrm{ex}}}{\tau_{\mathrm{sf}}}\right)^2}\left[\frac{\tau_{ex}}{\tau_{sf}}\frac{\mu_0}{M_s}\frac{\partial\vec{M}}{\partial t} - \frac{\mu_0}{M_s^2}\left(\vec{M}\times\frac{\partial\vec{M}}{\partial t}\right) + \frac{\mu_B P}{eM_s}\frac{\tau_{\mathrm{ex}}}{\tau_{\mathrm{sf}}}\left(\vec{j}_e\vec{\nabla}\vec{M}\right) + \frac{\mu_B P}{eM_s^2}\vec{M}\times\left(\vec{j}_e\vec{\nabla}\vec{M}\right)\right] \tag{1.91}$$

The acting torques caused by $\delta\vec{m}$ on the magnetization $\vec{M}$ are calculated as follows

$$T = \frac{SJ_{ex}}{\hbar M_s}\delta\vec{m}\times\vec{M}. \tag{1.92}$$

By the use of the following simplification

$$\vec{u} = \frac{P\mu_B g}{2eMs\,(1+\beta^2)}\cdot\vec{j}_e \approx \frac{P\mu_B}{eM_s}\cdot\vec{j}_e \qquad [u] = \frac{m}{s}, \tag{1.93}$$

with $g \approx 2$ and $\beta = \tau_{\mathrm{ex}}/\tau_{\mathrm{sf}} \ll 1$ the modified Landau-Lifshitz-Gilbert-equation is found, which describes both the field induced and the spin current induced dynamics of the magnetization $\vec{M}$:

$$\frac{\partial\vec{M}}{\partial t} = \gamma_0\vec{H}_{\mathrm{eff}}\times\vec{M} + \alpha\vec{M}\times\frac{\partial\vec{M}}{\partial t} - (\vec{u}\cdot\vec{\nabla})\vec{M} + \beta\vec{M}\times[(\vec{u}\cdot\vec{\nabla})\vec{M}]. \tag{1.94}$$

Two new terms are found, which describe the influence of spin currents on the magnetization $\vec{M}$:

- The first term governs the impact of the conduction electrons with parallel spin to $\vec{M}$ and is called the adiabatic spin transfer torque.
- The second term concerns the impact of the non equilibrium spin density and is the so called nonadiabatic spin transfer torque.

Both terms depend on the effective velocity $\vec{u}$ which for typical materials and achievable current densities can reach about 100 m/s [53, 59]. The nonadiabatic spin transfer torque depends additionally on β, where strongly varying numbers, depending on the material, growth mode, experimental technique etc. are found [60–64]. Even for Py as the prototype of a ferromagnetic material, numbers between 0.01 and 4.07 are determined [65, 66], clearing demonstrating that β is still under debate.

1.5.1. Examples of current-induced domain wall dynamics

As a first example to demonstrate that multiple domain walls can be moved simultaneously by spin currents, the situation depicted in Figure 1.8 is considered. In the initial configuration, a magnetic nanowire with one head-to-head and one tail-to-tail domain wall is shown. A spin current is applied in the $+x$-direction as shown in Figure 1.8b) with the electron flow direction drawn in black and the magnetic moment drawn in green, while the different domains are shown as red arrows and the domain walls as blue lines.

For simplicity, any possible internal structure of the domain wall is neglected and the spin current is assumed to be fully polarized. In Figure 1.8c), the spin transfer torque is applied on the first domain wall which moves to the $+x$-direction and the spin of the conduction electron flips. Due to the conversation of angular momentum, the localized electrons compensate the transfer of angular momentum which results in a movement of the domain wall.

The maximum torque which can be applied on the domain wall is therefore $1\cdot\hbar$ per electron since the conduction electron flips its spin from e.g. $+1/2\hbar$ to $-1/2\hbar$. In Figure 1.8d), the conduction electron flips its spin again and also the second domain wall moves to the positive x-direction, resulting in a simultaneous motion of multiple domain walls as experimentally shown in [67].

One drawback concerning the current induced domain wall motion, which is also a drawback for field induced motion, is the strong sensitivity of the motion on pinning centres like grain boundaries or edge roughness. As a result, the domain wall moves from pinning centres to pinning centres which results in stochastic motion [53]. One possible solution is to pattern artificial notches in the nanowires which act as pinning centres. The energy landscape of the domain wall is then modified and a deterministic motion from one pinning side to the next is possible [68].

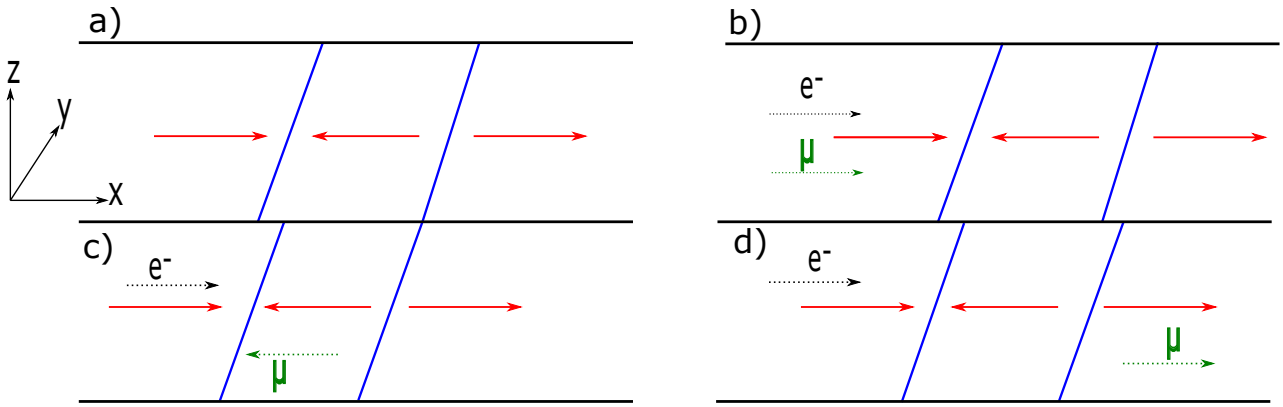

Fig. 1.8. Schematic motion of multiple domain walls by the spin transfer torque.
a) A magnetic nanowire is magnetized with one head-to-head and one tail-to-tail domain wall.
b) A fully spin polarized current is flowing in the $+x$-direction.
c) The conduction electron exerts the spin transfer torque on the head-to-head domain wall and its spin flips from $+1/2\hbar$ to $-1/2\hbar$. Due to angular conservation laws, the localized electrons compensate the transfer of angular momentum which results in a motion of the domain wall.
d) The conduction electron exerts the spin transfer torque on the tail-to-tail domain wall and as before its spin flips resulting in a domain wall movement. Both domain walls move simultaneously in the same direction.

Another interesting method to move multiple domain walls is to exploit perpendicular field pulses as shown in Figure 1.9 schematically, which was experimentally demonstrated in [69]. Here the chirality c defines whether the magnetization rotates counter-clockwise ($c = +1$) or clockwise ($c = -1$) when passing the domain wall from left to right.

The parameter p describes the orientation of the magnetization in the middle of the transverse wall which is either parallel ($p = +1$) or antiparallel ($p = -1$) to the y-axis. It turns out that for a given field pulse direction, which can be generated by a nonmagnetic strip line close to the magnetic wire, the domain wall movement direction only depends on the chirality c, which is shown explicitly for field pulses along the $+z$-direction in Figure 1.9b). Such pulses lead to a motion from right to left for a transverse wall with $c = +1$ and a motion from left to right for a wall with $c = -1$.

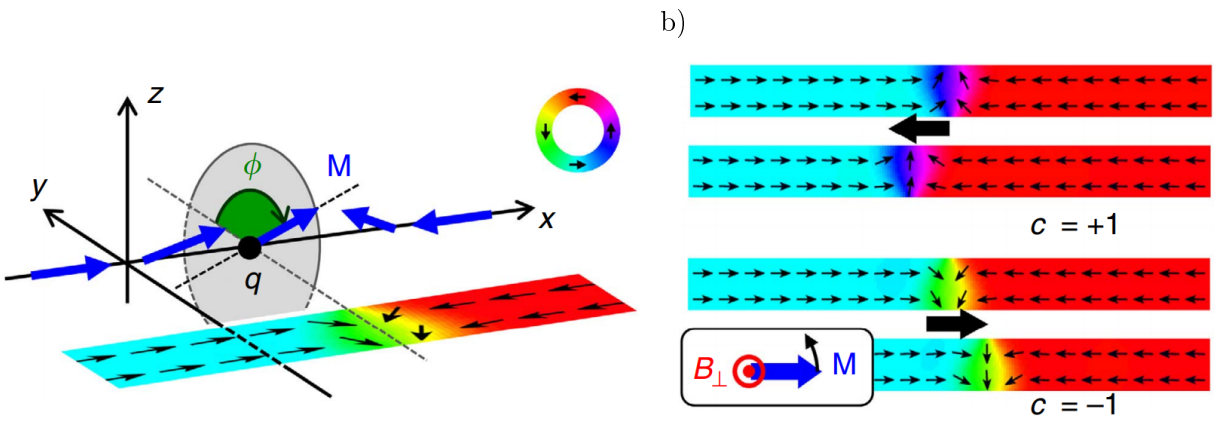

Fig. 1.9. Schematic illustration for a measurement scheme to move multiple domain walls by perpendicular field pulses. Reproduced from [69]. Depending on the chirality, the transverse wall moves for a given field pulse direction out-of-plane to different directions along the wire, avoiding domain wall annihilation provided homochiral domain walls are present.

As a simple example for domain wall motion based on both an applied external field and the adiabatic spin transfer torque, the situation as drawn in Figure 1.10 is considered. A magnetic nanowire has two magnetic domains which are aligned along the x-axis and which are separated by a head-to-head transverse wall pointing in the $+y$-direction. The external field points along the $+x$-direction while the applied spin current points in the $-x$-direction. The LLG-equation for this situation reads:

$$\frac{\partial \vec{m}}{\partial t} = \gamma_0 \vec{H} \times \vec{m} + \alpha \vec{m} \times \dot{\vec{m}} - (\vec{u} \cdot \vec{\nabla})\vec{m}. \tag{1.95}$$

The different directions of the acting torques are summarized in Table 1.1 with $H_{\mathrm{dip}}^{\mathrm{ad}}$ as the generated stray field and j^{ad} as the acting spin current caused by the adiabatic spin transfer torque:

Terms	Direct effect: torque/ stray field $\partial m/\partial t$	damping $\partial m/\partial t$
$H_{\mathrm{ext}}(+x)$	$+z$	$+x$
$H_{\mathrm{dip}}(-z)$	+x	$-z$
j^{ad} $(-x)$	$-x$	$+z$
$H_{\mathrm{dip}}^{\mathrm{ad}}$ $(-z)$	$+x$	$-z$

Tab. 1.1. Overview of the different directions of the various torques in the adiabatic case.

The applied spin current causes the magnetization to move in the $-x$-direction. This is evident due to the negative slope of the term $\vec{\nabla}\vec{m} = \partial/\partial x(m_y)$ together with $-u_x$ as the spin current velocity and the negative sign of the formula. The resulting damping term leads to an out-of-plane rotation in the $+z$-direction due to the asymmetry of the vector product.

This out-of-plane component leads to surface charges producing a stray field pointing in the $-z$-direction. The precession of the magnetization around this stray field is pointing in the $+x$-direction while the damping term points in the $-z$-direction. As a result, no stable domain wall motion at equilibrium is observed since all terms cancel out. Instead, by increasing the current density over a certain threshold, the domain wall moves by changing its structure periodically [70–73].

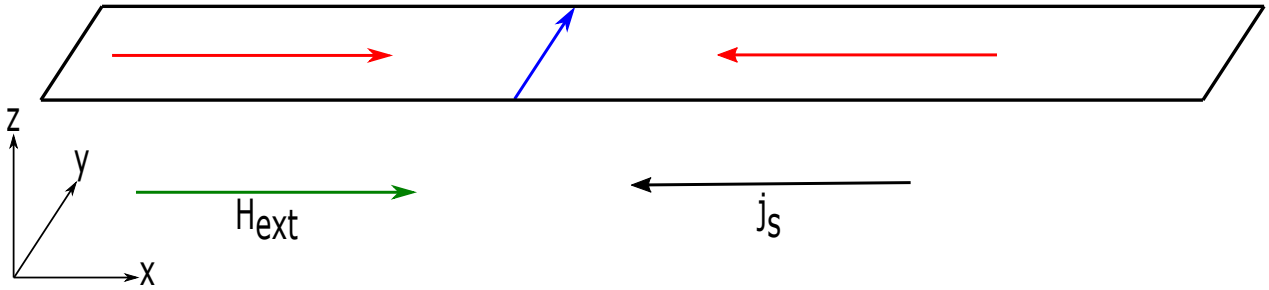

Fig. 1.10. Schematic example for the domain wall movement based on an external magnetic field and the adiabatic spin transfer torque.

By adding the non-adiabatic spin transfer torque, the situation changes and an effective domain wall motion parallel to the direction of the applied spin current is possible. To check this, the LLG-equation including the non-adiabatic spin transfer torque is studied:

$$\frac{\partial \vec{m}}{\partial t} = \gamma_0 \vec{H}_{\text{eff}} \times \vec{m} + \alpha \vec{m} \times \frac{\partial \vec{m}}{\partial t} - (\vec{u} \cdot \vec{\nabla})\vec{m} + \beta \vec{m} \times [(\vec{u}\vec{\nabla})\vec{m}]. \tag{1.96}$$

The different directions for the different acting torques are summarized in Table 1.2.

As before, the spin current velocity u_x points in the $-x$-direction as well as $\vec{\nabla}\vec{m} = \partial/\partial x(m_y)$ due to the negative slope. The last term in the LLG-equation as the cross product between m_y and $-u_x \cdot \partial/\partial x(m_y)$ results in a precession along the $-z$-direction. As a result of this precessional motion, a stray field is generated pointing in the $+z$-direction to reduce surface charges. The damping torque caused by this stray field leads to a motion in the $-x$-direction. The damping based on the non-adiabatic spin transfer torque and the precession caused by the stray field are both pointing in the $-x$-direction, resulting in an effective motion parallel to the applied spin current direction [64].

Terms	Direct effect: torque/ stray field ∂m/∂t	damping ∂m/∂t
$H_{\text{ext}}(+x)$	$+z$	$+x$
$H_{\text{dip}}(-z)$	+x	$-z$
$j^{\text{ad}}\ (-x)$	$-x$	$+z$
$H^{\text{ad}}_{\text{dip}}\ (-z)$	$+x$	$-z$
$j^{\text{nad}}\ (-x)$	$-z$	$-x$
$H^{\text{nad}}_{\text{dip}}\ (+z)$	$-x$	$+z$

Tab. 1.2. Overview of the different directions of the various torques in the non-adiabatic case.

1.6. Hall Effects

Up to now, effects like the adiabatic and the non-adiabatic spin transfer torque to manipulate the magnetization of a micro- or a nanostructure are based on spin polarized currents. Next to these spin polarized currents, where a flow of charges is connected with a flow of spins, it is also possible to generate pure spin currents where a flow of spins is present without any net charge current flowing. These two spin types of spin currents can be described as follows:

a) Spin polarized charge currents, described by $I_c \neq 0$ and $I_s \neq 0$.

b) Pure spin currents with no net charge current flowing characterized by $I_c = 0$ and $I_s \neq 0$.

The focus will be now on (pure) spin currents generated in nonmagnetic metals and use [74] as well as [75] as a guideline for the following discussion. The most important methods to generate (pure) spin

currents in non magnetic metals are discussed, e.g. electric and thermal spin injection in materials with low spin orbit coupling as well as the spin Hall effect which allows the generation of spin currents in heavy metals with large spin orbit coupling.

Before these effects are studied which allow for the creation of (pure) spin currents, the (conventional) Hall effect as well as the anomalous Hall effect are presented. Especially the latter effect provides a basis for a deeper understanding of the spin Hall effect due to its identical microscopic origins [76–78].

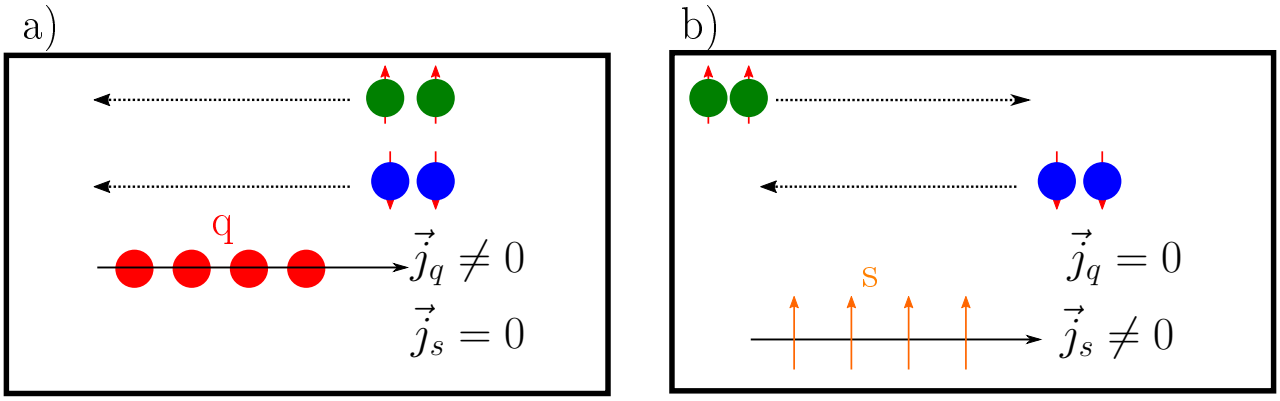

Fig. 1.11. Schematic illustration of a) a pure charge current and b) a pure spin current.
a) A pure charge current is flowing to the right represented as conduction electrons with equal distributed spins flowing to the left. As a result a charge current $\vec{j}_q \neq 0$ is measured while the spin current $\vec{j}_s = 0$ vanishes.
b) A pure spin current with no net charge current is generated by the separation of electrons with different spins flowing in different directions. In this case, the resulting net charge current $\vec{j}_q = 0$ vanishes while a pure spin current $\vec{j}_s \neq 0$ is obtained.

1.6.1. Ordinary Hall effect

The (ordinary) Hall effect, discovered in 1879, describes the influence of an applied external magnetic field acting on a current flowing perpendicular to the external field [79] as shown in Figure 1.12. Electrons are flowing in the $+y$-direction in a wire with length L, width w and thickness t with a drift velocity v_y. An external magnetic field $\vec{B}_{\text{ext}} = B_z$ is pointing in the $+z$-direction. As a result of the Lorentz force $\vec{F}_L$ acting on the electrons one finds:

$$\vec{F}_L = q\left(\vec{E} + \vec{v} \times \vec{B}\right), \tag{1.97}$$

$$\vec{F}_L = -e \cdot v_y \times B_z \propto -F_x. \tag{1.98}$$

Electrons are deflected in the $-x$-direction, which results in a Hall voltage V_H with electrons accumulating at the left edge and holes accumulating at the right edge of the sample. In the steady state, the Lorentz force caused by the external field and the generated electric field E_{-x} caused by the Hall voltage cancel out which reads

$$0 = q(\vec{E} + v_y \cdot B_z), \tag{1.99}$$

$$\Longrightarrow E_x = -v_y B_z. \tag{1.100}$$

The drift velocity v_y can be written with the aid of the charge current density $j_y = -n \cdot e \cdot v_y$ which yields

$$E_x = \frac{j_y}{ne} B_z. \tag{1.101}$$

The charged wire can be understood as a capacitor with $E_x = V_H/w$. Additionally the charge current I can be written as $I = j_y \cdot t \cdot w$ and one obtains

$$V_H = \frac{j_y \cdot w}{n \cdot e} B_z = \frac{I}{n \cdot e \cdot t} B_z \equiv A_H \frac{I B_z}{t}, \tag{1.102}$$

$$\Longrightarrow R_H = A_H \frac{B_z}{t}, \tag{1.103}$$

where $A_H = 1/(n \cdot e)$ defines the Hall-constant. In terms of devices, the Hall effect allows the measurement of magnetic fields if the Hall-constant is known trough of a measurement of the Hall resistance R_H. On the other hand, by measuring the Hall constant it is possible to determine the charge carrier density n and by an additional measurement of the resistivity of the sample, the charge carrier mobility μ.

Scientifically, Hall discovered two years later additionally the anomalous Hall effect (AHE) [80], which could be firstly explained by Karplus and Luttinger in 1954 [76] by considering the influence of spin orbit coupling. Subsequently, extrinsic mechanisms were proposed to explain the AHE as spin skew scattering [77] and side jump scattering [78]. Nowadays, a large range of "Hall effects" are known, e.g. the quantum Hall effect, proposed in 1975 by Ando [81] and discovered in 1980 by von Klitzing [82], the fractional quantum Hall effect discovered in 1982 by Tsui [83] and explained in 1983 by Laughin [84]. Many more are intensively studied and some effects are not completely understood yet.

Here, the anomalous Hall effect is briefly presented to get a deeper understanding of the spin Hall effect which is experimentally intensively studied in the subsequent section of this thesis.

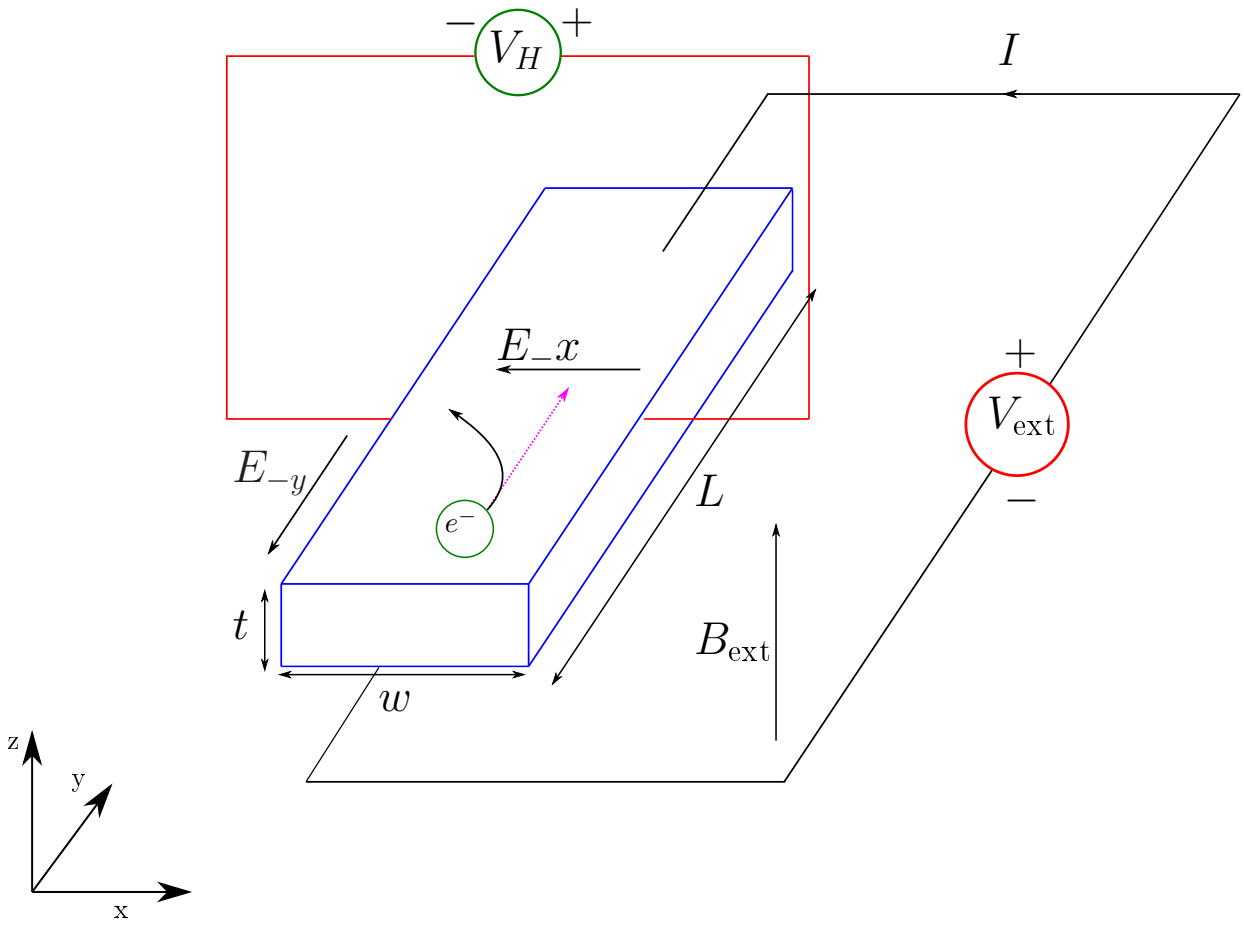

Fig. 1.12. Schematic illustration of the (ordinary) Hall effect. An external voltage V_{ext} is applied and a charge current I flows along the $-y$-direction in a metal or in a semiconductor wire while an external magnetic field B_{ext} is applied along the $+z$-direction. As a result of the Lorentz force, electrons are deflected to the left edge of the wire and an electric field E_{-x} is generated. A Hall voltage V_H can be measured between the left and the right edge of the wire which depends on the applied magnetic field, the charge carrier density, the applied current and the thickness of the wire.

1.6.2. Anomalous Hall effect

As mentioned before, the anomalous Hall effect was discovered in 1881 and firstly explained in 1954. Hall found in 1881, that the "pressing" of the electrons to one side caused by the Lorentz force is one order of magnitude larger for ferromagnetic conductors than for nonmagnetic conductors [80]. Additionally in 1893 Kundt found that the change of the Hall resistivity ρ_{xy} for ferromagnetic conductors is only linear for small applied external fields, as it is to be expected as a consequence of the Lorentz force [85]. Instead, for ferromagnetic conductors, a saturation of the Hall resistivity is seen which is proportional to the saturation magnetization of the ferromagnet. In 1932, Pugh and Lippert [86, 87] established the empirical relation

$$\rho_{xy} = R_0 \cdot H_z + R_s \cdot M_z, \tag{1.104}$$

where the second term describes the anomalous Hall effect which holds for many magnetic materials. While R_0 mainly depends on the charge carrier density n as mentioned before, R_s depends mainly on the resistivity ρ_{xx} of the material.

The three mechanisms, intrinsic band structure effects, spin skew scattering and side jump scattering which contribute to the anomalous Hall effect will be shown schematically and discussed, following the structure of [75, 88].

a) Intrinsic Band Structure Effects:

Karplus and Luttinger demonstrated that by the application of an external electric field to a solid, electrons feel an additional contribution to their group velocity. This anomalous velocity is perpendicular to the applied external field but is independent of scattering effects and does not cancel out in ferromagnetic conductors and only depends on the band structure. Furthermore, "it can be related to changes in the phase of Bloch state wave packets when an electric field causes them to evolve in crystal momentum space" [89, 90], as [88] mentions.

Nowadays, this transverse velocity is understood as a Berry curvature and is therefore an intrinsic quantum-mechanical property of a perfect crystal [91] and links the anomalous Hall effect and the topological nature of Hall currents, i.e. the quantum Hall effect. For such intrinsic effects, the Hall resistivity ρ_{xy} is predicted to be proportional to the square of the resistivity of the material ρ_{xx}. By assuming an ideal lattice, the spin Hall conductivity σ_{xy} can be directly calculated by the aid of the Kubo formula [92] with the eigenvalues $\epsilon_n(\vec{k})$ and the eigenstates $|n, \vec{k}>$ for a Bloch Hamiltonian:

$$\sigma_{ij}^{\text{AH-int}} = e^2\hbar \sum_{n \neq n'} \int \frac{d^3k}{(2\pi)^d} \left[f(\epsilon_n(\vec{k})) - f(\epsilon_{n'}(\vec{k}')) \right] \times \text{Im} \left(\frac{< n, \vec{k}|\hat{v}_i(\vec{k})|n', \vec{k} >< n', \vec{k}|\hat{v}_j(\vec{k})|n, \vec{k} >}{[\epsilon_n(\vec{k}) - \epsilon_{n'}(\vec{k})]^2} \right). \tag{1.105}$$

In this formula, the velocity operator $\hat{v}(\vec{k})$ is defined as

$$\hat{v}(\vec{k}) = -i\hbar \left[\hat{r}, \hat{H}(\vec{k}) \right] = -i\hbar \nabla_k \left[\hat{H}(\vec{k}) \right]. \tag{1.106}$$

The intrinsic contribution is directly linked to the topological properties of the Bloch states. In particular, it is proportional to the integral of the Berry phases over cuts of the Fermi surface segments [93]. This important result can be derived by identifying that

$$< n, \vec{k}|\nabla_k|n, \vec{k} >= \frac{< n, \vec{k}|\nabla_k \hat{H}(\vec{k})|n', \vec{k}}{\epsilon_n(\vec{k}) - \epsilon_{n'}(\vec{k})}. \tag{1.107}$$

Inserting this expression in Equation 1.105 yields

$$\sigma_{ij}^{\text{AH-int}} = e^2\hbar - \epsilon_{i,j,l} \sum_n \int \frac{d^3k}{(2\pi)^d} f(\epsilon_n(\vec{k}) b_n^l(\vec{k}), \tag{1.108}$$

with $b_n(\vec{k}) = \nabla_k \times a_n(\vec{k})$ as the Berry curvature and $a_n(\vec{k}) = i < n, \vec{k}|\nabla_k|n, \vec{k} >$ as the Berry phase connection. Detailed first principle calculations of the intrinsic contribution to the anomalous Hall effect for body centred cubic iron, face centred cubic nickel and hexagonal closed packed cobalt systems can be found in [94–96], while a schematic illustration is shown in Figure 1.13.

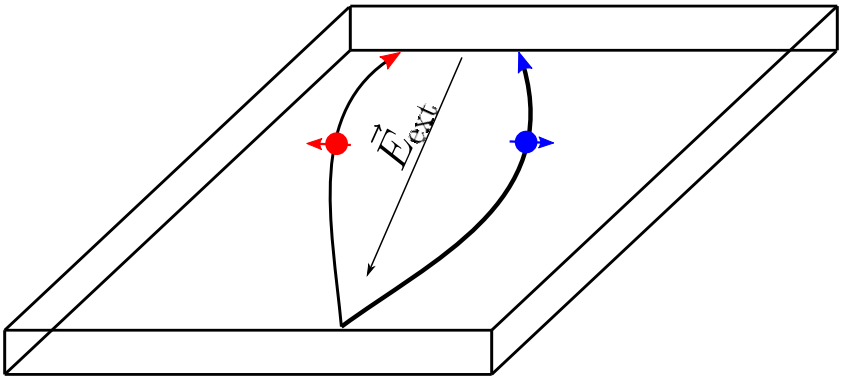

Fig. 1.13. Schematic illustration of the intrinsic contribution to the anomalous Hall effect. By the application of an external electric field, electrons feel a contribution to their group velocity which does not cancel out for ferromagnetic conductors. The velocity depends on the band structure, but is independent of scattering effects and leads to a quadratic relation between the Hall resistivity ρ_{xy} and the resistivity of the material ρ_{xx}, resulting in $\rho_{xy} \propto \rho_{xx}^2$.

b) Spin Skew Scattering:

Spin skew scattering is the contribution to the anomalous Hall effect being proportional to the life time of Bloch transport states and therefore tends to dominate in nearly perfect crystals. Due to spin orbit coupling, an effective magnetic field gradient occurs in the scattering plane which results in a force towards or away from the scattering centre, depending on the spin orientation and therefore the momentum of the spin becomes spin dependent by an inelastic scattering event.

When this contribution dominates, both the Hall conductivity σ_{xy} and the conductivity σ_{xx} of the material are proportional to the transport lifetime τ, resulting in a linear relationship between the Hall resistivity ρ_{xy} and the resistivity of the material ρ_{xx}. Skew scattering is the only one of the three contributions which can be treated within the classical Boltzmann transport theory, in which interband coherence effects are neglected. In terms of Fermi's golden rule, one can write

$$W_{n\to m} \propto | < n|V|m > |^2 \delta \left(E_n - E_m\right), \tag{1.109}$$

with $W_{n\to m}$ as the transition probability from state n to state m, V the distortion potential and E_n and E_m the energy of the different states, respectively. In the presence of spin orbit coupling, the transition probability $W_{n\to m}$ from state m to state n is different than from state m to state n. By evaluating the transition rates perturbatively, at third order asymmetric chiral contributions appear, which can be written in simple models as

$$W_{n\to m}^{\text{asym}} = \frac{1}{\tau_{\text{asym}}} \vec{k} \times \vec{k}' \cdot M_s, \tag{1.110}$$

with $\vec{k}$ as the momentum in the initial state n and $\vec{k}'$ as the momentum in the final state m. When this asymmetry is inserted into the Boltzmann equation, it results in a current proportional to the longitudinal current driven by $\vec{E}$ and being perpendicular to both $\vec{E}$ and $\vec{M}_s$ [88]. A schematic illustration of the skew scattering is shown in Figure 1.14.

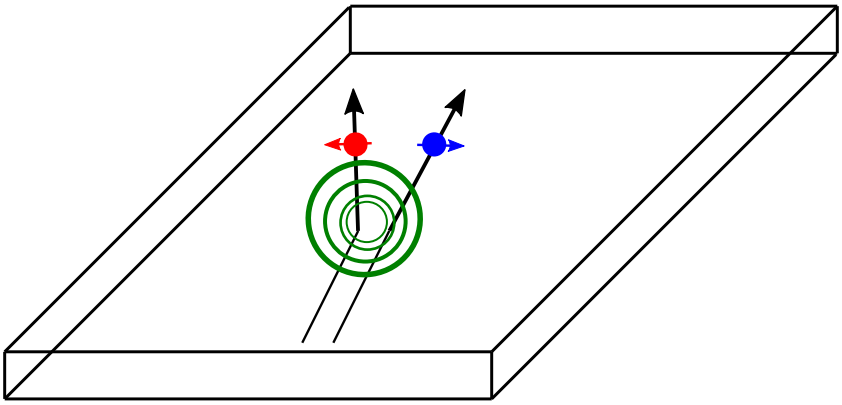

Fig. 1.14. Schematic illustration of spin skew scattering, a contribution to the anomalous Hall effect which tends to be dominant in nearly perfect crystals and leads to a linear relation ship between the Hall resistivity ρ_{xy} and the resistivity of the material ρ_{xx}. As a result of spin orbit coupling, an effective magnetic field gradient occurs in the scattering plane which results in a force towards or away from the scattering centre depending on the spin orientation of the electron. Since the wave vector $\vec{k}$ is not conserved, skew scattering is an inelastic process.

c) Side Jump Contribution:

Since the intrinsic contribution as well as the side skew scattering contribution to the anomalous Hall effect are precisely defined, the side jump contribution can be defined as the difference between the full Hall-conductivity $\sigma_{xy}^{\mathrm{AH}}$ and the two other contributions:

$$\sigma_{xy}^{\mathrm{AH}} = \sigma_{xy}^{\text{AH-int}} + \sigma_{xy}^{\text{AH-skew}} + \sigma_{xy}^{\text{AH-sj}} \tag{1.111}$$

In a semi-classical picture, the basic argument for the side jump contribution is straight forward: As a result of scattering of a Gaussian wave packet on a spherical impurity with spin orbit coupling, the system can be described by a Hamiltonian as follows:

$$H_{\mathrm{SOC}} = \frac{1}{2} m^2 c^2 \left(\frac{1}{r} \frac{\partial V}{\partial r} \right) S_z L_z.$$

This wave packet with incoming wave vector $\vec{k}$ gets disturbed by a displacement transverse to $\vec{k}$ equal to $1/6|\vec{k}|/(m^2c^2)$ [97] following an elastic scattering event. This mechanism cannot be explained in terms of classical Boltzmann transport theory, since within this theory only the transition probabilities between Bloch states can be calculated and not the microscopic details of the scattering process itself.

As for the intrinsic contribution, the side jump contribution is found to be independent of the transport lifetime τ and therefore follows the same power law as the intrinsic contribution in terms of the scattering rate. As reviewed in [98], side jump contributions and intrinsic contributions can be distinguished by their different dependence on specific system parameters, especially in systems with complex band structures.

Theories based on simple band structure models, e.g. the conduction band in a semi-conductor, demonstrated that the intrinsic and side jump contribution can be of same size but different sign and therefore cancel out [99]. However it turned out that such cancellations are unlikely, except in the mentioned simple band structure models which are e.g. classified by a constant Berry curvature [100].

This means that only by a comparison between fully microscopic linear response theoretical calculations, based on e.g. the Keldysh [101] or the Kubo [92] formalism and the developed semi-classical theory, a proper distinction between the intrinsic and the side jump contribution can be

possible. As a result, a practical approach is to firstly calculate the intrinsic contribution for a given material where the Hall conductivity σ^{AH} is expected to independent of the conductivity σ_{xx} of the material and to compare it with the experimental results. If the agreement between theory and experiment is sufficient, we can assume that the intrinsic contribution dominates. A schematic illustration of the side jump contribution is shown in Figure 1.15.

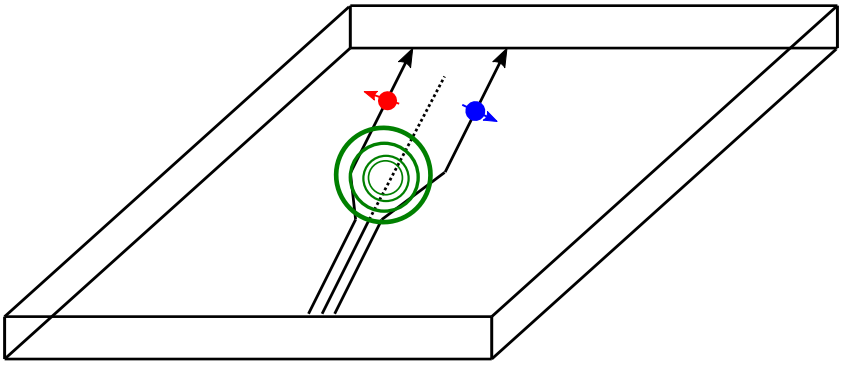

Fig. 1.15. Schematic illustration of the side jump contribution to the anomalous Hall effect. Electrons with different spins are deflected elastically in different directions by the opposite experienced electric field upon arriving and leaving an impurity. As for the intrinsic contribution, the side jump contribution is independent of the spin transport life time τ of the Bloch states which results it being difficult to distinguish the two effects.

1.6.3. Spin Hall effect

The spin Hall effect, observed first 2004 in semiconductors [102], describes the phenomenon whereby the application of a charge current in a nonmagnetic material can result in a spin current perpendicular to this charge current. The spin Hall effect in metals, which plays an eminent role within this thesis, can either be measured in materials with large spin orbit coupling as Pt [103, 104], W [8, 105] or Ta [7] or in heavy metal alloys such as CuBi [106, 107], CuIr [108] or AuTa [109].

As in the anomalous Hall effect case, the intrinsic, the skew scattering and the side jump contribution are the three mechanisms to explain the spin Hall effect which directly demonstrates the close relationship between both phenomena. To give some examples, in Pt as the standard spin Hall material, the intrinsic contribution is found to be independent of the resistivity of the Pt and therefore dominates in the moderately dirty regime, while skew scattering becomes dominant for very clean crystals [104]. The large size of the spin Hall effect in CuBi can be explained due to the large skew scattering contribution at the Bi impurities [106, 110, 111] while in AuTa side jump scattering at the Ta impurities increases the spin Hall effect compared to the intrinsic contribution in pure Au [109]. In pure Au, the spin Hall effect has been shown to drastically depend on the thickness [112–114]. In these experiments, quasiballistic effects which arise in a Hall-bar type geometry, can surpass the spin Hall effect and needs to be suppressed for a proper determination of the spin Hall angle [114].

Historically, Dyakonov and Perel were the first who described phenomenologically the coupling between spin and charge currents in 1971 [115]. In 1999, Hirsch could directly show that in a paramagnet the flow of a charge current leads to a perpendicular spin current [116]. This derivation follows the structure of [75] and [117]. Starting with the diffusion equation for the charge current [118], one finds

$$\frac{\vec{j}^{c}}{e} = \mu n \vec{E} + D\vec{\nabla}(n), \tag{1.112}$$

with μ as the electron mobility, $\vec{E}$ the electric field, D as the electron diffusion constant and n as the electron density. In a similar way, the diffusion of the spin current tensor j^{s}_{ij} can be defined in terms

of the j-th component of the spin polarization $\vec{P}$ flowing in the i-th direction and one obtains [119]

$$\frac{j_{ij}^{s}}{\hbar} = -\mu n E_i P_j + D\frac{\partial P_j}{x_j}. \tag{1.113}$$

Due to spin orbit coupling, spin and charge currents are coupled and for materials with inversion symmetry, the coupling can be written as

$$\frac{\vec{j}^{c}}{e} = \mu n\vec{E} + D\vec{\nabla}(n) + \theta_{\mathrm{SH}}\ \mu(\vec{E}\times\vec{P}) + \theta_{\mathrm{SH}}\ D\left(\vec{\nabla}\times\vec{P}\right), \tag{1.114}$$

$$\frac{j_{ij}^{s}}{\hbar} = -\mu n E_i P_j + D\frac{\partial P_j}{x_j} - \epsilon_{ijk}\left(\theta_{\mathrm{SH}}\ \mu N E_k + \theta_{\mathrm{SH}}\ D\right). \tag{1.115}$$

The third term in Equation 1.115 describes the direct spin Hall effect, where a spin current is generated by an applied electric field. The third term in Equation 1.114 describes the anomalous Hall effect in the presence of a net spin polarization $\vec{P}$ while the fourth term describes the inverse spin Hall effect as the generation of a charge current caused by a gradient of the spin polarization, i.e. the flow of a spin current. By writing the charge conductivity of the material $\sigma = ne\mu$ and the Hall conductivity $\sigma_{xy} = n\hbar\mu\theta_{\mathrm{SH}}$, the spin Hall angle θ_{SH} can be defined as

$$\theta_{\mathrm{SH}} = \frac{\sigma_{xy}}{\sigma}\frac{e}{\hbar}, \tag{1.116}$$

which means that θ_{SH} can be understood as a dimensionless material parameter describing the spin current to charge current conversation. θ_{SH} is roughly proportional to Z^4, with Z as the atomic number [120]. Additionally, different materials show different signs of the spin Hall angle with Pt showing a positive spin Hall angle while W and Ta have a negative spin Hall angle, which can attributed to the 5d-shell configuration [121]. Concerning quantitative numbers for the spin Hall angle, even in the case of Pt, the most widely studied spin Hall material, the quoted values differ significantly between 1 % and 20 % [103, 121–123] and additionally depend significantly on the growth methods. For different growth methods, differences in the resistivity of the material occur and one finds for very clean films skew scattering being dominant while for moderately dirty films the intrinsic contribution tends to be dominant [104].

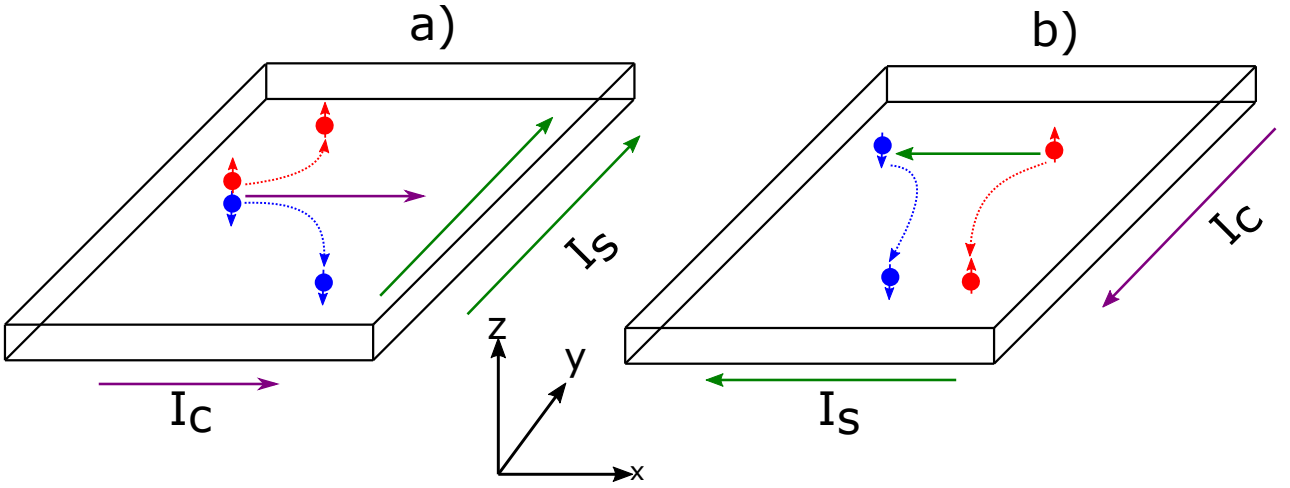

Fig. 1.16. Schematic illustration of the spin Hall effect a) and the inverse spin Hall effect b).
a) Spin Hall effect. The flow of an electric charge current I_c in a material with large spin orbit coupling but a lack of magnetic order and therefore an unpolarized charge current leads to a pure spin current I_s perpendicular to this charge current.
b) Inverse spin Hall effect. In this situation, a spin current flowing in a material with large spin orbit coupling generates a charge current perpendicular to the spin current.

1.7. Spin-Orbit-Coupling In Materials Lacking Inversion Symmetry

In contrast to the already discussed spin Hall effect, which arises by a flowing current in a nonmagnetic material with large spin orbit coupling and can be understood as a bulk effect, the Rashba-Edelstein effect is an interface effect that also allows for the generation of a spin current in a nonmagnetic material [124]. To shine light on this effect, we first study the spin-orbit-coupling in materials lacking inversion symmetry.

In general, time inversion symmetry and inversion symmetry in a crystal structure, mean that the eigenvalues of the electron states must fulfil the following relationship [9, 125]

$$E_{\uparrow,\downarrow,\vec{k}} = E_{\downarrow,\uparrow,\vec{k}}, \tag{1.117}$$

which is the usual spin degeneracy of single electron states in the absence of any external or internal magnetic fields. However, when the system lacks inversion symmetry only

$$E_{\uparrow,\downarrow,\vec{k}} = E_{\downarrow,\uparrow,-\vec{k}} \tag{1.118}$$

needs to be satisfied, which leads to a $\vec{k}$-dependent band splitting [126] and allows for a net spin polarisation in a nonmagnetic material in the presence of an electric current. Dresselhaus has shown in 1955 that bulk inversion asymmetry in noncentrosymmetric crystals with the zinc blende structure leads to spin splitting for the conduction bands which is both linear and cubic in $|\vec{k}|$. Furthermore Rashba could show in 1960 that a spin splitting linear in $|\vec{k}|$ arises also in a crystal with a single high-symmetry axis and an invariant vector oriented along this axis [127]. This situation is realized in wurtzite-type crystals [127, 128] and in layered heterostructures [129, 130] where the structure inversion symmetry is present along the surface normal. In total there are three possible planes where the electrons are confined ((100), (110) and (111)) and the corresponding Hamilton operators are given by [131]

$$\text{(100) layers}: \quad \hat{H}_{\mathrm{SO}}^{100} = \alpha\left(k_y\sigma_x - k_x\sigma_y\right) + \gamma\left(k_x\sigma_x - k_y\sigma_y\right), \tag{1.119}$$

$$\text{(110) layers}: \quad \hat{H}_{\mathrm{SO}}^{110} = \alpha k_y\sigma_x + \beta k_x\sigma_y + \lambda k_x\sigma_z, \tag{1.120}$$

$$\text{(111) layers}: \quad \hat{H}_{\mathrm{SO}}^{111} = (\alpha+\gamma)(k_y\sigma_x - k_x\sigma_y), \tag{1.121}$$

α, β, γ and λ are material dependent constants characterizing the spin orbit interaction while $\vec{\sigma}$=(σ_x,σ_y, σ_z) are the Pauli-spin matrices. In the case of metal surfaces [132, 133] and metal layers deposited between asymmetric cubic and amorphous interfaces [134], only the Rashba interaction survives (β, γ and λ vanish) and the Hamilton operator for the Rashba interaction can be written as

$$\hat{H}_{\mathrm{SO}} = \alpha\left(\vec{k}\times\vec{e}_z\right)\vec{\sigma}, \tag{1.122}$$

where $\vec{e}_z$ is a unitary vector perpendicular to the surface normal. Equation 1.119, Equation 1.120 and Equation 1.121 correspond to the influence of an effective $\vec{k}$-dependent magnetic field which can be seen by writing

$$\hat{H}_{\mathrm{SO}} = -\vec{m}\cdot\vec{B}_{\mathrm{SO}} = \mu_B\cdot\vec{\sigma}\cdot\vec{B}_{\mathrm{SO}}. \tag{1.123}$$

The orientation of $\vec{B}_{\mathrm{SO}}$ for three particular cases is shown schematically in Figure 1.17 and inspired from [125]. In the presence of external magnetic fields [135] or exchange splitting [136], both the time-reversal and the structural inversion symmetry might be broken, which leads to a more complex relationship between $\vec{k}$ and spin, depending on the relative strength of the spin orbit coupling compared to the exchange splitting.

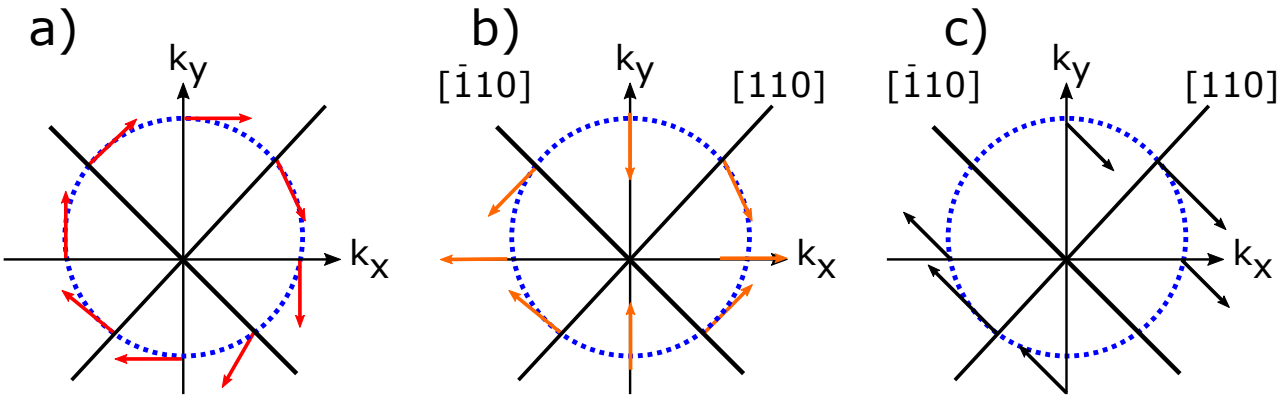

Fig. 1.17. Orientation of the spin orbit induced magnetic fields (arrows) as a function of the current direction (solid lines).
a) Rashba field originating from the Hamilton Operator given in Equation 1.119, assuming $\gamma = 0$.
b) Linear Dresselhaus field originating from the Hamilton operator given in Equation 1.119, assuming $\alpha = 0$.
c) Coexisting Rashba and Dresselhaus field originating from the Hamilton operator given in Equation 1.119, assuming $\alpha = \gamma$.

Either bulk or structure inversion symmetry result in a magnetic field-like interaction if the motion of electrons in an asymmetric crystal field potential V is considered. At non-relativistic speed $\vec{v}$, the net electric field originating from such a potential is given by

$$\vec{E} = -\vec{\nabla}\left(V\right), \tag{1.124}$$

which leads to a magnetic field as follows

$$\vec{B} = -\frac{\vec{v} \times \vec{E}}{c^2} \tag{1.125}$$

in the rest frame of the electron. Transforming back to the laboratory's reference frame, the magnetic induction field experienced by the electron is corrected by a factor of 2, resulting in

$$\vec{B}_{SO} = -\frac{\vec{v} \times \vec{E}}{2c^2} = \frac{\hbar\vec{k} \times \vec{\nabla}(V)}{2m_e c^2}. \tag{1.126}$$

The Hamilton operator $\hat{H}_{\mathrm{SO}}$ is then given by

$$\hat{H}_{\mathrm{SO}} = -\vec{m} \cdot \vec{B}_{SO}. \tag{1.127}$$

If structure inversion asymmetry is present, the conduction electrons feel at the same time the electrostatic potential of the nuclear charge V_{nuc} as well as the macroscopic interface potential V_{int} [126]. The electron wave function can be decomposed into quickly oscillating lattice-periodic Bloch waves and an envelope function which describes the electric field generated by the atomic nuclei together with the structure inversion asymmetry environment. Together, Hamilton operator $\hat{H}_{\mathrm{SO}}$ can be written as the sum of two terms [137]

$$\hat{H}_{\mathrm{SO}} = \frac{e\hbar^2}{4m_e c^2}\left[\vec{k} \times \vec{\nabla}(V_{\mathrm{nuc}} + V_{\mathrm{int}})\right]. \tag{1.128}$$

By the use of a tight-binding-model, one finds that the effective Rashba constant α is proportional to the product of the atomic spin orbit parameter multiplied with the hopping matrix element between orbitals with in-plane and out-of-plane asymmetry which represents the interface potential gradient [138]. In

contrast, for bulk inversion asymmetry only the nuclear term is relevant which is given in the central field approximation as

$$V_{\text{nuc}} \approx \frac{Ze}{4\pi\epsilon_0|\vec{r}|}, \tag{1.129}$$

with Z as the atomic number and r as the distance between the electron and the nucleus. By determining the gradient $\vec{\nabla}(V_{\text{nuc}})$ this yields

$$\vec{\nabla}(V_{\text{nuc}}) = -\frac{Ze}{4\pi\epsilon_O}\frac{\vec{r}}{|\vec{r}|^3}, \tag{1.130}$$

which results in the spin-orbit Hamiltonian similar to the well known Hamilton operator as in atomic physics

$$\hat{H}_{\text{SO}}^{\text{nuc}} = \frac{Ze^2\hbar^2}{8\pi\epsilon_0 m_e^2 c^2|\vec{r}|^3}\frac{\vec{\sigma}}{2}\cdot\vec{l} = \xi(r)\frac{\vec{\sigma}}{2}\cdot\vec{l}. \tag{1.131}$$

1.7.1. Inverse spin galvanic effect

In contrast to the spin Hall effect, which generates a non-uniform spin accumulation at the edges of a conductor with large spin-orbit-coupling, the inverse spin galvanic effect generates a homogeneous net spin polarisation by passing an electric current in a magnetic conductor lacking inversion symmetry [124, 139]. This spin accumulation is due to the uneven occupation of $\vec{k}$ and $-\vec{k}$ in the presence of a charge current which generates an average effective field acting on the spin density of the conduction electrons [125]. To understand the spin galvanic effect, first found in strained bulk semiconductors [140] and in heterogeneous quantum well structures [141], a simple model presented by Silsbee [142] is considered.

Starting with the Hamilton operator for a two-dimensional-electron gas with a Rashba type spin-orbit-interaction present, one can write

$$\hat{H} = \frac{\hbar^2|\vec{k}|^2}{2m_e^*} + \alpha\left(\vec{k}\times\vec{e}_z\right)\vec{\sigma}, \tag{1.132}$$

with m_e^* as the effective electron mass. The eigenvalues are given as

$$\epsilon_{\pm k} = \frac{\hbar^2|\vec{k}|^2}{2m_e^*} \pm \alpha|\vec{k}| \tag{1.133}$$

while the eigenvectors are determined to be

$$\psi_{\pm k} = \frac{e^{i\vec{k}\cdot\vec{r}}}{\sqrt{2A}}\begin{pmatrix}1\\ \mp e^{i\xi\cdot k}\end{pmatrix}, \tag{1.134}$$

with $\vec{k} = k(\cos\xi, \sin\xi, 0)$ and A as the area of the layer. For the spin expectation value $<\vec{\sigma}>_{\pm k}$ one obtains

$$<\vec{\sigma}>_{\pm k} = <\psi_{\pm k}|\sigma|\psi_{\pm k}> = \frac{1}{k}\begin{pmatrix}\pm k_y\\ \mp k_x\\ 0\end{pmatrix} = \begin{pmatrix}\pm\sin\xi\\ \mp\cos\xi\\ 0\end{pmatrix}. \tag{1.135}$$

As a result, the energy dispersion is no longer a paraboloid as in the free electron gas but the quadratic surface is generated by the rotation of the two branches $\epsilon_{+,k>0}$ and $\epsilon_{-,k>0}$ around the energy axis intersecting the Γ-point as shown in Figure 1.18. The radius of the two Fermi discs can be found by considering that the total electron density is the same as in the free-electron gas case, which means

$$\epsilon_{-,k_F-} = \epsilon_{+,k_F+} = \epsilon_F \tag{1.136}$$

for $k_{F\pm}$. In the first order of α one obtains

$$k_{F\pm} \approx k_F \mp \frac{m_e^* \alpha}{\hbar^2} \tag{1.137}$$

Although the total spin polarization in each branch cancels out, the direction of $\vec{k}$ and the spin orientation are related to each other. Together with the fact that $k_{F+} \neq k_{F-}$, this means that an applied charge current leads to a net spin polarisation which its orientation being transverse to the average electron momentum.

The combined action of present spin-orbit-coupling and exchange interaction in a single ferromagnetic layer with either structural inversion or bulk inversion asymmetry is described by a Hamilton operator as follows:

$$\hat{H} = \frac{\hbar^2 |\vec{k}|^2}{2m_e^*} + \hat{H}_{\mathrm{SO}} - J\vec{M}_N \cdot \vec{\sigma}, \tag{1.138}$$

where J is the exchange coupling constant and $\vec{M}_N = \vec{M}/Ms$ is the normalized magnetization. In the case of a pure Rashba type interaction, Equation 1.138 can be diagonalized for an arbitrary direction of $\vec{M}_N = (\sin\theta\cos\phi, \sin\theta\sin\phi, \cos\theta)$ and electric current $\vec{j} = j(\cos\xi, \sin\xi, 0)$ confined to the azimuthal plane, yielding

$$\epsilon_{\pm,k} = \frac{\hbar^2 |\vec{k}|^2}{2m_e^*} \pm \sqrt{J^2 + \alpha^2 |\vec{k}|^2 - 2\alpha |\vec{k}| J \sin\theta \sin(\xi - \phi)} \tag{1.139}$$

As evident for the energy eigenvalues $\epsilon_{\pm,k}$ from Equation 1.138, the resulting band structure depends on the relative strength of exchange and spin orbit coupling induced spin splitting, i.e. J/α. The situation is drawn for the nonmagnetic case (Figure 1.18a), $J = 0$) and for weak exchange (Figure 1.18b), $J/\alpha = 0.1$). The corresponding resulting Fermi contours and spin quantizations are shown in Figure 1.18c) and Figure 1.18d), respectively.

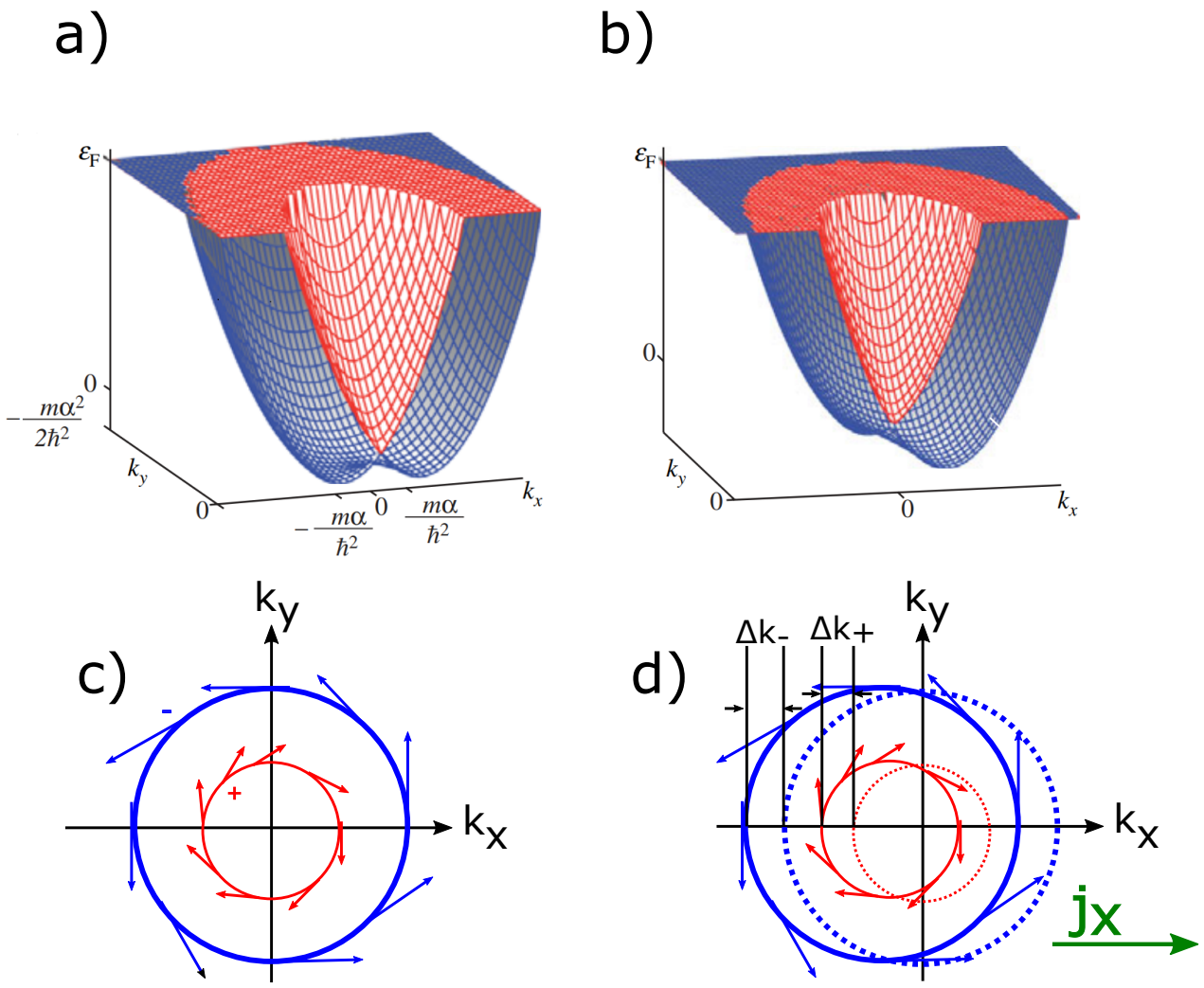

Fig. 1.18. Two dimensional energy dispersion $\epsilon_{\pm,k}$ for the nonmagnetic case ($J = 0$) in **a)** and for a weak exchange interaction ($J/\alpha = 0.1$) in **b)**. The resulting Fermi contours and spin polarization for the two cases are plotted in **c)** and **d)**, respectively. Reproduced from [125], with the permission of Royal Society.

1.8. The Lateral Spin Valve Geometry

Next to the spin Hall effect and the inverse spin galvanic effect which both allow to generate spin currents in materials with large spin orbit coupling, there is as a different approach electric spin current injection. Electric spin current injection is particular well suited to generate spin currents in nonmagnetic materials with low spin orbit coupling. A particular geometry to realize such spin currents is the lateral spin valve geometry. This geometry has been pioneered by Johnson and Silsbee in 1985 who employed a bulk Al stripe with NiFe stripes on top [10]. They explained the physics in detail in 1988 [143]. The first realisation in a nanostructure has been achieved by Jedema in 2001 [11]. In such a lateral spin valve geometry, a pure, diffusive, spin current (as introduced in section 1.6) is generated in a material with low spin orbit coupling such as Cu [144, 145], Ag [146], Al [147, 148] or graphene [149]. This pure spin current can then be used to efficiently manipulate the magnetization of a ferromagnetic electrode, i.e. a domain wall [14, 15] or switch the magnetization state of a small disc [12].

Typically, a lateral spin valve consists of two ferromagnetic electrodes with different widths, separated by a distance d of a few hundreds of nm and which are connected by the nonmagnetic bridge with

low spin orbit coupling, as shown in Figure 1.19. In literature, this nonmagnetic bridge is also termed spin current conduit (SCC). A spin polarized charge current $\vec{I}_c$ flows from the first ferromagnet FM_1 through the FM_1/SCC interface and a spin accumulation is generated in the nonmagnetic bridge as drawn in Figure 1.19. The formerly spin independent chemical potential of the SCC becomes spin dependent. This spin accumulation, drawn as green arrows, will diffuse towards the left where it is accompanied by the charge current as well towards the right as a pure spin current.

During the spin transport in the spin current conduit, the spin accumulation is reduced due to scattering events. To minimize this loss, materials for the spin current conduit with low spin orbit coupling are suitable. Since no net charge current is flowing within the central position of nonmagnetic bridge, this spin accumulation is a pure spin current. Once it enters the interface of the SCC and the second ferromagnetic electrode SCC/FM_2, also named detector, the spin current gets absorbed in the second ferromagnet.

As mentioned before, the pure spin current can be exploited to manipulate the magnetic state of the detector. As a result of the lack of a net charge current, Joule heating and generated Oersted fields are reduced in the manipulated region. The non-local voltage V_{NL}, measured between the detector and the second end of the nonmagnetic bridge, is directly proportional to the spin accumulation at the SCC/FM_2 interface and scales linearly with the applied charge current $\vec{I}_c$. The non-local resistance R_{NL} is therefore defined by

$$R_{\mathrm{NL}} \equiv \frac{V_{NL}}{I_c}. \tag{1.140}$$

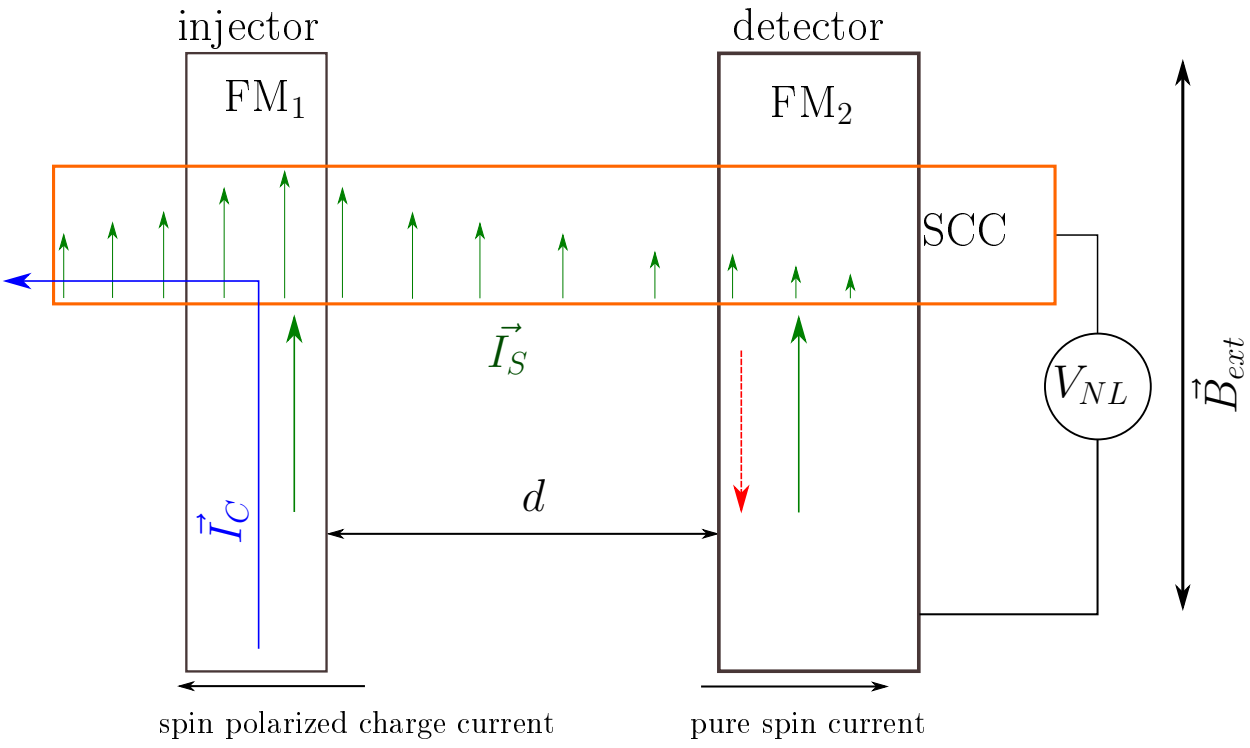

Fig. 1.19. Schematic illustration of a lateral spin valve device, which consists of two spatially separated ferromagnetic electrodes which are connected by a nonmagnetic channel, which is named the spin current conduit (SCC). A charge current is flowing from from the first ferromagnet FM_1 through the FM_1/SCC interface. A spin accumulation is then generated at the interface. As a result, the formerly independent density of states of the channel becomes spin dependent. This spin accumulation in the channel diffuses in all directions and is absorbed at the SCC/FM_2 interface. The measured non-local voltage is directly proportional to the spin accumulation at this interface and can be detected as the relative alignment between spin current orientation and detector magnetization orientation. For a parallel alignment, a large spin signal is found while for an antiparallel alignment, a low spin signal is observed.

To understand in more detail the origin of the non-local signal, the simplified density of states [150] as shown in Figure 1.20 is considered. In Figure 1.20a) the density of states for FM_1, the SCC and FM_2 with an assumed parallel magnetization alignment of the two ferromagnetic electrodes is shown. By the application of a voltage V_0, which drives the current in FM_1, the highest occupied state is shifted from the Fermi energy E_F to $E_F + e \cdot V_0$. Once the spin current enters the FM_1/SCC interface (we assume perfect metallic interfaces without any spin flip events), the formerly spin independent density of state becomes spin dependent due to the shift in the chemical potential for spin-down and spin-up electrons and we find a spin accumulation in the SCC with the filling of the density of states for the spin-up electrons of FM_1 and the SCC being on the same level. During the transport in the SCC, there will be some spin flip events, which means that the filling of the density of states for spin-down electrons will increase and for the spin-up electrons will decrease. However, if there is still an imbalance of the density of states of the SCC at the SCC/FM_2 interface (which we assume to be perfectly metallic again), the level of the highest filled state for **spin up electrons** for the SCC and FM_2 needs to be aligned. The detected non-local voltage is directly proportional to this shift of the chemical potential of FM_2. On the other hand, for an antiparallel alignment of the spin current and the FM_2 magnetization, the level of the highest filled state for **spin-down electrons** for the SCC and FM_2 needs to be aligned at the SCC/FM_2 interface.

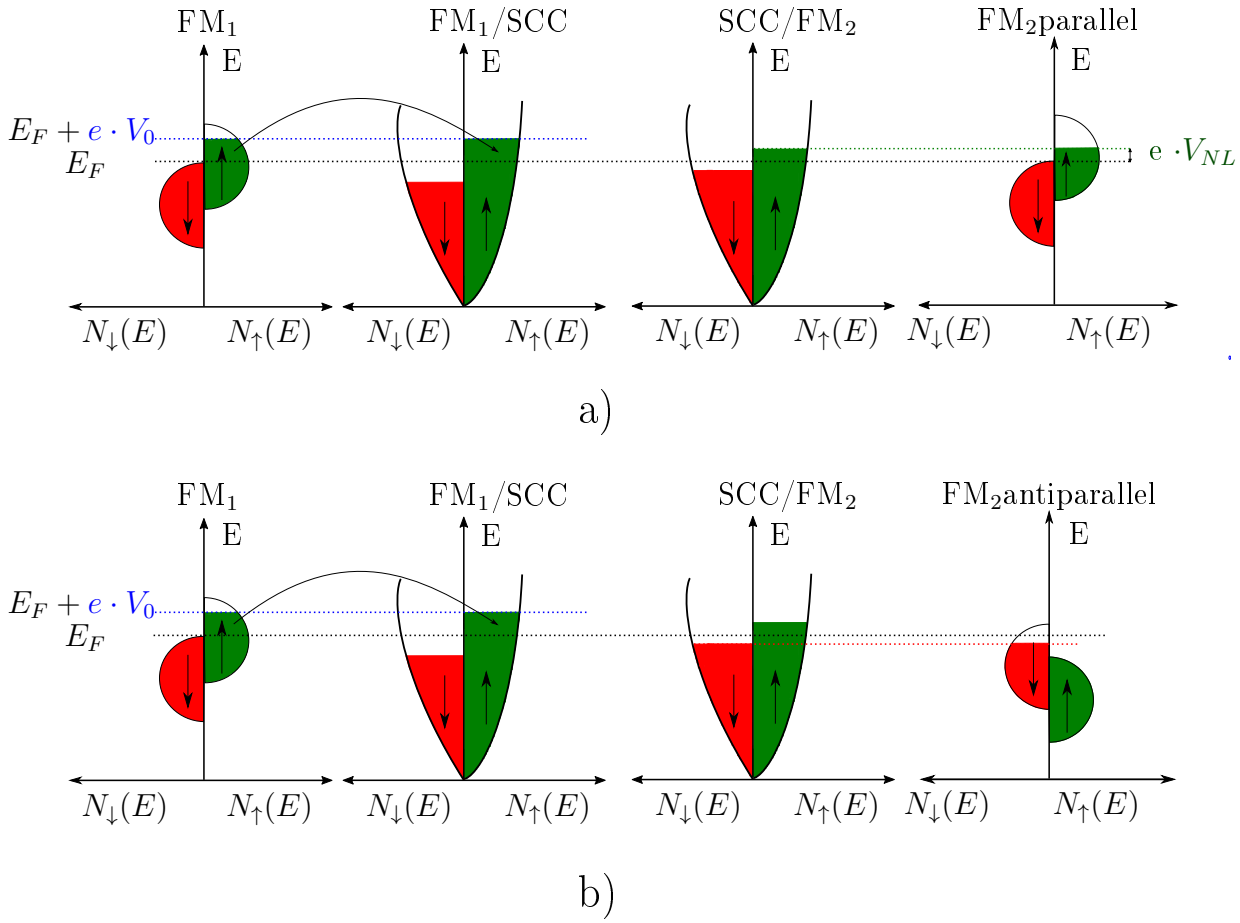

Fig. 1.20. Simplified energy dependent density of states for a lateral spin valve structure with a) parallel and b) antiparallel magnetization alignment of the two ferromagnetic electrodes. We assume both the FM_1/SCC and the SCC/FM_2 interface to be perfectly metallic.
a) Due to the applied voltage V_0 driving the current in FM_1, the density of states for spin-up electrons get shifted and the highest occupied state is found for $E_F + e \cdot V_0$. At the FM_1/SCC interface the chemical potential for spin-up electrons of FM_1 and the SCC are aligned due to continuity relations, resulting in a shift of the chemical potential of the SCC and a net spin accumulation in the SCC. During the transport, the shift in the chemical potential and the spin accumulation gets reduced due to spin flip events, impurity scattering etc. If there is a net spin accumulation left at the SCC/FM_2 interface, the chemical potential for spin up electrons of the SCC and FM_2 are aligned, resulting in an increase in the chemical potential of FM_2. The measured non-local voltage V_{NL} is proportional to the shift in the chemical potential.
b) Situation for an antiparallel magnetization alignment of the two ferromagnetic electrodes. Here, the chemical potential for spin down electrons for the SCC and FM_2 are aligned at the SCC/FM_2 interface.

1.8.1. Non-local spin signal as a function of the electrode separation

In this subsection, the non-local signal as a function of the electrode separation is determined by the 1D spin model, following [151]. Starting with the current density $\vec{j}_N$, driven by an electric field $\vec{E}$ and by the gradient of the charge carrier density deviation δn_N one can write

$$\vec{j}_N = \sigma_N \cdot \vec{E} - e d_N \vec{\nabla} \delta n_N. \tag{1.141}$$

σ_N is the conductivity and d_N the diffusion constant of the nonmagnetic, low spin orbit coupling material. Equation 1.141 can be simplified by introducing the density of states in the spin sub-band

N_N and by the shift of the chemical potential $\delta\epsilon_N$ from the equilibrium value. This yields

$$\begin{aligned} \delta n_N &= N_N \delta\epsilon_N, \\ \sigma_N &= e^2 N_N D_N, \end{aligned} \tag{1.142}$$

and one obtains for the current density $\vec{j}_N$

$$\vec{j}_N = -\frac{\sigma_N}{e}\vec{\nabla}\mu_N. \tag{1.143}$$

In Equation 1.143, $\mu_N = \epsilon_N + e\phi$ is introduced as the electrochemical potential. By the continuity equation for charge and spin in the steady state, one can write

$$\vec{\nabla}\cdot(\vec{j}_\uparrow + \vec{j}_\downarrow) = 0, \tag{1.144}$$

$$\vec{\nabla}\cdot(\vec{j}_\uparrow - \vec{j}_\downarrow) = -e\frac{\delta n_\uparrow}{\tau_{\uparrow\downarrow}} + e\frac{\delta n_\downarrow}{\tau_{\uparrow\downarrow}}, \tag{1.145}$$

where $\tau_{\sigma\sigma'}$ is the average scattering time of an electron from spin state σ to spin state σ'. By the aid of the continuity equation, a Laplace equation for the electrochemical potential μ is found which yields

$$\begin{aligned} \Delta(\sigma_\uparrow\mu_\uparrow + \sigma_\downarrow\mu_\downarrow) &= 0, \\ \Delta(\mu_\uparrow - \mu_\downarrow) &= \frac{\mu_\uparrow - \mu_\downarrow}{\lambda^2}. \end{aligned} \tag{1.146}$$

$\lambda_N = \sqrt{D_N \cdot \tau_{sf}}$ is introduced as the spin diffusion length of the nonmagnetic material. Furthermore $\tau_{sf}^{-1} = 1/2(\tau_{\uparrow\downarrow}^{-1} + \tau_{\downarrow\uparrow}^{-1})$ is defined as the reciprocal average time between spin flip events and the inverse diffusion constant as $D_N^{-1} = (N_\uparrow D_\downarrow^{-1} + N_\downarrow D_\uparrow^{-1})/(N_\uparrow + N_\downarrow)$.

To simplify the following calculation, a uniform distribution of the interface spin current is assumed over the contact area $S_J = w_F \cdot w_N$. w_F is the width of the injector and w_N the width of the spin current conduit. This assumption is valid since the spin diffusion length λ_N is in the order of a few hundred nm, while w_N and w_F are typically around 100-200 nm. Furthermore, a continuous drop of the electrochemical potential at the interface of each junction is supposed with the interface resistance R_i. The interface current I_i^N across the interface ($z = 0$) is given by

$$I_i^N = \frac{G_i^\sigma}{e}(\mu_{F|z=0^+}^\sigma - \mu_{N|z=0^-}^\sigma), \tag{1.147}$$

where $G_i = G_i^\uparrow + G_i^\downarrow = R_i^{-1}$ is the interface conductance. For transparent contacts ($G_i \to \infty$) the electrochemical potentials are continuous at the interfaces while for tunnel junctions the discontinuity is much larger than the spin splitting. If the typical situation of a charge current flowing from FM_1 to the left side of the spin current conduit is assumed and no charge current is flowing in the FM_2/SCC junction, the solution for Equation 1.146 can be determined as follows:

In the spin current conduit, the chemical potential $\mu_N^\sigma(x) = \bar{\mu}_N + \sigma \cdot \delta\bar{\mu}_N$ ($\bar{\mu}_N = (eI/\sigma_N) \cdot x$ for $x < 0$ and $\bar{\mu}_N = 0$ for $x > 0$) varies only in the x-direction as a result of the large spin diffusion length compared to the thickness of the spin current conduit and the contact dimensions. One finds for $\delta\mu_N$

$$\delta\mu_N = a_1 \exp\left(\frac{-|x|}{\lambda_N}\right) + a_2 \exp\left(-\frac{|x-d|}{\lambda_N}\right). \tag{1.148}$$

The a_1 term describes the shift in the electrochemical potential due to spin injection at $x = 0$ and the a_2 term considers the feedback shift due to the presence of the second ferromagnet at the end of the conduit $x = d$.

The situation is different in the case of the two ferromagnetic electrodes. In this case, the contact dimensions of each electrode are large compared to the spin diffusion length λ_F since the spin diffusion

lengths in FM are typically only a few nm [152–154]. Therefore the spin splitting of μ_F^σ decays quickly along the z-direction and the solution has the following form near the interface ($0 < z \leq \lambda_F$)

$$\mu_F^\sigma(z) = \bar{\mu}_F + \sigma \cdot b_i \left(\frac{\sigma_F}{\sigma_F^\sigma}\right) \exp\left(-\frac{z}{\lambda_F}\right) \tag{1.149}$$

with $\bar{\mu}_{F1} = (eI/\sigma_F A_J) \cdot z + e \cdot V_1$ as the chemical potential for the first ferromagnetic electrode and $\bar{\mu}_{F2} = e \cdot V_2$ as the chemical potential for the second ferromagnetic electrode. V_1 and V_2 are the voltage drops at the interfaces of junction one and two, respectively. Due to the continuity of the spin currents at the interfaces one finds

$$I_1^S = \alpha_F I - 2\left(\frac{\sigma_F S_J}{e\lambda_F}\right) \cdot b_1 \tag{1.150}$$

$$I_2^S = -2\left(\frac{\sigma_F S_J}{e\lambda_F}\right) b_2 \tag{1.151}$$

with α_F as the spin polarization of the ferromagnetic material. The constants a_1, a_2, b_1, b_2, V_1 and V_2 can be calculated by the continuity condition for the charge and spin currents at the interface. The spin dependent voltage drop at the interface of the spin current conduit SCC and the second ferromagnet FM_2 is given by

$$\frac{V_2}{I} = \pm 2R_{N,S} \exp\left(\frac{-d}{\lambda_N}\right) \prod_{i=1}^{2} \left(\frac{\alpha \cdot \frac{R_i}{R_{S,N}}}{1-P_j^2} + \frac{\alpha \frac{R_{S,F}}{R_{S,N}}}{1-\alpha^2}\right) \cdot \left[\prod_{i=1}^{2} \left(1 + \frac{2\frac{R_i}{R_{S,N}}}{1-P_j^2} + \frac{2\frac{R_{S,F}}{R_{S,N}}}{1-\alpha^2}\right) \exp\left(-2\frac{d}{\lambda_N}\right)\right]^{-1}. \tag{1.152}$$

The +-sign in Equation 1.152 is for a parallel magnetization alignment and the −-sign for an antiparallel magnetization alignment of the two ferromagnetic electrodes. $R_{S,N} = \rho_N \lambda_N / S_N$ and $R_{S,F} = \rho_F \lambda_F / S_J$ are the spin resistances of the SCC and the ferromagnetic materials with cross sections S_N and S_J.

$P_J = (|G_i^\uparrow - G_i^\downarrow|)/G_i$ is the interface current polarization and ρ_N and ρ_F are the electrical resistivities of the nonmagnetic and ferromagnetic material. The spin accumulation signal is then detected as the voltage difference between the parallel and antiparallel state $V_s = (V_2^P - V_2^{AP})$.

If typical values $\rho_F/\rho_N \approx 10$, $\lambda_F/\lambda_N \approx 0.01$ and $S_N/S_J \approx 0.1$ are assumed, this yields $R_{S,F}/R_{S,N} \approx 0.01$ and three limiting cases can be distinguished:

a) When both junctions are transparent (R_1,$R_2 \ll R_{S,F}$), one finds

$$R_{\mathrm{NL}}(d) = \frac{4\alpha^2}{(1-\alpha^2)^2} \cdot R_{S,N} \left(\frac{R_{S,F}}{R_{S,N}}\right)^2 \frac{\exp\left(-\frac{d}{\lambda_N}\right)}{1 - \exp\left(-2 \cdot \frac{d}{\lambda_N}\right)}. \tag{1.153}$$

b) When one junction is a tunnel barrier and the second one a transparent interface, (i.e. $R_1 \ll R_{S,F} \ll R_{S,N} \ll R_2$) one obtains

$$R_{\mathrm{NL}}(d) = \frac{2\alpha P_J}{1-\alpha^2} \cdot R_{S,N} \left(\frac{R_{S,F}}{R_{S,N}}\right) \exp\left(\frac{-d}{\lambda_N}\right). \tag{1.154}$$

c) When both interfaces are tunnel junctions (R_1,$R_2 \gg R_{S,N}$), one gets

$$R_{\mathrm{NL}}(d) = P_J^2 R_{S,N} \exp\left(\frac{-d}{\lambda_d}\right). \tag{1.155}$$

As can be seen in the three cases, the resistance mismatch $R_{S,F}/R_{S,N}$ depends on the number of tunnel junctions, resulting in the maximum spin signal for a full tunnel junction based device [155].

However, for such a device it is difficult to drive high currents across such a tunnel barrier, hence metallic transport interfaces can be more appropriate for magnetic state manipulation depending on the device. For a uniform current distribution across the junction and transparent interfaces, the distance d would be the centre-to-centre distance between the two ferromagnetic electrodes. In our experiments, we often observe that the signal is largely determined by hot-spots of conduction at the interfaces, which can be confirmed by absorption measurements as explained later in detail. The different interfaces which play a crucial role for the non-local signal are shown schematically in Figure 1.21.

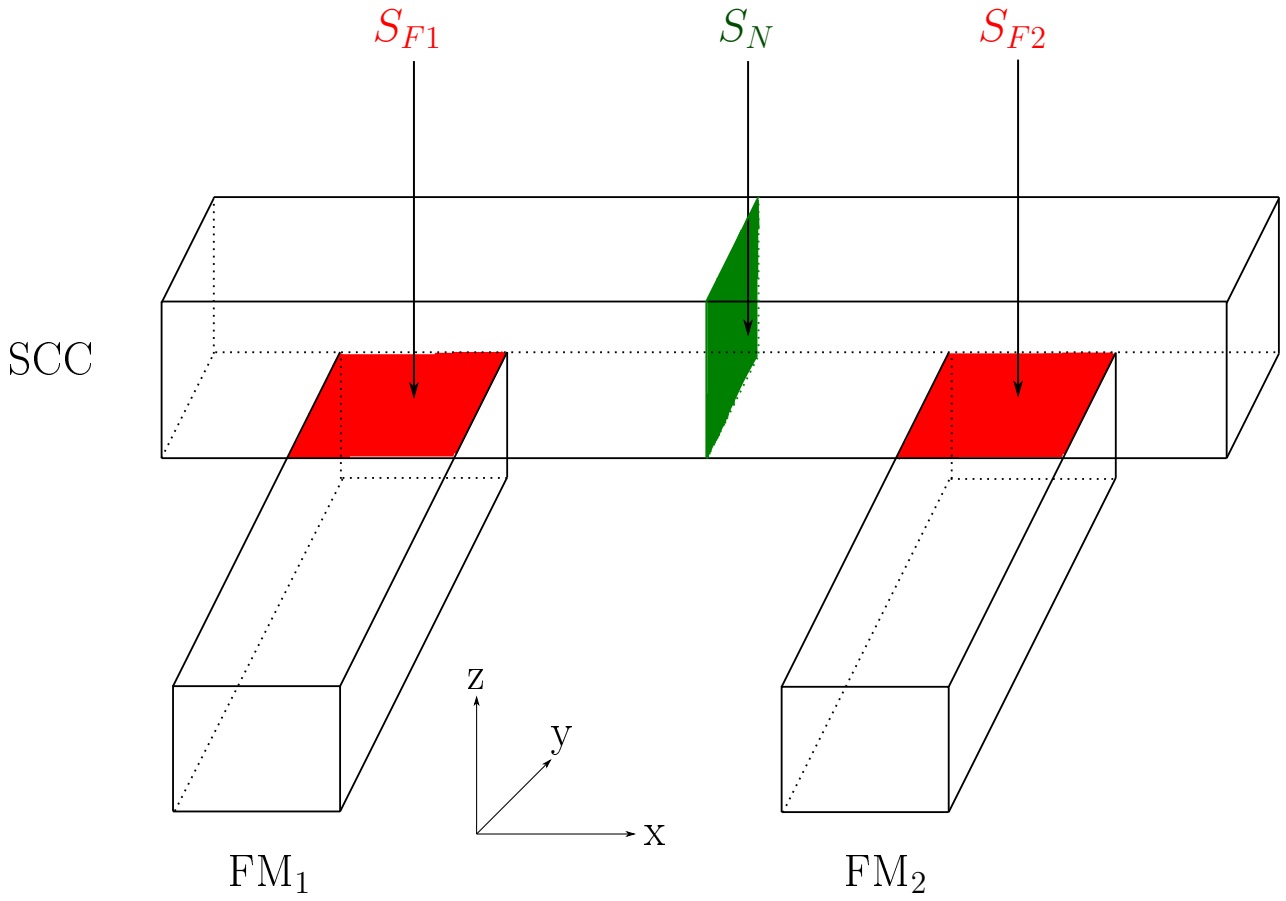

Fig. 1.21. Schematic illustration of a lateral spin device with the relevant interfaces drawn in red and green.

1.9. Thermal Spin Currents In Lateral Spin Valves

In addition to the already discussed electrically generated spin currents in lateral spin valves, there is also the possibility to study thermally generated spin currents, which arise due to the spin dependent Seebeck effect [156–158]. In this section, the explanation given in [156] is followed which has been the first report of the spin dependent Seebeck effect in a lateral spin valve. In a metallic lateral spin valve, the magnetic components typically have a much larger resistivity than the nonmagnetic bridge. In general, a heat gradient applied across a conductor leads to the (ordinary) Seebeck effect which generates an electric field. In a ferromagnet, the transport parameters for spin up and spin down electrons are different, leading to a spin dependent conductivity $\sigma_{\uparrow,\downarrow}$ and spin dependent Seebeck coefficients $S_{\uparrow,\downarrow}$. In order to understand what happens when a heat current Q is sent through the FM/NM interface, one starts with the spin dependent currents $J_{\uparrow,\downarrow}$ and can write

$$J_{\uparrow,\downarrow} = -\sigma_{\uparrow,\downarrow}\left(\frac{1}{e}\nabla(\mu_{\uparrow,\downarrow}) - S_{\uparrow,\downarrow}\nabla(T)\right), \tag{1.156}$$

with $(\mu_{\uparrow,\downarrow})$ as the spin dependent chemical potential. As a result of the heat current $Q = -k_{FM}\nabla T_{FM}$, a spin current $J_S = J_\uparrow - J_\downarrow$ is generated which can be written as

$$J_S = J_\uparrow - J_\downarrow \sigma_F \frac{(1-P^2)}{2} S_S \nabla(T). \tag{1.157}$$

$S_S = S_\uparrow - S_\downarrow$ is the spin dependent Seebeck coefficient which drives the spin current, P is the spin polarization of the ferromagnet and σ_F the conductivity of the ferromagnet. By solving the Valet-Fert equation as in [159], the spin accumulation at the interface is given as

$$\frac{\mu_s}{\nabla(T)_{FM}} = e\lambda_F S_S R_{\text{mis}}. \tag{1.158}$$

$R_{\text{mis}} = R_N/(R_N + R_F/(1-P^2))$ is a conductivity mismatch factor with $R_i = \lambda_i/\sigma_i$ being the spin resistances of the ferromagnetic and the nonmagnetic material, which depend on the spin relaxation lengths λ_i and the conductivities σ_i [160]. In metallic systems, the conductivity mismatch factor is typically close to 1. The induced spin accumulation only depends on the spin dependent Seebeck coefficient S_S and the spin relaxation length of the ferromagnet λ_F. Its direction depends on the spin dependent Seebeck coefficient S_S which changes sign when the magnetization orientation of the ferromagnet is reversed. The conceptual diagram together with the spin dependent chemical potentials at the FM/NM interface are shown schematically in Figure 1.22.

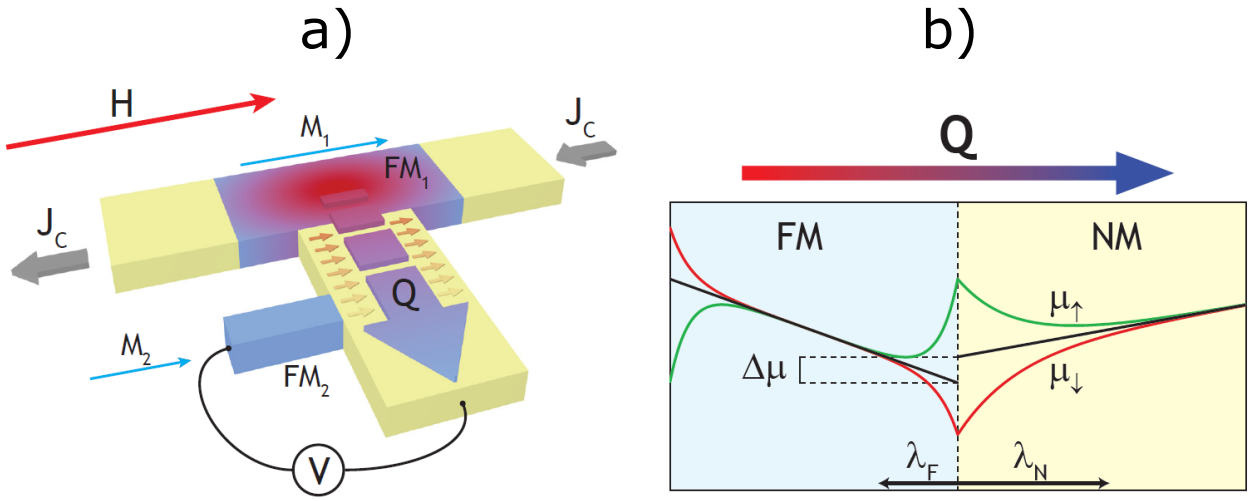

Fig. 1.22. a) Conceptual diagram of the spin dependent Seebeck effect in a lateral spin valve. A charge current J_C is sent through the first ferromagnet FM_1, which causes large Joule heating due to the large resistivity of FM1. The nonmagnetic, yellow contacts have a high thermal conductivity and act as heat sinks. The generated heat current Q through the FM_1/NM interface generates a spin current which depends on the magnetization orientation of FM_1. This spin current can be detected in a second harmonic scheme as a voltage at the NM/FM_2 interface. Reproduced from [156] with the permission of Springer Nature.
b) Spin dependent chemical potential at the FM/NM interface when a heat current Q crosses the interface. The heat current is continuous across the interface which leads to a discontinuity of ∇T. Although no charge current can leave the ferromagnet, a spin current proportional to the spin dependent Seebeck coefficient is generated which becomes depolarized in the bulk of the NM. As a result, a spin imbalance $\Delta_m u = \mu_\uparrow - \mu_\downarrow$ is generated, which relaxes on both the FM and the NM side of the interface on the typical length scales λ_F and λ_N, respectively. Reproduced from [156] with the permission of Springer Nature.

1.10. Non-Collinear Magnetization Orientation: Spin Transfer Torque

Up to now, only collinear magnetization orientations in a lateral spin valve structure have been discussed although of course in reality, there is always a small tilting of the two magnetization orientations at finite temperatures. However, the situation becomes more interesting when there is an angle between the spin current orientation and detector magnetization, yielding a spin transfer torque on the magnetization [6]. As mentioned before, this spin transfer torque can be exploited to efficiently manipulate the magnetization of the detector [14, 15].

For the analysis, [6] is followed and the pure spin current flowing in the spin current conduit is divided into one component parallel and one component perpendicular to the detector magnetization. Since, according to the assumptions, the parallel component of the spin current is absorbed in the detector without any further effect, the focus is on the perpendicular spin current component which is also named the transverse spin current.

This transverse spin current is not an eigenstate of the ferromagnetic system which consists of spin-up $\vec{k}_\uparrow$ and spin-down states $\vec{k}_\downarrow$, but rather a linear combination of these eigenstates. As a result, the coefficients of the spin-up and spin-down states will oscillate as a function of position and we observe a $\cos\left(\left[\vec{k}_{z,\uparrow} - \vec{k}_{z,\downarrow}\right] \cdot z\right)$ behaviour. $\left(\vec{k}_{z,\uparrow} - \vec{k}_{z,\downarrow}\right)$ is named the spin dependent Fermi wave vector. To calculate the overall transverse spin current at the position z in the detector, one integrates all possible wave vectors over the Fermi surface. Since the integrand is strongly oscillating, only short distances along the z-direction do not cancel out and as a result, the spin current gets absorbed close to the NM/FM_2 interface and the penetration depth, also named the magnetic coherence length, reads [51]

$$\lambda_c = \frac{\pi}{|\vec{k}_{z,\uparrow} - \vec{k}_{z,\downarrow}|}. \tag{1.159}$$

As a result of angular momentum conservation, the absorption of the transverse spin current is connected to a torque acting on the local magnetization of the detector within the magnetic coherence length. This torque is named the spin transfer torque, which is given by [161]

$$\vec{\tau} = -\frac{\hbar}{2e}\left(\vec{M} \times \vec{I}_s \times \vec{M}\right), \tag{1.160}$$

with $\vec{M}$ as the local magnetization of the detector and $\vec{I}_s$ as the spin current orientation. As a direct result of Equation 1.160, we notice that angles close to 90 ° between spin current orientation and detector magnetization lead to large spin transfer torques.
Since this formula is of vital importance to understand the experimental results, [161] is used in order to derive it. It is however mentioned that the pioneer work concerning non-collinear magnetization orientation and the resulting spin transfer torque is based on Slonczewski [162] while Brataas et al. studied in depth non-collinear magnetoelectronics [163].

The derivation starts with the electrochemical potential $u_0(x)$, which is given as

$$u_0(x) = u_{\mathrm{ch}}(x) - e\phi(x), \tag{1.161}$$

with $u_{\mathrm{ch}}(x)$ the chemical and $\phi(x)$ the electric potential. In order to describe a spin polarized system, $\vec{u}_s(x)$ is introduced. The direction of $\vec{u}_s(x)$ denotes the direction of spin accumulation while the magnitude of $|\vec{u}_s(x)|$ gives the energy splitting of the two spins in the local coordinate system. In a ferromagnetic system, $\vec{u}_s^F(x)$ is given as

$$\vec{u}_s^F(x) = \vec{m}[u_\uparrow^F(x) - u_\downarrow^F(x)], \tag{1.162}$$

where $\vec{m}$ is an unit vector along the magnetization in the FM and $u_{\uparrow(\downarrow)}^F(x)$ is the electrochemical potential of the majority (minority) in the local coordinate system with the quantization axis being parallel to the magnetization.

Since the magnetic coherence length in a conventional ferromagnetic is in the order of the lattice constant [164], only components which are parallel or antiparallel to $\vec{m}$ can survive which leads to

$$I_0^F(x) = -\frac{S^F}{e}\left(\sigma_\uparrow^F \nabla_x u_\uparrow^F(x) + \sigma_\downarrow^F \nabla_x u_\downarrow^F(x)\right) \tag{1.163}$$

$$\vec{I}_s^F(x) = -\frac{S^F}{e}\nabla_x\left(\sigma_\uparrow^F u_\uparrow^F(x) - \sigma_\downarrow u_\downarrow^F(x)\right)\vec{m} \tag{1.164}$$

for the charge current $I_0^F(x)$ and for the spin current $\vec{I}_s^F(x)$. The transport is assumed to be along the x-axis, S^F is the area of the cross section in the FM and $\sigma_{\uparrow(\downarrow)}^F$ is the conductivity of the majority (minority) spin channel. Analogously to the conservation of electric currents, the continuity equations of the spin currents are given as [165]

$$\frac{\nabla_x I_\uparrow^F(x)}{S^F} = -e\xi_\uparrow\left(\frac{u_\uparrow^F(x) - u_0^F(x)}{\tau_{\uparrow\downarrow}}\right) + e\xi_\downarrow\left(\frac{u_\downarrow^F(x) - u_0^F(x)}{\tau_{\downarrow\uparrow}}\right) \tag{1.165}$$

$$\frac{\nabla_x I_\downarrow^F(x)}{S^F} = -e\xi_\downarrow\left(\frac{u_\downarrow^F(x) - u_0^F(x)}{\tau_{\downarrow\uparrow}}\right) + e\xi_\uparrow\left(\frac{u_\uparrow^F(x) - u_0^F(x)}{\tau_{\uparrow\downarrow}}\right), \tag{1.166}$$

with $\xi_{\uparrow(\downarrow)}$ the density of states per unit volume at the Fermi level for one spin orientation while $\tau_{\uparrow\downarrow}$ and $\tau_{\downarrow\uparrow}$ are the spin flip scattering times for majority and minority spins. With detailed balance ($\xi_\uparrow/\tau_{\uparrow\downarrow} = \xi_\downarrow/\tau_{\downarrow\uparrow}$), one finds for the conjugated diffusions equations

$$\nabla_x^2 u_\uparrow^F(x) = \frac{u_\uparrow^F(x)}{D_\uparrow \tau_{\uparrow\downarrow}} - \frac{u_\downarrow^F(x)}{D_\uparrow \tau_{\uparrow\downarrow}}, \tag{1.167}$$

$$\nabla_x^2 u_\downarrow^F(x) = \frac{u_\downarrow^F(x)}{D_\downarrow \tau_{\downarrow\uparrow}} - \frac{u_\uparrow^F(x)}{D_\downarrow \tau_{\downarrow\uparrow}} \tag{1.168}$$

where $D_{\uparrow(\downarrow)}$ is the diffusion constant for the majority (minority) spin which is related to $\sigma_{\uparrow(\downarrow)}^F$ via the Einstein relation

$$\sigma_{\uparrow(\downarrow)} = e^2 \xi_{\uparrow(\downarrow)} D_{\uparrow(\downarrow)} \tag{1.169}$$

Solving the diffusion equations yields

$$\begin{pmatrix} u_\uparrow(x) \\ u_\downarrow(x) \end{pmatrix} = (\hat{A} + \hat{B}x)\begin{pmatrix} 1 \\ 1 \end{pmatrix} + \hat{C}e^{x/\lambda^F}\begin{pmatrix} \sigma_\uparrow^{F-1} \\ -\sigma_\downarrow^{F-1} \end{pmatrix} + \hat{D}e^{-x/\lambda^F}\begin{pmatrix} \sigma_\uparrow^{F-1} \\ -\sigma_\downarrow^{F-1} \end{pmatrix}, \tag{1.170}$$

with $\hat{A}$, $\hat{B}$, $\hat{C}$ and $\hat{D}$ as constants which need to determined by the boundary conditions and λ^F the spin diffusion length in the ferromagnet.

The transport in the NM is studied next, for which the electrical current $I_0^N(x)$ and the spin current are given as

$$I_0^N(x) = -\frac{\sigma^N}{e} S^N \nabla_x u_0^N(x) \tag{1.171}$$

$$\vec{I}_s^N(x) = \frac{\sigma^N}{2e} S^N \nabla_x \vec{u}_s^N(x), \tag{1.172}$$

where S^N is the cross section of the NM and σ^N is the conductivity. Conservation of electric current requires $\nabla_x I_0^N(x) = 0$, which yields

$$\nabla_x^2 u_0^N(x) = 0 \tag{1.173}$$

while the spin current continuity conditions is given as

$$\frac{1}{S^N}\nabla_x \vec{I}_s^N(x) = -e\frac{\xi^N \vec{u}_s^N(x)}{2\tau_{sf}^N}, \tag{1.174}$$

where ξ^N is the total density of states per unit volume at the Fermi level in the NM. τ_{sf}^N is the spin relaxation time in the NM. With the electric current condition and the spin current continuity equation, the diffusion equation for $\vec{u}_s^N(x)$ is given as

$$\nabla_x^2 \vec{u}_s^N(x) = \frac{\vec{u}_s^N(x)}{\lambda^N}, \tag{1.175}$$

with λ^N the spin diffusion length in the NM. The solution of Equation 1.175 can be written in the form

$$\vec{u}_s^N(x) = \hat{E}e^{x/\lambda^N} + \hat{F}e^{-x/\lambda^N} \tag{1.176}$$

with $\hat{E}$ and $\hat{F}$ as constant vectors depending on the boundary conditions. Next, the electrical and the spin current across the FM/NM contact can be written in the linear response regime (assuming the absence of interfacial spin-flip scattering events) as follows:

$$eI_0^{N|F} = \left(G_\uparrow^I + G_\downarrow^I\right)\left(u_0^N(x_I^-) - u_0^F(x_I^+)\right) + \frac{1}{2}\left(G_\uparrow^I - G_\downarrow^I\right)\left(\vec{m}\cdot\vec{u}_s^N(x_I^-)\; u_s^f(x_I^+)\right) \tag{1.177}$$

$$e\vec{I}_s^{N|F} = \vec{m}[\left(G_\uparrow^I - G_\downarrow^I\right)\left(u_o^N(x_I^-) - u_0^F(x_I^+)\right) - \frac{1}{2}\left(G_\uparrow^I + G_\downarrow^I\right)u_s^F(x_I^+) \tag{1.178}$$

$$-\frac{1}{2}\left(2\mathrm{Re}(G_{\uparrow\downarrow}^I) - G_\uparrow^I - G_\downarrow^I\right)\vec{m}\cdot\vec{u}_s^N(x_I^-)] + \mathrm{Re}(G_{\uparrow\downarrow}^I)\;\vec{u}_s^N(x_I^-) - \mathrm{Im}(G_{\uparrow\downarrow}^I)\;\vec{m}\times\vec{u}_s^N(x_I^-)),$$

where $u_0^F(x_I^+) = (u_\uparrow^F(x_I^+) + u_\downarrow^F(x_I^+))/2$. The index I refers to the interface contact and $x_I^{+(-)}$ denotes the position in the vicinity of the interface at the FM (NM) side. $G_{\uparrow(\downarrow)}$ is the conductance of the FM/NM interface for the majority (minority) spin while $G_{\uparrow\downarrow}$ is the spin mixing conductance, describing the non-collinear transport [166]. In a metallic system, the imaginary part of $G_{\uparrow\downarrow}$ is on the order of two magnitudes smaller than the real part and therefore neglected.

Since, in the steady state, the charge accumulation across the FM/NM interface is invariant, one finds

$$I_0^N(x_I^-) = I_0^{N|F} = I_0^F(x_I^+), \tag{1.179}$$

while the conservation of the collinear component of the spin accumulation across the interface can be written as

$$\vec{m}\left(\vec{m}\cdot\vec{I}_s^N(x_I^-)\right) = \vec{m}\left(\vec{m}\cdot\vec{I}_s^{N|F}\right) = \vec{I}_s^F(x_I^+). \tag{1.180}$$

In the adiabatic approximation, the suppression of the non-collinear part of the spin current results in a transfer of angular momentum into the local magnetization of the second FM. This torque, generated by the spin current, is given as

$$\vec{\tau} = -\frac{\hbar}{2e}\left[\vec{I}_s^{N|F} - \vec{m}(\vec{m}\cdot\vec{I}_s^{N|F})\right]. \tag{1.181}$$

In order to consider the non-local signal defined as $R_{\mathrm{NL}}(\theta)=V_{\mathrm{NL}}(\theta)/I_0$ with θ as the angle between spin current and local magnetization of FM_2, the voltage across the NM/FM_2 interface needs to be calculated. For FM2, the local electrochemical potential far away from the NM/FM_2 interface is the

experimentally measured non-local voltage $V_{\mathrm{NL}} = u_F(\infty)/-e$. Thus the angular dependence of the non-local signal can be obtained analytically as

$$R_{\mathrm{NL}}(\theta) = \left[2R_N e^{-L/\lambda^N}\cos\theta \prod_{i=1}^{2}\left(P_i^I\eta_i^I + \alpha_i^F\eta_i^F\right)\right] \cdot \left[e^{-2L/\lambda^N} - \prod_{i=1}^{2}\left(2\eta_i^I + 2\eta_i^F + 1\right) + \sin^2\theta\left[1 - e^{2L/\lambda^N}\cdot\prod_{i=1}^{2}(2\rho_i^I+1)\right]^{-1}\prod_{i=1}^{2}(2\eta_i^I + 2\eta_i^F - 2\rho_i^I)\right]^{-1} \tag{1.182}$$

where the subindex $i = 1(2)$ denotes $\mathrm{FM}_{1(2)}$ and the corresponding $\mathrm{FM}_{1(2)}$/NM interface. The introduced dimensionless parameters are defined as

$$\eta^I = \frac{R^I}{(1-(P^I)^2)\ R^N)} \tag{1.183}$$

$$\eta^F = \frac{R^F}{(1-(\alpha_F)^2)\ R^N} \tag{1.184}$$

$$\rho^I = \frac{(2Re(G^I_{\uparrow\downarrow}))^{-1}}{R^N} \tag{1.185}$$

with the interfacial resistance $R^I = (G^I_\uparrow + G^I_\downarrow)^{-1}$ and the resistances $R^N = \lambda_N/(\sigma^N S^N)$ and $R^F = \lambda_F/(\sigma^F S^F)$. $P^I = (G^I_\uparrow - G^I_\downarrow)/(G^I_\uparrow + G^I_\downarrow)$ is the spin polarization across the interface while $\sigma^F = \sigma^F_\uparrow + \sigma^F_\downarrow$ and $\alpha^F = (\sigma^F_\uparrow - \sigma^F_\downarrow)/(\sigma^F_\uparrow + \sigma^F_\downarrow)$ are the conductivity and the spin polarization of the FM. The angular dependence of the non-local signal is introduced by the cosine function of the numerator and the term depending on $\sin^2\theta$ in the denominator. While the cosine function describes the configuration between the two ferromagnetic electrodes, the term proportional to $\sin\theta$ describes the non-collinear transport across the NM/FM_2 interface. For any type of contact, the spin transfer torque acting on FM_2 can be formally determined as

$$\vec{\tau} = -\frac{\hbar}{2e^2}\mathrm{Re}(G^I_{\uparrow\downarrow})\ \vec{m}_x \times \vec{u}_s^N(x^-_{I_2}) \times \vec{m}_2 \tag{1.186}$$

with $\vec{m}_2$ as the magnetization direction of FM_2 and $\vec{u}_s^N(x^-_{I_2})$ as the spin accumulation at the NM side of the NM/FM_2 interface. Equation 1.186 can be rewritten as

$$\vec{\tau} = -\delta(\theta) I_0\,(\vec{m}_2 \times \vec{m}_1 \times \vec{m}_2) \tag{1.187}$$

where $\delta(\theta)$ can be understood as an effective spin torque, which scales the critical current of magnetization switching [167]. The analytic expression is given as

$$\delta(\theta) = \Gamma\frac{\hbar}{2e}\mathrm{Re}(G_{\uparrow\downarrow})\ \frac{R_{\mathrm{NL}}(\theta)}{\cos\theta} \tag{1.188}$$

with $\Gamma = 2\rho_2^I\Phi/\Omega$ where Φ is defined as

$$\Phi = 1 + e^{4L/\lambda^N}\prod_{i=1}^{2}(2\rho_i^I+1)(2\eta_i^I + 2\eta_i^F 1) - e^{-2L/\lambda^N}\prod_{i\neq j}^{2}(2\rho_i^I+1)(2\eta_j^I + 2\eta_j^F + 1), \tag{1.189}$$

while Ω is given as

$$\Omega = -\left[1 - e^{2L/\lambda^N}\prod_{i=1}^{2}(2\rho_i^I) + 1\right]\cdot(P_2^I\eta_2^I + \alpha_2^F\eta_2^F)\cdot\left[1 - (2\rho_2^I+1)(2\eta_1^F+1)e^{2L/\lambda^N}\right] \tag{1.190}$$

The angular dependence of $\delta(\theta)$ depends on $R_{\mathrm{NL}}/\cos\theta$. Since the numerator of R_{NL} also depends on $\cos\theta$, the angular dependence of $\delta(\theta)$ only depends on $sin^2\theta$. As a result, $\delta(0°) = \delta(180°)$ which is different than the angular dependence found in conventional local spin valves, e.g. the giant magnetoresistance effect [168].

With the theory provided in this chapter, it is now possible to discuss how lateral spin valves are fabricated and which are the most important important parameters in order to fabricate high quality devices. This will be part of the next chapter.

Chapter II

Sample Fabrication And Experimental Methods

In this chapter, in depth explanations concerning the patterning and fabrication process of lateral spin valves are provided. To fabricate these nanostructures, there are in general two stages. First the nanostructures need to be patterned by electron-beam lithography and second the metal layers need to be deposited by either ultrahigh vacuum (UHV) thermal evaporation or by sputter deposition. Alternatively if the thin film has been grown as the first step, ion beam etching is performed to fabricate nanostructures out of the thin film. To measure the thickness and roughness of thin films, X-ray reflectivity measurements are a simple and easy method. This technique has been intensively employed especially to determine and optimize the etching rates of the in-situ argon sputter gun of the UHV thermal evaporation chamber. To determine the thickness of fabricated nanowires, atomic force microscope has been used. All methods are explained in some detail, together with examples and measurements of important results for these fabrication methods and analysis techniques. In the last part of the chapter, the lock-in amplification technique is introduced as a powerful tool to measure small signals in the nV range for the electrical characterization of the devices. Finally the used bath cryostat measurement system is presented, which can apply in-plane magnetic fields in order to switch the magnetic state of the devices and is employed to measure the non-local signal as a function of the applied field and sample temperature.

2.1. Scanning Electron Microscopy (SEM)

2.1.1. Construction and basic principles

In order to pattern high quality lateral spin valves with lateral dimensions down to 50 nm, the commercial electron beam lithography system "Pioneer" by Raith has been used [169]. This system combines a scanning electron microscope together with an electron beam lithography system. The scanning electron microscope is based on the "Gemini" electron column by Zeiss [170], the fundamental construction of which is shown in Figure 2.1. Additional, in depth information concerning scanning electron microscopy can be found in the literature [171, 172].

In the system, electrons are generated by a thermal field emission tip which is also known as a Schottky emitter. The construction of the filament is shown in Figure 2.3a). The most important aspect for determining the electron energy spread and beam quality is the tip which consists of finely etched <100> tungsten with a sintered reservoir of zirconium oxide in the shank, as shown in Figure 2.2. The tip is heated up to around 1800 K by the bake-out filament current of 2.3 A. The use of ZrO has three main advantages:

a) If an electric field is generated by the extractor voltage (in the used system $U_{ex} = 3.75\,kV$), ZrO will diffuse to the cathode tip, forming an effective tip.

b) The thermal energy of the electrons is reduced from 4.6 eV to 2.8 eV and the spread of the electron energy is reduced.

c) The electron emission is restricted along the tip axis.

The only voltage which can be chosen by the user is the electron high tension voltage (EHT) which accelerates the electrons on their way to the specimen and which plays a key role for the beam properties and the required dose for the electron beam lithography. The EHT is chosen for the patterning to be between 10-30 kV, depending on the different layers and materials and will be specified for each patterned structure. Indeed, the chosen EHT plays a crucial role for the performance of the lateral spin valve samples, as investigated in the subsequent chapters.

After passing one of the six possible apertures (7.5, 10, 15, 20, 30, 60 and 120 μm), as drawn in Figure 2.3b), the beam passes the condenser lens which controls the initial spot size of the beam.

Next, if the EHT has been chosen within the range of 0.1-20 kV, the electrons are accelerated inside the electron optics by 8 kV by the beam booster. This additional acceleration (which is reversed by the final electrostatic lens which decelerates the electrons by 8 kV) reduces the sensitivity of the electron beam to magnetic stray fields within the column. Additionally, the generated secondary electrons, which are measured by the in-lens secondary electron SE-detector get accelerated by 8 kV by the electro static lens which dramatically increases the number of electrons reaching the in-lens detector, even for low EHT voltages. As a result, the in-lens detector does not work properly for EHT voltages higher than 20 kV, since hardly any electrons reach the detector due to the lack of the accelerating voltage of the electrostatic lens. After passing the beam booster, the beam is focussed by the user via the magnetic focus lens by way of the "aperture alignment" and "astigmatism" correction.

For aperture alignment, correction voltages in the vertical and horizontal direction are applied such that the beam passes centrally through the electron optics, which can be checked by applying the so-called focus wobble feature. For a well aligned beam, the image blurs symmetrically around the centre and the centre does not move. For a misaligned beam, the image blurs asymmetrically and the centre moves along the misaligned direction. To optimize the aperture alignment further, the user applies a very low focus wobble and very high magnification and checks if no movement of the image is observed. In the final step, the focus is varied and for a perfect aperture alignment, no movement of the image at all must be detected during the variation of the focus.

If instead of having not one common focus point for the horizontal and vertical direction the beam has two focus points, the electromagnetic lens is elongated and this phenomenon is known as astigmatism

in electron microscopy. As a result of astigmatism, round objects appear elliptical with perpendicular elongation when the image is over- or under-focused while when in focus, the image remains blurred. To correct for this, the image is over- and under-focussed and the stigmator is adjusted in both directions until the elongation vanishes. An example of an image with astigmatism and the resulting perpendicular elongation direction for the under- and over-focus conditions is shown in Figure 2.4, with the image taken from [173]. The image with corrected astigmatism is shown in Figure 2.5. The beam is finally scanned across the sample by deflection coils.

As drawn in Figure 2.1, there is a second electron detector mounted in the setup, the Everhart-Thornley SE2 detector [174]. The working principle of both detectors as well as their advantages and disadvantages will be explained in the next subsection. Furthermore, the different types of generated electrons when the beam hits the specimen will be studied.

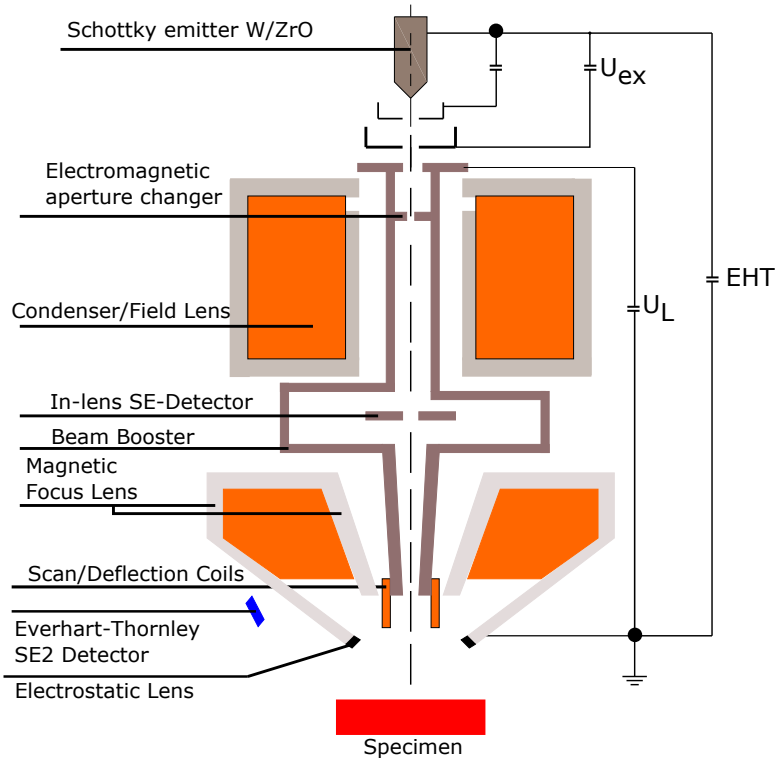

Fig. 2.1. Schematic drawing of the commercial Zeiss Gemini electron beam column which is mounted in the Raith Pioneer as part of the electron beam lithography system. A direct current of 2.3 A flows in a ZrO/W filament which heats up to around 1800 K. By the applied extractor voltage U_{ex} of 3.75 kV, electrons are emitted which are accelerated by the electron high tension voltage EHT which is chosen between 10 kV and 30 kV, depending on the used resist, the materials which are to be deposited etc. The beam next passes the electromagnetic aperture system. In total six different apertures are possible and for 10 kV EHT, the beam current varies between 10 pA (7.5 μm aperture) and 3000 pA (120 μm aperture). The beam passes in the next step the condenser lens which mainly determines the spot size and cannot be adjusted by the user. In the next step, if the EHT has been chosen to be between 0.1 kV and 20 kV, the electrons are additionally accelerated by 8 kV by the beam booster, which reduces the sensitivity of the beam to any magnetic stray fields in the column. The beam is finally focused and corrected for astigmatism by the magnetic focus lens before it is decelerated by electrostatic lenses by 8 kV and finally hits the specimen. By scan coils, the beam is deflected and the beam scans over all points on the specimen surface. By scanning over the specimen surface, an individual number of electrons is generated for each pixel which can be count and analysed by the two detectors.

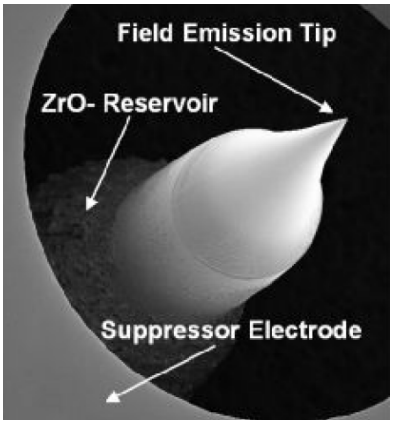

Fig. 2.2. Photograph of the thermal field emission tip which consists of <100> tungsten with a sintered reservoir of zirconium-oxide (ZrO) in the shank. As a result of the electric field generated by the extractor voltage, ZrO diffuses to the cathode tip and forms a nice tip. By the surrounding suppressor electrode, electrons which are emitted by the tungsten filament and therefore not aligned with the tip axis are efficiently suppressed. Image shown with permission from Raith GmbH [175].

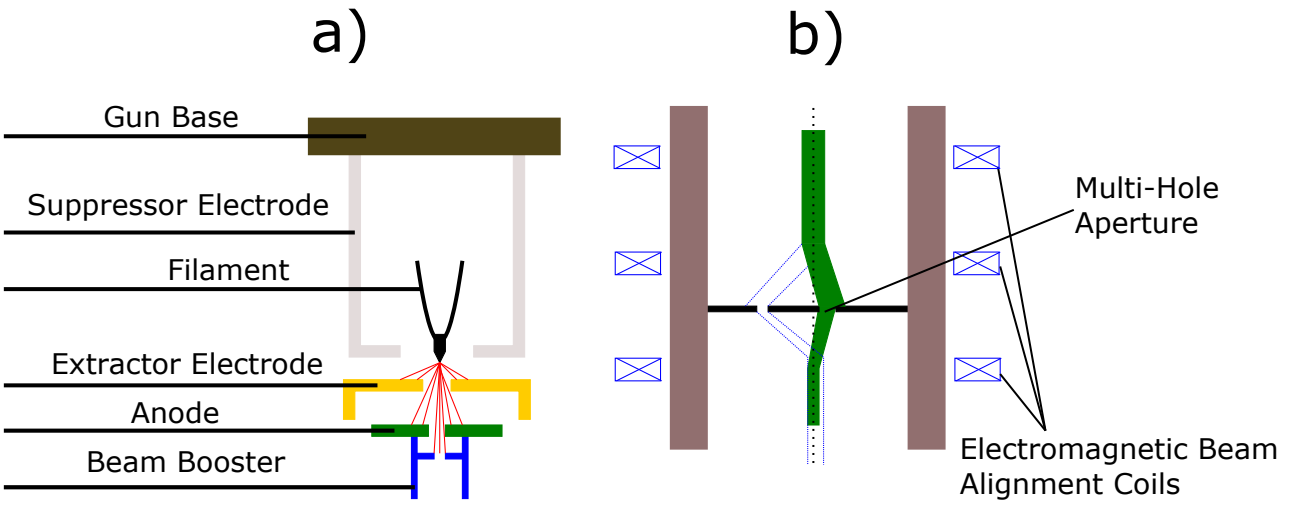

Fig. 2.3. a) Schematic illustration of the W/ZrO filament together with the suppressor electrode, extractor electrode, anode and the beam booster. A direct current of 2.3 A flows through the filament and heats it up to 1800 K. Electrons are emitted by the filament as well as by the W/ZrO oxide tip. By the surrounding suppressor electrode, electrons which are emitted by the filament and therefore not aligned with the tip axis are suppressed and do not affect the beam quality. By the extractor electrode, an electric field is generated which causes the ZrO to diffuse to the cathode tip to form a nice tip. The beam is accelerated by the EHT towards the anode and additionally, if the EHT is below 20 kV, the beam is accelerated by 8 kV by the beam booster.
b) Schematic illustration of the multi-hole aperture system which allows by way of electromagnetic beam alignment coils an electrical switching between the six aperture holes.

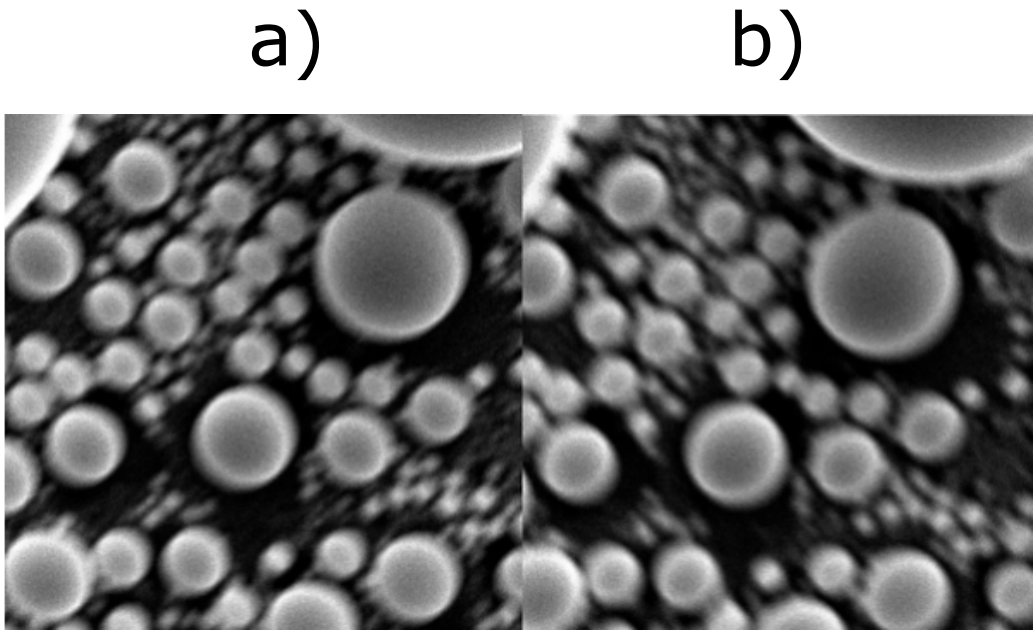

Fig. 2.4. Over- and under-focussed SEM images of bubbles with astigmatism present. As clearly visible, the circular bubbles appear to be elliptical with the elongated direction varying with over- and under-focusing the image. Image taken from [173].

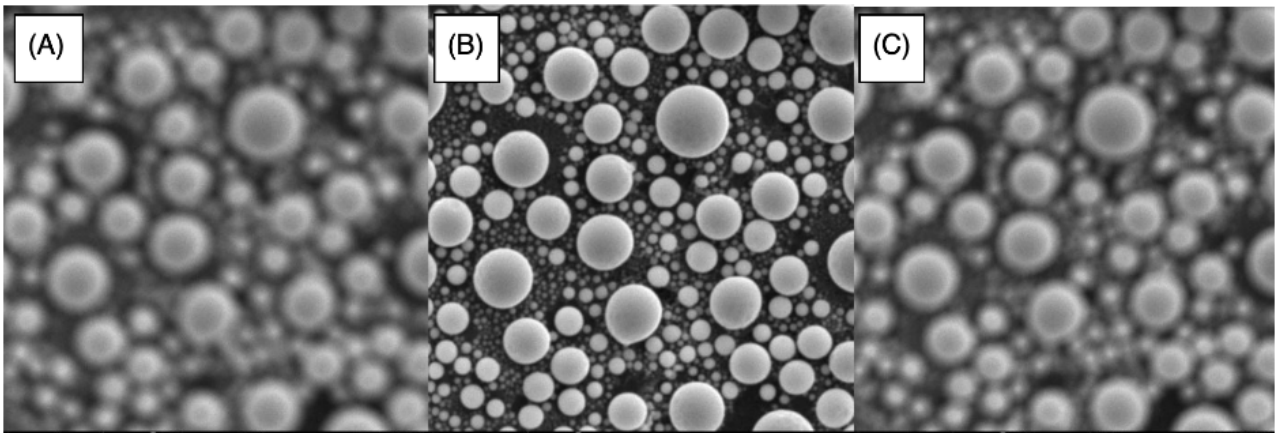

Fig. 2.5. SEM images with corrected astigmatism. Here, by over- and under-focusing the image the bubbles are blurred but not elongated. Image taken from [173].

2.1.2. Generated electrons and detector working principles

If the electron beam hits the specimen with energies between 10-30 kV, as the typically chosen EHT for an electron beam lithography process, many different effects take place and many different categories of electrons and photons are generated, as schematically drawn in Figure 2.6.

a) Secondary Electrons:

In total, three different types of secondary electrons are defined, depending on the mode of origin and where they leave the specimen surface. Secondary electrons are low energy electrons (<50 eV) which are generated by inelastic scattering of the primary electrons on the atomic core or on the electrons of the atomic shell of the specimen material. Both the in-lens detector and the

Everhart-Thornley detector mostly detect secondary electrons which are only generated in the upper part of the interaction region and therefore carry all surface information of the specimen.

b) Backscattered Electrons:

All electrons with energies higher than 50 eV are known as backscattered electrons (BSE). These electrons are generated by elastic scattering in a much deeper interaction range and therefore carry depth information. Since the backscatter coefficient crucially depends on the atomic number of the specimen, backscattered electrons provide material dependent contrast. In some SEM systems, an additional BSE-detector is mounted either in the column above the in-lens detector as an energy selective backscattered detector (ESBD) or at the side of the vacuum chamber. In the used electron beam lithography system, no BSE-detector is mounted.

c) Auger Electrons:

These electrons are ejected from an inner shell of the specimen by the energy released when an ionized atom returns to the ground state [176, 177]. The detection of Auger electrons, which have specific energies depending on the material of the specimen, allows for a material sensitive analysis of the surface of the specimen. The Auger yield is very high for materials with low atomic numbers.

d) Characteristic X-Rays:

Depending on the energy of the primary beam, characteristic X-rays are generated in the whole depth of the specimen. These characteristic X-rays originate from the inner-shell ionization process. In this process a primary electron from the initial beam interacts with the tightly bound inner-shell electrons and an atomic electron is emitted, leaving a vacancy in that shell. The atom then relaxes to its ground state through a limited set of transitions of outer-shell electrons to fill the inner-shell vacancy. The energies of the electrons in the shells are sharply defined, with values characteristic of the binding energies of the electrons. The characteristic X-rays are elemental specific which can be detected by energy-dispersive X-ray spectroscopy (EDX) [178]. EDX is a powerful tool which allows the determination of the material composition of the whole specimen.

e) Cathodoluminescence:

Photons in the visible spectrum are generated by the primary beam. In some systems, these photons are collected by an elliptical mirror, transferred out of the vacuum chamber by an optical fibre, split up by wavelength via a monochromator and finally analysed by a photomultiplier tube.

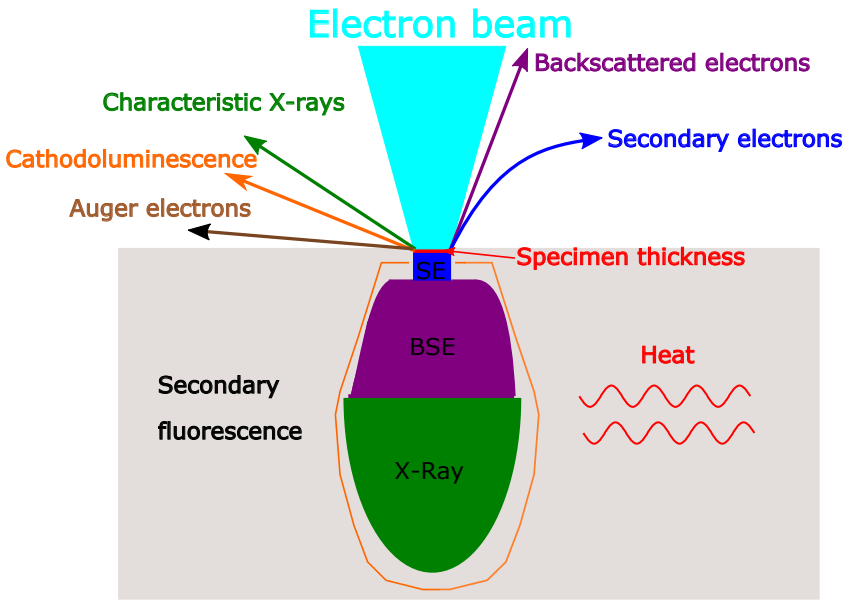

Fig. 2.6. Schematic illustration of the different generated electrons and photons when a primary electron beam with an energy of several keV hits a specimen. In the used system, both the in-lens detector and the SE2 Everhart-Thornley detector are optimized to detect secondary electrons. These secondary electrons are generated in the top few nm of the specimen and mostly provide surface information.

Next the different types of secondary electrons are discussed, as shown schematically in Figure 2.7.

SE1: These electrons are generated directly at the surface of the specimen with a high angle and carry most of the surface information.

SE2: This type of secondary electrons is generated by backscattered electrons after multiple scattering events. They leave the surface of the specimen at a much larger distance from the initial spot. SE2 carry less surface but more topographic information.

SE3: SE3 are generated by backscattered electrons far away from the spot size and typically do not contribute to the signal.

Depending on the energy of the primary beam, the ratio of the SE1 and SE2 electrons can be estimated as follows [179, 180]: The total number of detected secondary electrons δ is given by the sum of SE1 δ_1 and SE2 δ_2

$$\delta = \delta_1 + \delta_2 \tag{2.1}$$

As mentioned, SE2 are generated by backscattered electrons. This yields for δ_2

$$\delta_2 = \beta\eta\delta_1 \tag{2.2}$$

with η as the backscatter coefficient, which crucially depends on the atomic number and β as a factor which is typically lower than one for primary energies E_0 <1 keV and higher than one for higher energies. By the use of a low energy primary beam, it is possible to increase the number of SE1 electrons and therefore gain more surface information.

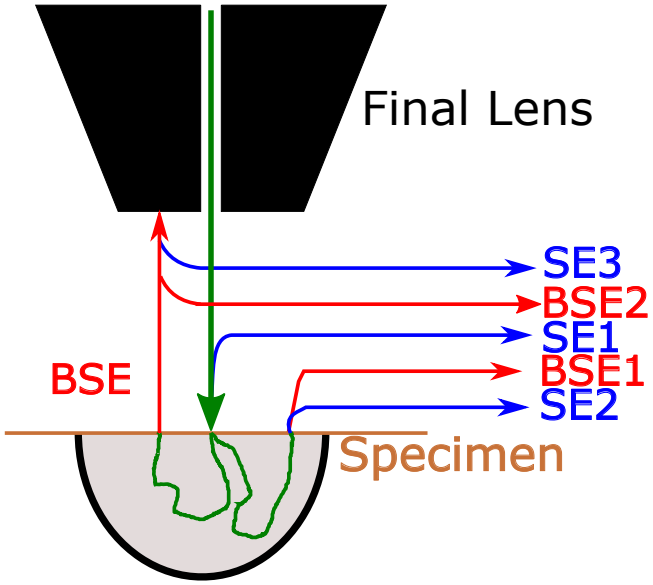

Fig. 2.7. Schematic illustration of the different generated secondary (SE) and backscattered electrons (BSE). In the used system, in both detectors mostly SE1 and SE2 are detected. SE1 electrons are directly generated by the primary beam and carry most of the surface information. SE2 electrons are generated by backscattered electrons and carry less surface but more topographic information. The ratio of SE1 and SE2 depends on the energy of the primary beam and the backscatter coefficient, which crucially depends on the atomic number of the specimen.

Finally the working principles of the two detectors are shortly explained. Furthermore SEM images taken by the different detector are presented to demonstrate their advantages and disadvantages:

In-Lens Detector:

As mentioned before, the in-lens detector only works properly for an EHT below 20 kV because for higher voltages, the beam booster is turned off and hardly any secondary electrons reach the detector due to their low energy and the lack of acceleration by the electrostatic lens. Electrons reaching the in-lens detector hit a scintillator and flash light is generated. The flash light is guided out of the beam path and is transferred to a photomultiplier tube. In the photomultiplier tube, photons hit the photocathode and electrons are ejected by the photoeffect. These electrons are focussed by a focussing electrode and accelerated towards a number of electrodes with different, increasing positive potential, termed dynodes. By secondary electron emission, out of a few electrons typically 100 million electrons can be generated and the generated signal is read out electrically. The contrast crucially depends on the electric field generated by the electrostatic field, which exponentially decays as a function of the working distance. However, in our system, only very high working distances of 8 mm and more are possible, leading to low contrast for low energy primary beams below an EHT of 5 keV. A major advantage of the in-lens detector is the easy detection of polystyrene beads, as shown in Figure 2.8a). By the use of these beads, a high quality SEM image with a magnification of better than 200 k can be relatively easy generated. Secondly, the in-lens detector is perfectly suited to detect carbon contamination spots, which enables to check and improve the beam quality further, as shown in Figure 2.8b). By the in-lens detector, nearly only SE1 are detected.

Everhart-Thornley Detector:

This detector is mounted on the wall chamber and views the specimen laterally. Since it allows to detect both SE2 and (a low amount of) backscattered electrons, the detected signal provides much more topographic and material dependent information compared to the in-lens detector.

As for the in-lens detector, electrons hit a scintillator, photons are generated which are guided to a photomultiplier and an electric signal is generated. As explained later in detail, to perform a high quality overlay-control, 20-30 nm thin metallic crosses have to be detected, which works much better with the Everhart-Thornley detector than with the in-lens detector due to the topographic information and the material dependent contrast and the high working distance. Another major advantage of the Everhart-Thornley detector is the possibility to vary the collector voltage between −250 V and +400 V. While a high collector voltage increases the contrast even for thin metals with low atomic numbers, the use of a high negative collector voltage allows efficient filtering of electrons which are generated e.g. in the photoresist when a very large aperture is used to pattern contact pads. As shown in Figure 2.8c), where 20 kV EHT has been used together with a 120 μm aperture, for very high collector voltages (+400 V) the image is completely over-exposed and the metallic cross is not visible. For a collector voltage of −250 V, most of the electrons generated in the resist environment are filtered and the cross can be detected, as shown in Figure 2.8d).

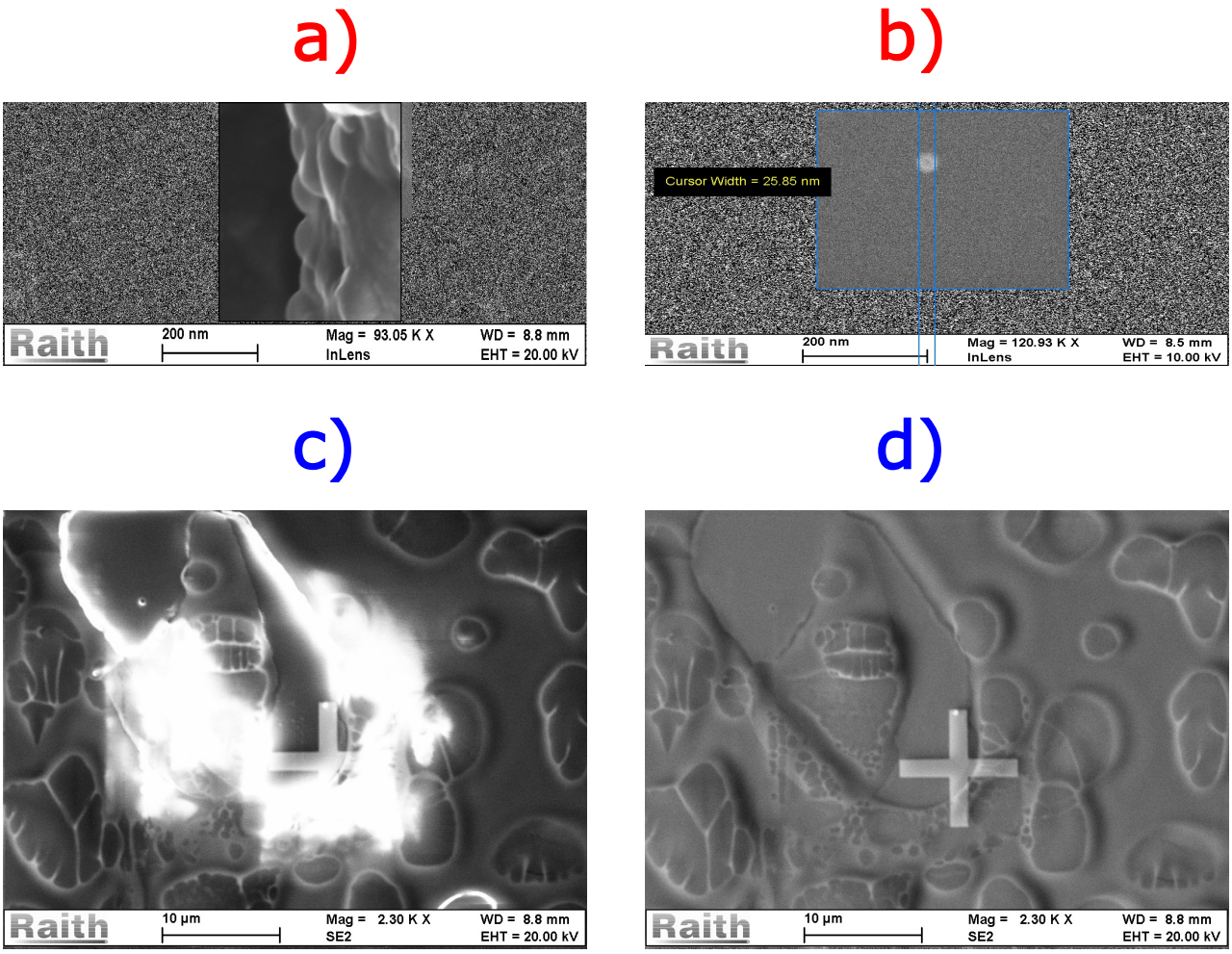

Fig. 2.8. Different SEM images demonstrating the advantages of the two detectors mounted in the electron beam lithography system.
a) High quality SEM image of polystyrene beads, which can be used to check and optimize the beam quality to magnifications of 200 k and better and which are easily detected by the in-lens detector.
b) Burnt carbon contamination spot, which can also be used to check and optimize the beam quality. These spots are usually just visible by the in-lens detector.
c), d) SEM images of a metallic cross taken with a very large aperture. By a suitable choice of the collector voltage of the Everhart-Thornley detector, electrons generated in the resist environment can be filtered and the cross is much more readily detectable.

After this introduction to the basic principles of scanning electron microscopy and the different types of secondary electrons and the advantages of the two detectors, electron beam lithography will be presented. In particular, the overlay-control, i.e. the alignment of a nanostructure on an already existing one, will be explained in detail.

2.2. Electron Beam Lithography And Overlay-Control

Since high precision overlay-control plays a crucial role for the fabrication of lateral spin valve structures, large effort has been spent in order to optimize this procedure. Together with Stefan Kauschke, a standard procedure has been established in our working group which will be explained in detail in the following.

First of all, after choosing a suitable beam aperture, EHT and working distance and aligning the beam properly, the origin correction and the angle correction needs to be performed. By these corrections

the U and V coordinates, which are the coordinates of the GDSII-layout, are matched to the X and Y coordinates of the laser stage. In the next step, a write field alignment is performed. Each working area, which is the user-defined area of the sample, is split up into write fields. The size of these write fields is typically $100{\cdot}100\,\mu m^2$ for a magnification of 1000 and small structures such as nanowires and $1000{\cdot}100\,\mu m^2$ for a magnification of 100 and large structures such as contact pads. By the writefield alignment, the deflection of the beam is matched with the physical movement of the laser stage. When a layer is patterned within one writefield, the stage is physically moved to the centre of the writefield and all positions within the particular writefield can be reached by the deflection of the beam in the X- and Y-direction.

An SEM image such as the one shown in Figure 2.9a) is taken and a magnification of 1000 is chosen. The system saves the SEM image, moves the laser stage for a chosen distance, e.g. $10\,\mu m$ in the X-direction, deflects the beam by $-10\,\mu m$ in the X-direction, takes a second SEM image and calculates the cross-correlation of both images. By the calculated cross-correlation, the correct deflection voltage for a given laser stage displacement for a given working distance can be determined.

The standard values for this procedure are a relative maximum deflection of 0.92 in both the X- and the Y-direction for a working distance of 10 mm. This means that for a proper write field alignment and a working distance of 10 mm, 92 % of the maximum deflection voltage in both directions is required to reach each point within the write field. If, as done here, the working distance is reduced to around 8.5 mm, about 97 % of the maximum deflection voltage is required. This means there is a convenient trade-off between a better quality of the SEM images and a better possible quality of the beam and the risk to overextend the deflection voltages.

To demonstrate the effect of the chosen working distance on the write field alignment, the result of the first write field alignment procedure is shown in Figure 2.9b). As clearly visible, the system uses correction values of the zoom in both the U- and the V-direction of 1.05 in order to increase the zoom factors from 0.92 to roughly 0.97. The zoom factor is a measure of the expected maximum deflection voltage compared to the real required one, which depends on the magnification, writefield size and working distance. The second important parameter, the shift, can be understood as the lateral difference in the expected origin of a particular writefield compared to the measured one.

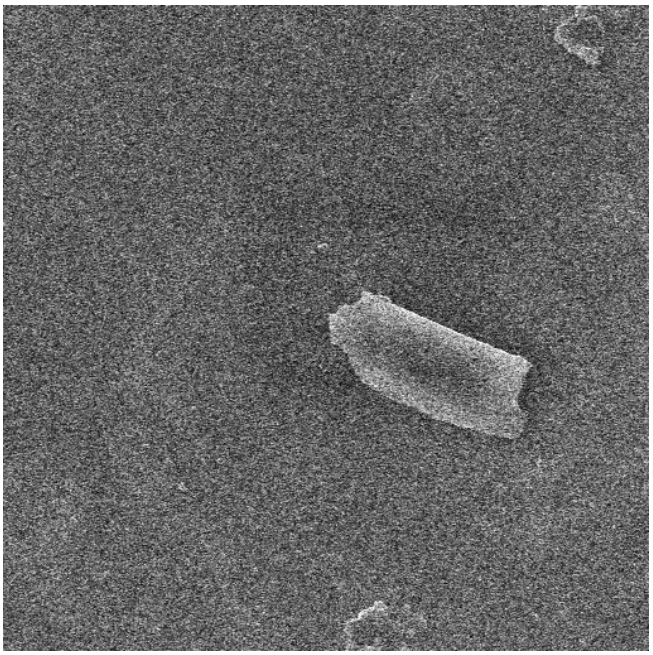

a)

General information

Comment:	*Procedure: 100 um WF - Manual ALWF 5 um marks (PLS: C:\PIONEER\User\Pfeiffer\Data\ScanPLS\Align005.PLS)*
Writefield size:	100 µm
Magnification:	1000×
Working distance:	8.519 mm
Acceleration voltage:	20.000 kV
Successfully scanned marks:	4
Unsuccessfully scanned marks:	0
Required marks:	3
Status limit check:	OFF

Coordinates

Stage X, Y, Z in mm:	(-0.247174, -0.521189, 22.876500)
Global U, V, W in mm:	(1.313440, 1.026122, 8.500223) → **used**
Local U, V in mm:	(1.313440, 1.026122)

Old values

Zoom U:	0.92000
Zoom V:	0.92000
Shift U:	0.000 µm
Shift V:	0.000 µm
Rotation U:	0.000°
Rotation V:	0.000°

New values

Zoom U:	0.97034
Zoom V:	0.97010
Shift U:	0.324 µm
Shift V:	0.001 µm
Rotation U:	1.580°
Rotation V:	2.001°

Correction values

Factor zoom U:	1.05472
Factor zoom V:	1.05446
ΔShift U:	0.324 µm
ΔShift V:	0.001 µm
ΔRotation U:	1.580°
ΔRotation V:	2.001°

b)

Fig. 2.9. a) SEM image of a dirt particle on the substrate, which is used to perform the first write field alignment. In such a write field alignment, an SEM image is taken, followed by a physical movement of the laser stage by e.g. $10\,\mu m$ along the X-direction. Subsequently, a deflection voltage is applied, which is expected to deflect the beam by $-10\,\mu m$ along the X-direction and the cross-correlation between both images is calculated. As a result, a perfect correlation means that for a given working distance, the physical displacement of the laser stage and the deflection of the beam are equivalent. b) Results for a write field alignment for a writefield of $100{\cdot}100\,\mu m^2$ in size and a working distance of 8.5 mm. The system expects for a standard working distance of 10 mm a relative maximum deflection voltage of 0.92. If, as here, smaller working distances are used, the relative maximum deflection voltages increase. All following screen shots of the "Raith Pioneer" software are shown with permission from Raith GmbH [175].

After explaining the write field procedure in general, the overlay-control, which means a precise alignment of one or more layers on an existing layer, is introduced. In Figure 2.10a), a 3-layer GDSII-layout is shown which consists of one Pt nanowire (purple) and Pt alignment crosses (light green), three Py wires (red) and a Cu bridge, together with small contacts (green). The idea is to pattern the Pt nanowire in the first step together with the crosses. Since both layers are patterned in the same step and in one write field (the dashed square), the shift between the Pt nanowire and the crosses is minimal, because within one write field only the beam is deflected but the laser stage is not moved.

As shown in Figure 2.10b), the automatic mark scan (Layer 61 in the software) is placed on two branches of each cross. Each of these automatic mark scans is one scan in either the U- or the V-direction. For each layer, four X- and four Y-scans are performed which means that for a 3-layer structure, eight crosses, four for the second and four for the third layer, are required. As shown in Figure 2.10b), different scanning parameters, i.e. the "Scan Points", "Average Points" and "Average" can be chosen in order to optimize the signal-to-noise ratio of the scan, as shown in Figure 2.10b).

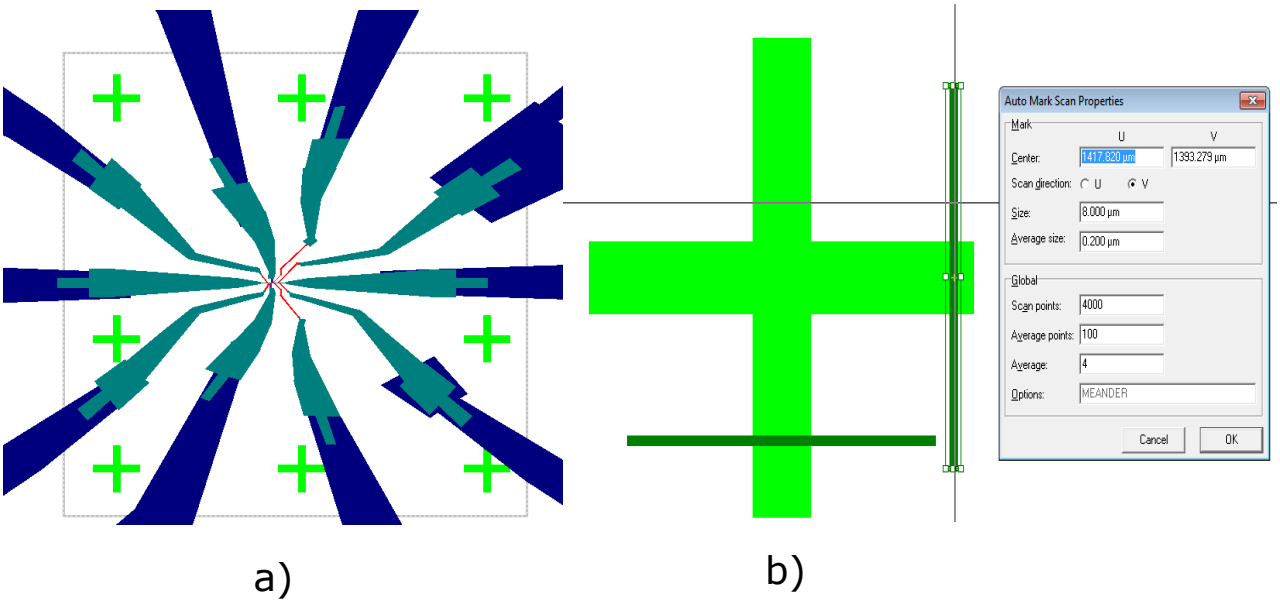

Fig. 2.10. a) 3-layer GDSII-layout which is used to pattern a lateral spin valve structure. A Pt stripe (purple) is patterned together with eight Pt alignment crosses (light green). In the next step, three Py wires (red) are patterned, which are aligned with respect to the deposited Pt crosses. Since both the Pt stripe and the Pt crosses are patterned together in one write field, no shift between the structures is present. As a result, a precise alignment of the Py wires with respect to the Pt stripe is possible. In the last step, the Cu bridge and the small contacts (both in green) are patterned onto the Pt stripe and onto the Py wires.
b) Two automatic mark scans (dark green) which are placed onto an alignment cross. By a suitable choice of the scanning parameters, i.e. the "Scan Points", the "Average Points" and "Average" a sufficient signal-to-noise ratio can be achieved even for materials with low secondary electron yield and for a small aperture and a high EHT.

An automatic mark scan performed along the X-direction is presented in Figure 2.11a). At the position of the alignment cross, a higher number of secondary electrons is emitted compared to the resist covered substrate. By the automatic mark scan, the centre of the alignment cross in the X-direction can be determined. These scans are performed eight times, four times for both the X- and the Y-direction in order to calculate the centre of the write field, which allows for a precise overlay-control. As shown in Figure 2.11b), performing the automatic write field alignment several times leads to shifts below 20 nm and to zoom factors close to 1.0000.

In particular the reduction of the shift plays a vital role because if the shift would not be corrected, the shift would increase for devices with increasing distance. If the shift becomes too large, the system is not able to detect the alignment crosses any longer and the patterning will stop. Since the Pt stripe and the Pt crosses are patterned in the same write field, scanning the crosses several times results in lateral shifts between the Pt stripe and the Py wires below 20 nm.

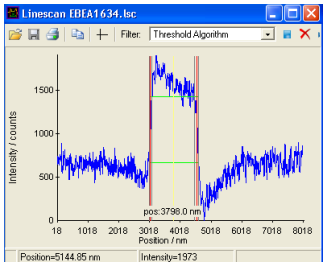

a)

Time	User	Sample	WF size (µm)	Mag.	WD (mm)	EHT (kV)	Factor zoom U	Factor zoom V	Delta shift U (µm)	Delta shift V (µm)	Delta rot. U (deg)	Delta rot. V (deg)
18:27:51	Pfeiffer	180319_20kV_CuPatterning_aufTa	800	100	8.593307808042	10	1.00002	1.00001	-0.019	0.003	-0.002	-0.001
18:27:38	Pfeiffer	180319_20kV_CuPatterning_aufTa	800	100	8.593307808042	10	1.00003	1.00004	-0.009	-0.032	0.005	-0.002
18:27:25	Pfeiffer	180319_20kV_CuPatterning_aufTa	800	100	8.593307808042	10	1.00002	0.99988	-0.019	-0.036	-0.006	0.008
18:27:14	Pfeiffer	180319_20kV_CuPatterning_aufTa	800	100	8.593307808042	10	1.00054	1.00007	0.010	-0.088	-0.063	-0.086
18:25:32	Pfeiffer	180319_20kV_CuPatterning_aufTa	800	100	8.597301319242	10	0.99998	0.99991	0.062	0.005	-0.008	0.004
18:25:19	Pfeiffer	180319_20kV_CuPatterning_aufTa	800	100	8.597301319242	10	1.00000	0.99988	0.113	0.014	-0.006	-0.001
18:25:08	Pfeiffer	180319_20kV_CuPatterning_aufTa	800	100	8.597301319242	10	1.00008	1.00004	0.239	0.062	0.004	-0.006
18:24:56	Pfeiffer	180319_20kV_CuPatterning_aufTa	800	100	8.597301319242	10	0.99969	1.00027	0.475	0.171	0.068	0.066

b)

Fig. 2.11. a) Successful X-direction line scan across a metallic alignment cross. Since the cross emits more secondary electrons than the resist covered substrate, the contrast from the cross is evident, which allows the calculation of the centre of the cross for the X-direction. For each write field alignment, eight line scans, four for both the X- and Y-direction are performed to determine the centre of all four alignment crosses and to finally determine the centre of the write field.
b) Results for the different write field alignments. The first scan shows a shift of 0.475 μm for U and 0.171 μm for V. Additionally, a zoom factor for U of 0.99969 and a zoom factor for V of 1.00027 is calculated. As a result, the deflection voltages and the beam shift for this particular write field need to be slightly optimized. After eight write field alignments, zoom factors very close to 1.00000 are determined and a shift both in the U- and V-direction below 20 nm is achieved.

After the explanation concerning the electron beam lithography and the overlay-control, the development step and the lift-off procedure are presented.

2.3. Development And Lift-Off Procedure

For sample fabrication by etching one starts with a thin film grown on a substrate. In the example shown in Figure 2.12, we have MgO as the substrate (shown in blue), 30 nm Co_2MnSi (shown in grey), 20 nm Cu (shown in orange) and 2 nm Ta and 4 nm Pt as the capping layer (shown in green and red). In the first step, a negative resist, in this case AR-N 7520.073 [181] is spin coated onto the sample at 3000 rotations per minute, resulting in a 130 nm thick photoresist which is drawn as a black layer. After spin coating, the photoresist is baked for 60 seconds in order to evaporate parts of the solvent of the photoresist.

In the next step, the EBL is performed which is depicted via the orange arrows in Figure 2.12b). For a negative resist as used here, by the EBL process, the photoresist becomes less soluble in the developer, while the unexposed parts are easily removed. In the present situation, the developer is four parts of AR 300.47 diluted in one part of H_2O and the sample is developed for 23 seconds. In Figure 2.13a), nanowires of 100 nm and 200 nm width are shown after the development step. A big advantage of this recipe is the relatively large insensitivity of the wire width on the applied electron dose. For this recipe, varying the dose between 280 $\mu C/cm^2$ and 360 $\mu C/cm^2$ changes the width of the nanowires by less than 10 %.

In the next step, ion beam etching (IBE) is performed with changing angles of incidence to achieve flat and homogeneous edges, as shown in Figure 2.13b) and Figure 2.13c). The optimization of this

procedure is one of the most important tasks for proper etched nanowires. As drawn in Figure 2.12d), also the photoresist becomes thinner by the ion beam etching. However, since its etching rate is much lower than the etching rate of the whole stack, approximately 90 nm of the photoresist layer remains on top of the nanostructures after the milling. The etching rates of the different materials, together with the used etching parameters, can be found in Appendix A.2. In the last step, the residual photoresist is removed by organic solvents, ultrasound cleaning and oxygen plasma treatment.

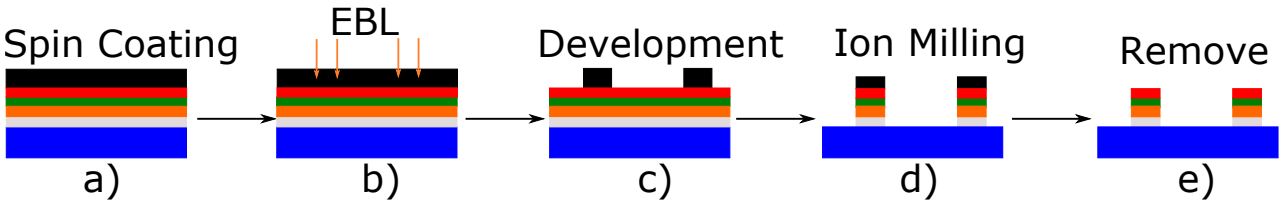

Fig. 2.12. Schematic procedure for the ion beam etching of nanostructures by a negative resist.
a) A negative resist, in this case AR-N 7520.073, is spin coated on the $MgO/Co_2MnSi/Cu/Ta/Pt$ thin film.
b) The EBL is performed. The exposed parts of the photoresist become less soluble in the developer.
c) By the development, the unexposed parts of the photoresist are removed while the exposed parts remain.
d) Ion beam etching is performed until the metal thin film is completely etched away. Due to the low milling rate, the photoresist becomes slighter thinner but is not completely removed.
e) By the removal step, the residual photoresist is removed by organic solvents, hot temperatures, some minutes in the ultrasonic bath and oxygen plasma treatment.

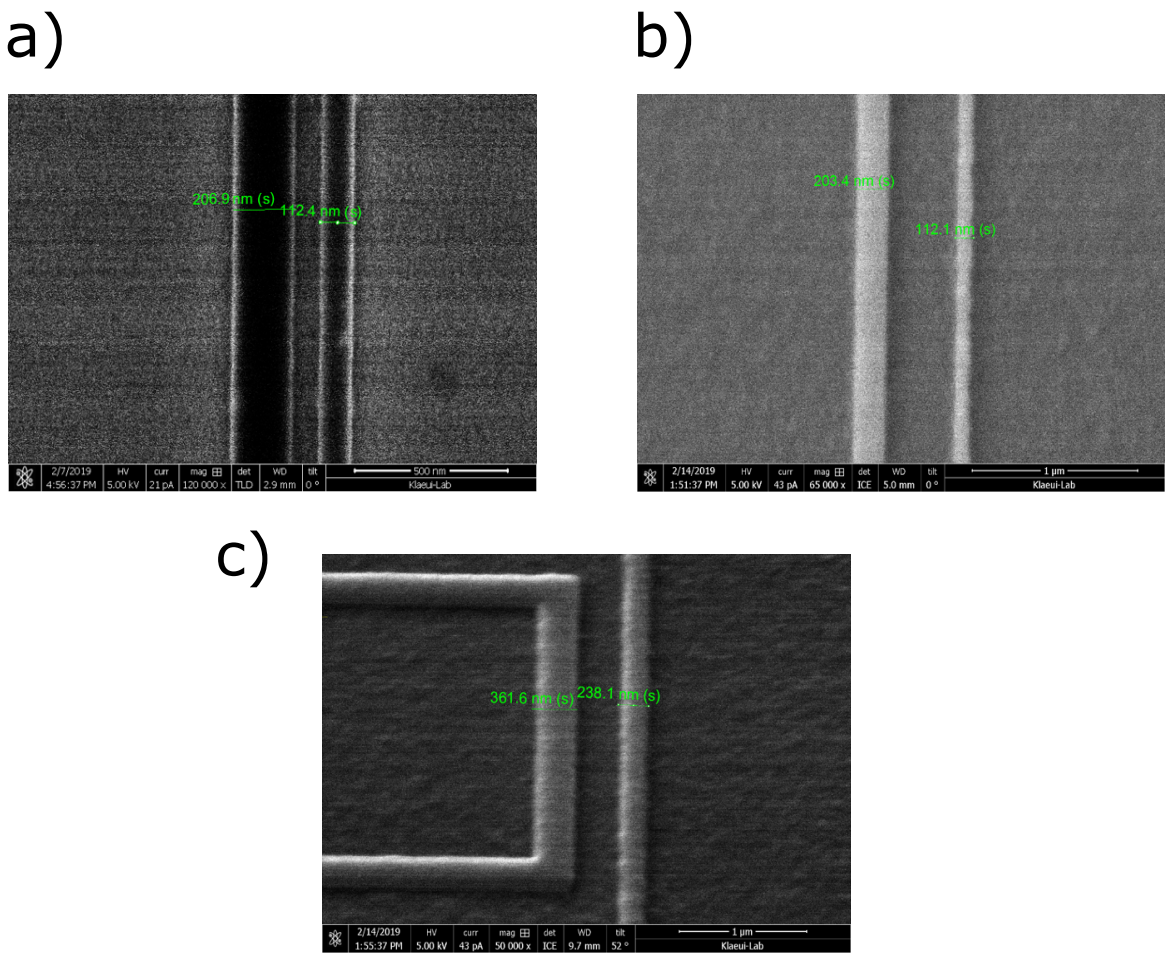

Fig. 2.13. SEM images of two nanowires of 100 nm and 200 nm width.
a) SEM image after the development.
b) SEM image of the metallic nanowires after the etching procedure and the removal of the residual resist with a tilting angle of 0 °.
c) SEM image of the same nanowires with a tilting angle of 52 °, which is the maximum titling angle of the SEM used.

If nanostructures need to be patterned on either a plain substrate or aligned on already existing structures as required for the fabrication of lateral spin valves, lift-off processing can be used, as shown schematically in Figure 2.14. By this technique, the photoresist, in this case poly(methyl methacrylate) (PMMA) 950K is used as a positive resist. After the exposure, the resist becomes more soluble in the developer and after the development, the exposed parts of the resist are removed while the unexposed parts remain, as shown in Figure 2.14c). In the next step, the metallic thin film is deposited by either UHV thermal evaporation or sputter deposition. As a result, parts of the substrate (the exposed ones) are covered with the thin film, while on the unexposed parts, the metallic thin film has been deposited on the residual resist, as shown in Figure 2.14d). This residual resist is removed together with the metal thin film on top by an organic solvent, as shown in Figure 2.14e). It is emphasized that the quality of the lift-off process, i.e. the edge roughness of the nanowires, crucially depends on the thickness of the resist, the thickness of the deposited film and the deposition method.

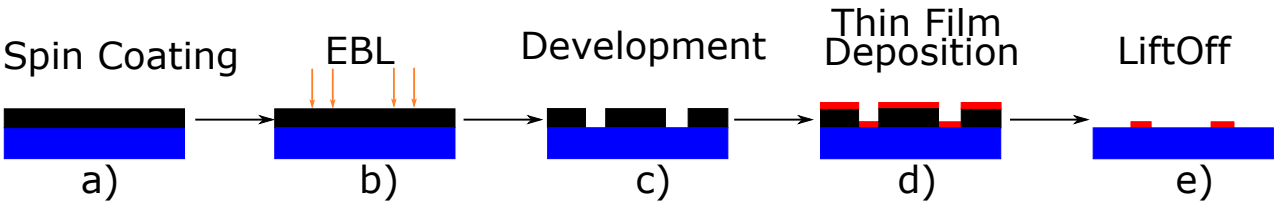

Fig. 2.14. Schematic illustration of the lift-off procedure to fabricate nanowires by a positive photoresist.
a), b) The photoresist is spin coated onto the substrate and the exposure is performed. By the exposure, the photoresist becomes more soluble in the developer.
c) After the development, the exposed parts are removed while the unexposed parts remain.
d) The thin film is deposited both onto the substrate and onto the residual resist.
e) Together with the residual photoresist, the parts of the thin film on top of the resist are removed by an organic solvent.

Both methods, ion beam etching (IBE) and the lift-off processing, which are used to fabricate nanowires, have several advantages and disadvantages as follows:

IBE has the advantage that thin films which need to be annealed at several hundreds °C, e.g. Co_2MnSi [182], can be processed. With a lift-off process, the residual resist would heat above its glass transition temperature due to this annealing process and the lift-off could not be performed. For such materials, **only** ion beam etching is possible.

IBE has the second advantage that the patterning for a whole chip of $10 \cdot 10\,mm^2$ size, which consists of nanowires and alignment crosses (which takes about 99% of the complete exposure time) is less time consuming due to the higher sensitivity of the resist and the lower required exposure dose.

IBE By the etching of the photoresist with argon atoms/ions, the resist becomes heavily cross-linked which significantly increases the difficulty to remove the residual resist.

IBE requires an individual sequence of incidence angles for the different materials in order to minimize the edge and the surface roughness.

Lift-off is required for the patterning and the deposition of the nonmagnetic bridge for a lateral spin valve structure.

Lift-off is much more standardized for the first layer since the patterning is material independent and just depends on the substrate and the EHT. The material dependent stage is for subsequent layers on top of other layers, where the required exposure dose depends on the material underneath.

Lift-off allows for an easier patterning of small, defined structures as notches and kinks with a structure size below 50 nm.

A direct comparison of nanowires patterned by ion beam etching and by a lift-off procedure is shown in Figure 2.15. In Figure 2.15a) the left wire is a Pt wire fabricated by ion beam etching. Although some time have been spent on optimizing the etching procedure for Pt, the edges are not as flat as the edges of the right Py wire which has been fabricated by a lift-off procedure. In Figure 2.15b) and Figure 2.15c), the same kind of structure is shown, this time with both the Pt and the Py wires fabricated by a lift-off procedure. In this case the Pt wire shows less edge and surface roughness compared to the two Py wires on the right. Clearly visible, in particular in Figure 2.15c), is the relatively poor edge and surface roughness of the Cu bridge on top of the other wires. Nevertheless, as later shown in detail, the obtained non-local signals are quite high compared to other literature reports which indicates that for the lateral spin valve performance, the interfaces between the different materials and not the Cu surface and edges play a dominant role.

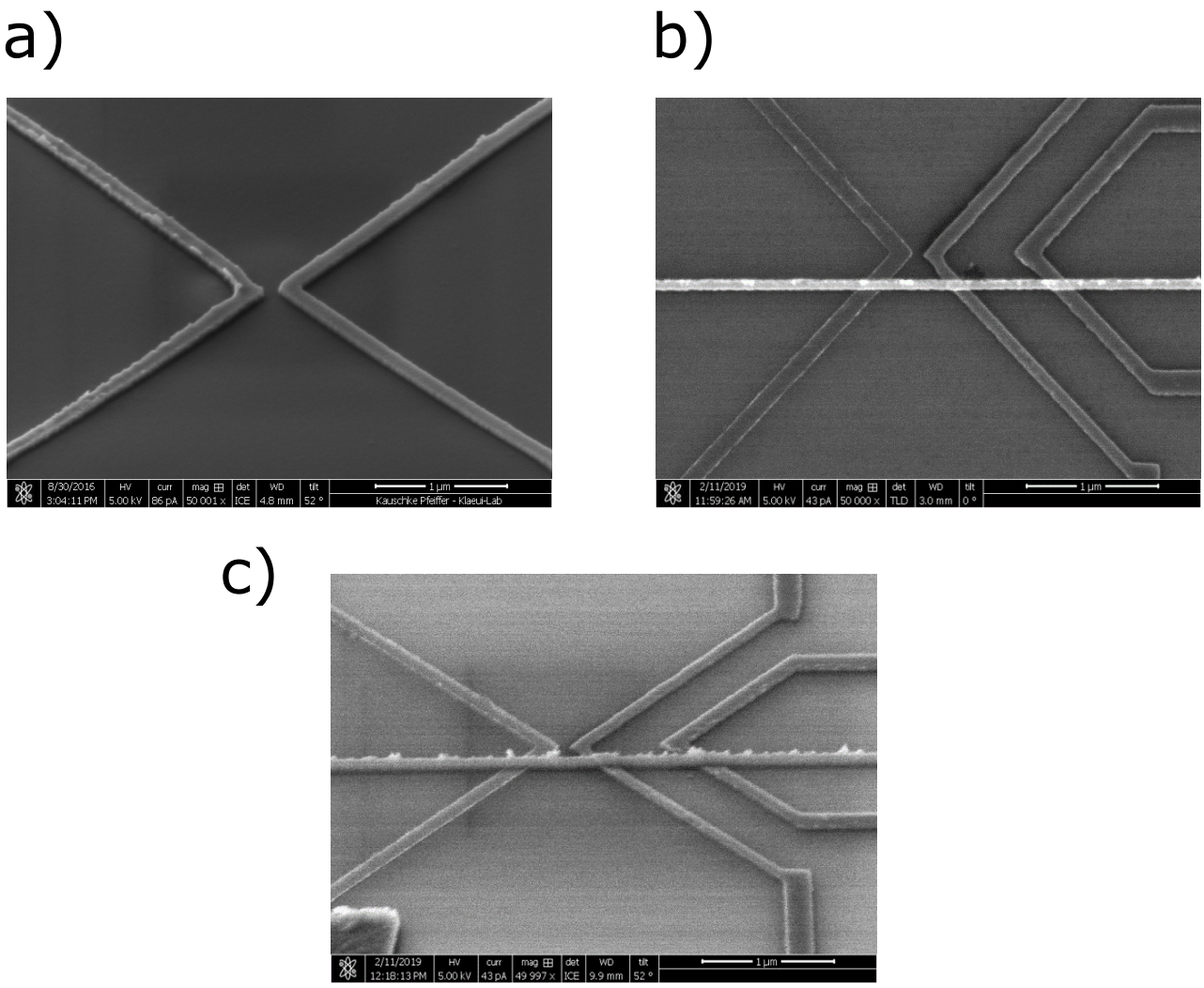

Fig. 2.15. Comparison of Pt and Py nanowires, patterned either via ion beam etching or by a lift-off procedure.
a) SEM image of one Pt wire (left) fabricated by ion beam etching and one Py wire (right) fabricated by a lift-off procedure. The SEM image has been taken with a sample tilting angle of 52 °. Although quite some time have been spent on the Pt etching, edge and surface roughness are worse than the edge and surface roughness of the Py wire, fabricated by a lift-off process.
b) SEM image of one Pt wire (left), two Py wires (right) and a Cu bridge on top of the three wires. In this case all wires have been fabricated in a lift-off process, resulting in a better surface and edge roughness quality of the Pt wire compared to the Py wires.
c) Same sample as b) with the SEM image taken from a 52 ° tilting angle of the sample. The Cu bridge shows large edge and surface roughness.

To sum it up, if possible a lift-off process will be used in order to fabricate the samples. If it is required, as in the case of the Co_2MnSi structures, ion beam etching will be exploited to pattern the nanostructures.

After this in-depth discussion concerning electron beam lithography, overlay-control and the development and removal step, there will be a discussion in the next sections of ion beam etching, sputter deposition and UHV thermal evaporation.

2.4. Ion Beam Etching (IBE)

In order to etch thin films which have been patterned with a negative-resist, the commercial (reactive) ion beam etching system "IonSys500" from "Meyer Burger" has been used [183].

In the system, a plasma is generated via a microwave excitation of 330 W with argon as a process gas in the large discharge chamber, as drawn in Figure 2.16a). Stable plasma conditions are found for an argon flow of the ion beam source (IBS) of 5 sccm, while the argon flow of the plasma bridge neutralizer (PBN) is chosen to be 4 sccm. In order to cool the sample during the process, the helium pressure of the helium back side cooling (HBSC) is chosen to be 2 mbar, which leads to a total working pressure of $3{\cdot}10^{-4}$ mbar.

In total, three Mo grids with different electric potentials are mounted close to the large discharge chamber to extract the ions. The first grid closest to the microwave excitation, also known as the screen grid S [184, 185], is at the plasma potential. This potential is mainly given by the beam voltage V_B=+300 V with respect to ground which is applied to the anode. However, the plasma potential might differ from the beam potential by typically 10 V. The next grid, known as the accelerator grid A, is biased with the accelerator voltage V_{acc} of −200 V with respect to ground. Positive ions in the large discharge chamber that drift close to the electric field generated by V_{acc} are accelerated. The third grid, the decelerator grid D, is on ground potential. As a result, the accelerated ions are decelerated again, resulting in a constant velocity of the ions. The different potentials and positions of the grids are shown in Figure 2.16b). As shown, the ion energy is only given by the applied beam voltage V_B. The acceleration voltage V_{acc} increases only the number of extracted ions, but not their energy.

After the beam has been accelerated and decelerated, the PBN is used to to de-ionize the ion beam back to an atomic beam. If the PBN is not used or does not work properly, insulating substrates such as Al_2O_3 or MgO might gain a floating potential, leading to large surface charges. These surface charges are a repulsive potential for the ions and reduce the ion current. Additionally the large surface charges may damage the substrate and the resist. A second problem is that the beam profile suffers, since the positive ions repel each other, leading to a widening and divergence of the beam. To use the PBN, a direct current of around 7 A flows through a tungsten filament which is mounted in the small second discharge chamber. The emitted electrons provide a charge balance for the ions. In the system, a neutralizer current of 100 mA is used while the total beam current is typically between 50 mA and 54 mA.

By the aid of the shutter, the rotating sample can be protected from the ion-beam, while with the endpoint detection (EPD), it is possible to detect the different ions from the etched thin film during the etching process by secondary ion mass spectrometry (SIMS). The EPD is especially useful if thin films are etched where it is required to stop the etching process after a certain layer in order not to etch the whole film.

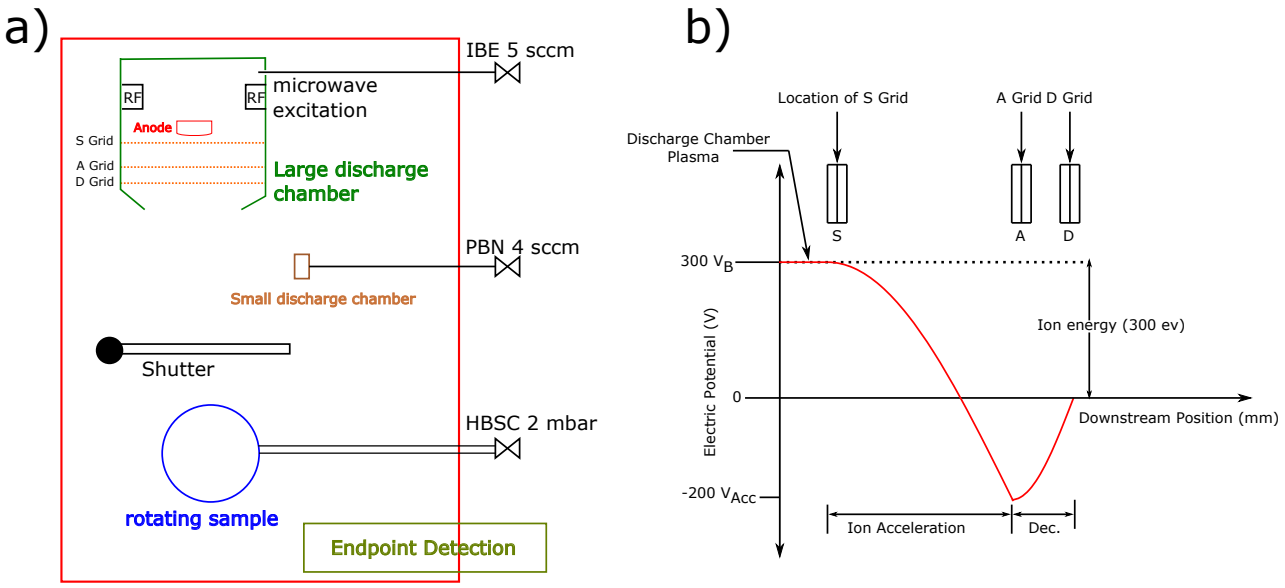

Fig. 2.16. a) Schematic illustration of the commercial IonSys 500 ion beam etching system. Argon flows into the large discharge chamber where by a microwave excitation, a plasma is generated. The argon ions are accelerated and decelerated by the different grids. The argon ions are de-ionized by the aid of the plasma bridge neutralizer, forming an atomic argon beam. The argon beam hits the rotating sample and the metallic thin films are etched with a typical rate between 10 nm/min and 30 nm/min. To cool the sample during the etching, helium back side cooling is used while with the endpoint detection, the etched materials can be detected by secondary ion mass spectrometry.
b) Overview of the different applied potentials of the three Mo grids as a function of the position within the system. The argon atoms are ionized and a plasma is generated in the discharge chamber. Here it is assumed that the plasma potential is the same as the potential provided by the beam voltage V_B.

One important issue concerning the ion beam etching is the angle of incidence of the argon ions/atoms with respect to the sample. As previously mentioned, each material stack needs its own optimization since the mass ratio between the argon atoms and the atoms of the thin film is crucial. Within the framework of this thesis, a sequence of different etching angles was developed together with Stefan Kauschke to perform a Pt etching with the desired conditions.

A second, different etching procedure has been developed for a CoFeB/Cu/Ta/Pt thin film (which acts as a dummy sample for the studied Co_2MnSi/Cu/Ta/Pt thin films) by myself. The results of both of these different etch sequences are shown in Figure 2.17. In Figure 2.17a), a resulting nanowire based on a 25 nm thick Pt film etched with an angle of incidence of only 90 ° is shown. Large side-deposition from the surrounding, resist free Pt, has stuck to the nanowire, resulting in a nanostructure of several hundred nm thickness. In Figure 2.17b), the optimized wire with varying angles of incidence between 0 ° and 90 ° is shown. A thinner and more homogeneous wire is achieved.

Figure 2.17c) shows the same etching recipe which worked well for Pt, applied to a CoFeB/Cu/Ta/Pt thin film. As compared to Figure 2.17d), the wires are narrower after the etching than originally patterned and additionally parts of the narrow wire are etched away. In this case, it helped to decrease the etching time under low angle of incidence, as shown in Figure 2.17d), where the resist pattern is well reproduced after the ion beam etching and the removal of the residual resist.

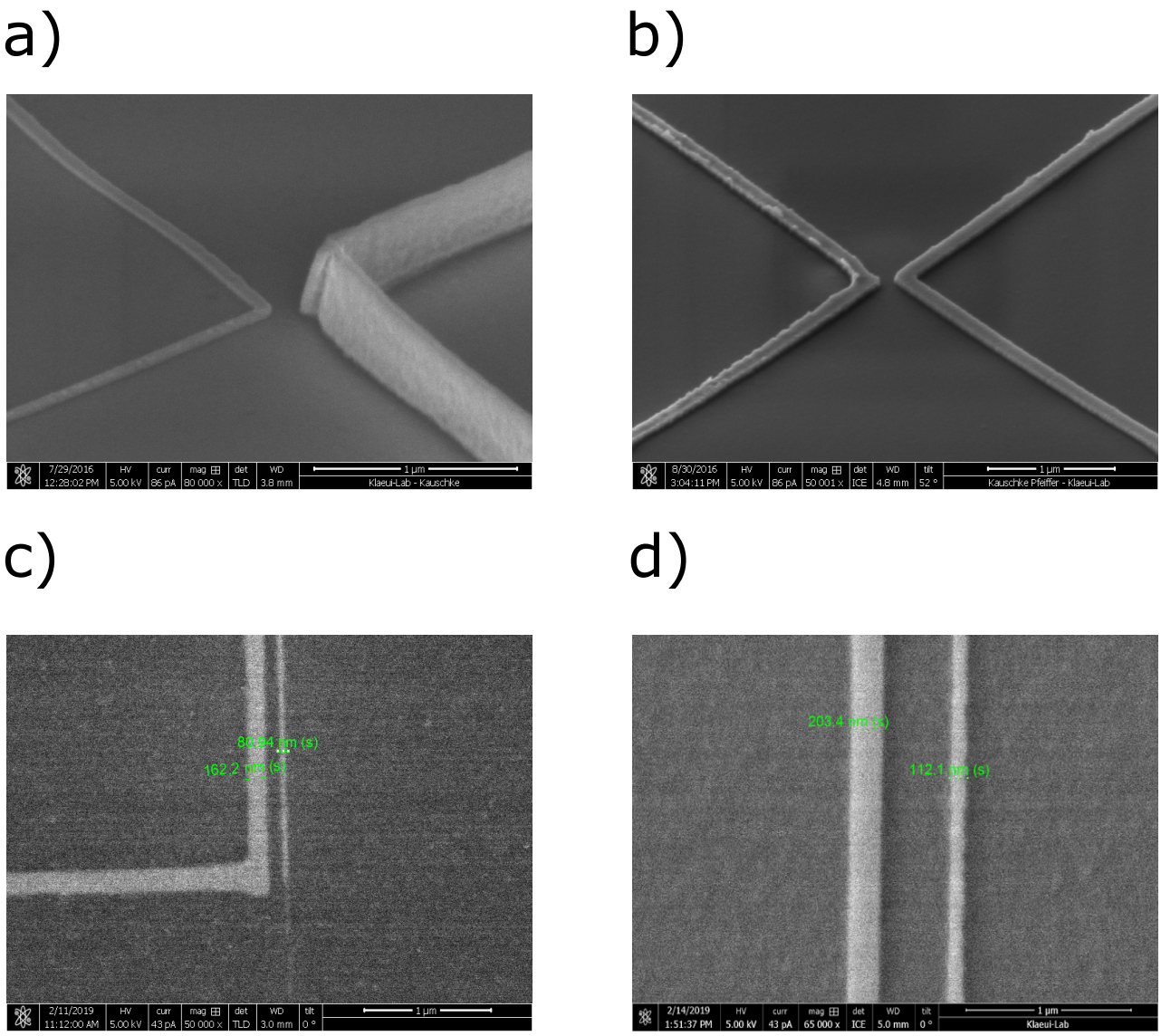

Fig. 2.17. a) SEM image of a Pt wire patterned from a 25 nm thick Pt film. As a result of the etching with an angle of incidence of only 90 ° with respect to the sample, large side deposition appeared, resulting in a several hundred nm thick wire.
b) SEM image of a patterned Pt wire with varying angles of incidence, resulting in thinner and more homogeneous nanowires.
c) Etching of a CoFeB/Cu/Ta/Pt thin film. Etching for too long under small angles of incidence leads to narrow, inhomogeneous and even completely removed wires.
d) Etching of a CoFeB/Cu/Ta/Pt thin film with an improved etching sequence. As a result, more homogeneous wires and a high quality reproduction of the resist pattern is achieved.

2.5. Sputter Deposition

Sputter deposition is a widely used technique to fabricate metallic thin films with very high quality, i.e. low surface roughness and epitaxial growth [182, 186, 187]. In the framework of this thesis, materials such as Pt and Ta, which are difficult to deposit via UHV thermal evaporation due to their high melting point, have been deposited by sputter deposition by colleagues. In this thesis, only the basic principle of sputter deposition is explained. For a much deeper insight into sputter deposition, the reader is referred to the common literature, e.g. [188, 189].

The basic principle is schematically shown in Figure 2.18, with the schematic illustration inspired

by [190]. An UHV chamber with a base pressure of typically $1{\cdot}10^{-8}$ mbar or lower is filled with a process gas, usually Ar, typically up to a pressure of $1{\cdot}10^{-1}$ mbar. Some single Ar atoms are randomly ionized by e.g. cosmic radiation. Since the sputter cathode is at a strong negative potential, the Ar^+-ions are accelerated by the electric field towards the cathode. Once the ions reach the cathode, secondary electrons are expelled which are accelerated towards the black shield and the substrate holder and as a result, more Ar-atoms are ionized and a chain reaction starts and finally, a plasma ignites. By applying a magnetic field, the electrons are forced to follow a spiral motion, resulting in a significantly longer path towards the black shield and thus, a higher sputter rate is achieved with the same working pressure compared to sputtering without an applied magnetic field. The sputter process itself is a ballistic process, since the Ar^+-ions collide with the surface of the target material, which results in an erosion of the target. The target atoms condensate on the substrate and the metallic thin film grows.

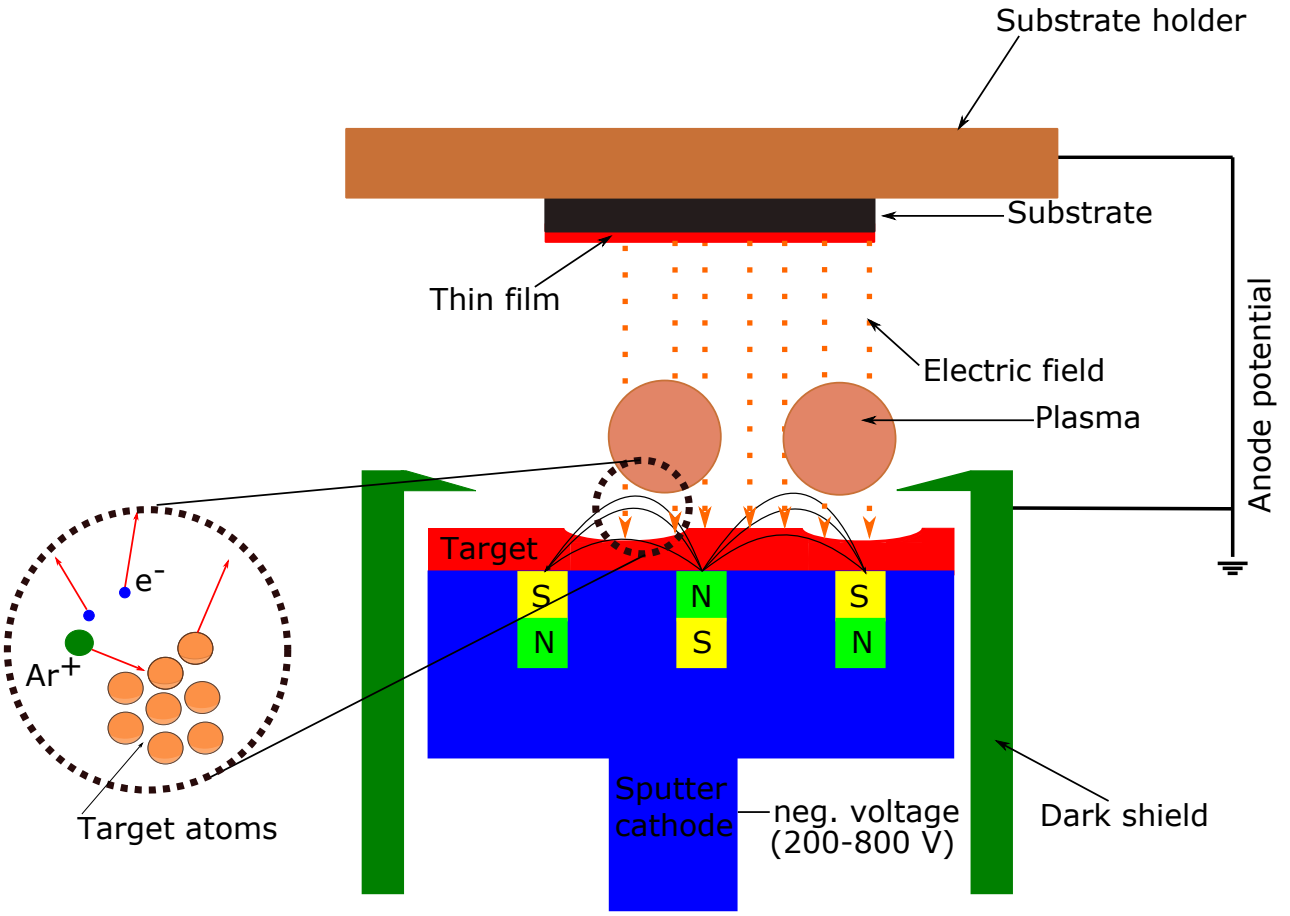

Fig. 2.18. Schematic illustration of the basic principle of sputter deposition. An ultrahigh vacuum chamber is filled with a process gas, typically Ar. Some of the Ar atoms are ionized by e.g. cosmic radiation and these Ar^+-ions are accelerated towards the cathode. By collisions with the cathode, secondary electrons are emitted, which ionize more Ar-atoms, resulting in a chain reaction and a plasma starts to ignite. By collisions with the target, the surface of the target is removed and the target atoms condensate on the substrate, forming a thin film. By the application of a magnetic field, electrons are forced to travel on a spiral path, which leads to increased argon ionisation and as a result a higher sputter rate.

2.6. Ultrahigh Vacuum Thermal Evaporation

The second method to deposit high quality metallic thin films, which has been extensively performed by myself is UHV thermal evaporation, which is explained in depth in [191].

In Figure 2.19, a picture of the custom made UHV thermal evaporation system is shown. The general working principle is shown schematically in Figure 2.20a), while a photograph of the relevant parts of the evaporator is shown in Figure 2.20b). A direct current of approximately 2.1 A flows through the polished thorium doped tungsten filament under ultra high vacuum conditions of about $1{\cdot}10^{-9}$ mbar.

As a result, electrons are emitted from the filament and are accelerated by the applied high voltage of about 800 V towards the source. As a result, the source, which is electrically isolated, is heated and materials such as Py or CoFe directly sublimate and condense on the substrate. The rate can be chosen in a wide range by varying the applied high voltage, the current flowing through the filament and the distance between sample and source. Compared with sputter deposition, the deposition rates are significantly lower. Typical deposition rates are around 15 nm/h for materials like CoFe and Py and rates up to 70 nm/h for Cu and Ag in the system used. The most important process parameter is the distance between source and substrate. During the deposition, the rate and the thickness are measured by a quartz-crystal micro balance [192], which allows for a precise control of the rate over several hours.

An advantage of UHV thermal evaporation compared to sputter deposition is the low working pressure, which is usually below $5{\cdot}10^{-8}$ mbar during the deposition. The mean free path of the particles is therefore in the range of 10 km [193]. As a result, a well defined, oriented particle beam is present, which allows for a much easier lift-off process compared to sputter deposition.

To perform lift-off processing, it is necessary to achieve an undercut profile of the resist, as shown in Figure 2.21a). Due to the undercut profile, the organic solvent can reach the resist during the lift-off and the solvent is able to remove it. For UHV thermal evaporation, the undercut is still free and the organic solvent can easily reach the resist, as drawn in Figure 2.21b). For sputter deposition a randomized beam is present which easily closes the undercut, as drawn in Figure 2.21c). When the undercut is closed, the organic solvent can not reach the area beneath the resist and therefore cannot remove it. As an example, Cu nanostructures of more than 130 nm thickness can be lifted with a single 300 nm thick PMMA-layer relatively easily by UHV thermal evaporation, which is difficult when the same material has been deposited via sputter deposition.

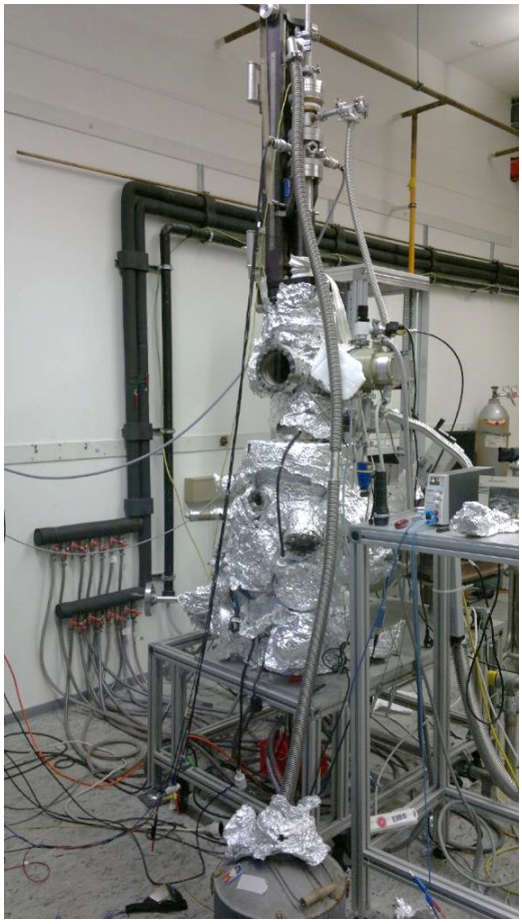

Fig. 2.19. Photograph of the custom made UHV thermal evaporation system.

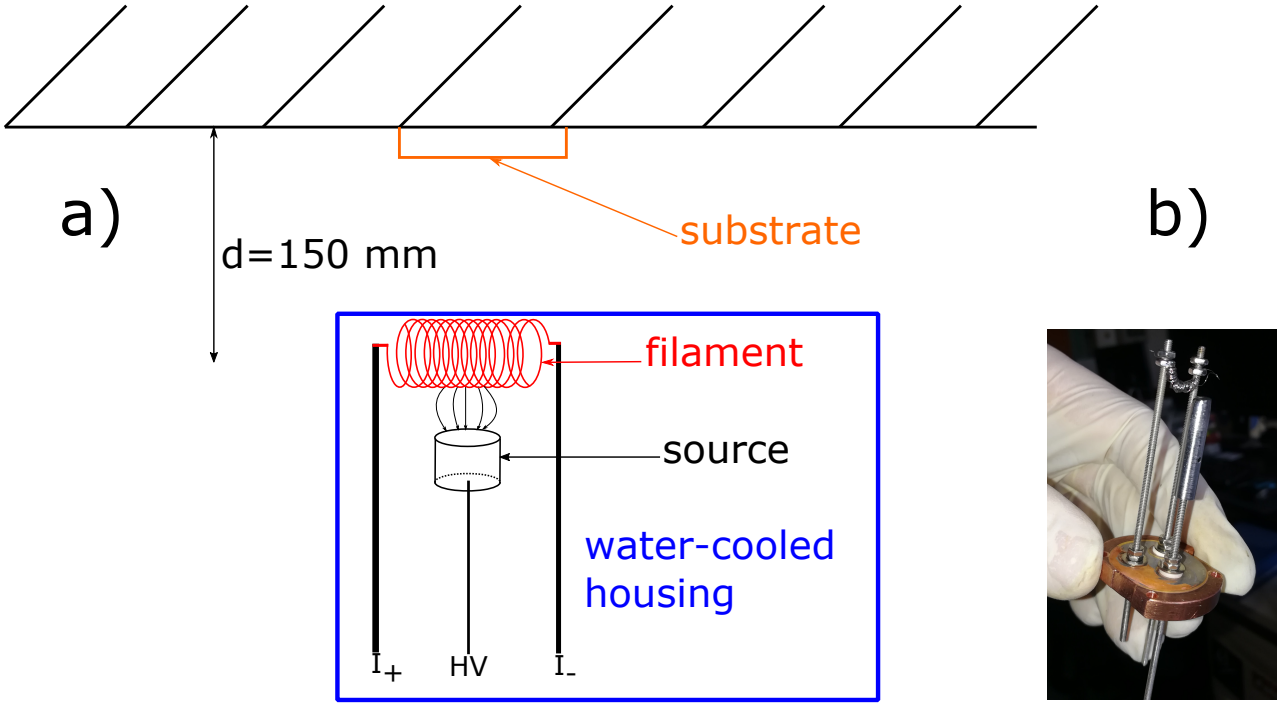

Fig. 2.20. a) Schematic illustration of the working principle of UHV thermal evaporation. A high current flows through a polished tungsten filament. Electrons are emitted which are accelerated by a high voltage of about 800 V towards the source, which is electrically isolated. As a result, the source, e.g. a CoFe rod is heated up and sublimates. Once the sublimated material reaches the substrate and condensates, layer by layer of the desired material is deposited and the rate of the deposition can be chosen in a wide range by the applied high voltage, the filament current and the distance between source and sample. The monitoring of the rate and the thickness is performed by a quartz-crystal micro balance.
b) Photograph of a prepared filament together with a CoFe rod.

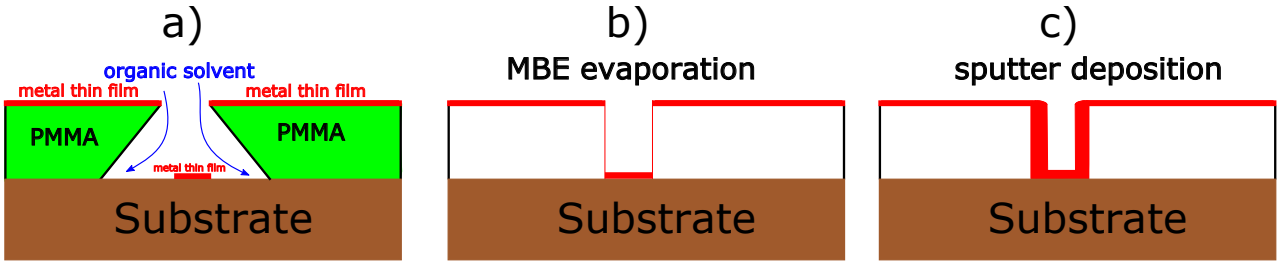

Fig. 2.21. a) Undercut profile after performing PMMA development and thin film deposition. Due to the undercut profile, the organic solvent is able to reach the residual resist after the deposition and can remove it.
b) Schematic profile when the deposition has been performed via UHV thermal evaporation. Very sharp edges are present which allow for an easy lift-off process and lead to sharp edges of the nanostructures.
c) Schematic profile when the deposition has been performed via sputter deposition. Wide edges are present and the organic solvent can not reach the region beneath the resist, resulting in a difficult lift-off process.

Prior to the deposition of the nonmagnetic bridge in the UHV thermal evaporation chamber, an in-situ argon milling step is required to remove the first few nm of the surface, which can be oxidized. To achieve this, a commercial “IQE 11/35” ion sputter gun from “SPECS Surface Nano Analysis” is

mounted within the chamber [194]. An important stage of the work for this thesis has been optimizing the in-situ etching conditions to achieve of a large spot size of at least $10{\cdot}10\,\mathrm{mm}^2$, as shown in Figure 2.22 and the best possible homogeneity of the etching. Since this homogeneity check has been performed via X-ray-reflectivity (XRR) measurements where the thickness and roughness of $10{\cdot}\,\mathrm{mm}^2$ thin-films has been determined before and after the etching, the next section will be an introduction to this technique.

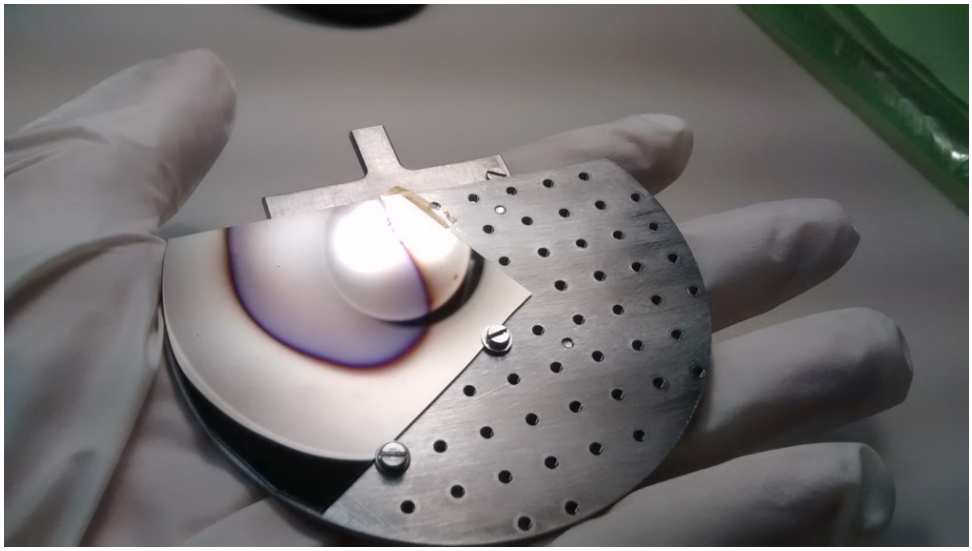

Fig. 2.22. Photograph of the size of the in-situ etch spot after optimizing the distance of the argon-gun and the sample, the fabrication of a new, larger sample holder and choosing the correct high voltage of the gun. The quality of the etching spot has been checked by X-ray-reflectivity measurements of the thin films before and after the etching. Details of the mounting of the samples are shown in Appendix A.1, together with the relevant parameters for the etching.

2.7. X-Ray-Reflectivity (XRR)

X-ray-reflectivity measurements have been intensively performed within this thesis to optimize growth and etching conditions by determining the thickness together with the surface and interface roughness of thin films. The basic principle of our commercial "Bruker D8 Discover" system is shown in Figure 2.23. The device operates in the Bragg-Bretano geometry, which means that the X-ray source and the detector are placed on a circle with the sample mounted in the centre of the circle [195]. For the X-ray source, a copper cathode with the wavelength of Cu-$K_{\alpha 1}$ =1.5406 Å and Cu-$K_{\alpha 2}$ =1.5444 Å is used. The next optical element is a parabolic shaped Göbel mirror which brings the beam to a parallel state by diffraction of the incoming X-rays. By action of the Göbel mirror, the X-ray beam not only becomes parallel, but additionally more brilliant.

The next optical elements are a slit and optionally a monochromator, the latter suppressing the Cu-$K_{\alpha 2}$ line by selected diffraction, resulting in a better resolution which might be required for materials with similar lattice constants. For a XRR-measurement, the X-ray beam hits the sample under a grazing incidence angle, which leads to a partial reflection of the X-rays at the interface of film and substrate and at the surface of the film [195]. As a result, the minima of these oscillations can be related to the thickness of the film, while the decay of the intensity can be connected to the roughness of the interface between substrate and film, as well as the surface of the film itself. The critical angle observed for small angles of typically below 1.0 °, contains information concerning the density of the sample material.

For the determination of the thickness and the roughness of the film "LEPTOS 7", a commercial

software based on the Parratt-algorithm [196], has been used. To indicate the high quality of the in-situ etching process, the XRR-measurement of a 45 nm thick Py film is shown in Figure 2.24a). The XRR measurement, after a 150 minutes in-situ etching procedure is performed, is shown in Figure 2.24b). The oscillations in Figure 2.24b) are less dense compared to Figure 2.24a), indicating a reduced thickness. Additionally oscillations up to $2\theta = 4°$ are found, which indicate a better film quality than the grown thin film. For the as grown thin film, oscillations up to only $2\theta = 3°$ are observed.

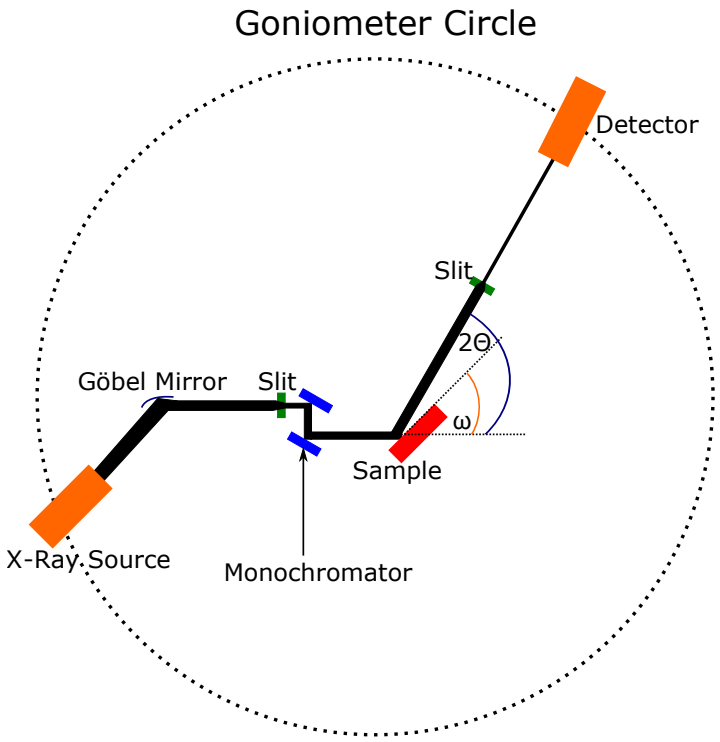

Fig. 2.23. Schematic illustration of the basic principle of a XRR measurement in the Bragg-Bretano geometry. X-rays are emitted by a copper cathode and made parallel by a Göbel mirror due to diffraction of the initial beam. Due to its parabolic shape, the initial beam becomes additionally more brilliant, since the preferred wavelengths are corrected from a divergent to a parallel beam. The beam goes through a slit, an optional monochromator and hits the sample under a grazing incidence angle. As a result, partial reflection of the X-rays occurs at the interface of the film and the substrate and at the surface of the film.

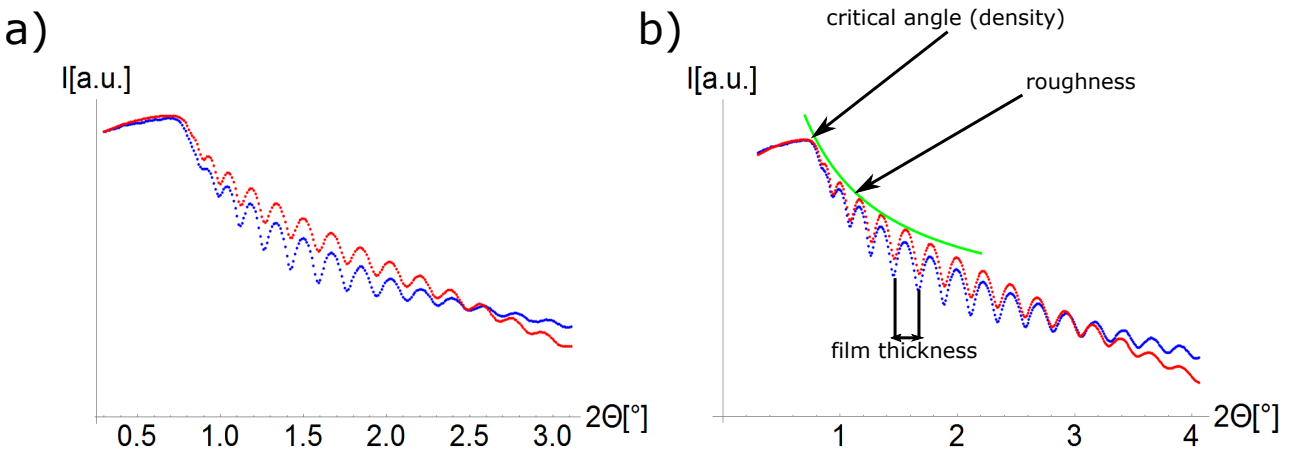

Fig. 2.24. Comparison of the XRR-measurement of a Py thin film grown by UHV thermal evaporation before and after the in-situ etching process in the UHV thermal evaporation chamber.
a) As grown thin film with a thickness of 45 nm and oscillations up $2\theta = 3°$ are observed. From a fit, the roughness is determined to be 1 nm.
b) Same thin film after a 150 minutes long in-situ etch process. The thickness is reduced to 36 nm and oscillations are found up to an angle of $2\theta = 4°$. From a fit, the surface roughness is determined to be 0.8 nm.

2.8. Atomic Force Microscopy (AFM)

As mentioned in the section concerning the different etching sequences, side wall deposition, leading to an increase in the total thickness, occurs when nanowires are etched out of a given thin film. To determine the total thickness and to estimate the thickness increase of the different materials, AFM has been used with the schematic working principle shown in Figure 2.25. For an in-depth introduction into AFM, the reader is referred to the common literature, e.g. [197].

AFM allows to directly probe soft and solid surfaces with nanometer resolution without any UHV conditions. The sample is probed by a cantilever which consists of a spring and a sharp tip at the end of the cantilever, being in contact with the surface. A laser beam is focussed on the cantilever and the reflected light can be measured as a function of the position via a photo detector. Depending on the height of the surface, the deflection of the cantilever leads to a deflection of the laser light which results in a change of the photo detector output. The output of the photo detector is fed back into the system and induces a movement of the piezoelectric element, together with the cantilever along the z-direction. By a line by line scan, a three-dimensional image of the sample can be gained.

When the tip is brought close to the sample surface, atoms of the tip (which are in this thesis "SNL-10" probes made by Bruker [198]), and atoms of the surface of the sample feel a Lennard-Jones potential [199] $V(r)$, which consists of an attractive term $\propto r^{-6}$ due to the van der Waals interaction and a repulsive term $\propto r^{-12}$ for very short distances between tip and sample due to the Pauli repulsion. In the used AFM system, three possible modes are possible:

Contact mode: This mode operates in the repulsive mode of the Lennard-Jones potential very close to the surface. The reflected beam signal of the cantilever enters the feedback loop and retracts the tip such that the acting force remains constant during the scan of the surface. The force is calculated by the deflection of the cantilever according to Hooke's-law.
In this thesis, all AFM measurements are performed in the contact mode.

Non-contact mode: The cantilever is forced to oscillate at its resonance frequency in the attractive interaction regime of the Lennard-Jones potential. Variations of the resonance frequency of the cantilever are caused by van der Waals forces, leading to different amplitudes. A modulation of

the amplitude is used in the feedback loop to maintain the tip in a constant height above the surface.

Tapping mode: In this mode, the cantilever oscillates at its or very close to its resonance frequency with the amplitude kept constant. Changes in the amplitude results to an adjustment of the cantilever height by the feedback loop. In the tapping mode, the tip touches the surface of the sample at its lower turning point and therefore probes the interacting forces acting on the tip.

The analysis of the AFM data has been done via "Gwyddion", an open source software for scanning probe microscopy data [200].

In Figure 2.26a), an overview AFM image of four nanowires is shown, while in Figure 2.26b) a scan across one of the nanowires is shown. While the original stack had a total thickness of 56 nm, the resulting nanowires are approximately 95 nm thick. By varying the different thicknesses of the different metals of the stack and comparing the resulting thicknesses, it is impossible to determine the influence of the different metals. As an example, increasing the Pt thickness from 4 nm (as the thickness of the original stack) to 16 nm leads to a total thickness of the nanowires of 120 nm. This means that each nm of Pt of the thin film increases the thickness of the nanowires by 2 nm.

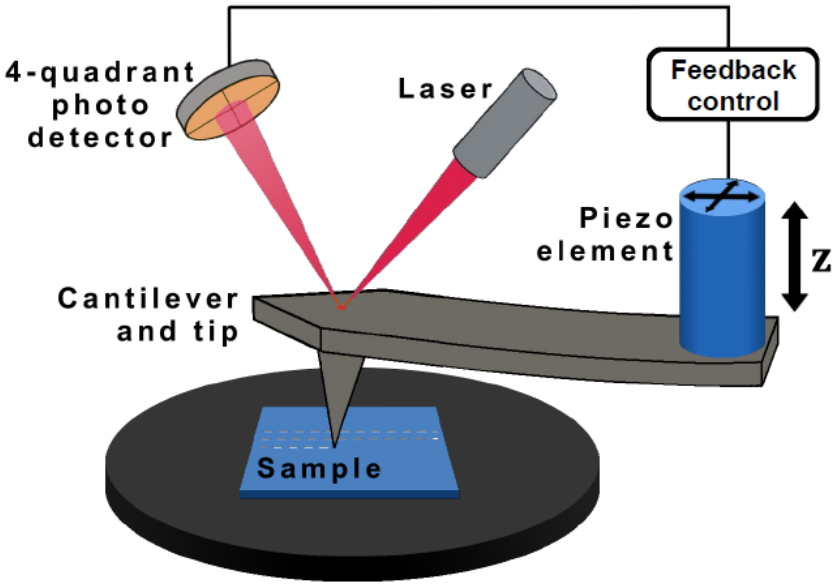

Fig. 2.25. Schematic illustration of the working principle of AFM. A cantilever, consisting of a spring and a sharp tip are brought close to the surface of the sample. Changes in the height of the sample change the reflected laser light which is measured by a photo detector. The output of the photo detector is fed into a feedback control which changes the height of the cantilever via a piezo element. Image taken from [201] with permission from L. Schnitzspan.

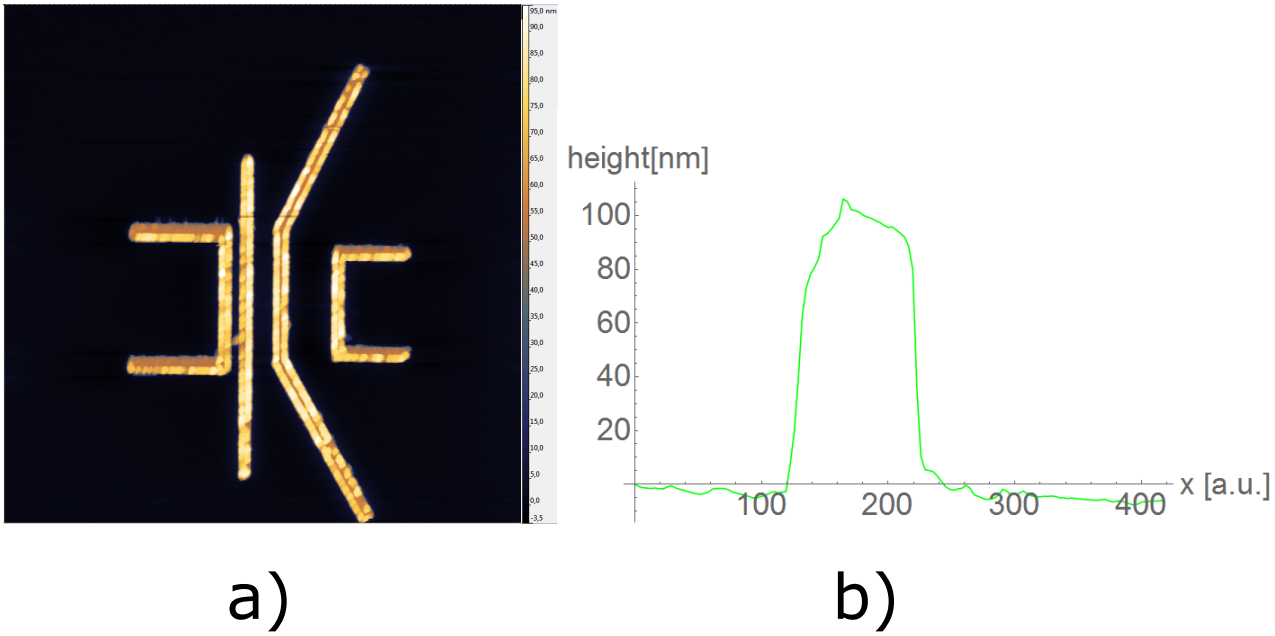

Fig. 2.26. a) AFM image of four patterned nanowires based on a 56 nm thick film, leading to approximately 95 nm thick nanowires.
b) Line scan across one of the nanowires.

With this section, the part of the chapter concerning the fabrication and the characterization of the fabricated nanostructures ends. In the second to last section, lock-in amplification is shortly explained which allows one to measure very small signals, e.g. the non-local voltage. Finally the experimental setup is presented.

2.9. Non-Local Voltage Measurement Via Lock-In Amplification

In lateral spin valves, the detected voltages are typically very small in the μV or even nV range, calling for amplification of the signals. In all the measurements, the commercial "7225 Dual Phase DSP Lock-In Amplifier" from Signal Recovery [202] has been used. An example demonstrates, that lock-in amplification is a powerful tool in order to measure very small voltages.

As described in [203], in the following it is assumed that the experimental response signal is a 10 nV small AC signal with a frequency of 10 kHz. The further assumptions are that the amplifier has a gain factor of 1000, a bandwidth of 100 kHz and an input noise of 5 nV/$\sqrt{Hz}$. The signal is then expected to be

$$10\ nV \cdot 1000 = 10\ \mu V \tag{2.3}$$

while for the noise one expects

$$\frac{5nV}{\sqrt{Hz}} \cdot \sqrt{100\ kHz} \cdot 1000 = 1600\ \mu V, \tag{2.4}$$

so without any filtering, the signal can not be detected. Assuming a narrow bandpass filter with $Q = 100$, any signal in a 100 Hz bandwidth will be detected and one obtains for the noise

$$\frac{5nV}{\sqrt{Hz}} \cdot \sqrt{100\ Hz} \cdot 1000 = 50\ \mu V, \tag{2.5}$$

which is still much larger than the signal. Now, the lock-in amplification with a very narrow bandwidth of just 0.01 Hz comes into play and the noise is determined to be

$$\frac{5nV}{\sqrt{Hz}} \cdot \sqrt{0.01\ Hz} \cdot 1000 = 0.5\ \mu V, \tag{2.6}$$

which results in a signal to noise ratio of 20. A lock-in amplifier can be understood as a very narrow bandpass filter. Its basic principles, based on [203], are explained in the following.

A lock-in amplifier uses a technique known as phase sensitive detection to single out the component of the signal at a specific reference frequency and phase, leading to the possibility to detect signals in the nV regime even when the signal is obscured by noise sources many thousand times larger.

Each lock-in measurement requires an external reference source ω_r, which can be e.g. the sync output of a function generator. The response of the sample by a sine wave excitation with the same frequency ω_r will be of the form $V_{\text{sig}} \sin(\omega_r t + \theta_{\text{sig}})$ with V_{sig} as the signal amplitude. On the other side the lock-in amplifier generates its own sine wave which can be written as $V_L \sin(\omega_L t + \theta_{\text{ref}})$. The idea is to amplify the signal and to multiply it by the lock-in reference. The output is therefore the product of two sine waves and one finds

$$V_{\text{psd}} = V_{\text{sig}} V_L \sin(\omega_r t + \theta_{\text{sig}}) \cdot \sin(\omega_L + \theta_{\text{ref}}), \tag{2.7}$$

$$V_{\text{psd}} = 1/2 \cdot V_{\text{sig}} V_L \left(\cos([\omega_r - \omega_L] \cdot t) + (\theta_{\text{sig}} - \theta_{\text{ref}}) - \cos([\omega_r + \omega_L] \cdot t) + (\theta_{\text{sig}} + \theta_{\text{ref}})\right), \tag{2.8}$$

which means two AC signals at the two frequencies $(\omega_r + \omega_L)$ and $(\omega_r - \omega_L)$ are determined. If these signals pass a narrow low pass filter, the sum of both frequencies will be filtered, and the overall output will vanish if $\omega_r \neq \omega_L$. If both frequencies are equal this yields

$$V_{\text{psd}} = 1/2 \cdot V_{\text{sig}} V_L \cos(\theta_{\text{sig}} - \theta_{\text{ref}}), \tag{2.9}$$

$$V_{\text{psd}} = 1/2 \cdot V_{\text{sig}} V_L \cos(\theta), \tag{2.10}$$

which is a DC signal proportional to the signal amplitude. Adding a second phase sensitive detector which multiplies the signal with the reference oscillator shifted by 90 °, one obtains for the second output

$$V_{\text{psd2}} = 1/2 \cdot V_{\text{sig}} V_L \sin(\theta). \tag{2.11}$$

Defining X and Y as follows, the vector representation of the signal can be written as

$$X = V_{\text{sig}} \cos(\theta) \qquad Y = V_{\text{sig}} \sin(\theta), \tag{2.12}$$

$$R^2 = X^2 + Y^2 \qquad \theta = \arctan(Y/X). \tag{2.13}$$

In the performed measurements, only the X-component of the signal is relevant and therefore the lowest possible sensitivity is used. Usually, the Y-component is much larger (but is independent of the external field) and goes into overload. The lock-in amplifier shows overload if the signal is three times larger than the sensitivity.

After this introduction and explanation of the lock-in technique, the last section of this chapter will be presented, which is an introduction into the experimental setup.

2.10. Sample Holder And Cryostat

For all measurements which will be presented in this thesis, the bath cryostat shown in Figure 2.27 has been used. In this system, possible stable sample temperatures are 4.2 K as the temperature of liquid helium and room temperature. Variable temperatures are achieved during the warming-up of the system once the liquid helium is evaporated, which takes approximately ten hours assuming the cryostat has been completely filled. Two in-plane external fields of 265 mT as the x-field and 125 mT

magnitude as the y-field can be applied to the sample. These magnetic fields are generated by a Helmholtz split coil (large, outer pairs of coils for the y-field) and an inner solenoid-coil for the x-field. An overview drawing of the magnet system is shown in Figure 2.28c). The outer pairs of coils has a total resistance of 1.74 Ω and is driven by a "BSMPS BIP 200/60 4Q" power supply from Bruker, which provides a maximum current of 60 A by a voltage of 200 V. In all measurements, never any problems concerning the relatively large resistance mismatch between power supply and coil occurred. However, the maximum current, guaranteed from "Oswald" [204] as the manufacturer of the coil-system, is 33.5 A while the field to current ratio is given by 3.73 mT/A.

The resistance of the inner solenoid-coil is 1.02 Ω and the coil is driven by by a "BOP 36-28MG" from Kepco [205] which provides a maximum current of 28 A by a voltage of 36 V. For this coil, the maximum current is 27 A while the field to current ratio is given by 9.839 mT/A.

A photograph of the sample holder, together with a sample is shown in Figure 2.28b). The sample holder consists of twelve DC-contacts and four AC-contacts with a maximum frequency of 18 GHz. Additionally, a "Cernox" temperature sensor is mounted close to the sample to read out the sample temperature [206].

The sample holder is mounted on the sample rod which is placed inside the cryostat. Electrical devices such as a pulse generator or a lock-in amplifier can be connected to the sample as shown in Figure 2.28a). In this particular measurement an alternating current of 1 mA amplitude and 2221 Hz frequency is applied from contact 7 to contact 11 and the non-local voltage is detected simultaneously with two lock-in amplifiers between contact 3 and contact 1 and between contact 4 and contact 1, respectively.

Fig. 2.27. Photograph of the bath cryostat used. In total, the sample can be connected with 16 contacts (twelve DC and four AC contacts) and stable temperatures of 4.2 K and room temperature are possible. The temperature dependent measurements are performed by warming up the system, once the liquid helium is evaporated. Two in-plane magnetic fields of 265 mT and 125 mT magnitude can be used to change the magnetic state of the samples.

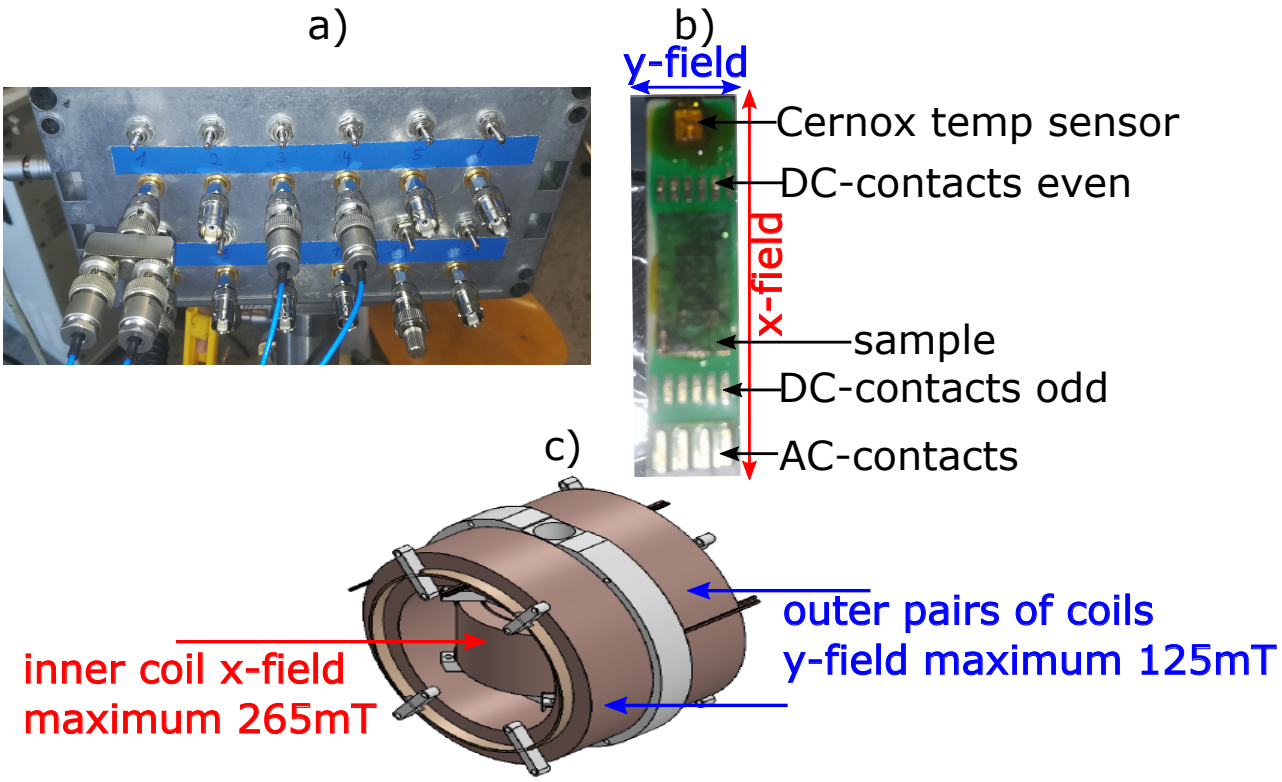

Fig. 2.28. a) Photograph of the sample rod with the twelve DC contacts. In this particular measurement, an alternating current of 1 mA amplitude and 2221 Hz frequency is applied between contact 7 and contact 11. The non-local voltage is read out by two lock-in amplifiers (between contact 3 and contact 1 and between contact 4 and contact 1) simultaneously.
b) Photograph of the sample holder with the twelve DC and the four AC contacts together with the "Cernox" temperature sensor and the orientations of the in-plane magnetic fields.
c) Overview drawing of the magnet system which allows to generate in-plane magnetic fields to switch the magnetic state of a sample.

Chapter III

Spin Current Assisted Magnetization Switching

In this chapter, pure spin current assisted switching of the magnetic state of a nanostructure is studied and discussed. In particular we demonstrate the manipulation of the magnetization of a small, 160 nm diameter Py disc in a lateral spin valve geometry, with the disc acting as the detector electrode. Spin current pulses are simultaneously generated in two CoFe wires and injected into a nonmagnetic Cu bridge, where they are subsequently transported to the disc. By a judicious choice of the applied field angle and the amplitude and polarity of the applied current pulses, the switching behaviour of the magnetic disc can be measured as a function of the resulting absorbed spin current.

We present results demonstrating that although the Py disc is nominally round and therefore no shape anisotropy is expected, small variations in the shape and randomly distributed imperfections can lead to significant changes in the device behaviour. Suitable field sweep directions are identified for which the magnetic switching takes place from a magnetic mono-domain state to a vortex state and from the vortex state to the opposite mono-domain state. Our results show that although most of the changes in the magnetic switching behaviour occur due to Joule heating, the spin transfer torque also contributes to the switching which can be detected thanks to our optimized geometry which allows for the synchronous application of current pulses from two injectors.

While the patterning of the samples in this chapter has been performed in Grenoble in the group of Laurent Vila and Jean-Philippe Attané, the measurements of the devices and the analysis of the results have been done in Mainz.

3.1. Motivation

The magnetic vortex state, found first in sub-micron magnetic discs [207, 208], enables possible efficient data storage with fast data manipulation due to the unique vortex properties. In this state, the magnetization curls in-plane around a central core region which is pointing out-of-plane. The sense of rotation is termed the chirality c, with c being defined as $c = +1$ for clockwise and $c = -1$ for counter-clockwise curling. The out-of-plane orientation (polarity) of the vortex core is defined as $p = +1$ for up and $p = -1$ for down.

Due to the alignment of the magnetic moments with the edges of the structure, the resulting stray field is low, which is of great importance to increase the storage density in a device and to minimize data loss due to interactions of the different bits [209]. In terms of fundamental physics, the study of vortex core dynamics by magnetic field pulses [210–212], electric current [213–215], spin waves [216] or by optical excitation [217] allows for the measurement of the stability of the vortex core as well as its velocity, along with other dynamic properties. For example, the β-parameter, which plays a vital role for current induced dynamics as described by the LLG-equation, can be robustly determined by the study of current driven vortex core dynamics. In these experiments, β can be determined independently from any assumptions concerning other important parameters such as the Gilbert damping α, or the spin polarization P [65, 218–221].

However, the magnetic vortex state, which is stable for a large geometrical parameter space in magnetic discs, also presents some challenges in certain applications. Due to its complex spin structure with many magnetization orientations present, the acting effective torques, induced by e.g. the spin transfer torque, Joule heating and Oersted fields on this state are complex to understand and additionally difficult to optimize. In the work presented in this chapter of the thesis, we aim to manipulate the magnetic state of very small and very thin Py discs via the application of pure spin current pulses. In these systems, not only the vortex state but also a quasi mono-domain state can be (meta)-stable at zero external field [222, 223].

These quasi-uniform states are particular well-suited for manipulation by the spin transfer torque since in this situation, the magnetization orientation of the detector electrode as well as the orientation of the manipulating spin current is well-defined. To study the spin current assisted magnetization switching in confined geometries such as discs or wires, lateral spin valves are a powerful tool due to the geometry based reduction of associated Joule heating and Oersted fields at the position where the spin current acts on the magnetization [12–15]. Furthermore, due to the low voltage-offsets present in the non-local signal, the signal is sensitive to very small magnetization changes in the probed area.

By designing a dual-injector device with a disc of Py as the detector and different materials with higher coercivity for the electrodes, we are able to control the magnetic state of the detector independently from the injector magnetization. We set the direction of the spin current relative to the absorbing magnetization. In this manner we investigate the efficiency of manipulating the magnetic states found in our discs by spin currents in order to understand the angular dependence of the torques, as well as assess the suitability of such non-local geometries for manipulating the mono-domain state and the vortex state in devices.

3.2. Sample Fabrication and Experimental Setup

Lateral spin valve devices have been fabricated consisting of two 30 nm thick and 70 nm wide CoFe injector wires, and a 10 nm thick and 160 nm diameter Py disc as the detector. 80 nm thick and 70 nm wide nonmagnetic Cu has been used as electrodes to contact the disc and as the spin current conduit, as shown in Figure 3.1. The structures have been produced in a three step electron beam lithography process and the materials have been deposited by UHV thin film deposition and by standard lift-off processes. The dual CoFe electrode geometry allows for the application of current pulses from either orientation of the electrode or alternatively synchronous application from both injectors. We note here that the right CoFe wire has a slightly higher resistance (130 Ω at 4.2 K) than the left CoFe wire (100 Ω

at 4.2 K). By using Pick-Off-T's, we are able to disentangle the low frequency and low amplitude lock-in excitation from the high frequency and high amplitude current pulses. Furthermore, any significant current pulse reflections up to the sample are suppressed. All connections marked "Osci" are connected to an oscilloscope with a 50 Ω input impedance, which allows for the measurement of the resulting charge current density for verification of the different applied pulse amplitudes.

Since the CoFe wires are magnetically hard and do not switch for the low external magnetic fields used in this measurement, all changes in the non-local signal are connected to the magnetic behaviour of the Py disc. The orientation of the different in-plane field angles is shown in the top left corner of Figure 3.1.

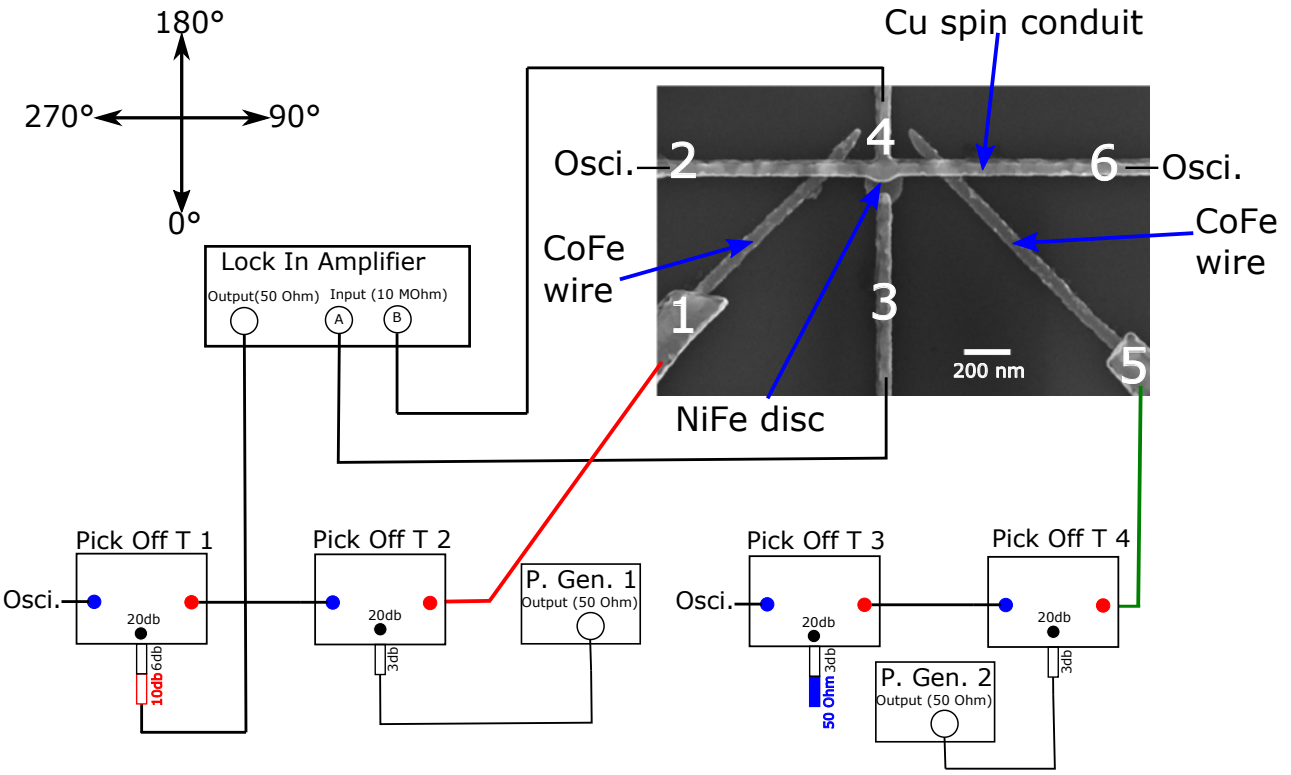

Fig. 3.1. Scanning electron microscope image of the measured sample together with a schematic of the used setup. By the synchronous application of current pulses in the injectors (contact 1 and contact 5) via the Pulse Generators (P. Gen.), spin currents are generated and injected into the nonmagnetic Cu bridge. Here they diffuse in all directions including in the direction of the disc, where the spin currents are absorbed at the Cu/Py interface. Once the spin currents are absorbed, the spin transfer torque acts on the local magnetization of the disc at the interface, which manipulates the magnetic state of the disc. These changes of the magnetic state can be detected via changes in the non-local signal by the lock-in amplifier. The injected pulses are checked with an oscilloscope (Osci.), which allows to determine the charge current density of the certain pulses. The measurement design is based on ideas from Hermann Stoll [224].

While the field dependent measurements without any applied assisting currents are standard non-local measurements, as described in section 1.8, the measurement with applied current pulses are performed as follows:

a) For a given applied field angle, the external field is increased by an increment of e.g. 1 mT.

b) After setting and reading the field, the measurement program triggers Pulse Generator 1, which applies a pulse from contact 1 to contact 2 from the left CoFe injector to the conduit (positive pulses) or vice versa for negative pulses. On being triggered, Pulse Generator 1 in turn triggers

Pulse Generator 2. By a suitable choice of delay times and cable lengths, the two Pulse Generators are synchronized.

c) The Pulse Generators are turned off so that the non-local signal is not affected by the current pulses.

d) The non-local signal is read out by the lock-in amplifier to see if the magnetic state has been changed by the current pulses.

e) Steps a) - d) are repeated until the measurement is finished.

To determine the resulting charge current density for a given pulse amplitude, we measure the voltage after the pulse with the oscilloscope and divide it by 50 Ω as the input impedance of the device. As a result of the higher resistance of the right CoFe wire, the measured voltage for a given pulse amplitude is lower. In Figure 3.2, we show the resulting voltage pulses after the two injectors for an applied output voltage of 270 mV of the given Pulse Generator. In the same figure, we show the resulting charge current density as a function of the applied output voltage of the two Pulse Generators. The lock-in current is, if not explicitly stated, for all measurements 85 μA and the lock-in current is flowing between contact 1 and contact 2, as drawn in Figure 3.1. All results shown in the following sections of this chapter are measured at a temperature of 4.2 K.

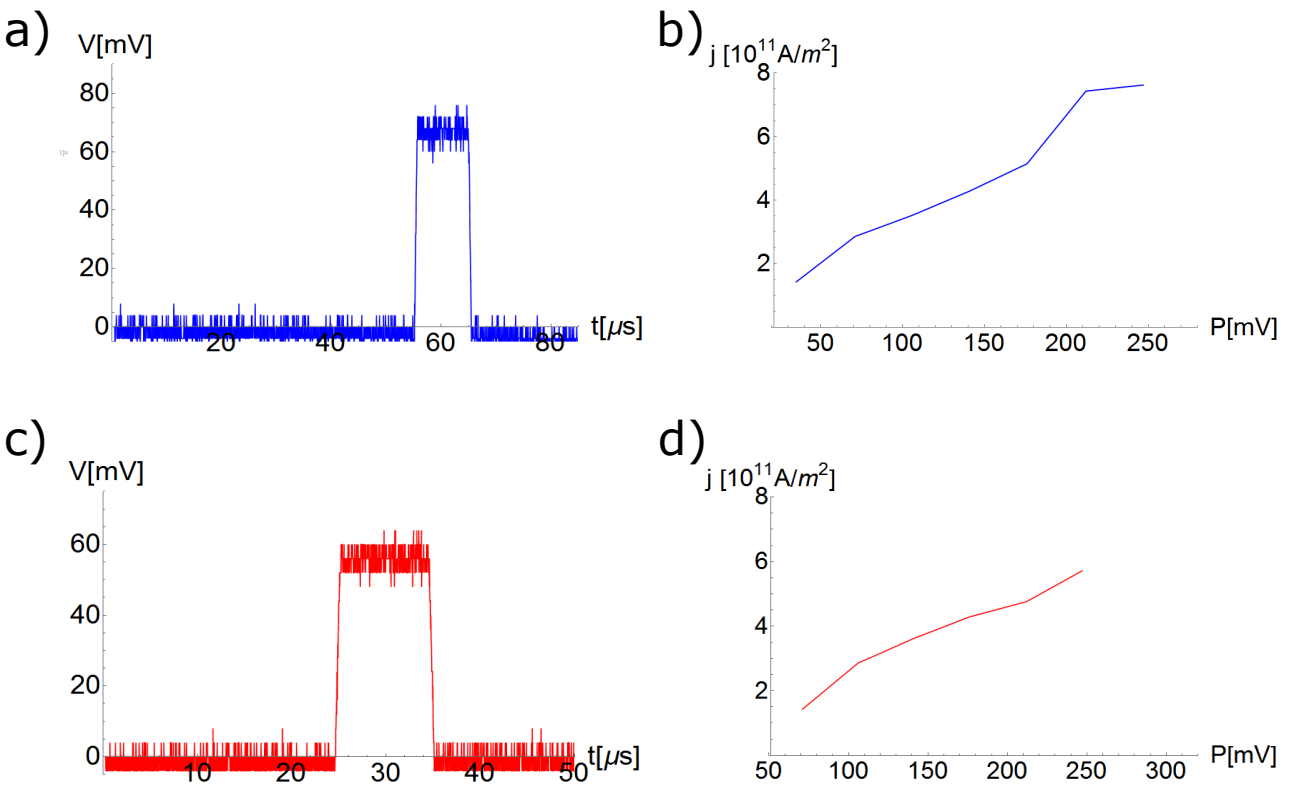

Fig. 3.2. Dependence of the charge current density on the applied initial output pulse voltage (P) of the Pulse Generator after the 23 db reduction for the two CoFe wires.
a) Measured voltage drop across the left CoFe wire with an applied pulse amplitude of 270 mV.
b) Determined charge current density in the left CoFe wire for applied pulses between 50 mV and 270 mV. a) Measured voltage drop across the right CoFe wire with an applied pulse amplitude of 270 mV.
b) Determined charge current density in the right CoFe wire for applied pulses between 50 mV and 270 mV.

3.3. Study Of The Magnetic Switching Behaviour Of The Py Disc

3.3.1. First characterization measurements

In order to characterize the magnetic switching behaviour of the Py disc, we perform external field sweeps for different field angles without any assisting current pulses. To this end, we measure the magnetic behaviour of the Py disc for different field angles in steps of 15 °.

Before these characterization measurements are performed, we determine the magnetization orientation of the two CoFe wires through a measurement of the non-local voltage at the disc, during injection from the particular electrode as a function of the applied field angle. A field amplitude of 120 mT is used in these measurements and the measurement scheme together with the used contacts is shown in Figure 3.3. Since the two CoFe wires have slightly different resistances (100 Ω for the left CoFe wire and 130 Ω for the right CoFe wire at 4.2 K), a 10 kΩ pre-resistor is used in order to apply the same effective current for both measurements.

For the left CoFe wire acting as injector (Figure 3.3a)), we find the maximum of the non-local signal at 135 °. For the measurement with the right CoFe wire as injector (Figure 3.3b)), we observe the maximum non-local signal at an angle of 45 °. This reveals that the magnetization of the left CoFe wire is pointing along the 135 °-direction while the magnetization of the right CoFe wire is oriented along the 45 °-direction, since the soft magnetic Py disc is aligned with the external field and the maximum non-local is found for a parallel magnetization alignment of injector and detector [225].

Furthermore, we notice that the spin signal generated with the right CoFe wire is lower than the signal with the left CoFe wire, which can be explained as arising from different qualities of the left CoFe/Cu interface and the right CoFe/Cu interface [226]. Nevertheless, the measured non-local signal with the right CoFe wire acting as injector is relatively large compared to experiments with pure Py based injectors [13–15], which can be attributed to the high spin polarization of CoFe [227], making CoFe an attractive injector material. Together with the selection of Py as a soft magnetic material for the disc, which provides low switching fields even for small dimension structures, our geometry allows both for a potential large spin torque effect and a simplified analysis procedure since all changes in the non-local signal can be attributed to the magnetization changes of the detector.

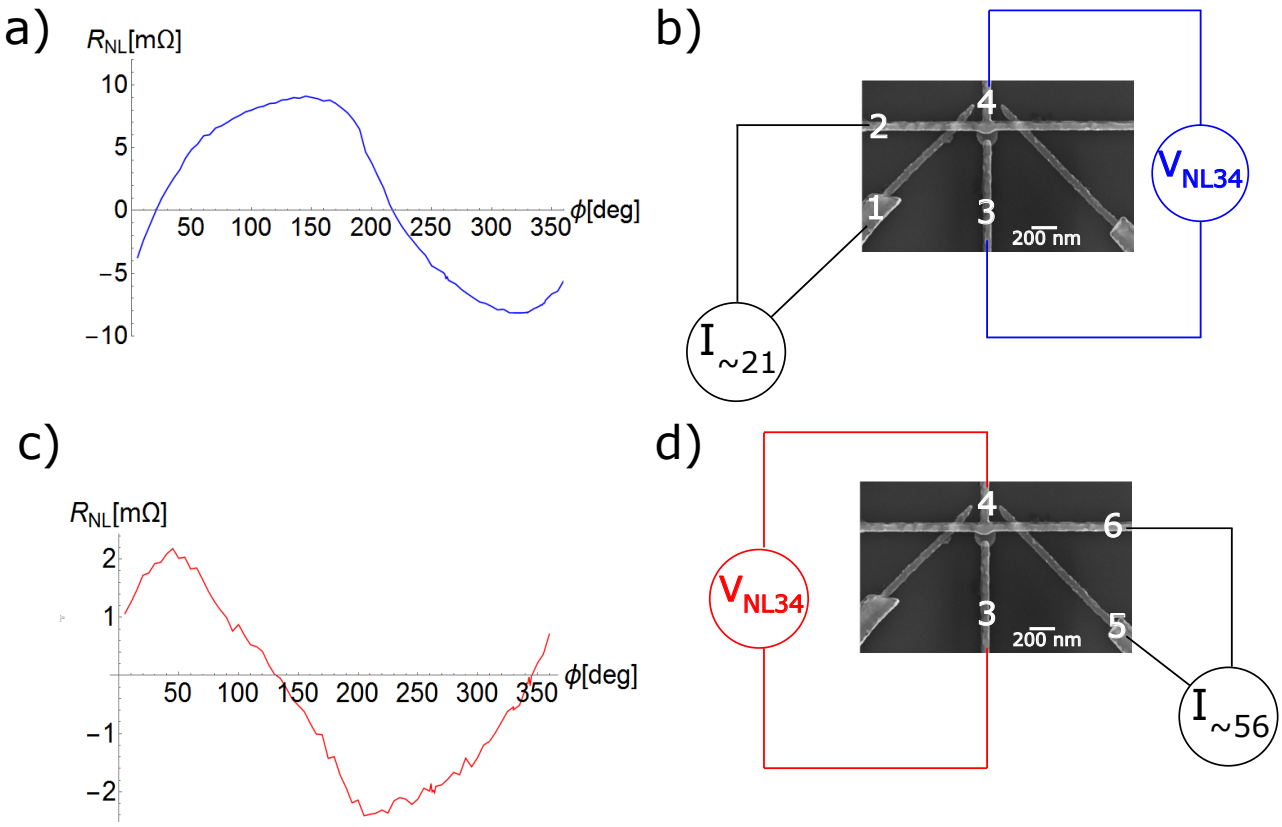

Fig. 3.3. Measured non-local signals with an applied field amplitude of 120 mT as a function of the applied field angle. The magnetization directions of the two CoFe injectors can be directly determined from the angle where the maximum non-local signal is obtained.
a) Measured spin signal with the left CoFe wire acting as the injector. We find the maximum spin signal at an angle of 135 °.
b) Current injection and voltage detection scheme for the measurement shown in a).
c) Measured non-local signal with the right CoFe wire acting as the injector. In this case, we find the maximum spin signal for an applied field angle of 45 °.
d) Current injection and voltage detection scheme for the measurement shown in c).

Before we show the results for the different field angles in detail, we show some representative curves in Figure 3.4 to demonstrate that depending on the applied field angle, the hysteresis loops are very different concerning their general shape, as well as the number of the observed jumps and their heights.

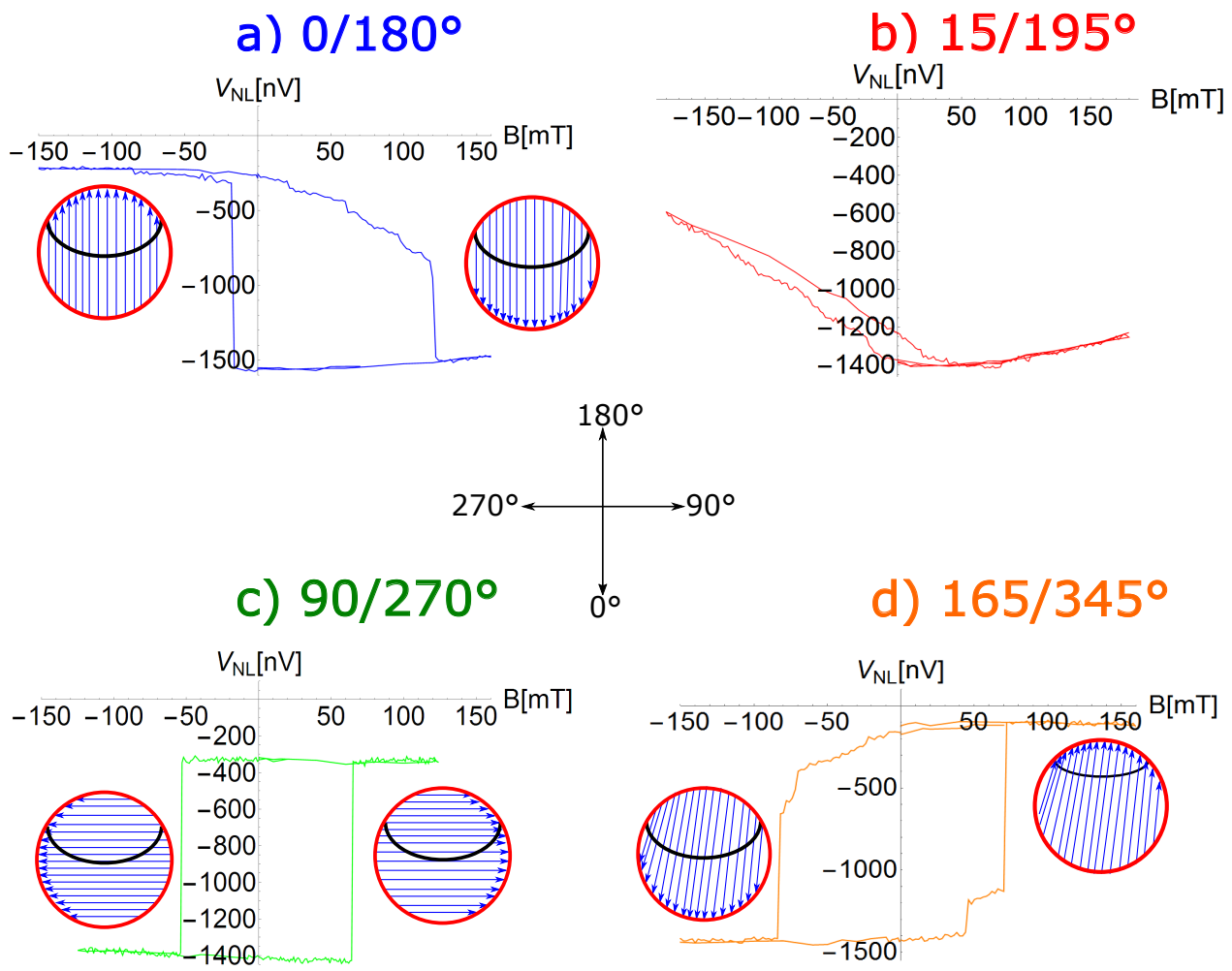

Fig. 3.4. Measured hysteresis loops for different external field angles. Expect for b), where hardly any hysteresis and no jumps are observed, we expect for the other three curves the magnetization of the disc to be aligned with the external field for high fields above ±125 mT in order to minimize the Zeeman energy.
a) Sweep along the 0/180 ° external field direction. Starting with positive fields, no change of the non-local signal is found, which indicates the magnetization of the disc is pointing along 0 °. At −18 mT a large jump and at −86 mT a small jump of the non-local signal are found. For fields between −87 mT and 0 mT no changes of the non-local signal are found, indicating that the disc is magnetized along 180 °. By returning to positive fields, small jumps of the signal are found at +22/+62/+100 mT. Between the jumps, we find a continuous reduction of the signal. At +123 mT a large jump is found. The magnetization of the disc is now aligned along 0 ° again.
b) Sweep along the 15/195 ° external field direction. Hardly any change of the magnetization of the disc is found and no abrupt jumps of the signal are observed.
c) Sweep along the 90/270 ° external field direction. Two large jumps, one for each field direction, are found at −54 mT and at +65 mT. Since no further changes of the signal are found and the switching fields for the two field directions are similar, we assume these states to be mono-domain states being aligned with the external field.
d) Sweep along the 165/345 ° external field direction. Here we find four clear jumps, two for each field sweep direction. We determine a continuous reduction of the signal by 270 nV in the field range between ±0 mT and −71 mT. At −72 mT, an abrupt reduction of the signal of 100 nV is found. We find a further reduction of the non-local by 150 nV before the large jump occurs at a field of −84 mT. We find this mono-domain state pointing along the 345 °-direction being stable up to an applied field of +46 mT where the non-local signal changes abruptly by 200 nV followed by a continuous increase of the signal in the field range between +47 mT and +70 mT. The full switching to the mono-domain state pointing along the 165 °-direction is found at +72 mT.

We emphasize here that different switching pathways for nominally identical conditions, i.e. the same field angle (and in later measurements the same amplitude of the applied current pulses) are possible [228]. However all the curves presented in this section are representative since the general behaviour and the shape of the hysteresis curves for the different field angles is robustly reproducible for a large proportion of the measurements. As an example, field sweeps along 90/270 ° (Figure 3.4c)) have reproducibly shown low or even no field dependent changes, except for the two large jumps of the signal. Field sweeps along 165/345 ° (Figure 3.4d)) have shown four or more jumps of the signal with the small jumps observed for lower fields. Field sweeps along 15/195 ° (Figure 3.4b)) have shown no detectable switching events and hardly any hysteresis.

Due to the Zeeman energy, which is minimal for the magnetization orientation of the disc being parallel to the external field and since Py is a soft magnetic material, we expect for large fields a mono-domain state where the magnetization is saturated along the external field. This is supported by the cases where abrupt one step switching occurs to the saturation level. While in these measurements transitions from one mono-domain state to the opposite one are found, we find for other measurement two or more significant jumps in the non-local signal for one external field sweep direction. These jumps can be attributed to vortex core nucleation and annihilation events [207, 222]. We can understand these curves by a simple model with the assumptions as follows:

a) Field dependent continuous changes of the signal, which are for some applied field angles found, are neglected.

b) Since the magnetization is time reversal invariant, we expect, assuming no impurities acting as nucleation centres for the vortex core, the nucleation and switching fields to be symmetric.

c) We assume the vortex core to be in the centre of the disc.

d) For sufficiently high fields, we assume the magnetization of the disc to be parallel with the external field in order to minimize the Zeeman energy.

e) All changes in the non-local signal are only caused by the change of the magnetization in the disc. Any possible small changes of the injector magnetization orientation are neglected.

We explicitly show schematically the four possible pathways of the mono-domain state to mono-domain state switching via the vortex nucleation/annihilation in Figure 3.5. In our simple example we assume the vortex core to be in the centre of the disc and assume the magnetic field to be swept along 90/270 °. The shown hysteresis curves are not real data, but just hypothetical curves in order to explain the principle of how to connect the size of the jump with the chirality of the vortex core. To this issue, we study the situation shown in Figure 3.5a) in detail.

In state I the full disc is magnetized along 90 ° in order to minimize the Zeeman energy and we assume this state to be stable at 0 mT. Then, at −10 mT we assume a small jump in the signal, which means only a few of the magnetic moments below the contact have changed their orientation and so the chirality must be clockwise, as drawn in II. For a negative applied field of −80 mT we assume to find the large jump and now the disc is fully magnetized along the 270 °-direction, as plotted in state III and again we assume this state to be stable on reducing the field back to 0 mT. For +10 mT we assume a second small jump and now the chirality of the vortex core is counter-clockwise in order to explain the small detected magnetization changes below the contact, which is drawn as state IV. Analogously, we are able to determine the different chirality for all combinations and conclude:

a) If two small jumps at low fields are measured as shown in Figure 3.5a), the chirality of the vortex is for state II clockwise ($c = +1$) and for state IV counter-clockwise ($c = -1$).

b) If two large jumps are found at both low negative and positive fields as shown in Figure 3.5b), the chirality of the vortex is for state II counter-clockwise ($c = -1$) and for state IV clockwise ($c = +1$).

c) If the large jump is found for low negative fields and the small jump is found for small positive fields as shown in Figure 3.5c), the chirality of the vortex is counter-clockwise ($c = -1$) for both states II and IV.

d) If the small jump is found for low negative fields and the large jump is found for small positive fields as shown in Figure 3.5d), the chirality of the vortex is clockwise ($c = +1$) for both states II and IV).

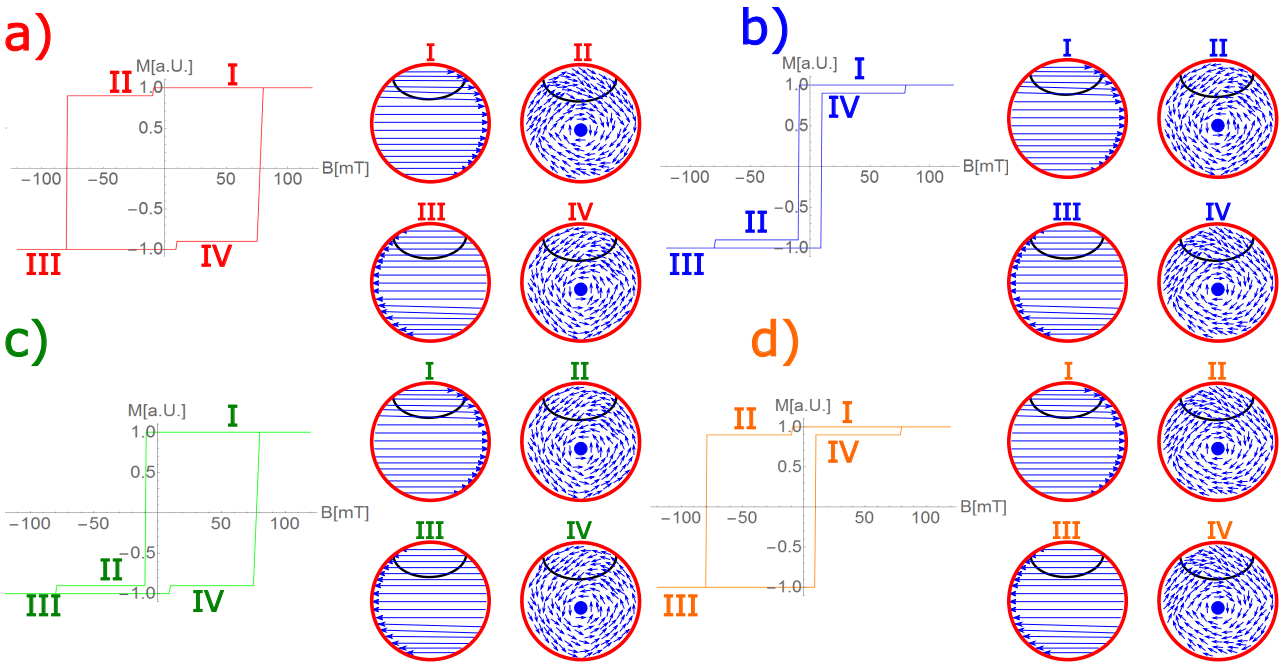

Fig. 3.5. Simplified model to explain the size of the measured jumps in the non-local signal based on vortex nucleation and annihilation events. Based on whether the small or the large jump is found for small or high external magnetic fields, the chirality of the vortex can be determined. The applied field angle is assumed to be 90° for positive fields and 270° for negative fields.
a) Situation when the two small jumps are found for low external fields. In this situation the chirality of the nucleated vortex is clockwise ($c = +1$) for state II and counter-clockwise ($c = -1$) for state IV.
b) Situation when the two large jumps are found for low external fields. We determine the chirality of the vortex to be counter-clockwise ($c = -1$) for state II and clockwise ($c = +1$) for state IV.
c) Situation when for negative fields the large jump is measured first while for positive fields, the small jump is measured first. In this scheme, we determine the chirality of the vortex to be counter-clockwise ($c = -1$) for both states II and IV.
d) Situation when for negative fields the small jump and for positive fields the large jump is measured first. Here the vortex chirality is for both states II and IV clockwise ($c = +1$).

While the model as shown in Figure 3.5 is based on many assumptions and does not treat real measured data, we now show and explain in detail first order reversal curves for which the conceptual switching shown here helps. By this measurement scheme, we are able to understand the switching of the disc for any arbitrary field angle in much more detail and are additionally able to connect the nucleation point of the vortex with the size of the signal.

3.3.2. First order reversal curves (FORC)

To identify the different switching events as either a transition from the mono-domain state to the opposing mono-domain state or as a transition from the mono-domain state to a vortex state and vice versa we use first order reversal curves [229, 230]. In such measurements (Figure 3.6), the external

magnetic field is applied under a certain angle up to a large positive field in order to establish the mono-domain state. In the second step, the external field is swept to negative values until an abrupt change in the non-local signal is measured, indicating a change in the magnetic state. Thirdly, the magnetic field is reduced back to 0 mT and the non-local voltage measured at this zero-crossing is compared to the non-local level measured at the zero-crossing after the initialization of the mono-domain state. In Figure 3.6a) we show firstly the complete hysteresis curve for an external field angle of 351 ° for positive field values and 171 ° for negative field values.

These measurements are performed with positive current pulses in the left injector with a current density of $7.6{\cdot}10^{11}\,\mathrm{A}/m^2$. As shown, we observe in total four main types of transition which are independently probed by the FORC measurements presented in Figure 3.6b) and Figure 3.6c). The corresponding states are labelled as **I**, **II**/**IIa**, **III** and **IV**/**IVa**. The direction of the injector magnetization $\mathrm{M_{inj}}$ is drawn in green and the orientation of the applied external field B is drawn in purple. We show both these directions, as well as the magnetization direction M of the disc below the contact (drawn in blue) in Figure 3.6d) and Figure 3.6e). The edge of the probed region of the contact is marked in black and the magnetization of the full disc is represented as blue arrows.

As mentioned before, the magnetization direction of the left injector is fixed along 135 ° due to the strong shape anisotropy, the choice of CoFe as a magnetic hard material and the relatively small applied external fields. This is valid for the field dependent measurements as well as the spin current assisted measurements. This magnetization direction of the injector $\mathrm{M_{inj}}$ defines the orientation of the relative angle between spin current and detector magnetization which is probed by the non-local signal. This spin current direction must not be mixed up with the orientation of the spin current pulses, which are either along 135 ° for positive pulses or along 315 ° for negative pulses and do not contribute to the non-local signal. For clarification, the probed area of the disc is enlarged in the schematic illustration. In the real sample, due to the small size of the Py discs stabilizing the mono-domain state [231], only the very upper edge of the disc is probed.

As described above, state **I** represents the mono-domain state formed at saturation where the magnetization of the disc is aligned parallel to the external field pointing in the 351 °-direction to minimize the Zeeman energy. We find for the average angle θ_I between spin current and magnetization [225], calculated from $V_{NL} \propto \cos(\theta)$, a value of $\theta_\mathrm{I}{=}144{\pm}1\,°$. As the field is reduced to zero there is likely to be some small canting of the magnetization at the edge of the disc [222, 232–234]. However, the magnetization for the main part of the disc remains quasi-uniform with little change to the integrated signal under the contact. As a result, for simplicity, we will continue to refer to this state as the mono-domain state while bearing in mind the small changes in the edge magnetization that will occur with applied field.

In state **IIa**, a vortex core is nucleated with the core position being expected to be at the edge of the disc, perpendicular to the external field [207, 222, 235, 236]. In state **IIa** some components of the average magnetization are more parallel to the direction of the spin current. As a consequence, the measured non-local voltage increases up to −600 nV, before we find the abrupt switching to the mono-domain state with the magnetization aligned in the 171 °-direction, as plotted in Figure 3.6c). As shown in Figure 3.6b), after the vortex nucleation, on reducing the external field back to 0 mT, the measured non-local voltage is −800 nV and therefore 100 nV larger than the mono-domain state and we name this state **II**. This confirms an irreversible switching and demonstrates that both configurations are metastable at zero field. We note here that the state drawn in Figure 3.6d) schematically indicates the magnetization orientation of state **II** with the vortex core in the centre of the disc by reducing the external field to 0 mT. The state **IIa** with the vortex core at the edge directly after the nucleation is shown in Figure 3.6e). The determined difference in signal for the two states **I** and **II** at zero field of 100 nV allows us to calculate the average angle between spin current and magnetization to be $\theta_\mathrm{II}{=}133{\pm}1\,°$ for state **II** with the vortex state present and the vortex core centred in the disc.

This is a very important result since it allows us to compare the calculated angle with the expected one based on our simple model shown before and drawn in Figure 3.5. From our simple model, which leads to a magnetization direction below the contact pointing along 270 ° for a counter-clockwise

vortex, we would have expected an theoretical angle $\theta_{\mathrm{II}}^{\mathbf{theo}}$ of 135 ° which fits our determined angle for of θ_{II}=133±1 °. We can therefore expect, that by vortex nucleation and relaxing the external field to 0 mT, the magnetization of the probed area is relatively homogeneously magnetized along 270 ° for a counter-clockwise vortex.

As presented in Figure 3.6c), the complete switching to the mono-domain state, now with the average magnetization of the probed disc pointing in the 171 °-direction, appears at an external field of −42 mT and we indicate this configuration as state **III**.

For state **III**, we determine the average angle between probed magnetization of the disc and spin current to be θ_{III}=36±1 °. Finally for state **IV**/**IVa**, where the vortex core has been nucleated for an applied external field of +8 mT, we find the measured non-local signal to be 100 nV lower than for the mono-domain state **III**, resulting in θ_{IV} =47±1 °, which is again very close to the theoretical angle for $\theta_{\mathrm{IV}}^{\mathrm{theo}}$ of 45 °. So for a clockwise vortex with the core in the centre of the disc, we expect the magnetization to be relatively homogeneously aligned along 90 °.

We emphasize here the difference in the non-local signal between the different mono-domain states (**I** and **III**) and the corresponding vortex states (**II** and **IV**) with the vortex core in the centre of the disc is in both cases 100 nV, demonstrating the symmetry of the switching.

Comparing state **IIa** with state **II** and then state **IVa** with state **IV**, we notice that the states **IIa** (directly after the vortex nucleation) and **II** (with the vortex in the centre of the disc) differ by 100 nV while the two states **IVa** and **IV** are identical. This is a second very important result because we gain information concerning the nucleation point of the vortex. For state **IIa** the vortex has been nucleated at the right edge of the disc and by the reduction of the external field, the vortex moves to the centre. By this vortex motion, as mentioned before, we expect the magnetization to be relatively homogeneously aligned along 270 °. Since the states **IVa** and **IV** are identical, is is possible that the nucleation has occurred slightly further away from the edge of the disc at a defect, which leads to a very similar magnetization configuration of state IVa and **IV** below the contact. However, by the comparison of the states directly after nucleation and at zero field, we are able to draw conclusions concerning the different nucleation points, caused by e.g. defects within the disc.

With the introduction of the first order reversal curve measurement scheme, we are now able to understand the different switching events, determine the different vortex chirality and study the vortex nucleation points. The detailed analysis for all field angles is shown in Section 3.3.3.

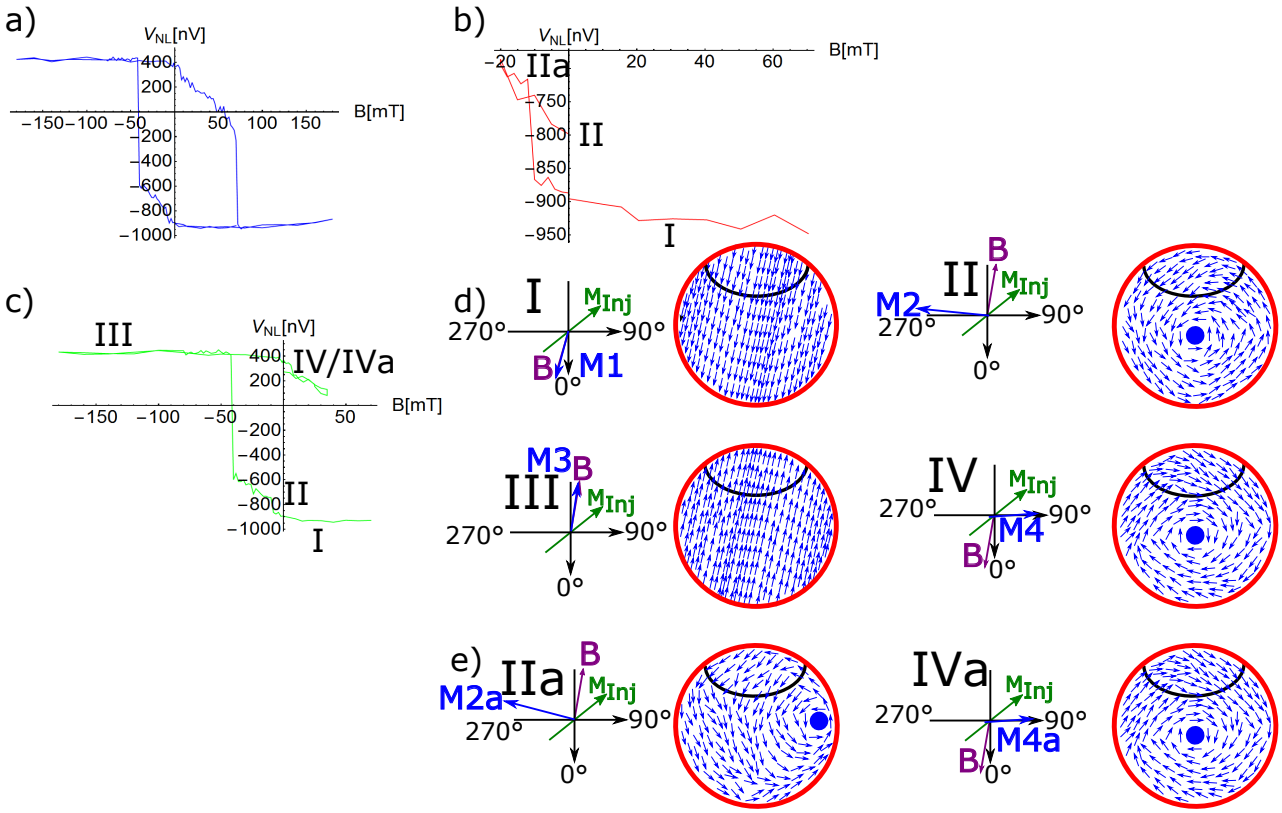

Fig. 3.6. a) Full hysteresis curve with four abrupt changes in the non-local signal which can be identified as mono-domain state to vortex state switching events and vice versa.
b) The external field is initially swept from 0 mT to +60 mT and back to 0 mT. No changes in the non-local signal from the saturation level of −900 nV are observed, indicating the mono-domain state **I** is still stable at zero field. The average angle between the spin current and magnetization θ_I is 144±1 °. After this, the external field is swept to −20 mT with an abrupt change of the signal at −10 mT (state **IIa**) and then back to 0 mT, indicated by **II**. At 0 mT, this state has a non-local signal of −800 nV with the vortex core in the centre of the disc, which results in an average angle between spin current and magnetization θ_{II} of 133±1 °. For state **IIa** we determine the non-local signal to be −700 nV directly after the nucleation, resulting in an average angle between spin current and magnetization θ_{IIa} of 123±1 °.
c) First order reversal curve for positive external fields. The mono-domain state **III** is initialized by a negative field of −150 mT resulting in a non-local signal of +400 nV. Then the external field is reduced to 0 mT without any observed changes in the non-local signal. The average angle between the spin current and magnetization θ_{III} is 36±1 °. Next, a positive field up to +20 mT is applied and an abrupt change of the signal is observed at +8 mT (**IVa**). The average angle between the spin current and magnetization, $\theta_{IV} = \theta_{IVa}$ is 47±1 ° for both states **IV** and **IVa**.
d, e) Schematic representations of the different magnetization states of the Py disc. The labels show the direction of the external field (purple arrows) and the spin current (green arrows) and the average magnetization of the probed area (blue arrow). The position of the vortex is drawn for state **IIa** at the edge directly after nucleation and for state **II** with the vortex core in the centre realised by reducing the field to 0 mT. Since state **IVa** and **IV** show the same non-local signal and thus the same magnetization below the contact, the nucleation has occurred close to the centre of the disc and no change in the signal by reducing the field from +8 mT (the nucleation field) to 0 mT is found.

3.3.3. Detailed analysis of the hysteresis loops for different field angles

To further understand the switching of the disc, we show the different hysteresis curves for different field angles in Figure 3.7, Figure 3.8 and Figure 3.9. We determine the switching fields for each individual jump for each curve and determine the magnetization orientation for each magnetic state. When we check the curves shown in Figure 3.7 for field angles between 0/180 ° and 45/225 °, we notice

that there are changes in the switching behaviour. For 15/195 ° there is hardly any hysteresis and no jumps are observed. Also for neighbouring field angles, either a very high field is required to saturate the magnetization of the disc (along 0 °, more than 120 mT are required) or no complete saturation is found (along 30/210 °) for the magnetization below the contact.

For 0/180 °, we find the mono-domain state being aligned along 0 ° for all positive fields and no continuous changes of the signal. By applying a negative field of −18 mT we observe a large jump which can be understood as a vortex state with clockwise chirality. Since the probed part of the disc is very small, this vortex nucleation drastically affects the magnetization of the disc below the contact with a lot of magnetic moments pointing along 90 ° and therefore the angle between spin current (which is as mentioned before, always along 135 °) and the probed detector magnetization becomes on average aligned along 50 °. For −86 mT we find a very small second jump which indicates the mono-domain state and the magnetization of the disc is now oriented completely along 180 ° in order to minimize the Zeeman energy. This jump of the signal is very small since for this mono-domain state, we expect an angle of 45 ° between spin current and probed detector magnetization which is a very similar angle after the first, large jump and therefore the relative angle, which we probe by the non-local signal, has hardly changed.

By sweeping along positive fields again, we find a small jump first (yet of a very similar size as the small jump for negative fields). This small jump is caused by a nucleation of the vortex core with same chirality, yet nucleated at a different position within the disc. We find for increasing positive field continuous changes of the signal as well as small jumps which can be probably attributed to vortex core movement through the disc perpendicular to the field until the vortex core is pushed out completely of the probed area for positive fields of +123 mT and higher.

As previously mentioned, we do not find any jumps and hardly any hysteresis for sweeping the external field along 15/195 °. Additionally we find a broken symmetry of the signal for field angles between 15/195 ° and 45/225 °. This is evident since the signals do not saturate for the applied fields and we would e.g. expect that the saturated signal for angles of 45 ° and 225 ° would be the same as we have seen it in Figure 3.3. The measurement shown in Figure 3.3 was the first measurement which was performed directly when the sample was at 4.2 K while the angle dependent measurements have been performed a few days later. For an unknown reason, the magnetic switching behaviour has been changed during the warming up and cooling down of the system, and we do not saturate the samples for angles between 15/195 ° and 45/225 °, at least below the probed contact. As a result, we cannot identify the magnetic states of the disc and also cannot identify the observed jumps seen for angles of 30/210 ° and 45/225 °.

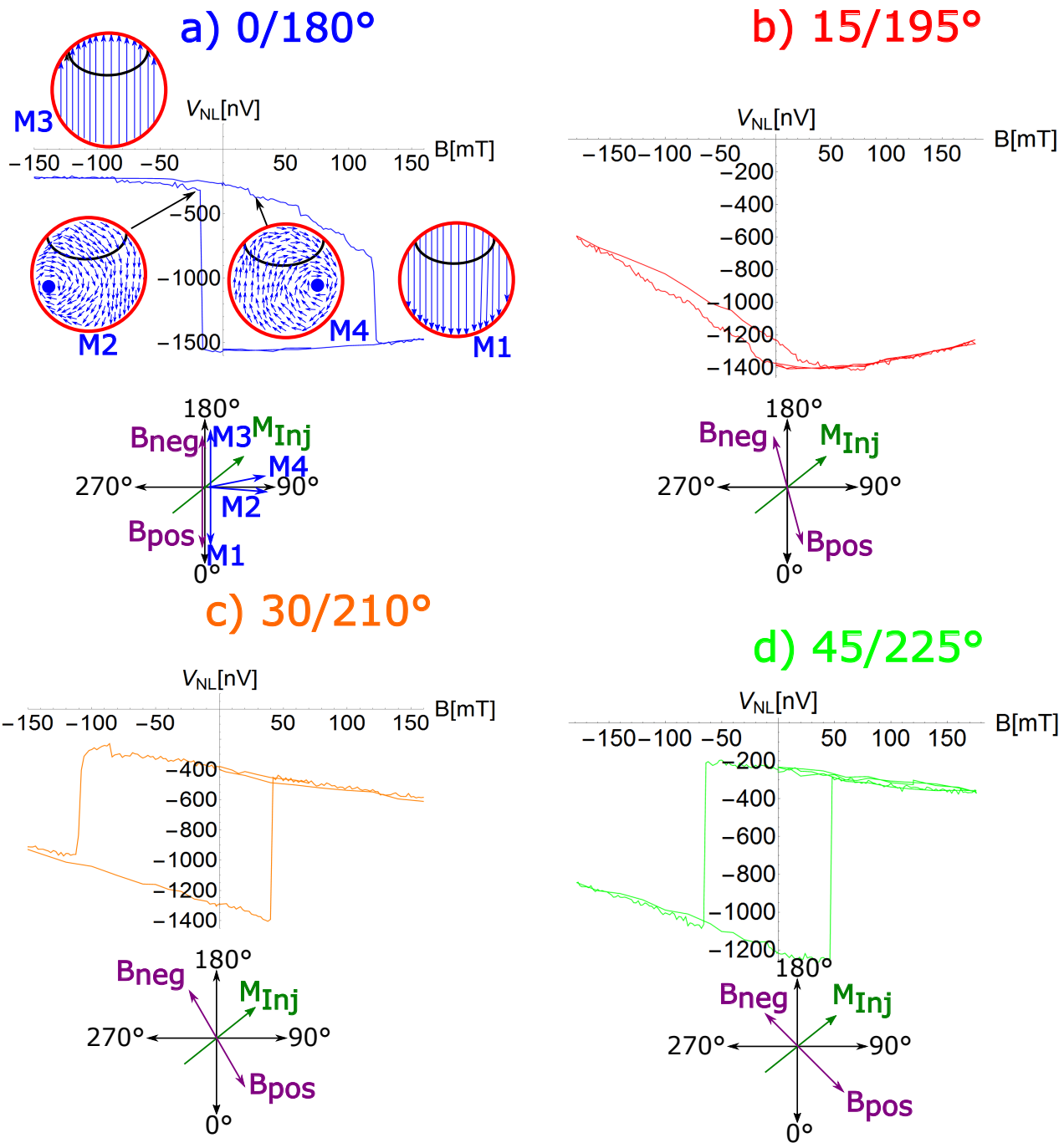

Fig. 3.7. Field dependent magnetization switching curves for field angles between 0 ° and 45 °.
a) Sweep along the 0/180 °-direction. Starting with positive fields and back to 0 mT, we find the mono-domain state being stable up to a field of −18 mT where a large jump in the non-local signal occurs. A very small jump is determined at −86 mT. Returning to positive fields, we find a decrease of the signal with an increase of the field and in total three small jumps at +22 mT, +62 mT and +100 mT while a large jump to the mono-domain state is observed for +122 mT.
b) Sweep along the 15/195 °-direction. Without any assisting applied current pulses, we do not observe a significant hysteresis indicating little change of the magnetic state in this field range.
c) Sweep along the 30/210 °-direction. We find a broken symmetry since we would expect for saturation along 30 ° the signal to be lower (here the relative angle between spin current and magnetization would be 105 °) than for the saturation along 210 ° since here an angle of 75 ° is expected. As mentioned before, we expect for smaller angles the signal to be higher.
d) Sweep along the 45/225 °-direction. As in the 30/210 °-measurement, we are not able to saturate the sample with the available field strengths and therefore we cannot identify the magnetic configuration of the disc.

Next we study external field sweeps for field angles between 60/240 ° and 105/285 °, as shown in Figure 3.8. Here we do not see any influence of chance of the switching paths and find the states at saturation in full agreement with our expectations based on Figure 3.3.

However, we find for sweeps along 60/240 ° and 90/270 ° very similar hysteresis curves with one large jump for each field direction and hardly any continuous changes of the signal with varying field. These measurements indicate again that the magnetic behaviour of the disc is strongly affected by defects which acts as nucleation points of the vortex core and cause the switching. As a result, similar hysteresis curves are found for similar external field angles. However, for 75/255 ° for negative fields and for sweeps along 105/285 ° we find clear differences for negative and positive fields which can be connected to vortex core nucleation events partly below the contact.

Starting with positive fields along 75 ° (Figure 3.8b)), we do not find any changes of the signal by reducing the field to 0 mT, indicating a stable mono-domain state with the magnetization being aligned along 75 °. We expect the angle between the probed magnetization for this state (M1) and the injector magnetization M_{inj} to be 60 °. However, for negative fields we observe large contentious changes of the signal in the field range between 0 mT and −24 mT before we observe a large jump reducing the signal at −25 mT, which can be explained by a vortex nucleation with counter-clockwise chirality partly below the contact. By the nucleation of the vortex, the magnetization below the contact M2 is now, based on the calculation, oriented along 280 °. As a result, we determine the angle between M2 and M_{inj} to be 145 °. After the observed very small jump at −83 mT and the observed increase of the signal, indicating the mono-domain state with all magnetic moments aligned along 255 °, we expect the angle between M3 and M_{inj} to be 120 °. We find the mono-domain state oriented along 255 ° to be stable up to an external field of +68 mT where a large jump, indicating the mono-domain state pointing along the 75 °-direction, is observed.

For this applied field angle, our model predicts the size of the two jumps correctly and also the expectation that the first jumps leads to a large reduction of the signal while the second jump leads to a small increase of the signal is in full agreement with the obtained data.

For 90/270 °, no changes of the signal except the two jumps at −54 mT and at +65 mT are found, while for 105/285 ° we find one jump for negative fields (−76 mT) and one very large jump at +42 mT and a tiny jump at roughly +55 mT. The large jump at +42 mT can be explained by a vortex nucleation with clockwise chirality. Due to the vortex, we expect the average magnetization below the contact M2 to be aligned along 95 °, which results in an angle between M_{inj} and M2 of 40 °. For the mono-domain state (at fields higher than +55 mT) we expect an angle of 30 ° and therefore a (small) further increase of the signal, which is however very tough to detect in the measurement. There is additionally a second argument that the vortex state is present for this applied field angle, which is based on time reversal symmetry. As mentioned before, we expect similar switching field for positive and negative fields. Since here, the two switching fields differ drastically (−76 mT and +42 mT), this asymmetry can be explained by the vortex core nucleation. If the small jump at roughly +55 mT is real, the difference in the switching fields would decrease significantly.

From the size of the jump it is not clear if there is the vortex state present for positive fields but in terms of symmetry, we would expect first a clockwise vortex state and then for larger positive fields (+55 mT and higher) the mono-domain state.

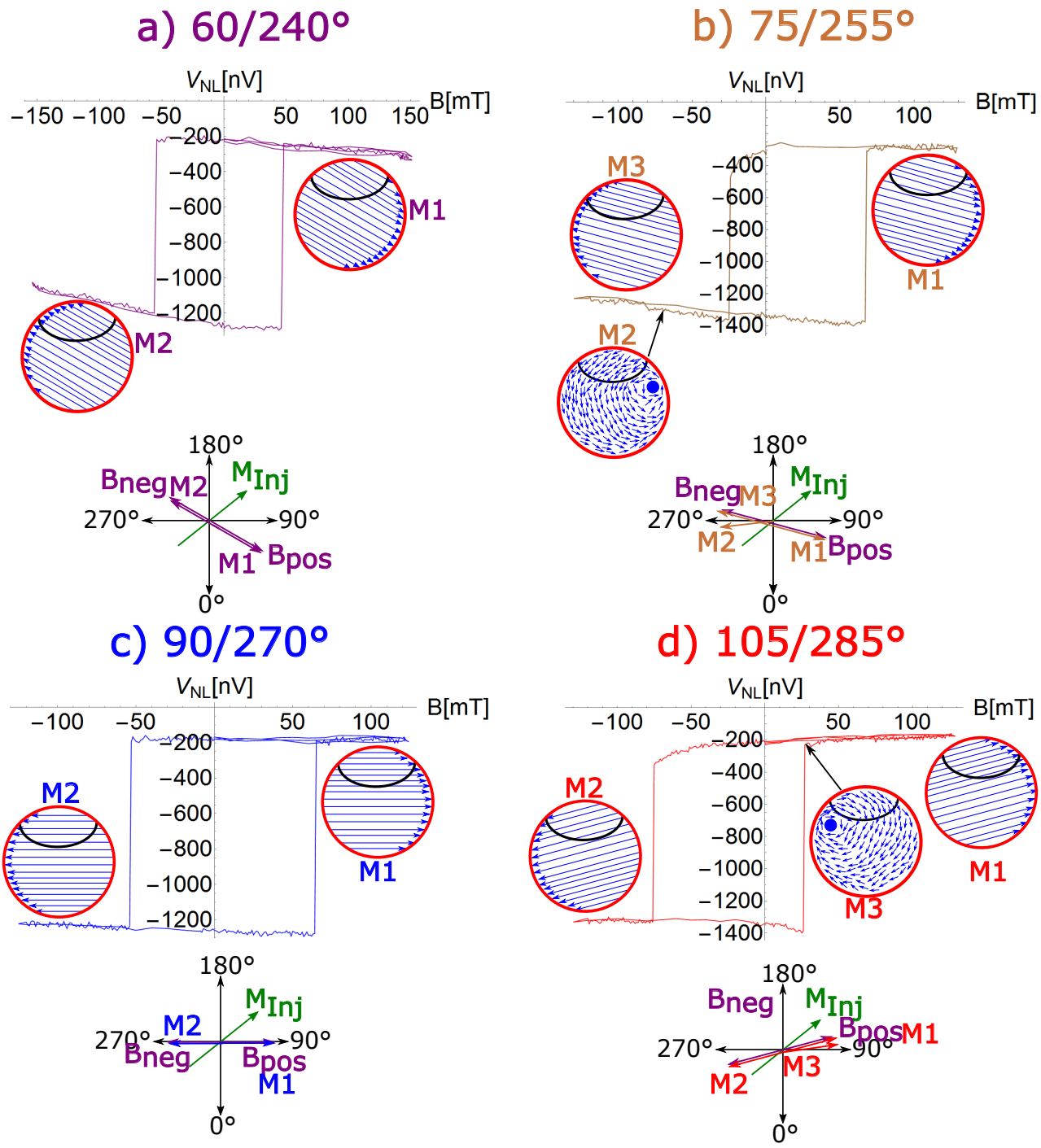

Fig. 3.8. Field dependent magnetization switching curves for field angles between 60 ° and 105 °.
a) Sweep along the 60/240 °-direction. In contrast to the 30/210 ° and the 45/225 ° case, no field dependent changes are observed. We find for each field direction one switching event at −48 mT and at +56 mT, respectively.
b) Sweep along the 75/255 °-direction. We observe one large jump at −25 mT, caused by the nucleation of a counter-clockwise vortex partly below the contact and a small jump at −83 mT, which indicates the mono-domain state. This state is stable up to an external field of +68 mT where the switching to the opposite mono-domain state occurs.
c) Sweep along the 90/270 °-direction. In total, two switching events are found, one at −54 mT and the other at +65 mT.
d) Sweep along the 105/285 °-direction. A gradual reduction of the signal by 150 nV in the field range between ±0 mT and −75 mT is observed. Two large switching events are found for external fields of −76 mT and +42 mT and a small jump, indicating the mono-domain state, is found for +55 mT.

Finally we analyze the results for sweeps along external fields angles between 120/300 ° and 165/345 °. Here we find for 120/300 ° and 135/315 ° external field angles, in both curves one large switching event for each field sweep direction, indicating either a mono-domain state to mono-domain state transition or a vortex state with the nucleation occurring too far away from the probed area. Since we find for an applied field angle of 135/315 ° no continuous changes of the signal with varying field and similar switching fields (−46 mT/+26 mT), we assume this switching to be a mono-domain state to mono-domain state switching. This is different for an applied field angle of 120/300 ° since here we observe for negative fields large continuous changes of the signal and the switching at −82 mT. This mono-domain state pointing along the 300 °-direction is stable up to +16 mT. As before, if the switching fields for the two field sweep directions vary much as in this measurement, it is likely to be a vortex state switching which can be however not detected.

For an applied field angle of 135/315 ° we do not find any continuous changes of the signal with varying field and observe the two large jumps at similar fields (−47 mT and +29 mT). For this field angle, either mono-domain state to mono-domain state switching is present or the vortex core nucleation/annihilation events occur so far away from the contact that the probed magnetization below the contact is not influenced.

For an applied field angle of 150/330 °, we start as usual with positive fields and we do not find any continuous changes of the signal, even at 0 mT. For negative fields, we find a small jump with a change of the signal of 200 nV at −60 mT. This jump can be explained by a nucleation of a clockwise-vortex at the edge of the disc. After the jump, we find a continuous decrease of the signal and then the large jump to the mono-domain state at −91 mT. This state is stable up to an external field of +41 mT where a large jump to the initial mono-domain state with the magnetization being aligned along 150 °. Also here we find large differences between the switching fields, which can be attributed to vortex nucleation/annihilation events.

In our last measurement we apply the external magnetic field along 165/345 ° and find for each field sweep direction two distinct jumps and continuous changes of the signal with varying field. As drawn, the first small jump for negative fields at −71 mT can be explained by a clockwise vortex and the observed jump is very similar to the 150/330 ° measurement, which is also indicated by the non-local signal which is in both cases −200 nV before and −400 nV after the jump. These measurements suggest again that the nucleation of the vortex occurs for similar field angles at the same defect, leading to very similar curves. As a result of the vortex nucleation, the magnetization below the contact M2 is oriented along 260 ° and, if we would drive a FORC measurement, we would expect an angle of 270 ° with the vortex core in the middle. The large jump to the mono-domain state is found at −84 mT and we find this state to be stable up to a positive field of +47 mT where again a small jump, leading to a change in signal of 200 nV, is found. This jump can be explained by a vortex, nucleated at the same position as the small jump for negative fields, yet with counter-clockwise chirality. The full mono-domain state is received at +70 mT.

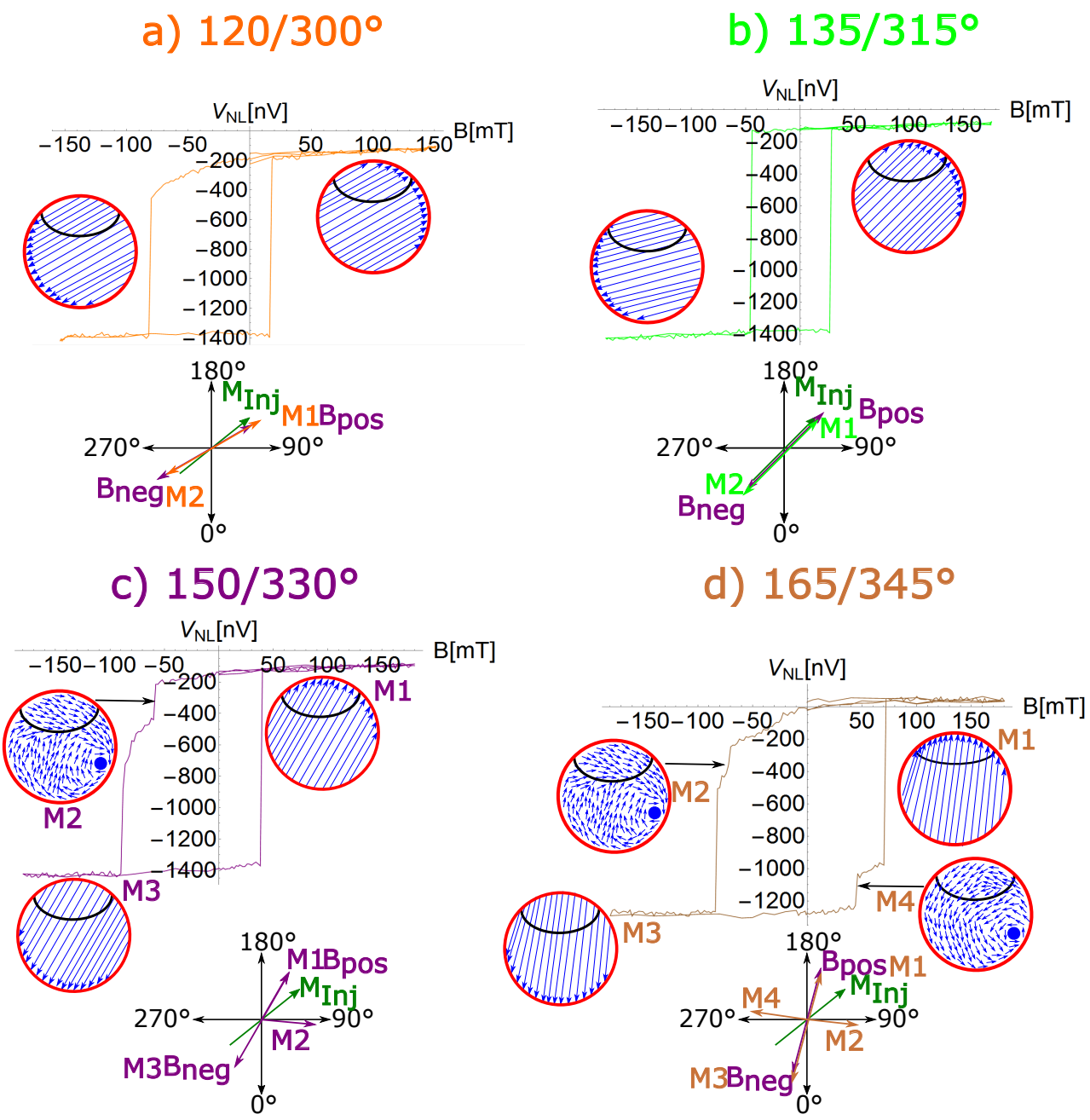

Fig. 3.9. Field dependent magnetization switching curves for field angles between 120 ° and 165 °.
a) Sweep along the 120/300 °-direction. A gradual reduction of the signal for negative fields is found, followed by an abrupt switching at −82 mT. For positive fields, an abrupt jump is measured at +16 mT.
b) Sweep along the 135/315 °-direction, where stable mono-domain states and two switching events at −46 mT and at +29 mT are observed. Here, the vortex core nucleation/annihilation events might occur at positions far away from the contact that the probed magnetization below the contact is not influenced.
c) Sweep along the 150/330 °-direction. In this measurement we find a stable mono-domain state pointing in the 150 °-direction with small field dependent changes down to a field of −60 mT, before an abrupt change in the non-local signal by 200 nV occurs. In the range between −60 mT and −90 mT we find a further gradual reduction of the non-local signal of 300 nV. The complete switching to the mono-domain state is found at −91 mT. For positive fields, we find one large jump at +42 mT.
d) Sweep along the 165/345 °-direction, where two distinct jumps for both field sweep directions are observed. We determine a field dependent reduction of the signal by 270 nV and at −72 mT, an abrupt reduction of the signal of 200 nV is found, followed by a gradual decrease of the signal and a large jump at −84 mT. We find this mono domain state being stable up to an applied field of +46 mT where the non-local signal changes abruptly by 200 nV followed by a continuous increase of the signal. The mono-domain state is found at a field of +72 mT.

From our detailed analysis of the different hysteresis curves, the different switching field and the sizes of the jumps, a number of points becomes apparent:

a) The energy landscape of the magnetization of the disc depends crucially on the applied field angle and can be broadly characterized by the number of switching events, which reveals the switching pathway, e.g. whether the mono-domain state switches to the opposing mono-domain state by vortex core nucleation/annihilation or by direct switching. Secondly, some measurements show a field dependent change of the non-local signal within one state before switching to the quasi-uniform state, which can be related to gradual changes of the vortex state, via e.g. a movement of the vortex core until it is located away from the contact. Since the non-local signal only probes the magnetization of the disc directly below the contact, motion of the vortex core sufficiently far from the contact does not significantly change the magnetization below the contact. By the size of the observed jumps, we are able to determine the chirality of the vortex states and also the nucleation point with some precision depending on the location. As explained in Section 3.3.2 in detail, reversible and irreversible changes of the non-local signal, as well as the stability of certain magnetic states at zero applied field, can be investigated via a first order reversal curve measurement scheme.

b) We emphasize here, that the orientation of the diffusive spin current pulses in the conduit only depends on the magnetization orientation of the injectors (which are fixed) and the polarity of the charge current pulses. To have a favourable configuration that both CoFe injectors can manipulate the magnetization switching of the mono-domain state of the disc, the chosen field angle should be either close to 0/180 ° or close to 90/270 °. In the alternative cases of 45/225 ° or 135/315 ° field sweeps the injector magnetization is either aligned parallel or orthogonal to the field sweep direction. In these situations, we expect that the spin transfer torque will be maximized for one injector but for the second it will be minimal, since the spin current orientation and the detector magnetization orientation will be collinear. This argument is supported by the formula of the damping like spin transfer torque, which is given by [161]

$$\vec{\tau} = -\frac{\hbar}{2e}\left(\vec{M} \times \vec{I}_s \times \vec{M}\right) \tag{3.1}$$

with $\vec{M}$ as the magnetization of the disc and $\vec{I}_s$ as the spin current orientation. It is mentioned that due to present metallic contacts, the field-like torques are expected to be significantly smaller than the damping like torques [161, 163]. Additionally the side of the disc where the vortex core nucleates is relevant in determining whether the spin transfer torque can assist the nucleation. Depending on the asymmetries and inhomogeneities of the disc which determine the core nucleation and spin current absorption locations, the generated spin currents can efficiently manipulate the magnetic state of the disc.

From this characterization for the cases without any assisting applied current pulses, both the field sweeps along the 0/180 °-direction and along the 90/270 °-direction are promising for a more focussed investigation. For the field sweeps along the 0/180 °-direction, we find in total four switching events, which enables the study of the impact of the spin transfer torque on the switching from a mono-domain state to the vortex state and vice versa. By sweeping the external field along the 90/270 °-direction, we observe two or three switching events. These switching events can be either connected to a mono-domain state to mono-domain state switching path or with a vortex core nucleation close to the contact. We will therefore study the hysteresis curves for different pulse polarities for field angles close to 0/180 ° and close to 90/270 °.

3.4. Current Assisted Switching For Field Angles Around 0 ° And 90 °

In this section, the influence of 10 μs current pulses between the injectors and the conduit on the field assisted switching of the disc for field angles along 0/180 ° and along 90/270 ° is studied. The employed

current densities are $7.6{\cdot}10^{11}\,\mathrm{A/m^2}$ (for the left injector) and $5.7{\cdot}10^{11}\,\mathrm{A/m^2}$ (for the right injector). The two directions of the applied external field are drawn for each measurement as brown arrows while the orientations of the generated spin current pulses are drawn as red arrows for Pulse Generator 1 and as a blue arrow for Pulse Generator 2. When positive pulses are applied by Pulse Generator 1, the orientation of the generated spin current is along 135 ° while for positive pulses applied by Pulse Generator 2, the spin current is oriented along 45 °.

For each applied field angle of 165/345 °, 0/180 °, 75/255 °, 90/270 ° and 105/285 °, we show in total four curves which correspond to different pulses schemes as presented in Figure 3.10, Figure 3.11, Figure 3.12, Figure 3.13 and Figure 3.14, respectively.

The blue curves are the measurements without any applied pulses. The red curves correspond to measurements with positive current pulses of $7.6{\cdot}10^{11}\,\mathrm{A/m^2}$ current density applied by Pulse Generator 1, while the orange curves are measurements with negative current pulses of $7.6{\cdot}10^{11}\,\mathrm{A/m^2}$ amplitude by Pulse Generator 1. Finally we show the measurements with positive pulses of $7.6{\cdot}10^{11}\,\mathrm{A/m^2}$ current density applied by Pulse Generator 1 and positive pulses of $5.7{\cdot}10^{11}\,\mathrm{A/m^2}$ amplitude applied by Pulse Generator 2 in green. In these measurements, we only draw the average magnetization for the vortex states without any pulses and with applied positive pulses from Pulse Generator 1, since the overall shape of all curves with applied current pulses does not depend significantly on the pulse orientation or on the number of used pulse generators. However, as is evident for all the sweep angles, there is clearly a strong influence on the magnetic switching behaviour of the disc when the pulses are applied as compared to the pure field induced switching case.

First, we study the influence of current pulses for a field sweep angle of 165/345 °, as shown in Figure 3.10. Comparing Figure 3.10a) with Figure 3.10b), Figure 3.10c) and Figure 3.10d), we clearly see an influence of the current pulses not only on the four switching events but additionally on the shape of the hysteresis curve. In Figure 3.10a), a gradual reduction of the non-local signal by 270 nV in the field range between ±0 mT and −71 mT is found and at −72 mT, an abrupt change of the signal of 100 nV is observed. In the other three measurements, we do not find a gradual reduction before the low field transition occurs but instead a stable mono-domain state up to a field of −8 mT where an abrupt jump of the signal of 70 nV is found. This difference could be possibly be explained by a change of the nucleation point of the vortex core.

In the measurement without any pulses, the vortex core nucleates relatively far away from the detection point very close to the edge of the disc. The magnetization below the contact M1 is in this measurement oriented along 80 °, which results in an angle between M_{inj} and M1 of 55 °. In the pulse assisted measurements, the nucleation could be triggered slightly closer to the nucleation point, which results in an average magnetization below the contact M1 of 100 °. This slight change of the magnetization orientation below the contact reduces the angle between M_{inj} and M1 and therefore the signal after the jump is higher, since we expect for a smaller angle a larger signal.

However, by a further increase of the negative field, we find a continuous reduction of the signal until the switching to the mono-domain state occurs. Since the initial non-local level in the measurement shown in Figure 3.10a) is different from the initial non-local level measured in the three other measurements (which indicates a different magnetization orientation of the detector), these states are different and a quantitative comparison of the switching fields is difficult.

This is different for positive external fields: Here, in all four measurements the mono-domain state is stable until the first jump occurs which is followed by a continuous, field dependent increase of the signal and finally we observe the full switching to the opposite mono-domain state. Also the signal before the jump occurs is in all measurements the same. We conclude that the nucleation occurs at the same points for the measurements with and without pulses, which demonstrates the importance of the exact nucleation point for the analysis of the switching fields. We emphasize again that all changes in the non-local signal are due to changes of the magnetization of the disc, indicating that lateral spin valves are a powerful tool to measure even small magnetization changes within the probed area.

However, in all measurements, the applied current pulses lead to a strong reduction of the first, small jump switching fields for both sweep directions. In Figure 3.10b) and Figure 3.10c), measurements

with the same current pulse amplitude but opposite polarities are shown. Here we find the switching field of the low field transitions to be largely independent of the current polarity for both field sweep directions and these high current densities. In general, we would expect the spin transfer torque to support the switching when the spin current has parallel components to the external field (positive pulses for positive fields and vice versa) and hinder the switching for antiparallel components (positive pulses for negative fields and vice versa).

However, in the first stage of the two level switching, a nucleation of a vortex core and the transition to the vortex state is observed which complicates this simple picture. Furthermore, depending on defects, the vortex core will nucleate at one or the other edge of the disc, which will determine whether or not the magnetization of the detector is changed significantly. The vortex core then moves across the structure and is annihilated at the opposite edge at higher fields [222]. The independence of the switching field on the applied pulse polarity demonstrates that the details and location of the nucleation of the vortex core at the edge of the disc plays a critical role for the efficiency of the spin transfer torque manipulating the switching behaviour. Since the spin diffusion length in Py is only a few nm [152, 153], the spin transfer torque will only act very locally on the detector magnetization with respect to the injection point.

As a consequence, only for a nucleation below the contact, the spin transfer torque can effectively manipulate the switching. As a surprising result we do not find any difference in the switching field if additionally Pulse Generator 2 is used as shown in Figure 3.10d) where the first negative switching field is also determined to be $-8\,\mathrm{mT}$.

As shown in Figure 3.3 the spin signal from the right CoFe wire is significantly smaller than the spin signal from the left CoFe wire for the same applied current. Nevertheless, the charge current densities for the two injectors in these measurements are comparable. If Joule heating would be the dominant effect, we would expect that the switching field of the measurement shown in Figure 3.10d) would be significantly smaller than the switching field determined in Figure 3.10b) and Figure 3.10c) due to additional heating from the second injector, which has not been observed here.

An equivalent device behaviour is seen for the first jump for positive fields, where we also observe in all three measurements with applied pulses a switching field of $+12\,\mathrm{mT}$, independent of the total charge current density and the pulse polarity.

What does indeed differ for the different cases are the two second switching events. We find for positive pulses the switching field at $-44\,\mathrm{mT}$, while for negative pulses we determine the switching field to be at $-70\,\mathrm{mT}$. It turns out that for both external field directions, the second, large switching events can differ significantly for nominally the same measurements with the same applied current pulses. These differences in the switching fields are much larger than can be explained by statistical fluctuations. A similar behaviour has been studied in literature [228, 237]. In Section 3.5.3 we study these second switching events in detail.

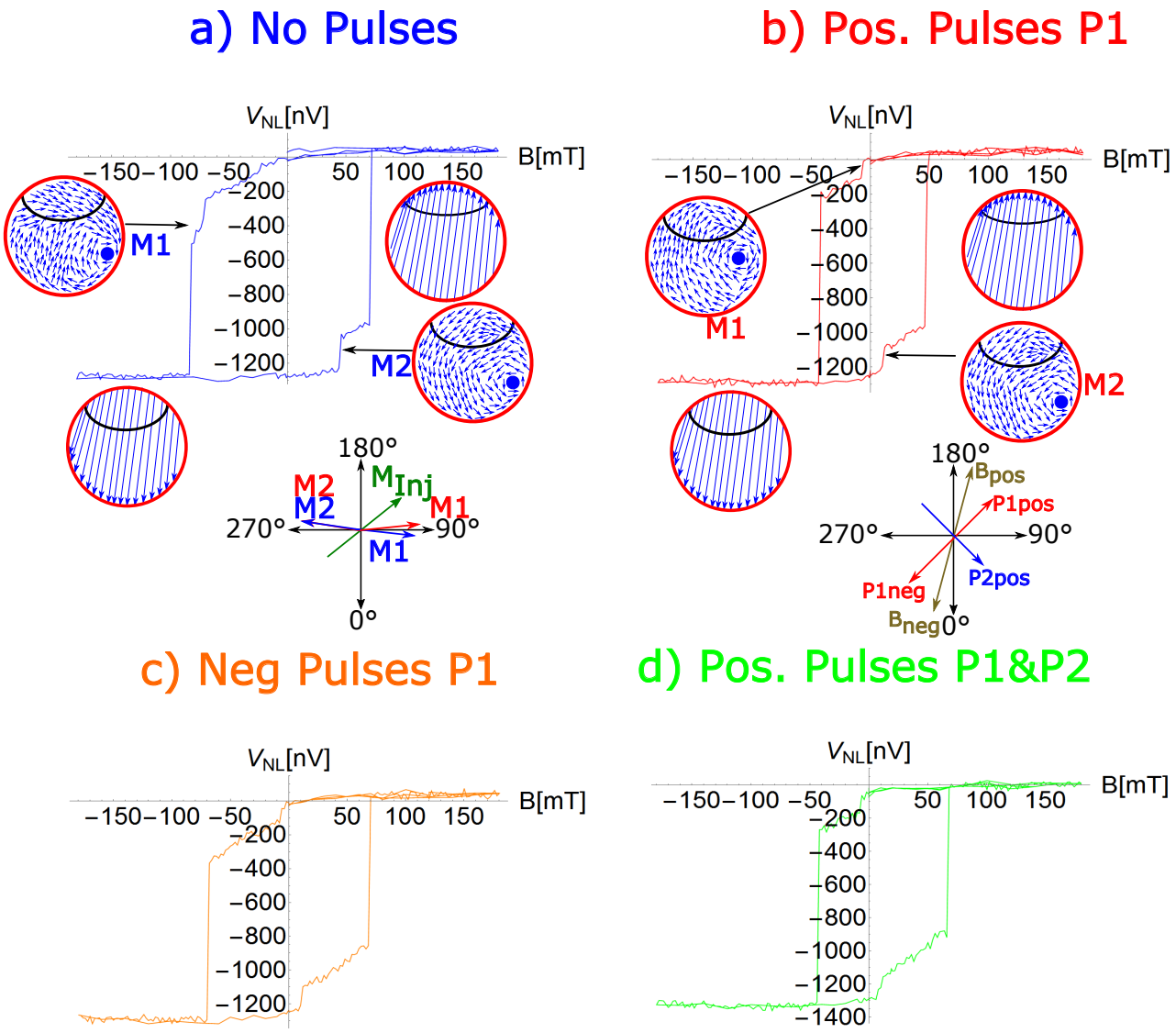

Fig. 3.10. Sweep along the 165/345 °-direction for certain applied pulse schemes. For this field sweep direction, we find four different jumps indicating transitions of mono-domain states to the vortex state and vice versa. Starting with positive fields, we stabilize the mono-domain state pointing along the 165 °-direction. The first, small jump for negative fields then indicates the nucleation of a vortex core with clockwise-chirality while the second, large, jump in the non-local signal is the full switching to the reverse mono-domain state. For positive fields we identify the first small jump at lower fields as the nucleation of a counter-clockwise vortex (yet at a similar position as the vortex for positive fields) and the large jump at higher fields as the switching to the mono-domain state.
a) Measurement without any applied current pulses. The four switching fields are determined to be −72 mT, −84 mT, +46 mT and +72 mT. Prior to the first switching event at negative fields, a gradual reduction of the signal by 270 nV is found.
b) Measurement with positive applied current pulses by Pulse Generator 1. In this situation we find the four switching events at −8 mT, −44 mT, +12 mT and +50 mT.
c) Measurement with negative current pulses applied by Pulse Generator 1. We measure the four switching events at external fields of −8 mT, −70 mT, +12 mT and +70 mT.
d) Measurement with positive current pulses applied in both injectors. We observe the four jumps at fields of −8 mT, −44 mT, +12 mT and +70 mT.

Next we discuss the measurements for an applied field angle of 0/180 ° and show the results in Figure 3.11. As a first result, we find a reversal in the order of the large and small switching events going from maximum positive fields to negative fields by the application of current pulses, which can

be contributed to vortex nucleation events with difference chirality.

In Figure 3.11a), we find the large jump at −18 mT and the small jump at −86 mT. In the other three measurements, we observe first the small jump and for higher negative fields the complete switching to the mono-domain state. These measurements show that the overall reversal process including different types of switching of the Py disc can be manipulated by current pulses. We note that in the three latter measurements the first switching event always occurs at −10 mT. This result can be interpreted as follows:

The spin transfer torque, together with local heating, can change the nucleation point and the chirality of the vortex core depending on the nature of the defect. For a strong defect, it is likely for the nucleation to occur at that side of the disc [222]. In the present situation, current pulses can assist the nucleation to occur at a different point and as a result this leads to a change of the chirality. In our measurements, we find for the situation without any assisting current pulses (Figure 3.11a)), the nucleation to be occurring at an applied field of −18 mT and a clockwise chirality of the vortex, while in the other measurements, the nucleation is found at −10 mT with a counter-clockwise chirality of the vortex. Due to the application of the current pulses, the position of the nucleation as well as the chirality of the vortex changes, which leads to different sizes of the jumps.

By comparing the first of the low switching fields shown in Figure 3.11b), Figure 3.11c) and Figure 3.11d), we note that they are equivalent and independent of the total applied spin current and the current polarity. As before this result indicates that the exact nucleation point and the chirality of the vortex core are crucial for the size of the jump and will determine whether the switching behaviour can be manipulated by the spin transfer torque. For the second switching event, we find comparable switching fields of −40 mT if only Pulse Generator 1 is used or −38 mT if both Pulse Generators are used. As in the 165/345 °-measurements, different switching paths occur for the second, large switching events.

Interestingly, the total number of occurring jumps is different in these measurements. In Figure 3.11a), for positive fields in total four switching events are observed at +22 mT, +62 mT, +100 mT and +122 mT. In Figure 3.11b) and Figure 3.11c), three jumps at fields of +8 mT, +44 and +52 mT and +8 mT, 34 mT and +50 mT are found, respectively. In Figure 3.11d) only two jumps for positive fields at +6 mT and at +80 mT are observed. Since the voltage levels for the first switching events are equivalent, we can compare these jumps and identify them as levels with the vortex being partly below the contact. The varying number of jumps indicates a different switching behaviour for the three different scenarios, probably corresponding to different pinning sites of the vortex core as it traverses the disc.

We treat the four measurements here as three scenarios since the second jumps in Figure 3.11b) and Figure 3.11c) have the same non-local resistance level (which means the same detector magnetization) and therefore are understood as equivalent. We also note that the second jump in Figure 3.11a) starts from the same non-local level, which can be understood as follows:

In Figure 3.11a), the vortex core moves from defect to defect, which act as pinning centres until the vortex core is annihilated at the other edge for +122 mT. In Figure 3.11b) and Figure 3.11c), the vortex core gets pinned at defects but the spin transfer torque together with Joule heating is strong enough to completely depin and annihilate the vortex core for much lower fields. In Figure 3.11d), only two switching events are found and no intermediate pinning centres are observed, which can be attributed to the additional spin torque effect and Joule heating acting on the local magnetization of the disc. Since the switching fields (of the second small switching event for positive fields) in Figure 3.11b) and Figure 3.11c) differ by 10 mT and the same Joule heating is present, this difference in depinning from the defect can possibly be attributed to the spin transfer torque.

Since the results of the measurements for an applied field angle of 165/345 ° and of 0/180 ° are similar, we conclude again that the energy landscape of the Py disc is mainly governed by inhomogeneities. As a consequence, similar field angles lead to similar results because the nucleation of the vortex core is triggered and controlled by similar inhomogeneities. Depending on the chirality of the vortex and the exact nucleation point, the magnetization of the probed area changes differently for different applied

field angles and a different number of jumps is observed.

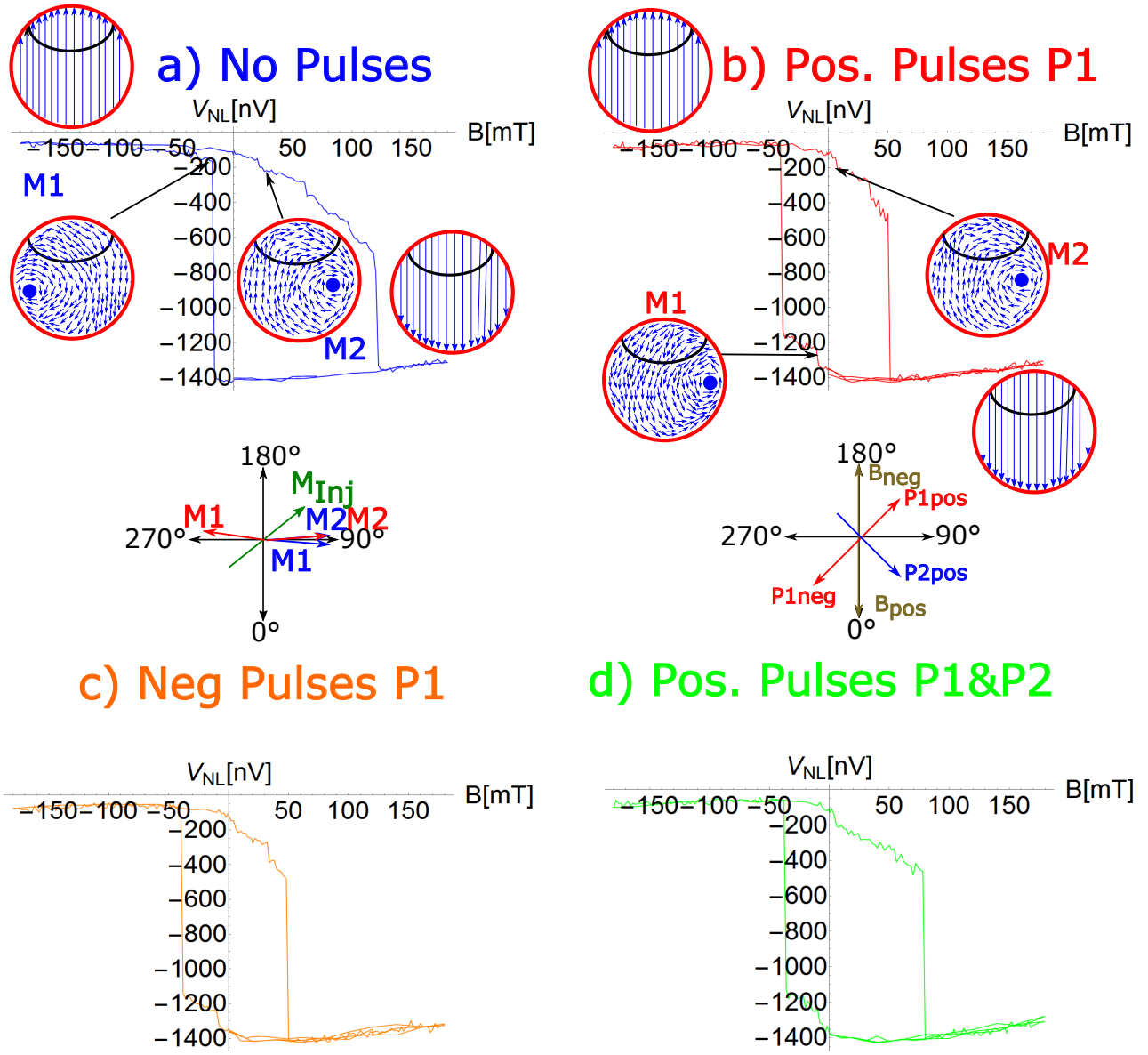

Fig. 3.11. Sweep along the 0/180 °-direction for certain applied pulse schemes. For this external field angle, we observe reversibly different switching paths depending on whether current pulses are applied or not. By the application of high current pulses, the nucleation position of the vortex core as well as its chirality changes which leads to different magnetization orientations of the disc for the different measurements which can be detected as different heights of the jumps. We expect the first small jump at positive fields for each measurement to be caused by a clockwise vortex nucleation at the same position since the signal before and after the jump is the same for all measurements.
a) Measurement without any applied current pulses. We find a large switching event at −18 mT due to the nucleation of a clockwise vortex and a small jump at −86 mT. For positive fields, we find small jumps within a gradual decrease in signal at fields of +22 mT +61 mT and +100 mT before the large jump occurs at +122 mT.
b) Measurement with positive current pulses applied by Pulse Generator 1. In this situation we find the small jump first (due to the nucleation of a counter-clockwise vortex) at a field of −10 mT and the large jump at −40 mT. For positive fields we find two small jumps (+8 mT and +44 mT) and the large jump at +52 mT.
c) Measurement with negative current pulses applied by Pulse Generator 1. The small jump for negative field is observed at −10 mT and the large jump is found at −40 mT. For positive fields, as in b) two small jumps at +6 mT and at +34 mT are determined while the large jump is measured at +50 mT.
d) Measurement with positive current pulses applied in both injectors. Here we observe in total four switching events which are determined to be −10 mT, −38 mT, +6 mT and +80 mT.

We will now study the results for the four different cases with applied external field angles of 75/255 °, 90/270 ° and 105/285 °, as shown in Figure 3.12, Figure 3.13 and Figure 3.14. As before for the 0/180 ° and the 165/345 °-direction (Figure 3.11 and Figure 3.10) we observe a similar switching behaviour for similar field angles, emphasizing the role in angle dependent inhomogeneities for the determination of the probed magnetization below the contact.

We first consider the results for an external field sweep direction of 75/255 °, as shown in Figure 3.12. We note that we observe single step switching in those measurements with applied pulses while in Figure 3.12a) we observe two jumps, one very large and one very small jump. As explained before, the first, large jump can be explained by a counter-clockwise vortex core nucleation partly below the contact while the second, very small jump, can be attributed to the full mono-domain state. This is different for measurements with applied pulses. As shown in Figure 3.12b), Figure 3.12c) and Figure 3.12d), the application of current pulses leads to abrupt jumps of the signal without any gradual changes by varying field. We conclude that these jumps represent real mono-domain to mono-domain switching events since the measured switching fields are very similar for the two field sweep directions ($-45/+43$ mT, $-45/+42$ mT and $-44/+42$ mT). We expect, as explained before, similar switching fields for mono-domain state to mono-domain state switching due to time reversal symmetry. By the application of sufficient strong current pulses, we are able to stabilize the mono-domain state (no field dependent gradual reduction of the signal is observed) and find pure mono-domain state to mono-domain state switching.

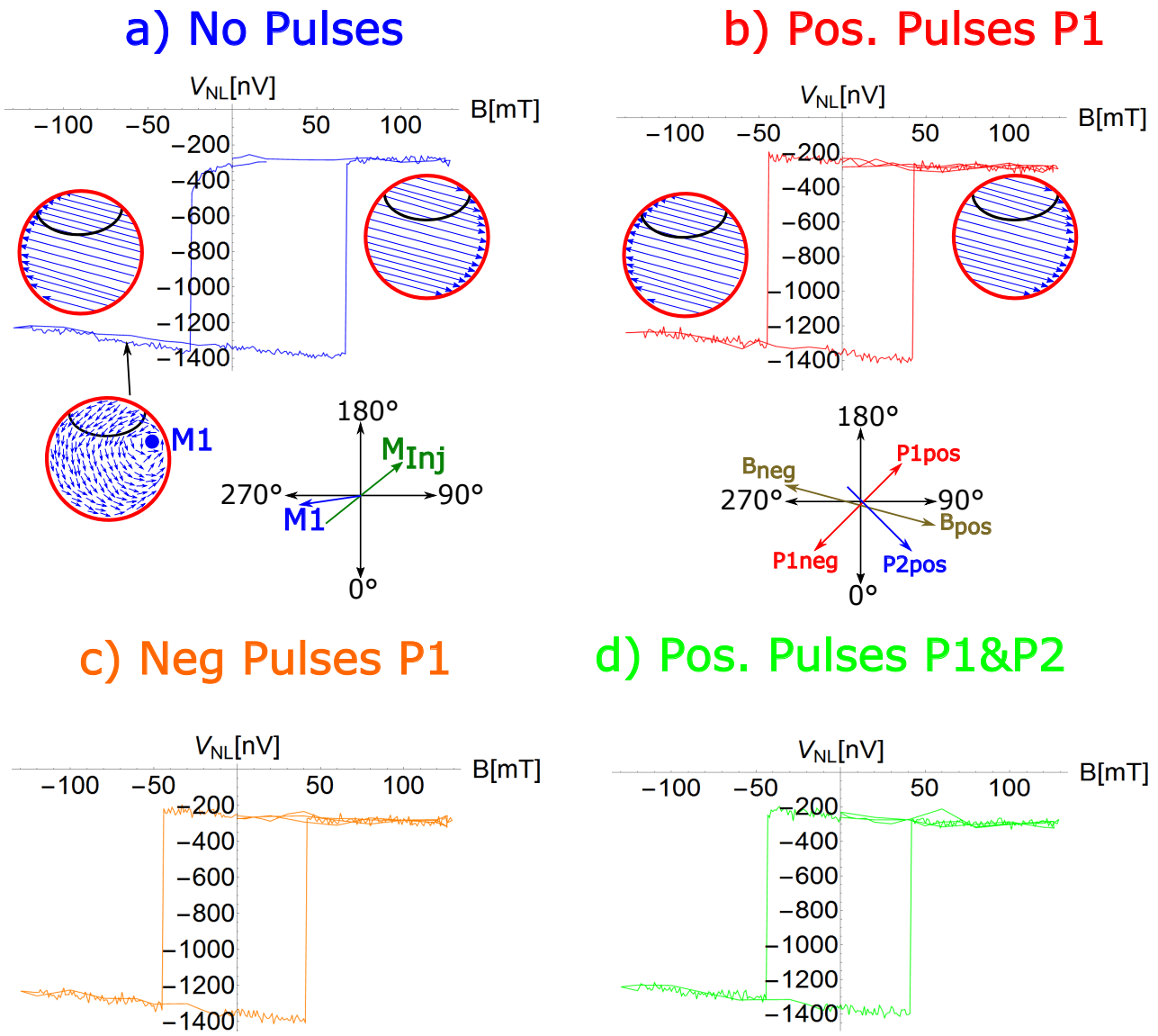

Fig. 3.12. Sweep along the 75/255 °-direction for certain applied pulse schemes. By the application of strong current pulses, we observe similar switching fields for the two field sweep directions, which is due to time reversal symmetry a strong argument for mono-domain to mono-domain state switching.
a) Measurement without any current pulses. For negative fields, a reduction in signal is found before the large switching event occurs at −25 mT. This state can be attributed to the nucleation of a counter-clockwise vortex partly below the contact. A very small jump, indicating the mono-domain state is found at −83 mT. For positive fields, one large jump at +68 mT is observed.
b) Measurement with positive current pulses applied by Pulse Generator 1. Two large jumps are found at −45 mT and +43 mT, indicating mono-domain state to mono-domain state switching.
c) Measurement with negative current pulses applied by Pulse Generator 1. Two switching events are found for external fields of −45 mT and +42 mT.
d) Measurement with positive current pulses applied in both injectors. As in b) and c), we find for each field sweep direction one large switching event. The determined switching fields are −44 mT and +42 mT.

In the measurements with an applied field angle of 90/270 ° as shown in Figure 3.13, we can summarize the results as follows:

In all four measurements, a switching from one mono-domain state to the opposite one is observed for negative fields. With applied current pulses a reduction of the switching field by 13 mT is found which is independent of current polarity or Joule heating, since in all three measurements with applied

pulses (Figure 3.13b), Figure 3.13c) and Figure 3.13d)), we observe the switching at −41 mT. This is different for positive fields. Here the switching field changes drastically by the application of current pulses:

On reducing negative fields from −50 mT to 0 mT we find a reduction of the signal by 200 nV, while in Figure 3.13a), where no current pulses are applied, no change of the signal has been found in this region. The reduction of the signal can be explained by the nucleation of a vortex core with counter-clockwise chirality at the bottom end of disc which is triggered due to the current pulses. Due to the nucleation of the vortex, we find a massive reduction of the switching fields by the application of current current pulses. In Figure 3.13a), we find the switching at +65 mT, while in the measurements with pulses, we find the switching at +5/6 mT. Once again these results demonstrate that (small) changes in the detector magnetization, due to vortex nucleation/annihilation events, can lead to drastic changes of the switching fields.

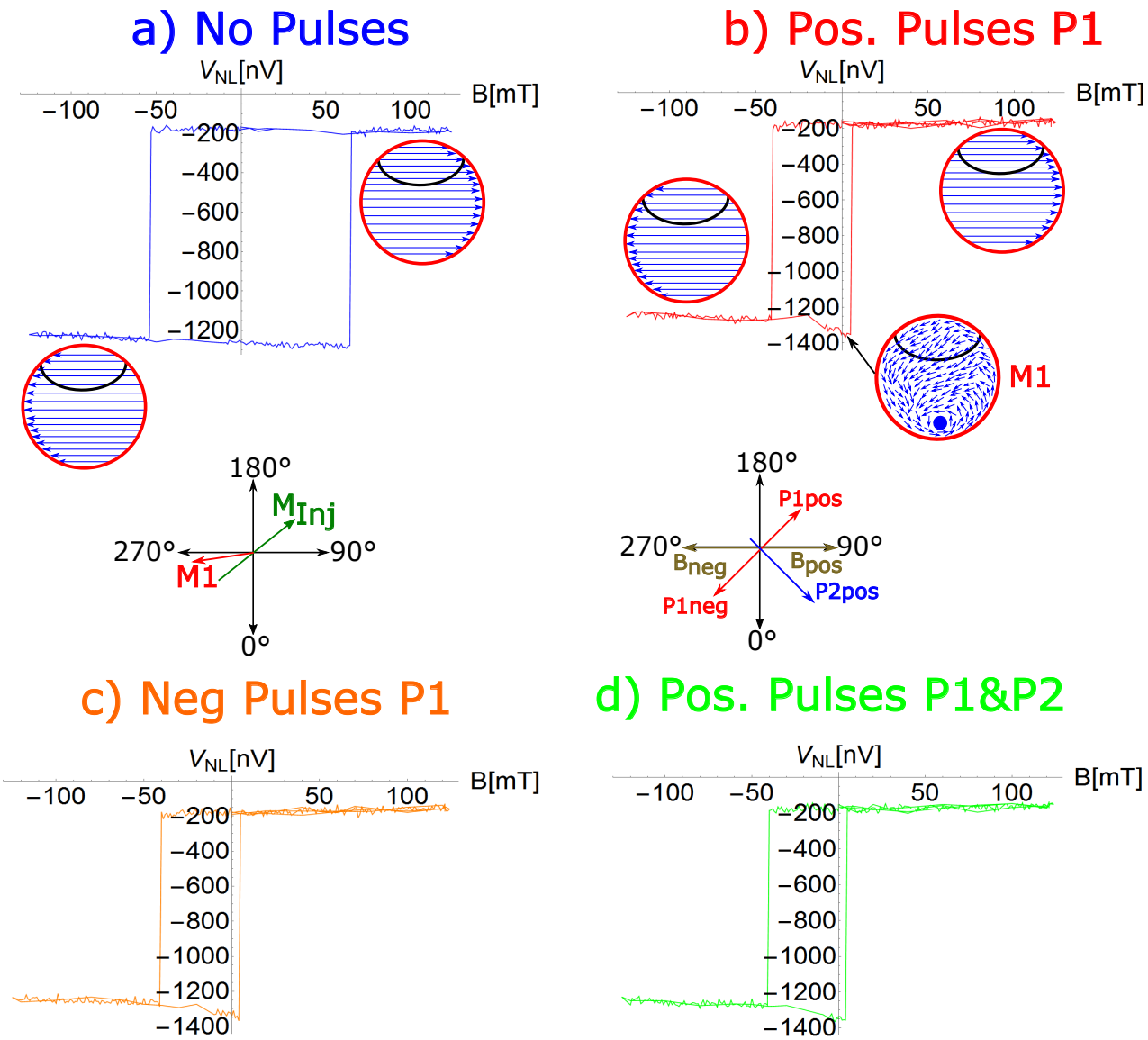

Fig. 3.13. Sweep along the 90/270 °-direction for certain applied pulse schemes. For this applied field angle, the application of current pulses reduces the switching fields along the 270 °-direction drastically, which can be explained by the nucleation of a vortex core with counter-clockwise chirality at the bottom edge of the disc.
a) Measurement without any current pulses. Two mono-domain state to mono-domain state switching fields are observed for external fields of −54 mT and +65 mT.
b) Measurement with positive current pulses applied by Pulse Generator 1. We find a small reduction of the signal by decreasing the field from −50 mT to 0 mT which can be explained by the nucleation of a counter-clockwise vortex core at the bottom edge of the disc. Two switching events at −41 mT and +6 mT are found which means a small reduction of the switching field for negative fields and a very strong reduction of the switching field for positive fields compared to a) as the situation without any assisting current pulses.
c) Measurement with negative current pulses applied by Pulse Generator 1. Here the switching fields are determined to be −41 mT and +5 mT.
d) Measurement with positive current pulses applied in both injectors. In this case, two switching fields are observed for −41 mT and +5 mT.

Finally we study the results for an external field sweep direction of 105/285 °, as plotted in Figure 3.14. Also for this field angle, the application of current pulses leads to changes of the initial magnetization orientation, which leads to significant changes of the switching pathway and can be

identified by small changes of the initial non-local level.

In Figure 3.14a) a field dependent reduction of the signal of 150 nV in the field range between ±0 mT and −75 mT is found before the switching occurs at −76 mT. Furthermore, we note that the non-local signal is −200 nV at zero field if the magnetization of the disc is aligned parallel to the positive external field. In the other measurements where pulses have been applied, there is a small increase of the signal of 50 nV as the field is decreased from +30 mT to ±0 mT indicating very small changes of the detector magnetization by a reduction of the field. As a result, the initial detector magnetization is different compared to the measurement without any applied current pulses. We then find in all three measurements with applied pulses a very large jump at −11 mT, which can be explained by a nucleation of a counter-clockwise vortex partly below the contact. The full mono-domain state is then however very difficult to exactly determine since the signal difference between the vortex state and the mono-domain state is only 40-50 nV. We can estimate that the full mono-domain state is found for roughly −40 mT.

This mono domain state is stable in the measurement without any pulses (Figure 3.14a)) up to +26 mT where a vortex state with similar nucleation point, yet with clockwise chirality is found. For the measurements with applied pulses, we find the same vortex state and observe a reduction of the switching field to +6/7 mT. As in the 75/255 ° and in the 90/270 °-measurements, the switching fields for the two field sweep directions as well as the switching fields with and without current pulses differ drastically if vortex core nucleation/annihilation events are triggered by the current pulses.

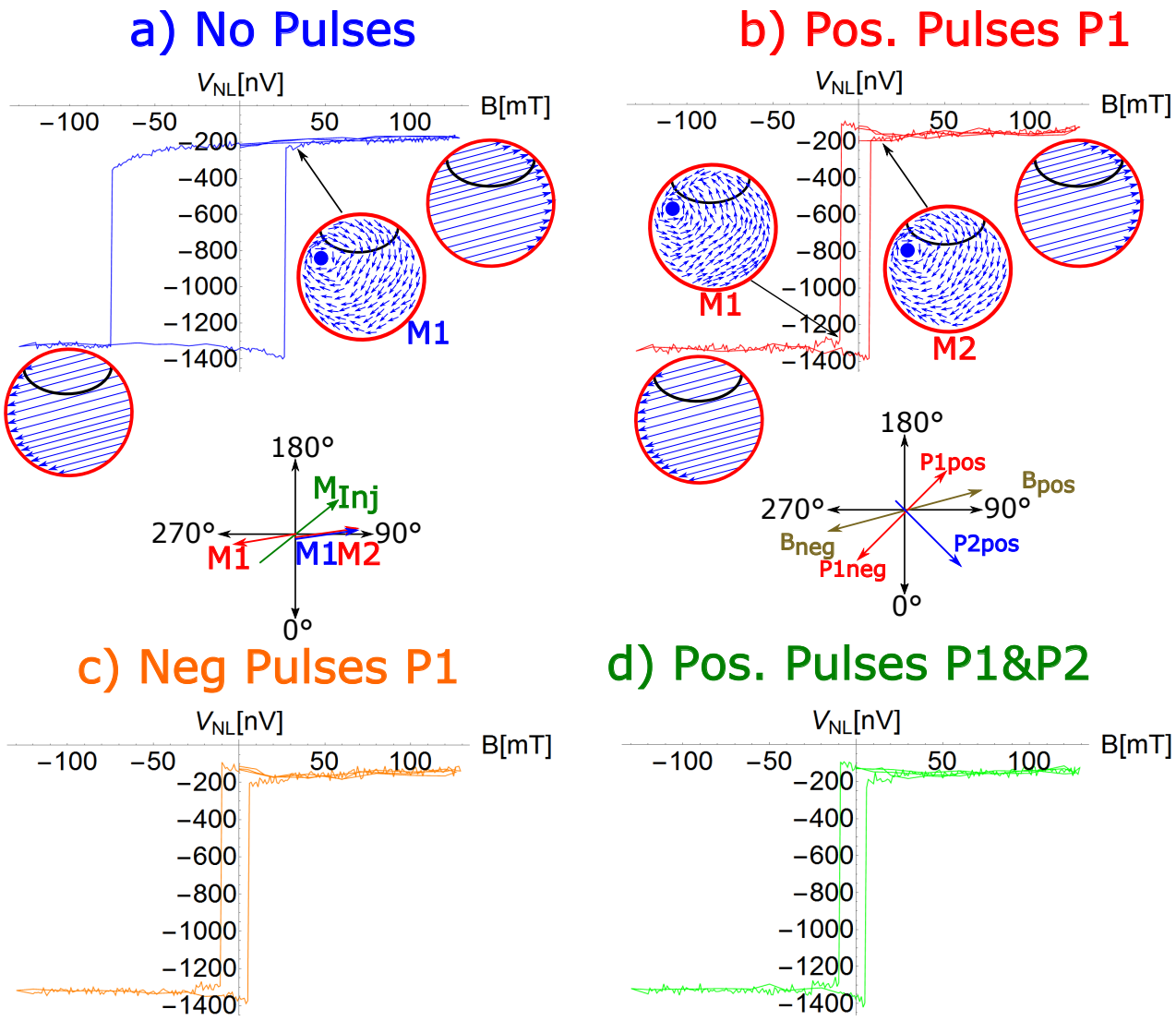

Fig. 3.14. Sweep along the 105/285 °-direction for certain applied pulse schemes. The shape of the hysteresis depends strongly on the initial detector magnetization orientation and can be manipulated by applied current pulses.
a) Measurement without any applied current pulses. For negative external fields, we find one switching event −76 mT. Prior to the switching, we find a field dependent reduction by 200 nV in the field range of ±0 mT and −75 mT. For positive fields, we observe one very large jump at +26 mT which can be explained by a nucleation of a clockwise vortex partly below the contact. The full mono-domain state however is very difficult to determine. We observe a very small jump at +55 mT, which we connect to the mono-domain state.
b) Measurement with positive current pulses applied by Pulse Generator 1. We find one very large jump at −11 mT and one very small jump at −26 mT. For positive fields, one jump at +7 mT is observed. Here we do not see any differences for positive fields between the vortex state and the mono-domain state.
c) Measurement with current negative pulses applied by Pulse Generator 1. Here the switching events are observed at −11 mT, −26 mT and at + 6mT.
d) Measurement with positive current pulses applied in both injectors. The switching fields are found at −11 mT and −26 mT for negative fields and at +6 mT for positive fields.

To summarize the results shown in Section 3.3 and Section 3.4, we have shown that the lateral spin valve geometry allows for a precise study of small magnetic elements, e.g. a Py disc, since the non-local signal is very sensitive to magnetization changes within the probed area. By the application of an external field in different directions, we are able to study different switching paths, e.g. mono-

domain to mono-domain switching events or vortex state to mono-domain state switching events. The exact details on the switching paths, transition fields and associated energy barriers for the different processes crucially depend on the chirality of the vortex and on the exact nucleation and annihilation points which are determined by defects within the disc or by edge roughness.

We have furthermore shown that the detector magnetization (which can be read out as the non-local signal at zero field) and as a result, the switching behaviour, can be strongly modified by the application of current pulses and the resulting spin transfer torque and Joule heating, which can lead to drastic changes of the measured switching fields due to nucleation/annihilation of a vortex state. Since the influence of the spin transfer torque depends very strongly on the exact magnetization configuration below the contacted area due to short diffusion length of Py, we expect the spin transfer torque in these measurements to have a modest but detectable influence.

To study the spin transfer torque in detail and distinguish between this effect and Joule heating, we measure the mono-domain state to vortex state switching of the Py disc for an external field angle of 351/171 ° which turned out to be particularly convenient. For this field angle, we do not observe any changes of the initial detector magnetization orientation at zero field by the application of current pulses as seen e.g. for field sweeps along 0/180 °. This stability of the initial state as well as the (meta)-stability of the vortex state at zero applied field plays a vital role in the switching behaviour, which has also been confirmed by first order reversal curves and explained in detail before. For this field angle, we show results for the current assisted mono-domain state to vortex state switching events as a function of the current density (first, low field switching events) for the positive and negative field sweep direction in Section 3.5.2. Finally, we study the second, high field switching events which can be identified as vortex state to mono-domain state switching events in Section 3.5.3.

3.5. Switching Fields As A Function Of The Applied Current Density

3.5.1. Representative curves and data analysis

For the measurements presented in this section, the external field is swept at an angle of 351/171 ° and the four switching events are detected as a function of the current density and polarity. In general, in the whole applied field angle range between 345/165 ° and 06/186 ° a similar switching behaviour with four or more distinct jumps has been observed. The field angle of 351/171 ° is chosen since for this field angle, the measurements have shown the most robust and reproducible switching behaviour. We first show in Figure 3.15 six representative plots with positive pulses of different current density from Pulse Generator 1. These measurements have been repeated with identical pulse amplitudes several times to achieve robust statistics and are shown to exhibit large differences between the nominally identical measurements. This is in contrast to the previous measurements for no or large applied pulses, where more reproducible switching paths were seen as presented and discussed in the previous sections.

We emphasize here again that although the curves show different switching fields, which can be identified as different switching paths, the overall shape for this applied field angle is robustly similar. In all measurements, there is a large probability that four or more jumps are observed in total. However, similar large differences in switching and depinning fields have been intensively studied in the literature [228, 237–239]. In a simple model, such depinning (in our case the depinning of the vortex core) experiments have been understood as resulting from thermal activation with the characteristic activation time being described by an Arrhenius law, similar to the switching of a single magnetic particle [240]. In such a simple model, the depinning/switching field distribution should show a single peak [241]. Briones et al. however demonstrated that the depinning probability can be rather complex and shows multiple peaks as also seen for the second (high field) switching path events in this study. This is indicative of different potential switching pathways in addition to a thermal distribution in switching fields.

We notice that in some measurements, three switching events for one field direction are observed and in some measurements just two. If three switching events are found, the vortex core initially nucleates, changing the magnetization partly below the contact. However instead of a continuous displacement by

the field across the disc, it likely becomes pinned by a defect and subsequently depins to a new position in a stepwise transition. In all six shown measurements, the large jump in the non-local signal (for both sweep directions) at high fields indicates a transition from the vortex state to the mono-domain state.

In the case of the curves shown in Figure 3.15a) and Figure 3.15b), we determine the switching fields to be $-27/-53/-69/+22/+52/+63\,\mathrm{mT}$ and $-24/-53/-63/+15/+50\,\mathrm{mT}$, respectively. In these measurements, no current pulses have been applied. These examples indicate that the switching field for the first switching event for both negative and positive field values can vary significantly, although the same initial configuration with the same stable mono-domain state is present. The variation of the first, lower switching field is reduced for larger pulse amplitudes, as can be seen as smaller error bars in Figure 3.16 and Figure 3.17.

If we compare the measured second switching fields, we note that these switching events to the mono-domain state are found for either $-69\,\mathrm{mT}$ or $-63\,\mathrm{mT}$. The positive switching events to the mono-domain state are found for fields of $+63\,\mathrm{mT}$ and $+50\,\mathrm{mT}$, indicating large variation in the switching events. This becomes more evident in Figure 3.15d) and Figure 3.15e) where the results for applied pulses corresponding to a current density of $4.3{\cdot}10^{11}\,\mathrm{A/m^2}$ are presented. Here we determine the switching fields to be $-12/-80/+8/+42/+56\,\mathrm{mT}$ and $-12/-44/+9/+41/+52\,\mathrm{mT}$. Although in both measurements the same number of switching events is observed, the switching fields to the mono-domain state differ drastically in the case of negative fields.

For very high current pulses, the situation is a bit easier. In these measurements only two jumps are seen for one field sweep direction, suggesting a role of the spin torque or associated Joule heating in helping to depin the vortex core, as exemplary shown in Figure 3.15f). Here we only find large differences for the second jump for each field sweep direction, which is explained and analysed in detail in Section 3.5.3. In order to take into account these differences, the analysis is performed as follows:

a) For each current density and polarity between four and six measurements are performed.

b) The first jumps for each field sweep direction are assumed to start from the same initial magnetization configuration as set at high fields, since no changes of the non-local signal are determined on reducing the field to zero. The errors are determined by the standard derivation. In general this yields a relatively high statistical error for low amplitude current pulses and a small standard derivation for high amplitude current pulses. If no error bar is drawn, it means that for the particular current density, all switching events are found in the same applied field range of 1 mT which is sometimes observed for high amplitude current pulses.

c) For the final transition to the mono-domain state, all large jumps are taking into account if they do not differ by more than 5 mT. Within this range, all jumps which belong to a certain switching path are selected, while the jumps belonging to a second switching path show a much higher/lower switching field which can not be explained by statistical fluctuations and therefore are not selected. As later shown in detail, the low field switching path (for both positive and negative external fields) results in switching fields of approximately $\pm 40\,\mathrm{mT}$ while the high field switching path means switching fields of approximately $\pm 70\,\mathrm{mT}$ for high amplitude current pulses. For current pulses below a certain threshold of roughly $5{\cdot}10^{11}\,\mathrm{A/m^2}$, these two switching paths are not observed. For a given path, the switching fields vary typically by $\pm 3\,\mathrm{mT}$ or less for a given current density, which means all relevant data points are taken into account with our chosen range of 5 mT. If no error bars are drawn, only one measurement curve belongs to the low field switching path or all obtained switching fields are equivalent within our chosen field range of 1 mT.

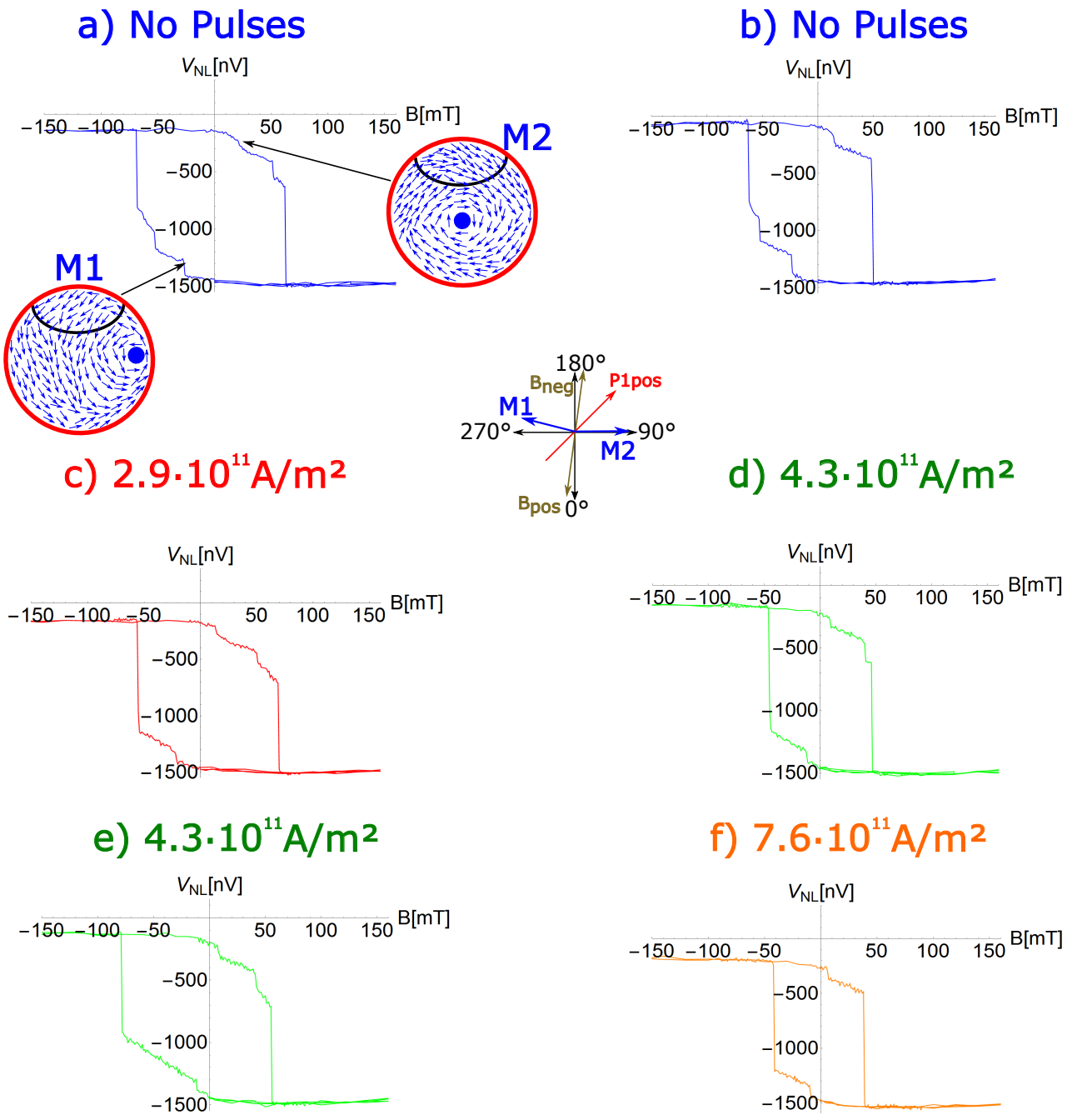

Fig. 3.15. Field Sweep curves along 351/171 °. Measurements with the same applied current densities are shown in the same colour.
a), b) Measurements without any current pulses. In case a) we find three jumps for negative fields of −27 mT, −53 mT and −69 mT and three switching events for positive pulses of +22 mT, +52 mT and +63 mT. In measurement b) three jumps for negative fields of −24 mT, −53 mT and −63 mT are observed while for positive fields, two jumps at +15 mT and 50 mT are found.
c) Measurement with applied current pulses corresponding to a current density of $2.9{\cdot}10^{11}$ A/m^2. Two jumps for negative fields are found at −21 mT and −56 mT. For positive fields, we observe three switching events at +14 mT, +51 mT and +70 mT.
d), e) Measurements with applied current pulses corresponding to a current density of $4.3{\cdot}10^{11}$ A/m^2. Five switching events are observed for both measurements. In d) we determine the switching fields to be −12/−79/+8/+42/+56 mT. In case e) we find the switching events at −12/−46/+10/+41/+47 mT.
f) Measurement with applied current pulses corresponding to a current density of $7.6{\cdot}10^{11}$ A/m^2. In this situation four switching events at −10 mT, −42 mT, +7 mT and +39 mT are found.

3.5.2. Analysis of the first switching event for negative and positive fields

In this subsection, the results for the first switching events for both field directions are shown as a function of the applied current density. In both Figure 3.16 and Figure 3.17 we present the results as follows:

- In total four different plots for each figure are shown.
- The first plot a) of each figure shows the results with positive (negative) pulses applied by Pulse Generator 1 in red (blue).
- The second plot b) shows the results with positive (negative) pulses applied by Pulse Generator 2 in green (orange).
- In the third plot c), the measurements with pulses of similar amplitudes but different polarities are shown. The results for positive (negative) pulses applied by Pulse Generator 1 and negative (positive) by Pulse Generator 2 are shown in purple (brown).
- In the fourth plot d) measurements are shown with a pulse amplitude ratio of about 35 % but different polarities. As an example, Pulse Generator 1 applies a positive pulse corresponding to a current density of $4{\cdot}10^{11}\,\mathrm{A/m^2}$ and pulse Generator 2 a negative pulse corresponding to a current density of $2.6{\cdot}10^{11}\,\mathrm{A/m^2}$. Pulses with positive (negative) polarity by Pulse Generator 1 and negative (positive) by Pulse Generator 2 are shown in grey (cyan).

As is evident by the negative first switching fields (Figure 3.16), for high amplitude pulse measurements, a switching field of roughly 10 mT is seen while for low pulse amplitude measurements, the switching fields are found to be approximately 30 mT. Since only small differences between the plots (which are different in terms of the current pulse polarity and therefore the spin current orientation) for a given sub-figure are observed, we conclude that the spin transfer torque only has a modest but in some cases detectable influence. Most of the reduction of the switching fields results from Joule heating, which is independent of the current polarity. For the cases of spin current injection from just one side (Figure 3.16a) and Figure 3.16b)) the different curves largely overlap within the error bars, which means that the spin transfer torque is insignificant in these measurements.

However, for Figure 3.16c) where the strongest effect is expected due to the highest total charge current density and simultaneous injection from both Pulse Generators, we find modest differences on the reversal of pulse polarity at the highest current densities.

The purple curve, representing positive (negative) pulses applied by Pulse Generator 1 (2) shows a lower switching field for a charge current density above $2.5{\cdot}10^{11}\,\mathrm{A/m^2}$. Additionally we note that the brown curve is only plotted for current densities of $2.5{\cdot}10^{11}\,\mathrm{A/m^2}$ and higher. Indeed, for lower current densities only a direct switching from one mono-domain state to the other has been found for these measurements. These results demonstrate again that the choice of current amplitude and polarity plays a crucial role for the qualitative device behaviour, although the quantitative differences are only modest.

In contrast to Figure 3.16c), no effect is observed for the measurement with same current polarities but lower amplitudes as shown in Figure 3.16d). Here we would expect to see for the grey curve (which is analogous to the purple curve in Figure 3.16c)) a lower switching field, but within the error bars, both the grey and the cyan curve are equivalent. From the comparison of the measurements, it is not clear why this is the case. In general, it could be due to an unfavourable resulting spin current angle for the measurements in Figure 3.16d). However, since a vortex state has a complex spin structure with many magnetization orientations present, it is also possible that the total spin current is too low to see a significant effect.

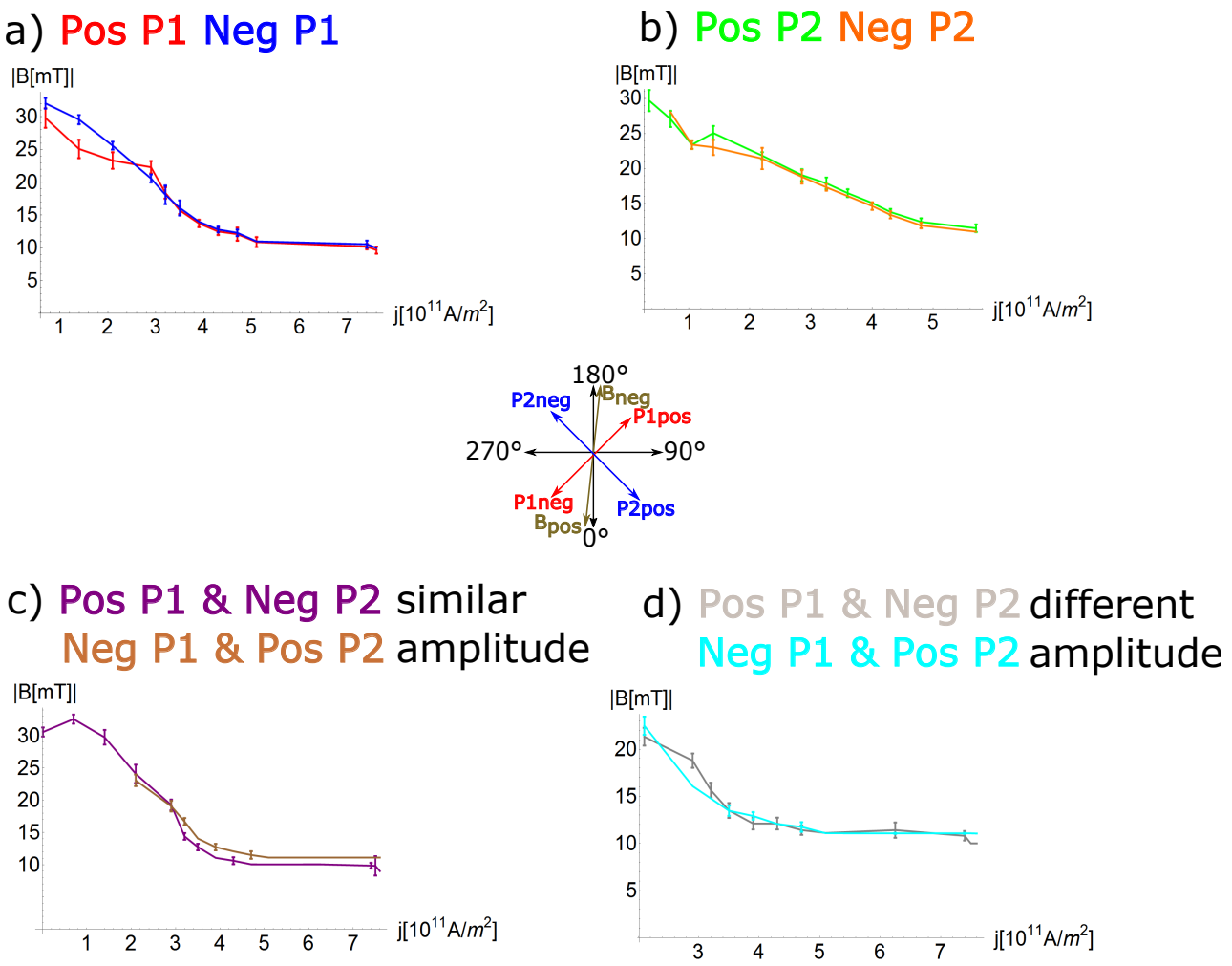

Fig. 3.16. Absolute values of the switching fields for negative field sweep directions as a function of the applied charge current density and polarity.
a) Curves with positive (red) and negative pulses (blue) applied by Pulse Generator 1.
b) Curves with positive (green) and negative pulses (orange) applied by Pulse Generator 2.
c) Curves with positive pulses by Pulse Generator 1 and negative pulses by Pulse Generator 2 shown in purple and vice versa shown in brown. The same voltage has been applied, resulting in similar pulse amplitudes for the two measurements. Modest differences between the curves, which are outside of the error bars, are found for high current densities.
d) Curves with positive pulses by Pulse Generator 1 and negative pulses by Pulse Generator 2 shown in grey and vice versa shown in cyan. Here, the pulse amplitude of Pulse Generator 2 is 35 % reduced compared to the pulse amplitude of Pulse Generator 1.

Next we study the results for the positive external field sweep direction, as shown in Figure 3.17. If we compare the general trend with the results shown in Figure 3.16, we note that the overall reduction of the switching field is approximately 50 % lower. In Figure 3.16, the reduction of the switching field over the complete current density range has been found to be approximately 20 mT, while for positive fields, a reduction of only approximately 10 mT has been observed. Since the spin transfer torque is expected to be only modest in both measurements, the different reductions of the switching fields are likely to be based on different Joule heating contributions.

In Section 3.3.2, where the first order reversal curves have been introduced, we have drawn the vortex core for the different field sweep orientations with opposite chirality and different nucleation points. The first small jump for negative fields was explained by a counter-clockwise vortex nucleation at the right edge of the disc while the first jump for positive field was explained by the nucleation of a clockwise vortex which could be nucleated slightly closer to the centre. These measurements agree well with this

picture, since the overall reduction of the switching fields for the two field sweep directions different which can be explained by different nucleation points of the vortex core or by different pathways of the vortex core (e.g. different defects) after the nucleation before it gets annihilated.

If we now study the differences for the plots within the same sub-figure, we note again that the curves largely overlap within the error bars. In Figure 3.17a), we find hints that for negative curves (blue curve) the switching fields are slightly lower than for positive pulses (red curve) for high current densities above $5.5{\cdot}10^{11}\,\mathrm{A/m^2}$. In Figure 3.17b), no differences of the two curves are observed which is consistent with the lower spin signal generated by the right CoFe injector and the lower applied current density.

If we compare Figure 3.17c) with Figure 3.17d) we notice that in situation d) we observe modest differences between the curves at least in the high current pulse regime above $3{\cdot}10^{11}\,\mathrm{A/m^2}$ while in c) no differences are found at all, although here, the higher total current density has been used.

To sum our results up so far, modest differences for the different applied current polarities have sometimes been found for high current densities, indicating an influence of the spin transfer torque on the switching. However, about 90 % of the reduction of the switching field can be explained by Joule heating, which is therefore the dominant effect and independent of the pulse polarity. Previous work demonstrated that the spin transfer torque in a lateral spin valve is an efficient way to manipulate a domain wall [14, 15] which can even depin a domain wall from a notch in the absence of a supporting magnetic field. In this experiment, much larger spin currents are expected based on the non-local signal, yet they do not as efficiently manipulate the vortex state. This can be connected to the non-optimal and uncontrolled position of the nucleation of the vortex core, in contrast to the previous studies where the transverse domain wall spin state has been carefully tailored. Furthermore, the more complex vortex spin state is expected to have a more complicated relationship between the spin current direction and the resulting torques than the previously studied relatively simple transverse domain wall.

In the case where the vortex core nucleation occurs on the opposite side of the disc to the contact, it is expected that the annihilation will occur at the same side as the position of the contact, since the core moves perpendicularly to the field across the disc during switching [222]. Hence in this case the annihilation of the core as seen in the final jump may be more likely to be affected by the spin transfer torque.

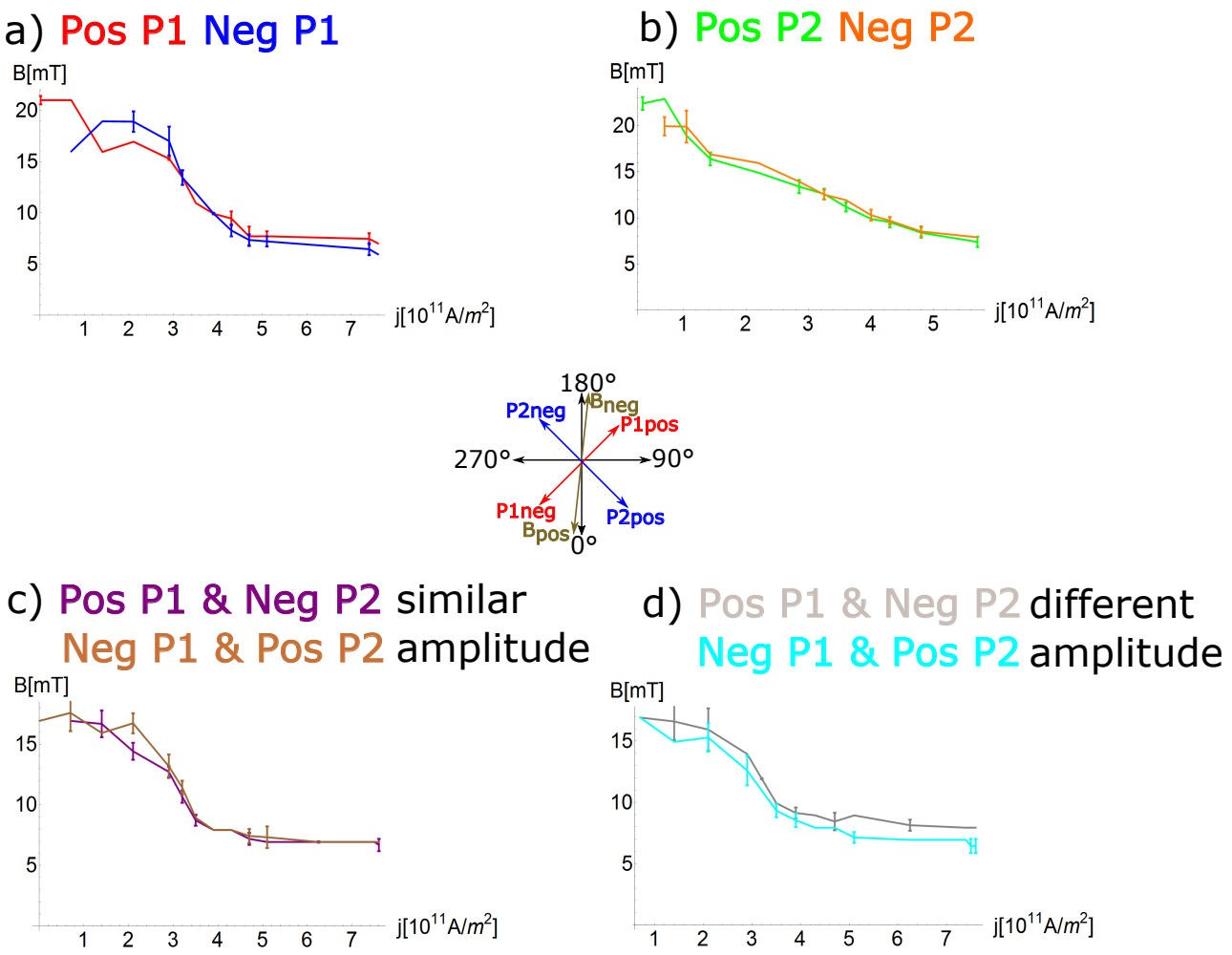

Fig. 3.17. Reduction of the switching fields for the positive field sweep direction as a function of the applied charge current density and polarity.
a) Curves with positive (red) and negative pulses (blue) applied by Pulse Generator 1.
b) Curves with positive (green) and negative pulses (orange) applied by Pulse Generator 2. The two curves are equivalent within the error bars.
c) Curves with positive pulses by Pulse Generator 1 and negative pulses by Pulse Generator 2 of similar amplitude shown in purple and vice versa shown in brown. Within the error bars, no differences are found.
d) Curves with positive pulses by Pulse Generator 1 and negative pulses by Pulse Generator 2 with a 35 % amplitude of Pulse Generator 2 shown in grey and vice versa shown in cyan. Slightly lower switching fields for negative (positive) pulses applied by Pulse Generator 1 (2) are found compared to the measurements with opposite current polarities.

3.5.3. Analysis of the second switching event for negative and positive fields

In this subsection, we study the transition of the vortex state to the mono-domain state for both positive and negative external fields. As previously mentioned, different switching paths are observed for the same measurement where the switching fields can differ by more than 30 mT, as shown in Figure 3.18. Here we study the low switching field path, since only this path has been observed across the whole charge current density range. In contrast, the high field switching path has been only found for current densities higher than $4{\cdot}10^{11}$ A/m^2, indicating a significant change of the switching for high current pulses.

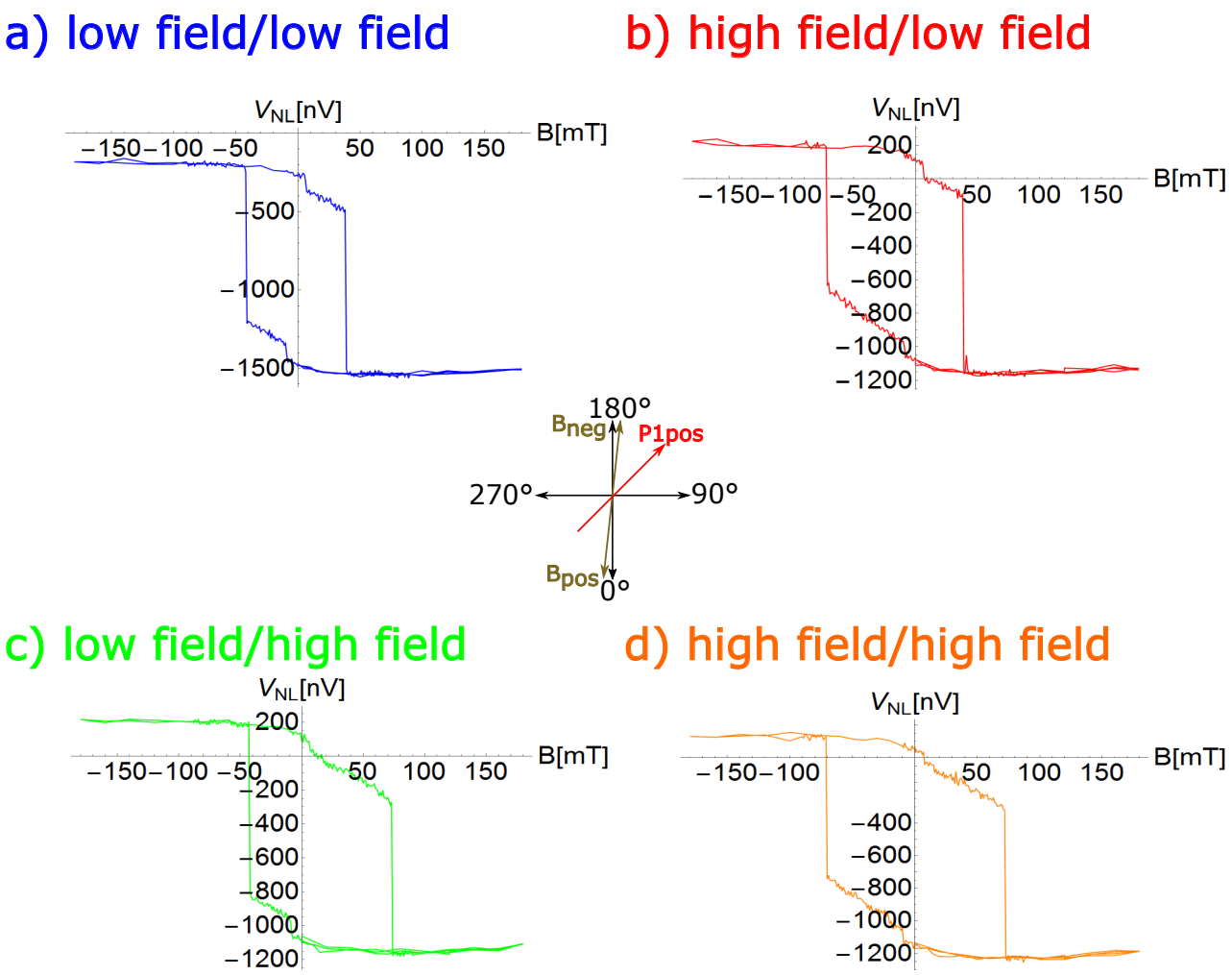

Fig. 3.18. Measurements with positive applied pulses of $7.6{\cdot}10^{11}$ A/m^2 by Pulse Generator 1. Two possible switching paths can be found for each external field direction.
a) First possible switching path, where both second switching events occur at fields about ±40 mT.
b) Second possible switching path with the second switching event for negative fields at about −70 mT. For positive fields, the second switching event is found at about +40 mT.
c) Third switching path with the second switching found at low negative fields (−40 mT). The second switching for positive fields is found for large fields of about +70 mT.
d) Fourth switching path with both second switching events at high fields of ±70 mT.

As before in Section 3.5.2, we plot the change in the switching fields with current pulse application, using the same colours for the same current polarities and amplitudes. The results for the second negative switching fields as a function of charge current density are shown in Figure 3.19. As before, only modest differences between the two plots within one sub-figure are found, indicating that for negative fields, the switching from the vortex state to the mono-domain state occurs relatively far away from the contact.

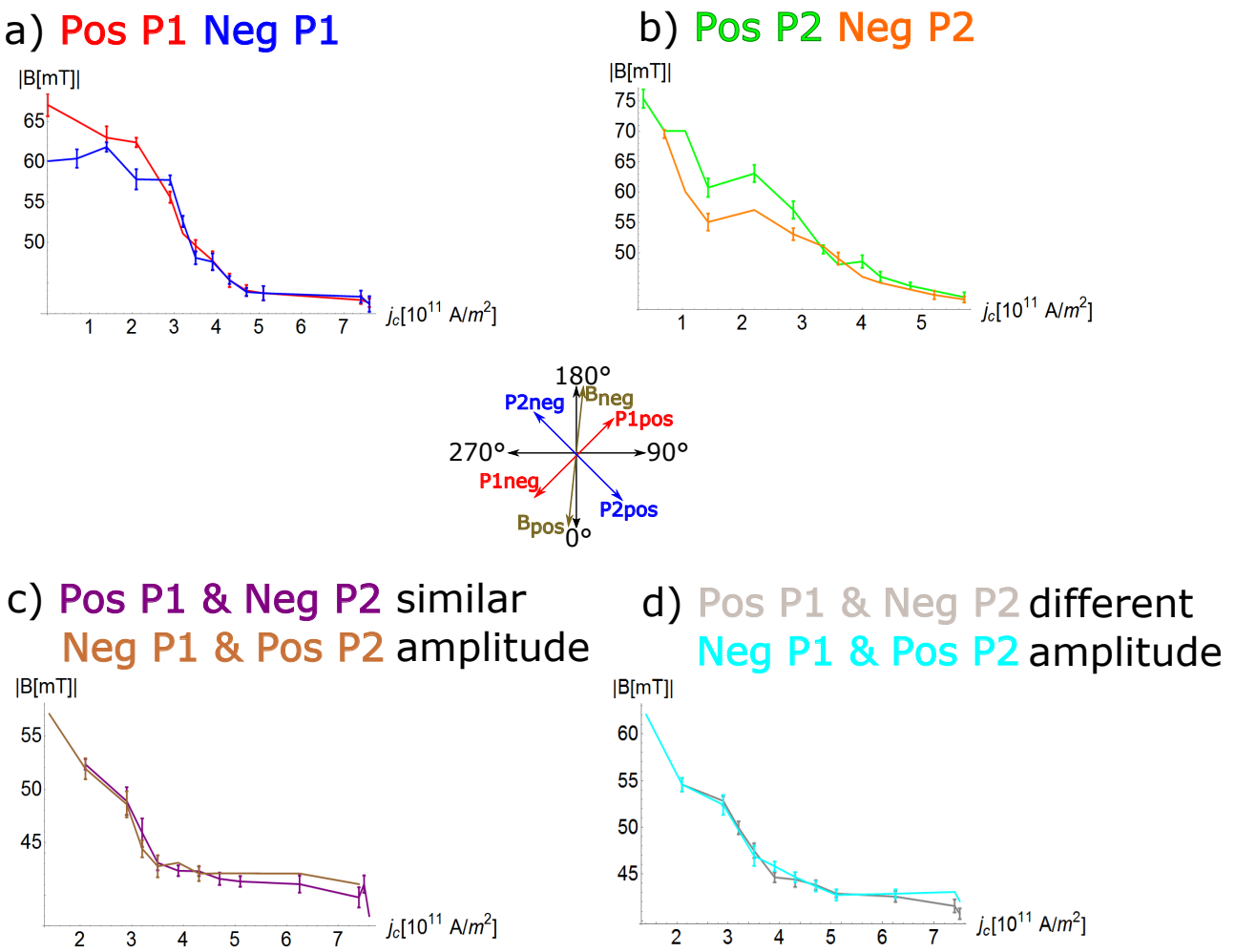

Fig. 3.19. Absolute values of the second switching field as a function of charge current amplitude and polarity for negative field sweep directions.
a) Determined switching fields with positive pulses applied by Pulse Generator 1 shown in red and negative pulses shown in blue.
b) Measured switching events with positive (negative) pulses applied by Pulse Generator 2 shown in green (orange).
c) Switching events measured with synchronous pulses by both Pulse Generators. The results for positive (negative) pulses by Pulse Generator 1 and negative (positive) pulses by Pulse Generator 2 are shown in purple (brown).
d) Switching events based on synchronous but 40 % reduced pulses by Pulse Generator 2 compared to Pulse Generator 1. The results for positive (negative) pulses by Pulse Generator 1 and negative (positive) pulses by Pulse Generator 2 are shown in grey (cyan).

We present the results for the second switching events for positive external fields in Figure 3.20. In this situation we find larger differences between the two curves shown in each plot. Especially in Figure 3.20c) we find a significantly lower switching field for negative pulses applied by Pulse Generator 1 and positive by Pulse Generator 2 (brown curve) than vice versa (purple curve). Since we have observed for negative fields with the same pulse polarities a statistically but significant smaller difference between the two curves we conclude that also the two second switching events are dominated by different defects resulting in different effective torques for different field sweep directions.

To sum it up, for both switching events the spin transfer torque is relevant, although due to an unfavourable position of the vortex core nucleation, the effect is relatively small and the reduction of the switching field is dominated by Joule heating. Nevertheless Figure 3.16c), Figure 3.17d) and Figure 3.20c) reveal a statistically significant lower switching field for the preferred current polarities

compared to the unfavourable ones. Furthermore, thanks to our geometry which allows the simultaneous application of current pulses from both sides, the effect can be determined which has been not easily possible with just pulses from one side.

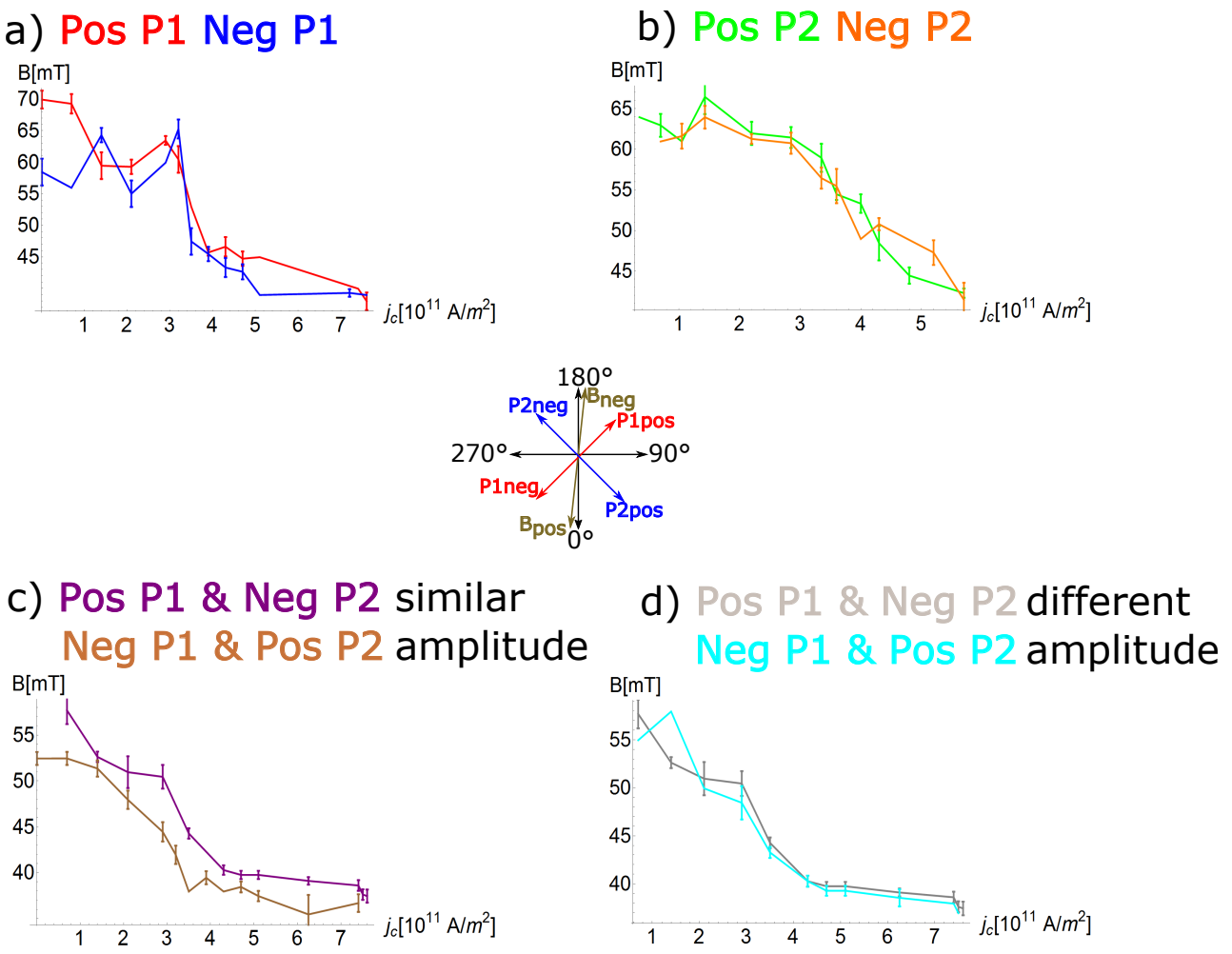

Fig. 3.20. Second switching events for positive field sweep directions for different charge current amplitude and polarities.
a) Results for positive pulses applied by Pulse Generator 1 in red and negative pulses applied by Pulse Generator 1 in blue.
b) Results for positive pulses applied by Pulse Generator 2 in green and negative pulses applied by Pulse Generator 2 in orange.
c) Measurement with synchronous pulses from both Pulse Generators with similar amplitude. The results for positive (negative) pulses by Pulse Generator 1 and negative (positive) pulses by Pulse Generator 2 are shown in purple (brown).
d) Switching events based on synchronous but 35 % reduced pulses by Pulse Generator 2 compared to Pulse Generator 1. The results for positive (negative) pulses by Pulse Generator 1 and negative (positive) pulses by Pulse Generator 2 are shown in grey (cyan).

Finally, we study the probability for the different second switching paths. As already mentioned, only the low field switching path has been taken into account in the previous analysis since the high field switching path only occurs for high amplitude current pulses. To shine light on this, multiple repeat measurements with pulse amplitudes of $7.6{\cdot}10^{11}\,\mathrm{A/m^2}$ for Pulse Generator 1 and $5.6{\cdot}10^{11}\,\mathrm{A/m^2}$ for Pulse Generator 2 have been performed. In these measurements, the polarities of the Pulse Generators and the number of used Pulse Generators is varied. We mention here again, that only two different switching paths for the second, large jump of the signal are observed for both external field sweep

directions.

In Table 3.1, the probability for the occurrence of the low field switching path for negative external fields is named "Neg. Low Field Probability". The probability of the low field switching path for positive external fields is named "Pos. Low Field Probability". P is the pulse polarity with the plus-sign indicating positive pulses and the minus-sign indicating negative pulses. The first symbol is the polarity of the first Pulse Generator and the second symbol the polarity of the second Pulse Generator, while 0 means no pulses from the particular Pulse Generator. From these measurements, we are able to draw an important conclusion:

By the application of synchronous pulses, the probability of the low field switching path (for both external field directions) can be strongly suppressed, which demonstrates that the low field switching path cannot be caused by only thermal activation. If this was the case, we would expect that by synchronous pulses and the resulting large total current density, the low field switching path would be supported and not suppressed. Our work demonstrates that the switching behaviour depends crucially on the process parameters and can be directly manipulated. The main findings of our study concerning the different probabilities for the different Pulse Generator combinations are shown in a histogram in Figure 3.21.

P	Neg. Low Field Probability [%]	Pos. Low Field Probability [%]	# Measurements
$+/0$	71	80	21
$-/0$	61	71	21
$0/+$	61	39	13
$0/-$	66	50	6
$+/-$	0	8	24
$-/+$	0	0	22

Tab. 3.1. Probability of the low field switching path for different current polarities combinations of the two Pulse Generators. In all measurements where Pulse Generator 1 has been active, the applied current density is $7.6{\cdot}10^{11}\,\mathrm{A/m^2}$, while if Pulse Generator 2 has been used, the current density is $5.6{\cdot}10^{11}\,\mathrm{A/m^2}$. The first two rows show the results when only Pulse Generator 1 is used, the two rows in the middle present the results when only the second Pulse Generator is used and the last two rows indicate the results for synchronous pulses from both Pulse Generators. P is the polarity of the given Pulse Generator, with the $+$-sign indicating positive and the $-$-sign indicating negative pulses. "Neg. Low Field Probability" indicates the probability for the low field switching path for negative field sweeps, while "Pos. Low Field Probability" is the probability for the low field switching path for positive field sweeps. Since for both field sweep directions, only two switching paths occur, the probability for the certain high field switching path can directly be read out of the table.

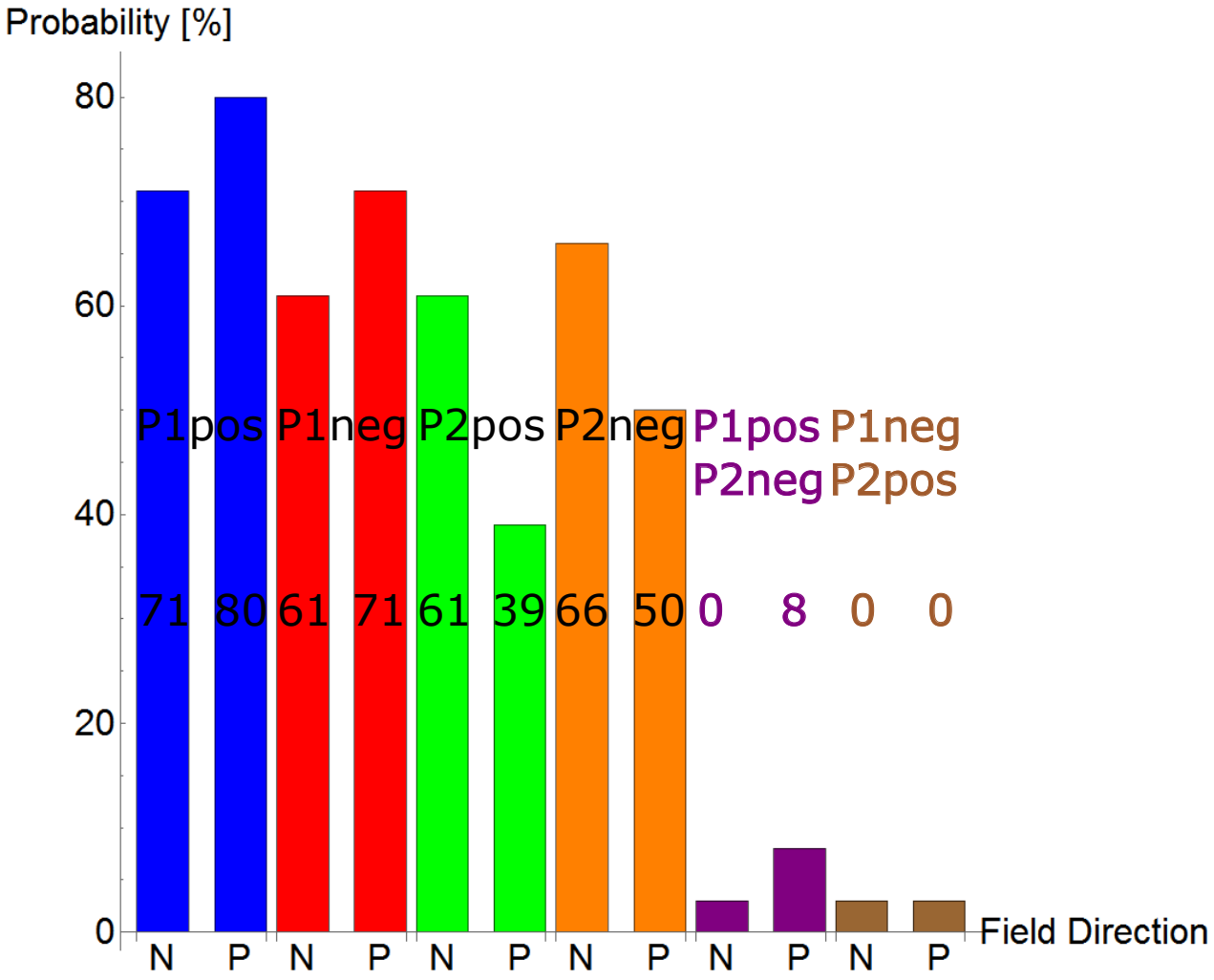

Fig. 3.21. Histogram of the different probabilities for the low field switching paths for the different current polarities of the given Pulse Generators. The polarities of the certain Pulse for the certain measurements is labelled in the bars, while the N and P stands for the negative and positive external field sweep direction. We find a strong reduction of the probability for the low field switching path down to 8 % for positive pulses by Pulse Generator 1 and negative by Pulse Generator 2 and do not observe this path for the opposite polarity. Since for both field sweep directions only two switching paths occur, the probability for the certain high field switching path can directly be read out of the histogram.

3.6. Summary Of The Spin Current Assisted Switching Measurements

In summary we have studied the spin current assisted switching of a ferromagnetic Py disc as a function of the charge current amplitude and polarity for different external field angles. Different switching paths for different field angles have been observed, indicating a dominant influence of inhomogeneities, which affect the details of the switching and lead to deviations from the nominally isotropic behaviour for a perfectly symmetric disc. For some field angles, direct mono-domain state to mono-domain state transitions are found while for other field angles, switching paths with the vortex state as an intermediate state are present. The chirality of the vortex state can hereby by identified by the size of the occurring jumps of the non-local signal. The disc has been characterised for a range of field angles in order to determine suitable configurations to study the influence of the spin transfer torque on the device. The indirect mono-domain to mono-domain switching of the disc via an intermediate vortex state has been studied for a field sweep angle of 171/351 °. For this field angle additional first order

reversal curve have been performed in order to demonstrate the stability of the four different magnetic states occurring during the reversal at zero external field. The first order reversal curves also have demonstrated that the nucleation point of the two vortex states can be determined by a comparison of the non-local signal directly after the nucleation and at zero field where the vortex is expected to be in the centre of the disc.

For the current polarity and amplitude dependent measurements, although Joule heating dominates, we nevertheless observe a statistically significant effect of the spin transfer torque in those measurements with synchronous application of current pulses in both injectors, which is a particular possibility with our optimized geometry. A further improvement of the device would be even a smaller contact area, leading to an even more homogeneous magnetization below contact when the vortex state is present. Additionally it would be useful to cause the nucleation, maybe be an artificial defect, beneath the contact in order to increase the effect of the spin transfer torque due to the short spin diffusion length. By doing so, it could even be possible to measure the spin transfer torque efficiency as a function of the effective spin current angle, given by the ratio of the two spin currents, and the magnetization orientation of the disc beneath the contact.

Chapter IV

Comparison of Spin Hall And Electric Spin Signals

We present in this chapter the temperature dependence of the spin current generated by two different spin current generation (and detection) methods. As the first method, we exploit the conventional electric spin current injection and detection based on two parallel ferromagnetic wires bridged by a nonmagnetic Cu conduit. As the second method, we either generate spin currents by the spin Hall effect and detect them by conventional non-local detection or we generate spin currents by conventional spin current injection and detect them by the inverse spin Hall effect.

Our multi-terminal Py-Pt-Cu lateral spin valve are based on an optimized kinked geometry where the Pt stripe and the Py wires are fabricated perpendicularly to each other. This new geometry allows us to link the detected signals with the magnetization orientation of the probed Py wires. In order to compare the different signals, the conventional non-local signal and the (inverse) spin Hall effect signal are studied in one single device.

We find differences in the temperature dependences of these two detection methods, which reveals their importance for the temperature dependence of the signals which is therefore not only governed by the spin transport and spin injection as previously claimed. We determine a different sensitivity of the observed effects on the Py/Cu and Pt/Cu interfaces, which highlights the importance of the exact current path in the device for the understanding of the device operation.

The EBL patterning of the samples in the chapter has been performed by myself as well as the growth of the Py wires and the Cu bridge and the optimization of the in-situ etching prior to the Cu deposition. The Pt deposition has been done by colleagues via sputter deposition. The data analysis has been done by myself.
Prof. Kläui had the original idea of the study and he proposed the geometry. He additional gave valuable input in order to understand the results.
Dr. Reeve gave a lot of valuable input and helped in great measure to understand the results and write the publication [242].

4.1. Motivation

As explained in the theory part of this thesis, the lateral spin valve geometry allows one to easily generate pure spin currents based on electric spin injection with reduced Joule heating and Oersted fields at the position of the manipulated magnetic state [11, 143]. In the most simple geometry, these devices consist of two ferromagnetic (FM) electrodes which are spatially separated but are connected via a nonmagnetic bridge (NM). By the application of a spin polarized charge current from the first ferromagnetic electrode, the injector, through the FM_1/NM interface, a spin current is generated at this interface which diffuses in all directions including towards the second ferromagnetic electrode. At the NM/FM_2 interface, the spin current is absorbed and applies a spin transfer torque which can be exploited in order to switch the magnetic state of the detector [12–15].

A second intensively used approach to generate pure spin currents in a lateral spin valve geometry is the spin Hall effect (SHE) which arises in heavy metals (HM) with large spin orbit coupling. If a charge current flows through a SHE material, a spin current is generated perpendicular to this charge current. While in materials such as Pt [103, 104] and W [8] intrinsic contributions to the SHE usually dominate, extrinsic effects are crucial to explain the SHE in heavy metal alloys such as CuBi [106, 107], CuIr [108] or AuTa [109]. The reciprocal effect, the inverse spin Hall effect, converts a spin current back into a measurable charge current.

As explained in detail in the theory of this thesis, the microscopic reason for the (conventional) non-local signal is the non-equilibrium of the chemical potential of the NM at the FM_1/NM interface. If a spin accumulation persists at the NM/FM_2 interface after the spin current transport in the NM, the chemical potential of FM_2 needs to be aligned at this interface due to continuity relations. The associated shift in the chemical potential of the NM can be detected as a non-local voltage V_{NL}.

This is very different for the inverse spin Hall effect. Here, once the spin current enters the SHE material, it gets absorbed and a charge current is generated which means properties such as the electric conductivity of the NM spin conduit and the HM are crucial [107] since a large part of the generated charge current in the HM can be shunted by the NM. The aim of our study has been to understand if these very different injection and detection methods affect the device behaviour for varying temperatures.

The temperature dependence of the (conventional) non-local signal has been intensively studied in lateral spin valves [145, 148, 243]. When the temperature is reduced from room temperature, it is observed that within a certain temperature range, the detected non-local signal increases. This result can be well explained by the Elliot-Yafet mechanism [244, 245], which connects the reduction of the resistivity of the NM with an increase of the spin diffusion length. However, for very low temperatures (typically around 30-80 K) a non-monotonic behaviour of the non-local signal is sometimes seen with an explicit maximum of the signal and a downturn of the signal for a further decrease of the temperature. Many different explanations have been put forward to explain this non-monotonic behaviour, e.g. increased surface scattering [243] and magnetic impurity scattering as a manifestation of the Kondo effect both at the interface [148] and in the bulk of the device [246]. All these explanations are focused to explain the temperature behaviour on spin transport effects within the NM conduit and do not consider effects concerning the spin current injection or detection.

In a previous work, we compared electrically generated and thermally generated spin signals and we found significant differences in the temperature behaviour of the two signals [247]. Since in these two approaches the spin current injection mechanism is different, while the spin transport and spin current detection are the same, all appearing differences can be connected to the spin current injection mechanism.

Next to these two approaches, the spin Hall effect is very promising in order to study pure spin currents in lateral spin valves. Either a spin current is generated by the spin Hall effect and conventional non-local detection is exploited to detect it or a spin current is generated via conventional spin injection and detected via the inverse spin Hall effect [248, 249].

These two ingredients are the motivation for this study. From [247] we know that not only spin transport but additional spin current injection needs to be taken into account to explain the temper-

ature dependence. From the reciprocity between spin Hall and inverse spin Hall effect [248, 250], we know that if differences would be found in the temperature behaviour for the spin current generation by the spin Hall effect, there should also be differences in the spin current detection by the inverse spin Hall effect. The best method to determine such differences is to measure both the conventional non-local signal and the (inverse) spin Hall effect in one single device, at varying temperatures.

4.2. Temperature Dependent Van Der Pauw Measurements

Before we show the results of the Pt-Py-Cu and later the CoFe-Cu spin valves, we show the resistivities of the used materials as a function of temperature in Figure 4.1. For all curves, a thin film of the material has been grown on a natural oxidized Si substrate and a Van der Pauw measurement [251] has been performed during the warm-up of the cryostat. We find for all metals the expected curve with a decrease of the resistivity with deceasing temperature and a saturation of the resistivity for low temperatures.

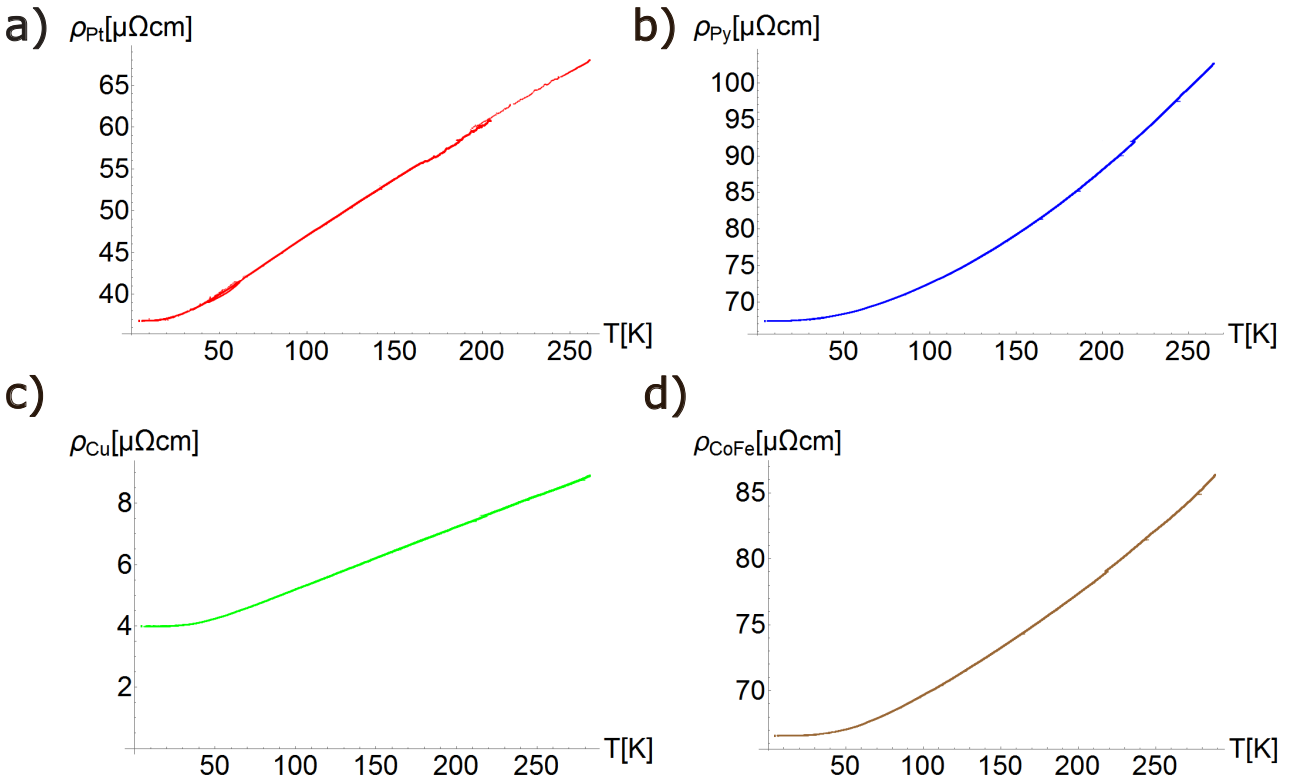

Fig. 4.1. Measured resistivities of different materials as a function of temperature which have been used to fabricate the studied lateral spin valves. All measured thin films have been grown on natural oxidized Si substrates while the lateral spin valve samples have been fabricated on sapphire substrates.
a) Resistivity curve of a 16 nm thick Pt thin film grown by sputter deposition.
b) Resistivity curve of a 31 nm thick Py thin film grown by UHV thermal evaporation.
c) Resistivity curve of a 85 nm thick Cu thin film grown by UHV thermal evaporation.
d) Resistivity curve of a 27 nm thick CoFe thin film grown by UHV thermal evaporation.

The parameters to fabricate the samples in this chapter are as follows:

Pt stripe: The Pt stripe has been patterned using a single PMMA layer with 200 nm thickness. The used EHT for the EBL is 30 kV. The deposition has been done by magnetron sputtering without any rotations of the substrate during the deposition.

Py wires: The Py wires have been patterned using a single PMMA layer with 200 nm thickness. The used EHT for the EBL is 10 kV. The deposition has been done by UHV thermal evaporation without any rotations of the substrate during the deposition.

Cu bridge: The Cu bridge has been patterned using a double MMA-PMMA layer with 450 nm total thickness. The used EHT for the EBL is 10 kV. The deposition has been done by UHV thermal evaporation without any rotations of the substrate during the deposition.

More details concerning the sample fabrication such as the EBL patterning and the deposition conditions including the in-situ etching prior to the Cu deposition can be found in Appendix A.1.

4.3. Sample Fabrication

Lateral spin valve samples with a kinked geometry as shown in Figure 4.2 have been fabricated on a sapphire substrate by electron beam lithography (EBL) and lift-off-processes. In the first step, a 100 nm wide and 10 μm long wire has been patterned together with alignment markers and 12 nm of Pt has been deposited by magnetron sputtering (blue stripe, contact 2 and contact 3). In the second step, two 15 μm long and 100 nm and 150 nm wide wires have been patterned perpendicularly to the Pt wire and 35 nm of Py (81 % Ni and 19 % Fe) has been deposited by UHV thermal evaporation. The different widths have been chosen to assure that the two Py wires have different switching fields, with the left Py wire (green wire, contact 4 and contact 5) 100 nm in width and the right Py wire (green wire, contact 6 and contact 7) 150 nm in width. In the last step, in-situ argon milling is used to clean the Pt and the two Py surfaces before the 100 nm wide and 150 nm thick Cu bridge (orange wire, contact 1 and contact 8) is deposited, together with electric contacts.

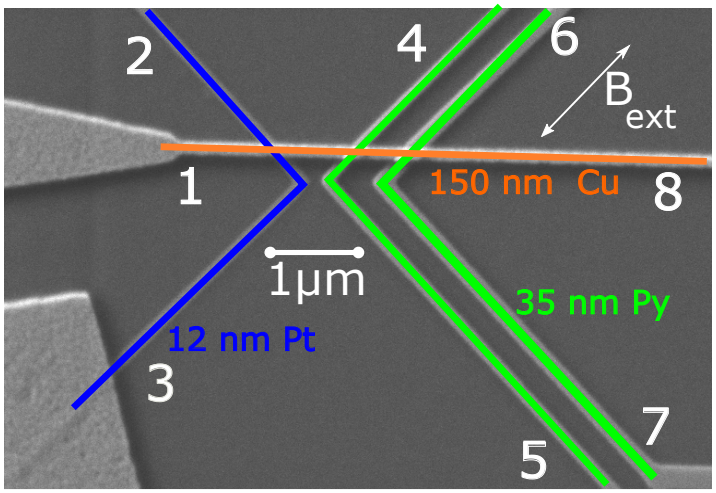

Fig. 4.2. Scanning electron microscope image of a fabricated lateral spin valve which allows the study of the (inverse) spin Hall effect and the conventional non-local signal in one single device. The sample consists of one 12 nm thick and 100 nm wide Pt stripe which is drawn in blue, two Py wires which are 100 and 150 nm wide and 35 nm thick (drawn in green) and one 100 nm wide and 150 nm thick Cu bridge, which is drawn in orange.

4.4. Results

4.4.1. Field dependence of the iSHE signal

To measure the inverse spin Hall effect signal at 4.2 K, the probe configuration as shown in Figure 4.3 has been used. An alternating current of 1.4 mA amplitude and 2221 Hz frequency is generated by

an applied alternating voltage of 7 V and a used pre-resistor of 5000 Ω before the sample. Since the resistances of our nanostructures (several hundred Ω) are small compared to the pre-resistor we assume the same current for all measurements and all (small) variations of the sample resistance with varying temperature are neglected. The alternating current is applied between the top end of the left Py wire (contact 4) and the right end of the Cu bridge (contact 8). The inverse spin Hall voltage V_{iSHE} is measured simultaneously with two Lock-In Amplifiers between the top end of the Pt stripe (contact 2) and the left end of the Cu bridge (contact 1) and completely between the two ends of the Pt stripe (contact 2 and contact 3). The inverse spin Hall effect resistance R_{iSHE} is defined by dividing the measured voltage by the applied current. For a better comparison of the plots, all hysteresis curves are shifted to 0 mΩ for the high spin signal state. The error bars for the different temperature dependent curves are calculated as $\Delta_{\mathrm{tot}} = \sqrt{(\Delta_{\mathrm{AP}})^2) + (\Delta_{\mathrm{P}})^2}$ with $\Delta_{\mathrm{AP,P}}$ as the standard derivation of the signals for high and low spin signal states.

In order to measure V_{iSHE}, an external magnetic field B_{ext} is swept parallel to the easy axes of the Py wire, as shown in Figure 4.3. Since the generated charge current due to the inverse spin Hall effect is given by

$$J_{\mathrm{iSHE}} \propto J_s \times \sigma \tag{4.1}$$

the polarity of the generated charge current J_{iSHE} changes sign by changing the orientation of the absorbed spin current J_s in the Pt. By sweeping the external magnetic field B_{ext}, the magnetization orientation of the Py injector changes which results in a change of the pure spin current orientation in the Cu bridge. As a result, the iSHE signal consists of two states which can be directly linked to the magnetization orientation of the left Py wire, which is drawn as a green arrow above the plot in Figure 4.3. The field is swept from 0 mT to 150 mT and back to 0 mT without any changes of the measured signal. For this state, the Py wire is magnetized parallel to positive external fields and we shift this state to 0 mΩ and name it the high spin signal state. However, at a field of −50 mT a large jump of the signal is found since the magnetization of the Py wire switches to align with the negative field and we name this state (−0.08 mΩ for the blue curve and −0.06 mΩ for the red curve) the low spin signal state. This state is stable for all negative fields and also at 0 mT. By the application of a positive field of +100 mT, the magnetization of the wire switches again and we find the high spin signal state again.

In previous publications, the HM and the FM wires were often all patterned parallel and for such a geometry, a field perpendicular to the easy axes of the FM was swept in order to generate the maximum (inverse) spin Hall effect signal. One major advantage of our kinked geometry is that the maximum signal is generated for a field parallel to the easy axes, which enables exact control of the magnetization of the Py wires. Furthermore, much lower fields are required to generate the signal and both spin states are (meta)-stable at remanence, which simplifies the interpretation of the results.

While the blue curve, measured between both ends of the Pt stripe (contact 2 and contact 3), is the standard method to measure the iSHE, the red curve, measured between contact 1 and contact 2, provides valuable information concerning the Cu/Pt interface. The signal shown in red is caused by (partial) shunting of the generated charge current in the Pt by the very thick and highly conductive Cu. This phenomenon has been previously accounted for theoretically by the implantation of a shunting factor x in the $1D$-diffusion model [252] or is automatically taken into account using $3D$ modelling [104, 107]. Our work demonstrates this shunting experimentally.

We additionally note that the signal measured between contact 1 and contact 3 is 0.02 mΩ which means that the signal shown in blue is the sum of both signals. Additionally, we conclude that the Pt/Cu interface is not perfectly homogeneous (otherwise both signals probing half the interface would be the same). This inhomogeneity can be caused, for example, by an angle between the sample normal and the Pt source and a consequent inhomogeneous growth. It can also be caused due to an inhomogeneous in-situ argon etching before the Cu bridge is deposited. A third reason could be an angle between the sample normal and the Cu source during the deposition. However, it turns out that the inhomogeneous Cu/Pt interface will play an important role, since the inverse spin Hall effect is

very sensitive to all sources of electrical conductivity inhomogeneities, varying the exact charge current path across the interface.

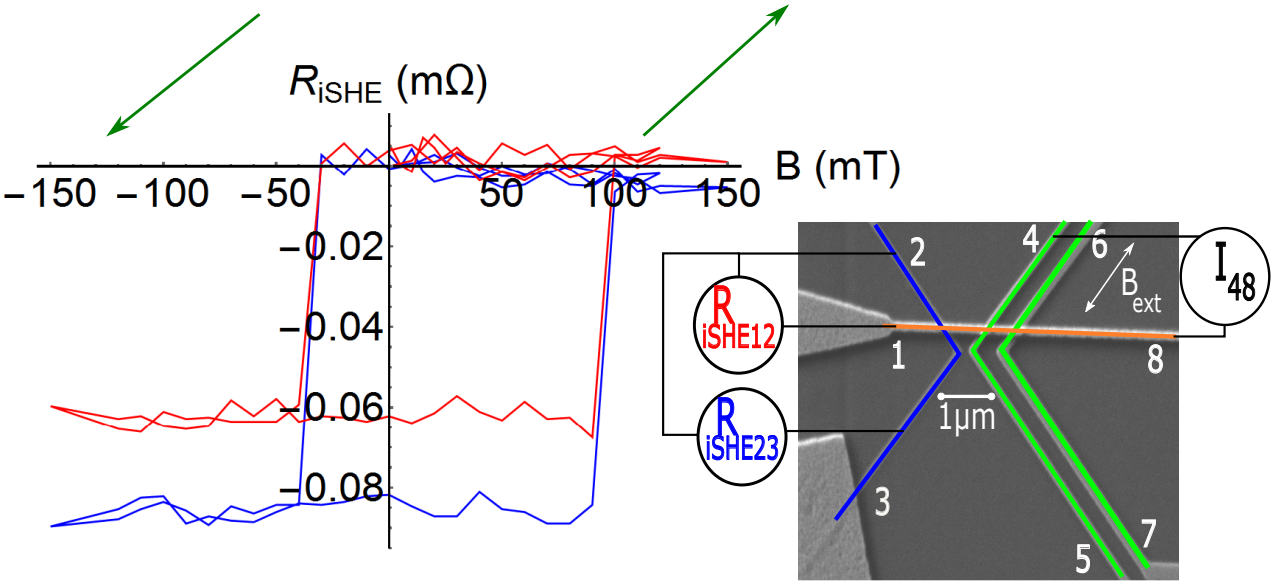

Fig. 4.3. Inverse spin Hall effect signal measured at 4.2 K as a function of the applied external field. An alternating current is applied between the top part of the left Py wire (contact 4) and the right end of the Cu bridge (contact 8). The inverse spin Hall effect signal is measured either between the two ends of the Pt stripe (contact 2 and contact 3) or between the top end of the Pt stripe (contact 2) and the left end of Cu bridge (contact 1). A signal of 0.08 mΩ is found when measuring between the two ends of the Pt stripe (blue curve) while a signal of 0.06 mΩ is found when measuring between the top end of the Pt stripe and the Cu bridge.

4.4.2. Field dependence of the conventional non-local signal

To measure the conventional non-local signal, the same current with the same frequency as for the inverse spin Hall effect has been applied between the top end of the left Py wire (contact 4) and the left end of the Cu bridge (contact 1). The non-local voltage is measured simultaneously either between the top end (contact 6) or the bottom end (contact 7) of the right Py wire and the right end of the Cu bridge (contact 8). The external field is swept as for the inverse spin Hall effect signal parallel to easy axes of the Py wires.

In this measurement, first a negative external field is swept from 0 mT to −150 mT and back to 0 mT without any changes of the non-local signal. This means that in this measurement, the magnetization of both wires is aligned parallel to the negative external field as drawn as green arrows above the left part of the plot. This state is shifted to 0 mΩ and is the high spin signal state. By the application of +50 mT we find an abrupt jump in the signal of −2.0 mΩ which indicates the antiparallel spin state. Since the right Py wire is wider than the left Py wire, it switches for lower fields which can also be seen by a comparison of the inverse spin Hall effect and the non-local signal. We therefore can draw the right green arrow, indicating the magnetization of the right Py wire, pointing along positive fields while the left green arrow is still aligned parallel to negative fields.

By the increase of the external field to +100 mT we find a second abrupt jump and the high spin signal state is measured again. We now draw both green arrows, representing the magnetizations of the Py wires being aligned with the positive external field. We mention here that the jump at a positive field of +100 mT is the same as for the iSHE signal which means that each wire can be identified by its switching field. Furthermore we note that both determined non-local signals are the same and no dependence on the probe configuration is found.

The differences in the two observed signals reflect the differences in the underlying detection mech-

anisms. The non-local signal probes the shift in the chemical potential at the Cu/FM_2 interface. Furthermore, the signal is independent of the probe configuration. For the inverse spin Hall effect, an electric charge current is generated in the Pt stripe due to spin dependent scattering and this charge current can be (partly) shunted by the Cu bridge. The measured signal is much smaller due to this shunting and crucially depends on the current path through this interface. Therefore the signal is highly sensitive to the properties of the detector element and the employed detection method.

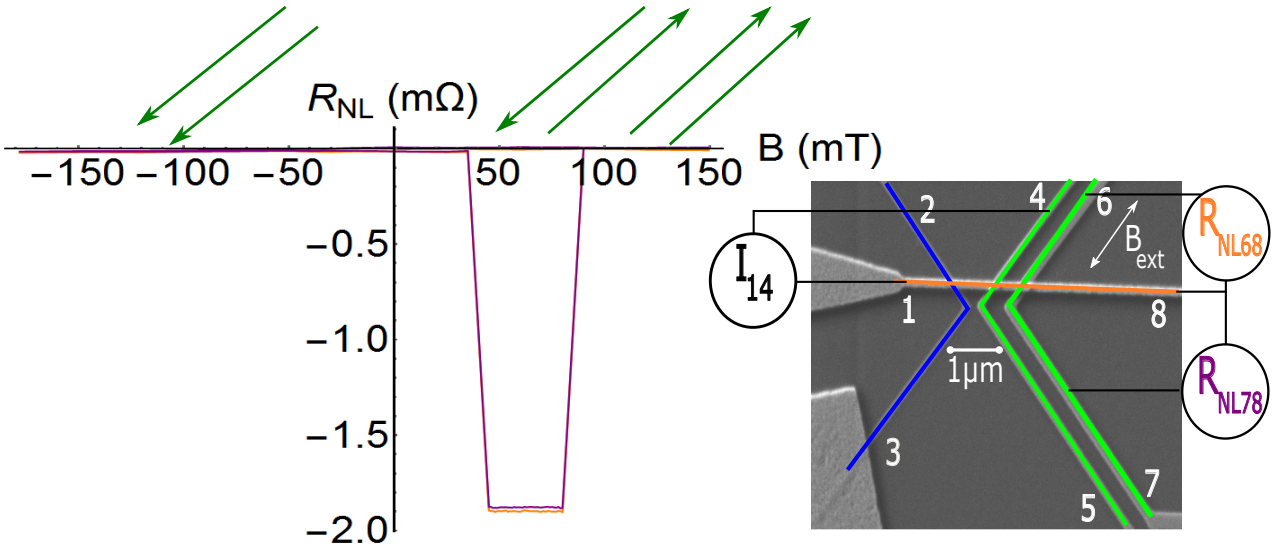

Fig. 4.4. Conventional non-local signal as a function of the applied external field at 4.2 K, with the magnetization orientation of the two Py wires drawn as green arrows above the plot. An alternating current is applied between the top end of the left Py wire (contact 4) and the left end of the Cu bridge (contact 1). The two non-local signals are measured simultaneously either between the top end (contact 6, orange curve) or the bottom end (contact 7, purple curve) of the right Py wire and the right end of the Cu bridge (contact 8). In this measurement scheme, the measured signal is 2.0 mΩ for both possible probe configurations.

4.4.3. Reciprocity between SHE and iSHE

In order to study the reciprocity between the SHE and the iSHE, current injection and voltage detection are reversed, as shown in Figure 4.5. The charge current is either applied completely through the Pt stripe (brown curve in Figure 4.5) or between the top end of the Pt stripe and the Cu bridge (green curve in Figure 4.5). The flowing charge current in the Pt stripe leads to a spin current in the Pt which is perpendicular to the charge current. This spin current enters the Cu bridge with its orientation either parallel or antiparallel to the magnetization of the left Py wire, acting as detector. Analogous to the conventional non-local signal, a high spin signal is found for a parallel alignment between spin current and detector magnetization, while for an antiparallel alignment a low spin signal is found. As also seen in previous publications, we find a high noise level when the current flows completely through the Pt stripe, which makes a proper determination of the SHE signal in the whole temperature range very difficult [149]. However, it can be seen that the second probe configuration with the current flowing partly in the Pt stripe yields a comparable signal (0.08 mΩ for the brown and 0.06 mΩ for the green curve) with much less noise, which allows to measure the SHE signal in the whole temperature range from 4.2 K to 200 K. We find for the SHE and the iSHE based signals the same temperature behaviour in the whole temperature range, as expected from Onsager reciprocity [250]. The results are shown in Figure 4.6.

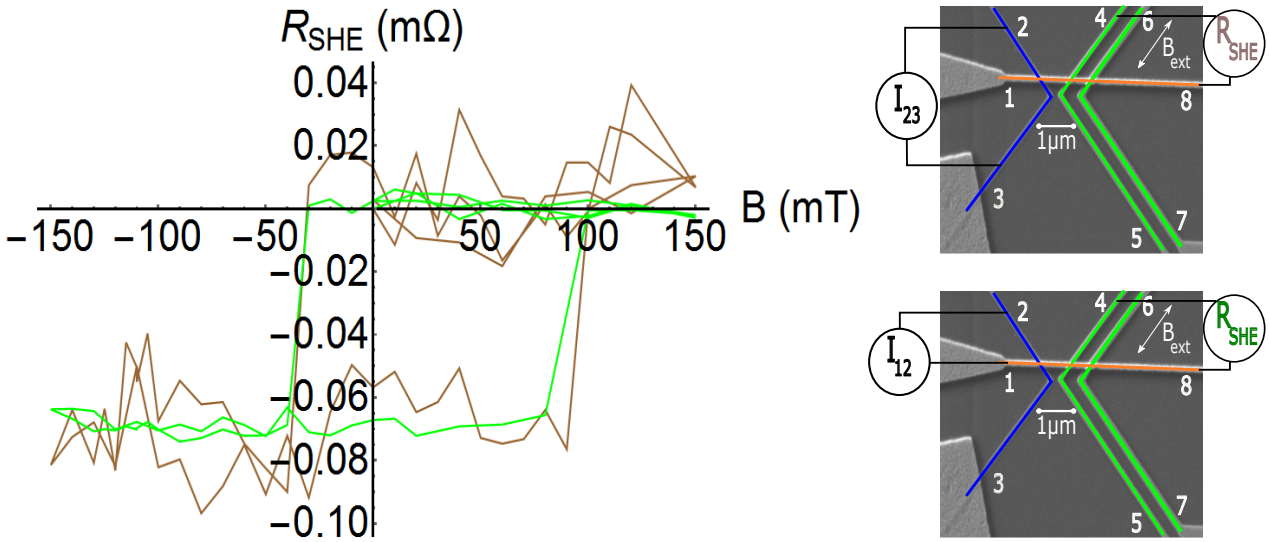

Fig. 4.5. Hysteresis curves based on the spin Hall effect at 4.2 K. A charge current is applied either completely through the Pt stripe (brown curve) or between the top end of the Pt stripe and the left end of the Cu bridge (green curve). The signal is measured between the top end of the left Py wire and the right end of the Cu bridge. The signal generated by the current flowing completely through the Pt stripe is 0.08± mΩ. The signal generated by the current partly flowing through the Pt stripe is 0.06± mΩ, yet with much lower noise compared to the first signal.

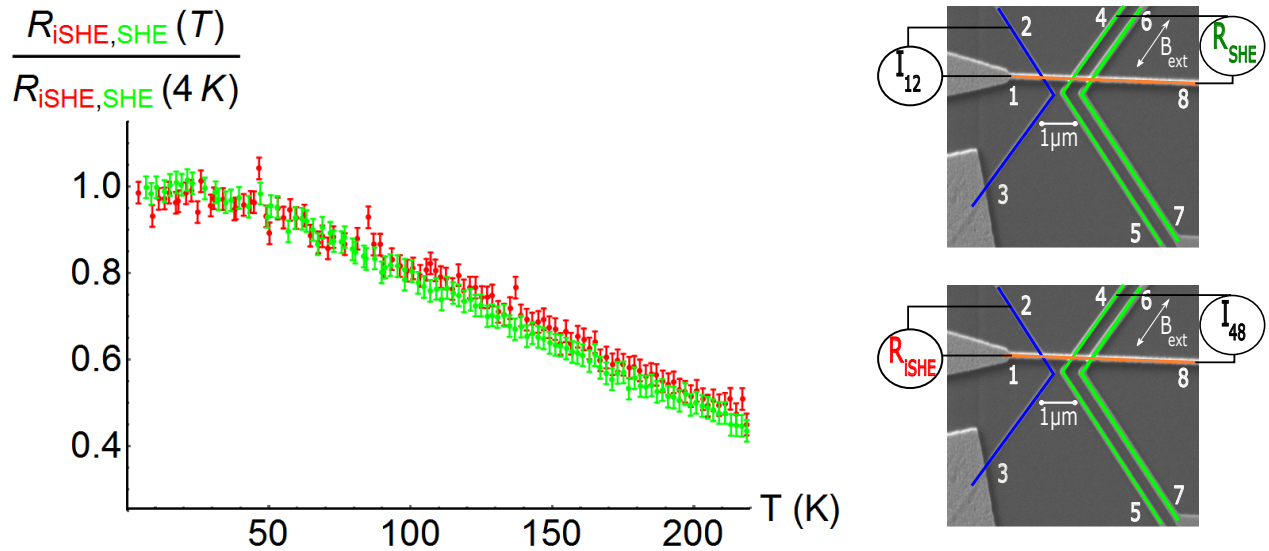

Fig. 4.6. Normalized SHE (green curve) and iSHE (red curve) based spin signal. As expected from Onsager reciprocity, we find within the error bars the same temperature dependence for both curves in the whole temperature range between 4.2 K and 200 K.

4.5. Temperature Dependence Of Signals For Different Detection Methods

The main part of this work is to compare the temperature dependence of the normalized conventional non-local signal and the normalized iSHE signal. As plotted in Figure 4.7, we find in the very low temperature range between 4.2 K and 30 K in both cases a constant signal. In the temperature range

between 60 K and 200 K we find a linear decrease of the signals with decreasing temperature and observe for both curves the same slope. However, in the intermediate temperature range between 30 K and 60 K, the two signals differ with an evident shift of the onset of the reduction for the iSHE signal.

As previously mentioned, the temperature dependence of the conventional non-local signal [147, 148, 243, 247] and the iSHE signal [104, 107, 249] has been intensively studied. For the non-local signal, similar curves to the one shown were found, where the signal behaviour in the high temperature behaviour between 60 K and room temperature is usually explained by the Elliot-Yafet theory [244, 245]. In this model, the decrease of the resistivity of the NM with decreasing temperature leads to a reduction of spin scattering in the NM during the spin transport. This leads to an increase of the spin diffusion length of the NM, increasing the number of spins reaching the NM/FM_2 interface. As a result, the measured signal is increased. However, many different explanations have been put forward to explain the low temperature regime, e.g. increased surface scattering [243] and the Kondo effect [148].

Strikingly, most of the previous explanation are based on the spin current transport in the FM and do not consider possible influences of the spin current injection and detection. While we could show in our previous work that also the spin current injection needs to be taken into account, the present work clearly demonstrates that there is an additional contribution of the spin current detection mechanism.

A number of different factors need to be considered when describing the influence of temperature on the signals. For both signals, the general trend can be explained by the temperature evolution of the spin diffusion length in the conduit. The exact values depend crucially on the purity and growth of the material. For Cu typically an increase of the spin diffusion length of nearly 100 % from around 500 nm at room temperature to 900 nm at 4.2 K is observed [144, 145, 247]. This behaviour is also reflected in our measurements and explains the large signal increase with decreasing temperature.

However, since the same Cu conduit has been used for both signals, such transport explanations can not explain the differences in the temperature behaviour we observe. Another possible contribution to the signal is thermal spin currents, which can arise due to the spin dependent Seebeck effect or spin Seebeck effect. For our samples, the main heating is expect to arise at the injection Py/Cu interface, which is the same for both measurements. In order to quantify such possible contributions, we tried to measure the thermal spin current in the second harmonic probe as explained in [247]. However, no signal within the noise level could be detected, which can be attributed to low heating from the low resistive interfaces. These findings confirm that thermal spin currents as possible contributions are negligible in this work.

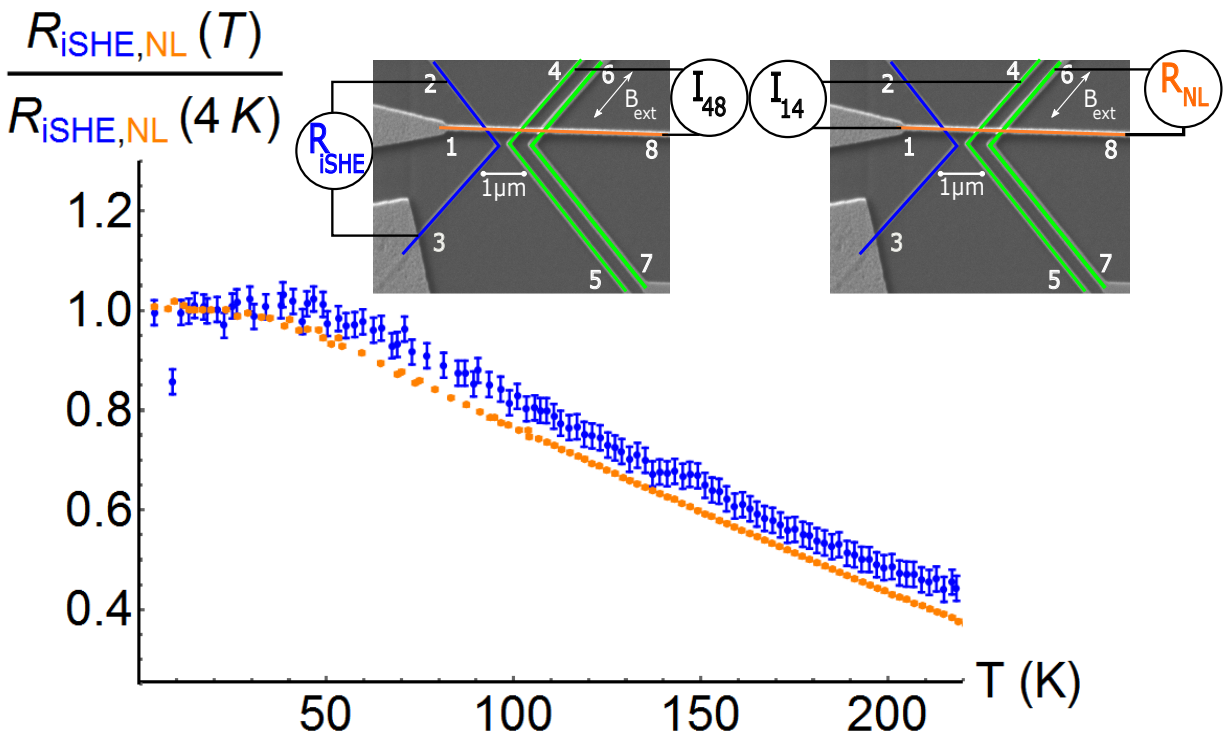

Fig. 4.7. Temperature dependence of the normalized inverse spin Hall effect signal (blue curve) and conventional non-local signal (orange curve). For these measurements, the spin current injection mechanism is the same while the spin current detection mechanisms are different. Differences in the temperature dependence are observed, which reveal a contribution of the detection mechanism in addition to the usually considered spin transport effects.

4.6. Analysis And Discussion

4.6.1. Possible contributions to the differences in the detection schemes

We now focus on possible contributions which are different for the detection scheme, e.g. a possible temperature dependent spin polarization P_{Py} of Py and a possible temperature dependence of the spin Hall angle θ_{SH} of Pt.

P_{Py}: Previous studies, including our own work, found that the spin polarization of Py is only weakly temperature dependent in the probed temperature region [147, 225, 243]. This can be explained due to the high Curie temperature of Py of 850 K.

θ_{SH}: As shown before, we find a change of the resistivity from 61 $\mu\Omega$ cm at 300 K to 36 $\mu\Omega$ cm at 4.2 K which should lead to a change of the spin Hall angle of around 1 % [253, 254].

The expected size of both these effects is not sufficient to explain the observed differences. However, they could still partly contribute to our results. A third possible contribution could arise from Kondo magnetic impurity scattering in the vicinity of the interface as a result of interdiffusion [246, 255]. This contribution could suppress the detection of the signal for the Py/Cu interface even up to room temperature [148] but would not be present for the Pt/Cu interface. However, the size of such signal suppression would be expected to be strongly temperature dependent in the here studied temperature range, since the effect only emerges around the Kondo temperature of the system. In our measurements, we essentially find a constant offset between the two normalized spin signals and we therefore exclude this explanation as the dominant contribution.

The effect we expect to be most relevant is the change of the charge current shunting by the Cu. As mentioned before, a large amount of the generated charge current in the Pt gets shunted by the very thick and highly conductive Cu. The shunting crucially depends on the changing resistivity ratio of the two materials. We find a resistivity of 8 $\mu\Omega$ cm for Cu at room temperature and a 50 % decrease to 4 $\mu\Omega$ cm at 4.2 K. Hence we expect the shunting to be more relevant for low temperatures since the reduction in resistivity is for Cu stronger than for Pt, where the resistivity changes from 61 $\mu\Omega$ cm at room temperature to 36 $\mu\Omega$ cm at 4.2 K. The resulting ratio of Cu/Pt resistivity changes by over 15 %, which is about the order of the size of the effect we find in our measurements.

4.6.2. Influence of detection probe configuration

To gain more information concerning the temperature dependent contributions of the different interfaces, we performed further temperature dependent measurements with varying detection configurations, as shown in Figure 4.8. For the case of conventional non-local injection/detection and the spin Hall effect based signals, where also conventional non-local detection is employed to detect the signals, no differences in the temperature dependence are found, as can be seen in Figure 4.8a) and Figure 4.8b), respectively. These results confirm the previous conclusions regarding the robustness of the conventional non-local detection scheme. This is different for signals which are detected by the inverse spin Hall effect, since here, depending on whether the whole Pt/Cu interface (blue curve in Figure 4.8c)) or just one side of the interface is probed (red curve in Figure 4.8c)), differences are found. This result suggests that the differences in the signals we found by the comparison of the signals for conventional non-local injection/detection and the iSHE (Figure 4.7) can be attributed to effects at the Pt/Cu interface. We can understand these findings as follows:
The conventional non-local detection is based on a generated voltage arising from chemical potential differences between the detector and the end of the conduit. In contrast, the iSHE is a generated current and therefore the signal depends crucially on the exact charge current path in the device and associated shunting. The temperature dependence of the interface modifies thereby potential current injection hotspots, which influences the iSHE signal more strongly than the conventional non-local signal. We therefore conclude that conventional non-local signals are more resilient compared to signals based on inverse spin Hall effect detection.

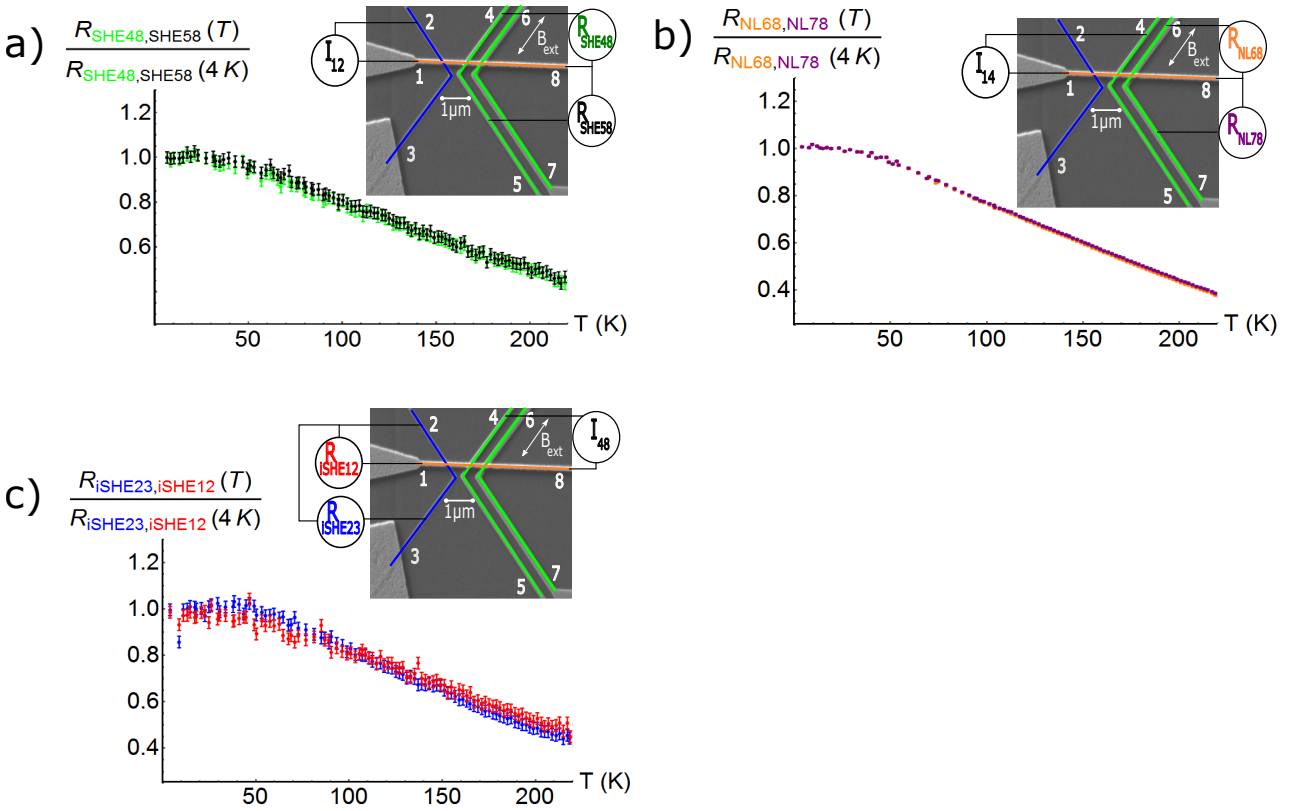

Fig. 4.8. Temperature dependence of the different effects for different injection and detection mechanisms.
a) Temperature dependence of the two normalized spin Hall effect signals measured on either side of the spin conduit. No differences between the two signals are found.
b) Temperature dependence of the two normalized conventional non-local signals measured on either side of the spin conduit. As in a), no differences between the two signals are observed.
c) Temperature dependence of the two normalized iSHE signals with the signal measured either along the whole length of the Pt stripe (blue curve) or to one side of the Pt stripe (red curve). Here we observe modest differences between the two curves in the low temperature regime.

4.7. Summary And Motivation For Further Experiments

In summary, multi-terminal Pt-Py-Cu based lateral spin valves with a special kinked geometry have been studied. The pioneered geometry allows us to connect the switching of the magnetization of the Py wires with the (inverse) spin Hall effect signal and the conventional non-local signal in one single device. All different magnetic are stable at remanence, ruling out possible fields effects and furthermore making the geometry more suitable for applications.

For the iSHE and the SHE, a signal is found which depends on the probe configuration which we explain by significant shunting of the charge current in the Cu bridge. The dependence of this signal on the used probe configuration shows that the device behaviour crucially depends on the different interfaces. The temperature dependence of all three signals is studied in the temperature range between 4.2 K and 200 K. While we find for the iSHE and the SHE the same temperature dependence as expected from Onsager reciprocity, differences are observed when comparing detection via the iSHE and conventional non-local detection. These differences clearly demonstrate that for a full description of the device both spin current injection and detection and not only spin current transport need to be taken into account.

In the last section of this chapter we show additional unpublished data. We also find quite a large iSHE signal when the right Py wire instead of the left Py wire is used as injector, as shown in Figure 4.9. Taking into account the wide separation between the right Py wire and the Pt stripe and

the fact that the right Py is 50 % wider than the left one, the observed signal implies that no significant spin absorption occurs at the left Cu/Py interface.

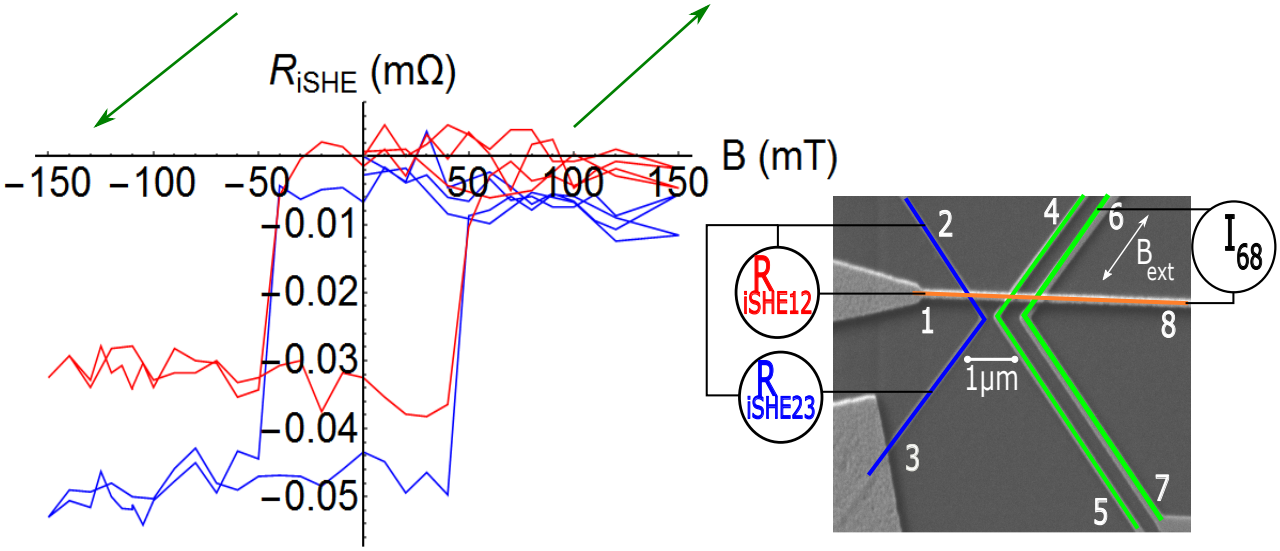

Fig. 4.9. Measured inverse spin Hall effect with the right Py wire acting as injector. In contradiction to expectations, we find a relatively large signal which can be explained by a lack of spin current absorption at the left Cu/Py interface.

This surprising result is in clear contradiction to previous measurements where the lateral spin valve geometry has been used to study spin absorption [104, 106, 107, 154, 252]. In such studies, a lateral spin valve with two FM wires and one HM/FM wire in between the two FM wires is used, as shown in Figure 4.10. By the comparison of the measured non-local signal with and without the central absorber wire, material parameters including the spin diffusion length λ, the spin polarization P_{FM} and the spin Hall angle θ_{SH} can be determined. In our measurements, we do not find significant spin absorption, calling for further investigation. Our surprising results based on Pt-Py-Cu spin valves, which allow the measurement of the conventional non-local signal, the spin absorption signal and the (inverse) spin Hall signal are shown in the next chapter.

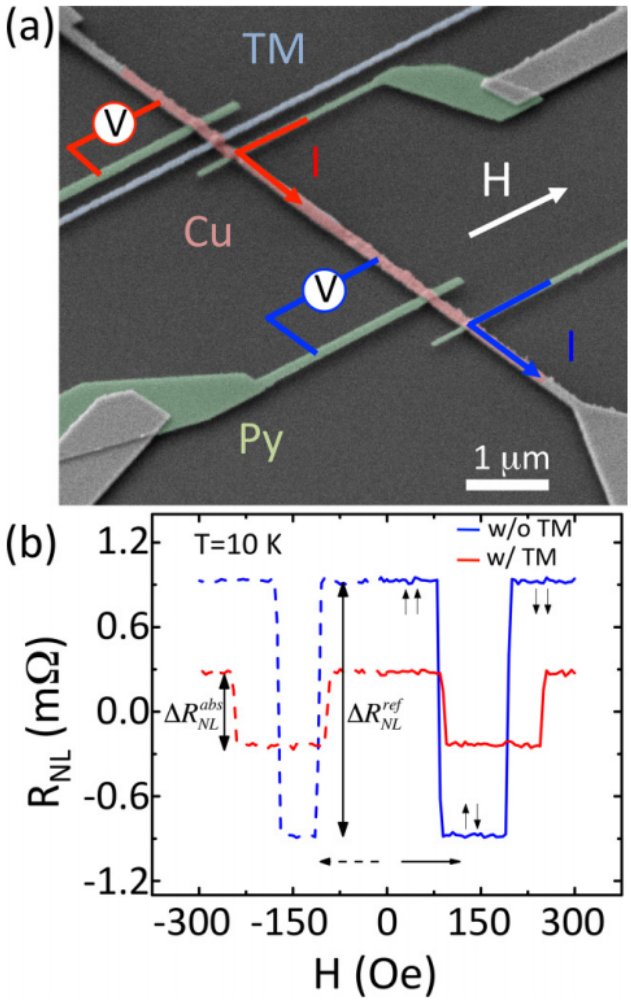

Fig. 4.10. a) Lateral spin valve geometry to study spin absorption by a HM metal, which is here a transition metal (TM).
b) Results for the conventional non-local signal (shown in blue) and the spin absorption signal (shown in red). A reduction of the signal of several hundred % is found by placing a HM/TM wire between the two FM wires. Reprinted figure 1 with permission from [254]. Copyright (2015) by the American Physical Society.

Chapter V

Spin Absorption In Ferromagnetic Metals And Nonmagnetic Heavy Metals

In this chapter we compare the non-local signal, the spin absorption signal and the (inverse) spin Hall effect signal in multi terminal Pt-Py-Cu lateral spin valves for samples based on two different recipes used to pattern the Cu bridge. For the sample based on the first recipe, we find a large (inverse) spin Hall effect but no significant spin absorption is detected. For the sample fabricated by the second recipe, strong spin absorption but a relatively low (inverse) spin Hall effect signal is determined. Furthermore, we observe differences in the temperature dependence which cannot be attributed to differences in the spin current injection/detection or spin current transport in the Cu alone but rather are explainable by the Pt/Cu interface contributions. These large differences are not apparent from conventional imaging and are not reflected in the electrical charge transport properties of our devices, which are for samples based on the different recipes very similar. Rather, we employ a special scanning electron microscope technique for buried interface imaging pioneered by Hirohata et al [256, 257] revealing important details of the interfaces, which explain the spin transport results. The work reveals the vital role of the interface quality for spin transport, which in turn is strongly dependent on the employed fabrication method.

Additional measurements in CoFe-Cu spin valves with varying fabrication methods for both the CoFe wires and the Cu bridge are performed in order to check the reliability and reproducibility of our results measured for Pt-Py-Cu lateral spin valves. Also for these measurements, here with a very wide CoFe absorption wire (a width of approximately 300 nm) we find the counter-intuitive relationship between conventional non-local signal and spin absorption, i.e. the higher the conventional non-local signal is, the lower the determined spin absorption is and vice versa. Also in these samples, the electric charge transport properties across the interfaces are very similar and cannot explain the large differences in the spin transport signals. Again, we rather connect the spin transport results with the fabrication induced interface quality.

By temperature dependent studies of these samples, we observe the same temperature behaviour for the conventional non-local and the spin absorption signal for samples with a higher interface quality. For samples with a lower interface quality, significant differences in the temperature behaviour of the two curves are determined. This is consistent with the previous results for the Pt-Py-Cu multi terminal spin valves, demonstrating that the fabrication induced interface quality is a general property of the recipes. As before, such interfacial spin transport properties are not reflected in either conventional imaging nor in the electrical charge transport properties of the interfaces.

Prof. Kläui, together with myself had the idea about the experiments based on previous counter-intuitive spin absorption results. He furthermore suggested in particular the focus of this work and to discuss in detail the role of contributions such as spin memory loss and spin transparency.

Dr. Kelvin Elphick performed the buried interface imaging and the energy-dispersive X-ray spectroscopy measurements and determined the different regions of the images of the certain interfaces.

Dr. Reeve gave a lot of valuable input and helped in great measure to understand the results and write the publication, which is currently (October 2019) under review.

5.1. Motivation And Introduction

Based on the results shown in Chapter 4, which are only explainable by very low (or even absent) spin absorption by the left Py wire, additional measurements with an optimized geometry are performed. As mentioned before, spin absorption in a lateral spin valve geometry is one of the widely used techniques for the determination of key transport parameters due to its simplicity. Here, all required parameters to determine the spin Hall angle θ_{SH} (or the spin polarization P_{FM} in the case of a ferromagnetic absorber) and the spin diffusion length λ of the absorber material are directly accessible from the experiment.

A robust method to determine θ_{SH} as the dimensionless parameter describing spin to charge conversion is of particular interest. Many different methods including spin pumping [258–260], spin Hall magnetoresistance [261] and spin orbit torque measurements [262] are exploited to determine θ_{SH} experimentally. However, even in the case of Pt, the typical spin Hall material, the determined spin Hall angles differ considerably between 0.01 and 0.20 [103, 122, 123], depending on the particular study and the technique employed. One major origin of the discrepancies is the varying material parameters of the different samples, depending on the growth mode and material purity. For instance, Sagasta et al. demonstrated that depending on the resistivity of Pt, θ_{SH} can be tuned between 0.02 and 0.01 due to varying contributions from intrinsic and extrinsic contributions [104]. Additionally the different techniques for θ_{SH} determination are based on different assumptions and therefore their validity and applicability needs to be checked.

This is in particular valid for the spin absorption method in lateral spin valves since conventional analysis assumes the spin current to be preserved across the interfaces. Therefore, the influence of the transparency of the interface [123] and spin memory loss [260, 262–264] across the interface are often not considered. Spin transparency describes the relative transmission of different spin channels across the interface based on the spin mixing conductance [163]. Spin memory loss describes the partial depolarization of the spin current caused by spin flip events as the spin current traverses the relevant interfaces. For a proper description of the spin transport through interfaces and the determination of the key transport parameters, e.g. θ_{SH} and λ_{HM} of the HM, it is required to understand these contributions to the spin transport signals. Furthermore it is necessary to correlate the amplitude of the spin signals with the quality of the interfaces, which in turn is governed by the fabrication process.

In this part of the chapter, we investigate the spin absorption method in Pt-Py-Cu multi-terminal lateral spin valves. Two different types of devices are fabricated for which different processes have been employed to pattern the nonmagnetic Cu bridge. These two different processes lead to different interface properties and in particular to fabrication induced inhomogeneities, while the charge transport properties are very similar. For samples based on both recipes, the conventional non-local signal, the spin absorption signal and the (inverse) spin Hall effect signal are compared for varying temperatures. For the sample based on the first recipe, we find a very large (i)SHE signal but no significant spin absorption. For the sample fabricated by the second recipe, we observe a low (i)SHE signal but large spin absorption. We discuss these counter-intuitive results in terms of the interface properties of our devices which are imaged via a special SEM technique for buried interface characterization. Our results highlight the sensitivity of spin transport to the interface properties that in turn strongly depend on the fabrication method.

5.2. Sample Fabrication

Lateral spin valve samples with a kinked geometry as shown in Figure 5.1 are fabricated on a sapphire substrate by electron beam lithography and lift-off techniques. In the first step, a 100 nm wide and 1 μm long wire is patterned, together with alignment markers and 16 nm of Pt is deposited using magnetron sputtering (red stripe in Figure 5.1). The Pt stripe has been fabricated with the same fabrication process as the Pt stripe of the samples presented in Section 4.3. A 200 nm thick single PMMA layer has been used and the chosen EHT for the EBL is 30 kV. In contrast to the Pt stripe fabricated in

Section 4.3, the Pt has been deposited for these samples with a rotating substrate during the growth.

In the second step, three wires, one 140 nm and two 180 nm in width, are patterned perpendicularly to the Pt wire and 25 nm of Py is deposited by UHV thermal evaporation, as for the Py wires presented in Section 4.3 (green wires in Figure 5.1). Here, the used resist is the same as for the samples presented in Section 4.3, yet with 20 kV instead of 10 kV EHT for the EBL patterning. The different widths are chosen to ensure that the Py wires have different switching fields, with the central Py wire 140 nm and the left and the right Py wires 180 nm in width. After the deposition and the lift-off process of the Py wires, the substrate has been cut in two 5·10 mm^2 pieces. For the patterning of the nonmagnetic Cu bridge, two different recipes have been used.

Recipe 1: 300 nm of PMMA has been used and the EBL has been performed using 20 kV EHT.

Recipe 2: The Cu bridge has been patterned the same as for the Cu bridges presented in Section 4.3 with a double MMA-PMMA layer with 450 nm total thickness and 10 kV EHT.

For both recipes, the expired dose to achieve high quality low ohmic interfaces has been independently optimized. The development has been performed for both recipes using one part of Methyl isobutyl ketone (MIBK) diluted in three parts of IPA for 45 seconds. The Cu growth has been performed as for the previous samples with the same in-situ etching conditions and the samples have been placed next to each other with the same orientation with respect to the in-situ argon gun. Either a 170 nm wide or a 190 nm wide Cu bridge (85 nm thick) has been deposited via UHV thermal evaporation for recipe 1 or 2, respectively, together with electric contacts (orange wire in Figure 5.1). The (slight) widening of the Cu bridge for recipe 2 is connected to the larger undercut which is caused by the use of the double layer resist compared to the single layer resist for recipe 1.

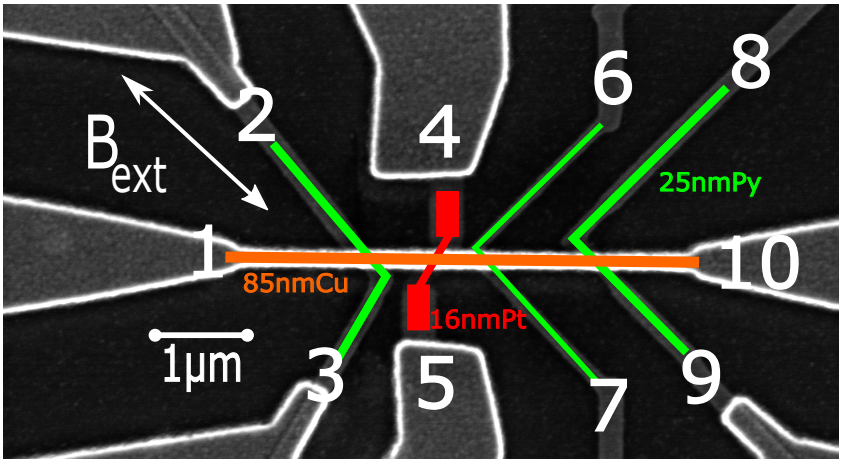

Fig. 5.1. Scanning electron microscope image of a fabricated lateral spin valve which allows a study of the non-local signal, the spin absorption signal and the (inverse) spin Hall effect in one single device. The samples consist of a 16 nm thick and 100 nm wide Pt stripe which is drawn in red and three Py wires which are 140 and 180 nm wide and 25 nm thick (drawn in green). The width of the 85 nm thick Cu bridge, which is drawn in orange, is either 170 nm for samples based on recipe 1 or 190 nm for samples fabricated by recipe 2.

5.3. Results

5.3.1. Comparison of conventional non-local and spin absorption signals

To measure the three different signals, i.e. the conventional non-local, the spin absorption and the (inverse) spin Hall effect signal at a temperature of 4.2 K, an alternating current of 1.0 mA with a frequency of 2221 Hz is applied. To generate this current, an alternating voltage of 5 V amplitude has

been applied and a 5000 Ω pre-resistor has been used before the sample. Since the nanowires have low resistances (some hundred Ω), we assume the same current for all temperatures. The small variations of the sample resistance with varying temperature which are on the order of 200 Ω for the central Py wire and less than 40 Ω for the left and right Py wire and the Pt stripe are neglected.

For the later studied temperature dependence of the signals for the sample based on recipe 2, a pre-resistor of 1100 Ω has been used in order to apply higher currents. However, since the probe configuration has been changed, the left and right Py wire as well as the Pt wire act as injector electrodes which have resistances below 120 Ω at room temperature and less than 80 Ω at 4.2 K. We therefore assume also for these measurements the same current for all measurements.

As shown in the insets of Figure 5.2, to measure the conventional non-local signal for the sample fabricated by recipe 1 (2), the current is applied between contact 6 (7) as the top (bottom) part of the central Py wire and contact 1 as the left end of the Cu bridge. The non-local voltage is measured between contact 9 (10) as the bottom (top) end of the right Py wire and contact 10 as the right end of the Cu bridge. To measure the spin absorption signal, we apply the current between contact 6 (7) and contact 10 and the non-local voltage is measured between contact 3 (2) as the bottom (top) part of the left Py wire and contact 1.

To generate both the conventional non-local and the spin absorption signal, an external field is swept between −100 mT and +100 mT parallel to the easy axes of the Py wires, as indicated in Figure 5.1. For an antiparallel magnetization alignment of the two probed Py wires, we find a low spin signal while for a parallel alignment we observe a large spin signal. The magnetization orientations of the different Py wires are drawn as green arrows above the plots in Figure 5.2. As for the previous measurements, the non-local resistance R_{NL} is defined as the measured non-local voltage, divided by the applied current. The (inverse) spin Hall effect resistance $R_{\mathrm{(i)SHE}}$ is defined as the measured (i)SHE voltage, divided by the applied current. All hysteresis curves are shifted to 0 mΩ signal for a parallel magnetization alignment which allows a better comparison of the different plots. The error bars for the different temperature dependent curves are calculated as $\Delta_{\mathrm{tot}} = \sqrt{(\Delta_{\mathrm{AP}})^2 + (\Delta_{\mathrm{P}})^2}$ with $\Delta_{\mathrm{AP,P}}$ as the standard derivation of the signals for positive and negative spin states, just as for the previous measurements. The reduction of the spin signals via spin absorption is calculated as $(1\text{-}(R_{\mathrm{Abs}}/R_{\mathrm{NL}}))$.

Firstly, we compare the two conventional non-local signals for the samples based on the two different recipes, as shown in Figure 5.2a). We observe a signal of 1.10±0.01 mΩ for the sample based on recipe 1 (red curve) and a signal of 0.34±0.01 mΩ (blue curve) for the sample fabricated by recipe 2. We find that samples fabricated by recipe 1 consistently yield a factor of 3 higher spin signals compared to samples based on recipe 2. Since the electric interface resistances are very similar for samples based on the two recipes (in the mΩ-range), the differences in the signals cannot be explained by different charge transport interface resistances. Additionally we emphasize that for all measurements the different possible injector/detectors permutations have been checked, with at most 25 % variations of the different signals for the different configurations within one device. In this chapter, the highest measured spin signals are shown, which accounts for the different indicated probe configurations for the different recipes.

Next we compare the spin absorption signals for the samples based on the two recipes, as shown in Figure 5.2b). Here even larger differences for samples based on the two recipes are observed. For the sample based on recipe 1, the spin absorption signal is 0.90±0.01 mΩ (green curve) and thus about 20 % smaller than the conventional non-local signal. Hence within our variations of 25 % for the injector/detector configurations, we do not determine significant spin absorption at the Pt/Cu interface for the samples fabricated by recipe 1.

For the sample fabricated by recipe 2, however, we observe a spin absorption signal of 0.08±0.01 mΩ (orange curve), resulting in a reduction of 76±3 % of the non-local signal from the case without the intermediate Pt electrode and therefore a large spin absorption. The determined results for the sample based on recipe 2 with a reduction of the signal of 76 % for Pt as an absorber material with large spin orbit coupling agree well with findings in the literature, where the absorption of various spin Hall effect materials including Pt [104, 154], CuBi [107] and AuTa [109] has been studied in lateral spin

valves. However the lack of differences in the two signals for the samples based on recipe 1, despite the very high non-local signal for an electrode separation of 1.1 μm is unexpected and calls for further investigation. In order to get further insight into the differences we compare in the next subsection the spin absorption signals to the (inverse) spin Hall effect signals in the heavy metals.

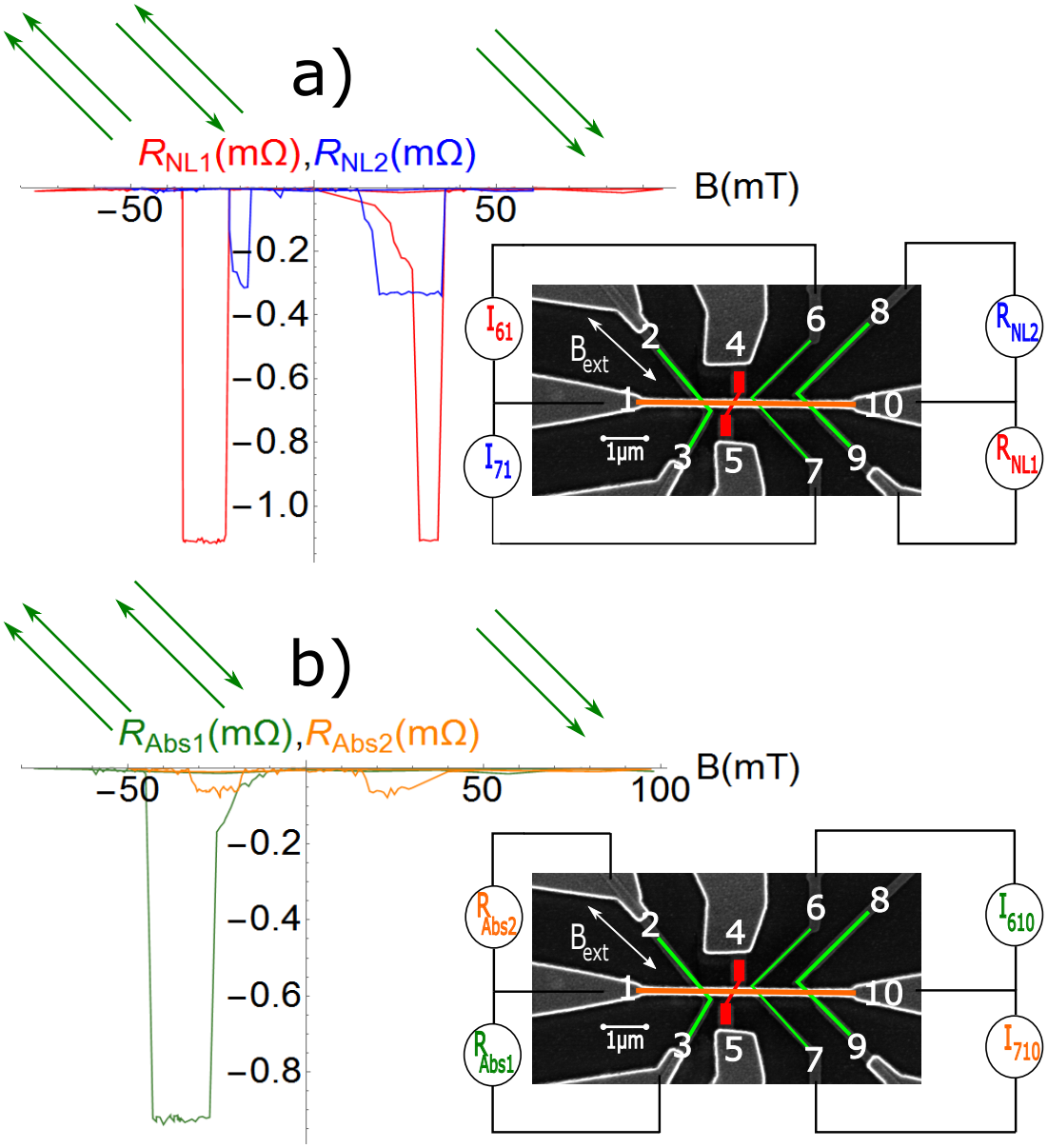

Fig. 5.2. Conventional non-local signal and spin absorption signal as a function of applied external field at 4.2 K and the used probe configuration for the samples based on the different recipes. To generate both signals the external field is swept along the easy axes of the Py wires and the magnetization orientations of the probed wires are drawn as green arrows above the plots.
a) Conventional non-local signal. For the sample based on recipe 1, a signal of 1.10±0.01 mΩ is found (red curve), while for the sample fabricated by recipe 2 a signal of 0.34±0.01 mΩ is determined (blue curve).
b) Spin absorption signal. For the sample based on recipe 1, we find a signal of 0.90±0.01 mΩ (green curve) while for the signal fabricated by recipe 2, a signal of 0.08±0.01 mΩ is found (orange curve).

5.3.2. Comparison of (inverse) spin Hall effect signals

As in Chapter 4, the inverse spin Hall effect signal is measured by applying the same current with the same frequency as for the conventional non-local signal and the spin absorption signal in the central

Py wire. Since the generated charge current in the Pt stripe J_{iSHE} is given as

$$J_{\mathrm{iSHE}} \propto J_s \times \sigma \tag{5.1}$$

J_{iSHE} changes its polarisation by an reversal of the spin current orientation J_s. By sweeping the external field H_{ext} the magnetization orientation and therefore the spin current orientation of the injector reverses and we observe two levels in the iSHE signal. The results for the measurements at 4.2 K are shown in Figure 5.3 for the sample based on recipe 1 in brown and for the sample based on recipe 2 in purple. The magnetization orientation of the central Py wire is indicated with a green arrow above the plot. We find for the sample fabricated by recipe 1 an inverse spin Hall effect signal of $0.40\pm0.01\,\mathrm{m\Omega}$ and for the sample based on recipe 2 an inverse spin Hall effect signal of $0.08\pm0.01\,\mathrm{m\Omega}$. It is emphasized that the size of the signal for the sample based on recipe 2 is the same as observed in Chapter 4 where also recipe 2 has been used for the fabrication of the Cu bridge, demonstrating the reproducibility of the measurements.

However, the difference of the iSHE signals in relation to the difference of the spin absorption signals is at first sight counter-intuitive:

One would expect that a large reduction of the spin signal by absorption into the Pt stripe should be connected with a large inverse spin Hall effect signal in the Pt, if both signals are based on the same spin current. From these measurements, we conclude that the size of the so-called spin absorption signal is not only related to the intrinsic properties of the Pt stripe. Rather the Pt/Cu interfaces are of key importance. As a result, additional contributions, which reduce the spin current without contributing to the inverse spin Hall effect, such as interface spin memory loss, need to be taken into account [260, 262–264].

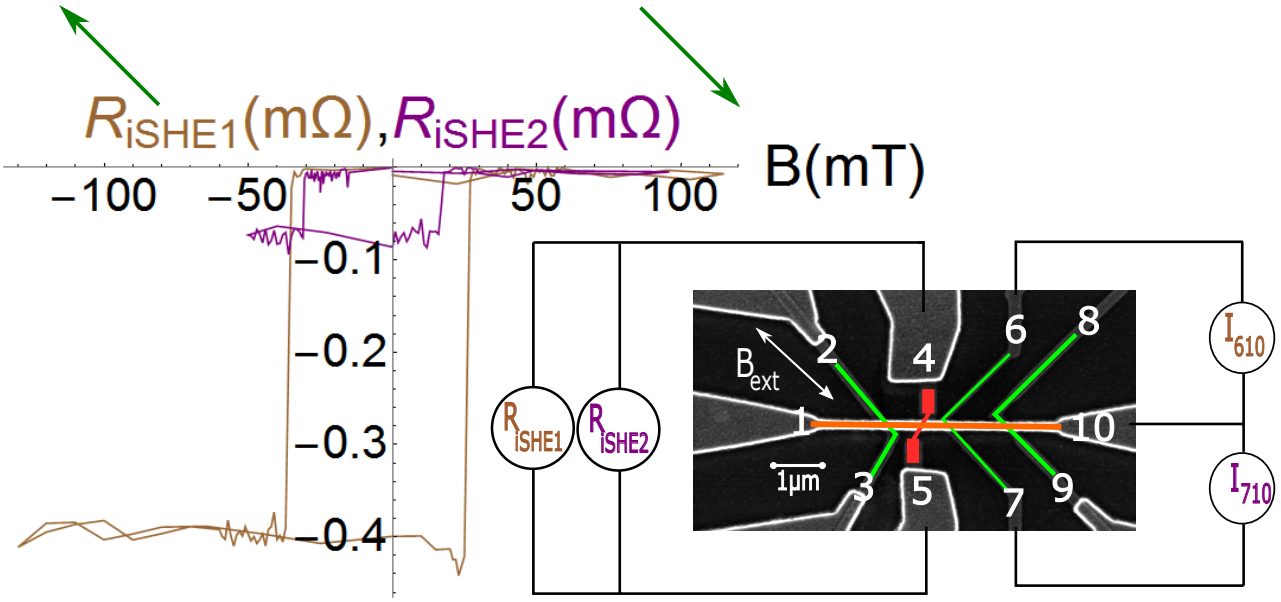

Fig. 5.3. Measured iSHE signals for the samples based on the different recipes at 4.2 K by sweeping the external field along the easy axis of the central Py wire. For the sample based on recipe 1, a signal of $0.4\pm0.01\,\mathrm{m\Omega}$ is found (brown curve) while for the sample based on recipe 2, a signal of $0.08\pm0.01\,\mathrm{m\Omega}$ is determined (purple curve).

To study the impact of contributions which reduce the spin current without contributing to the (i)SHE, we probe the normalized temperature dependence of the spin Hall effect signal for the samples based on the two recipes, as shown in Figure 5.4a). As mentioned before, the spin Hall effect has been used since the Pt stripe has a very low resistance and therefore a pre-resistor with lower resistance could be used in order to apply higher currents. Due to Onsager reciprocity, which has been explicitly

checked again for the sample based on recipe 1 (Figure 5.4c)), varying the probe configuration does not change the signal.

We find for temperatures between 50 K and 200 K a stronger decrease of the normalized spin Hall effect signal measured for the sample based on recipe 1 compared to recipe 2. These differences can be explained by a strong temperature independent reduction of the spin current, which partially supersedes and thus masks the temperature dependent contribution. As a result, the decrease of the spin diffusion length in the Cu bridge with increasing temperature as expected from Elliot-Yafet theory, as explained in Section 4.5, is less dominant for the sample fabricated by recipe 2 compared to the sample fabricated by recipe 1. If the two Pt/Cu interfaces for the samples based on the two recipes are indeed significantly different (despite the very similar electric interface resistances) it is expected that these differences should also affect the temperature behaviour of both the conventional non-local and the spin absorption signal for samples based on the different recipes. This will be checked in the next subsection.

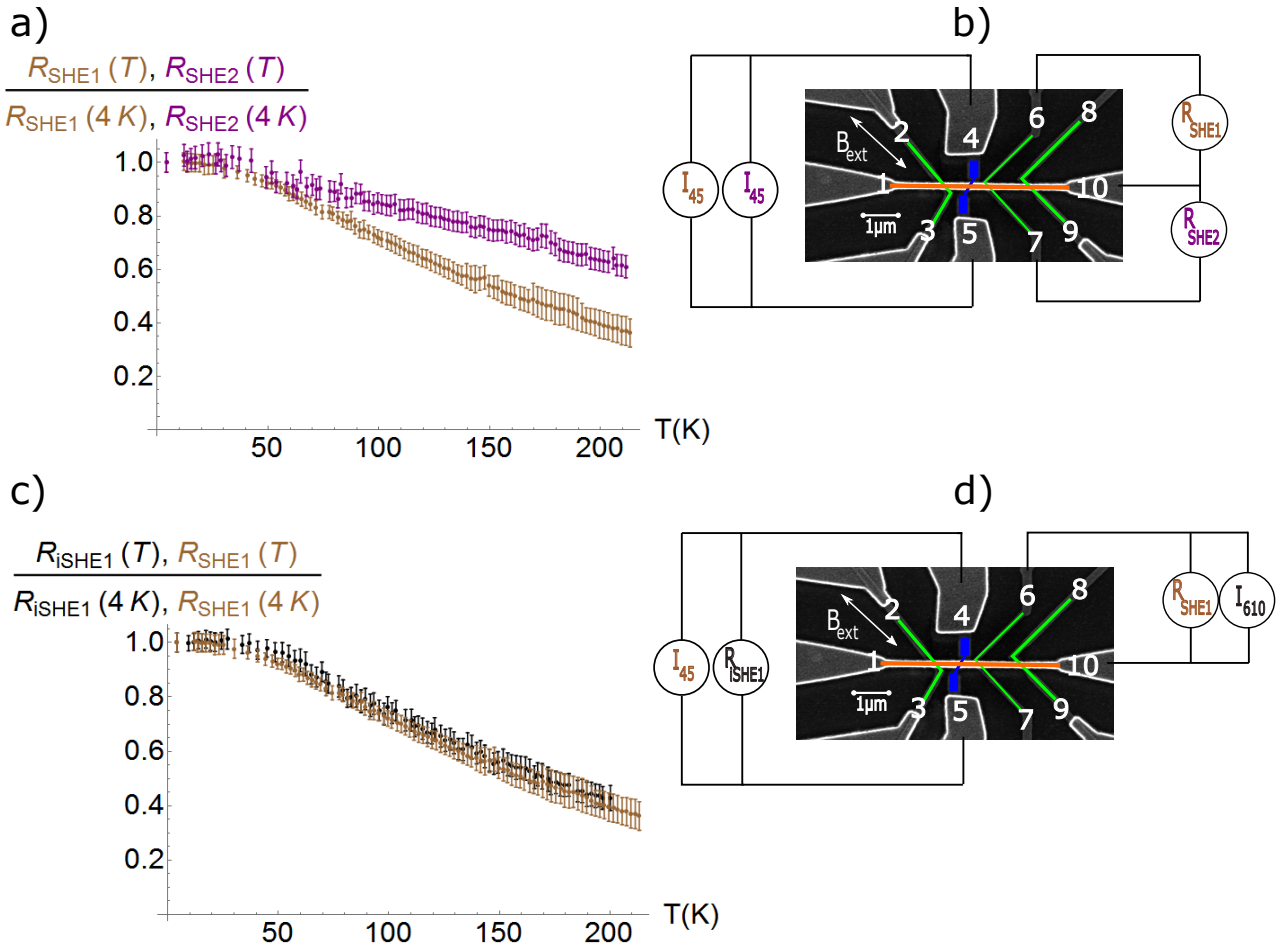

Fig. 5.4. (Inverse) spin Hall effect signals for varying temperatures for the samples based on the two different recipes.
a) Normalized spin Hall effect signal as a function of temperature for the sample based on recipe 1 (brown curve) and recipe 2 (purple curve). We find for the sample based on recipe 1 a much stronger decrease of the signal with increasing temperature.
b) Probe configuration for the two signals shown in a).
c) Normalized spin Hall effect (brown curve) and inverse spin Hall effect (black curve) signal as a function of temperature for the sample fabricated by recipe 1. As expected from Onsager reciprocity, we find the same temperature behaviour.
d) Probe configuration for the two signals shown in c).

5.3.3. Temperature dependence of conventional non-local and spin absorption signals

In this subsection, we compare the temperature dependence of the conventional non-local and the spin absorption signal for the samples based on the two recipes, as shown in Figure 5.5. As expected from the measurements at a temperature of 4.2 K, the two signals, measured in the sample based on recipe 1, are equivalent within the error bars (red and green curve). This is different for the signals measured in the sample fabricated by recipe 2, where we observe a significant stronger reduction of the spin absorption signal for increasing temperatures.

In previous publications, differences in the temperature behaviour during the spin transport have been usually attributed to spin transport effects such as increased surface scattering [145, 243] or the Kondo effect [148]. Since here, the Cu conduit and the Py/Cu interfaces are the same for a given recipe, all changes between the non-local and the spin absorption signal must be connected to the additional Pt/Cu interface.

These large differences, combined with the equivalence of the signals for the sample based on recipe 1, support our findings concerning the (inverse) spin Hall effect signals. A significant amount of the generated spin current in the sample based on recipe 2 is thus lost due to spin flip events at the interface and does not contribute to the (i)SHE signal. To understand the origin of the different behaviour one needs to characterize the interfaces. Conventional structural imaging using scanning electron microscopy techniques do not allow for imaging interfaces. Consequently, a technique for buried interface imaging by employing a decelerated electron beam has been used to reveal important details of the relevant interfaces, as explained in detail in [256, 257]. The analysis of the buried interfaces is shown in the next subsection.

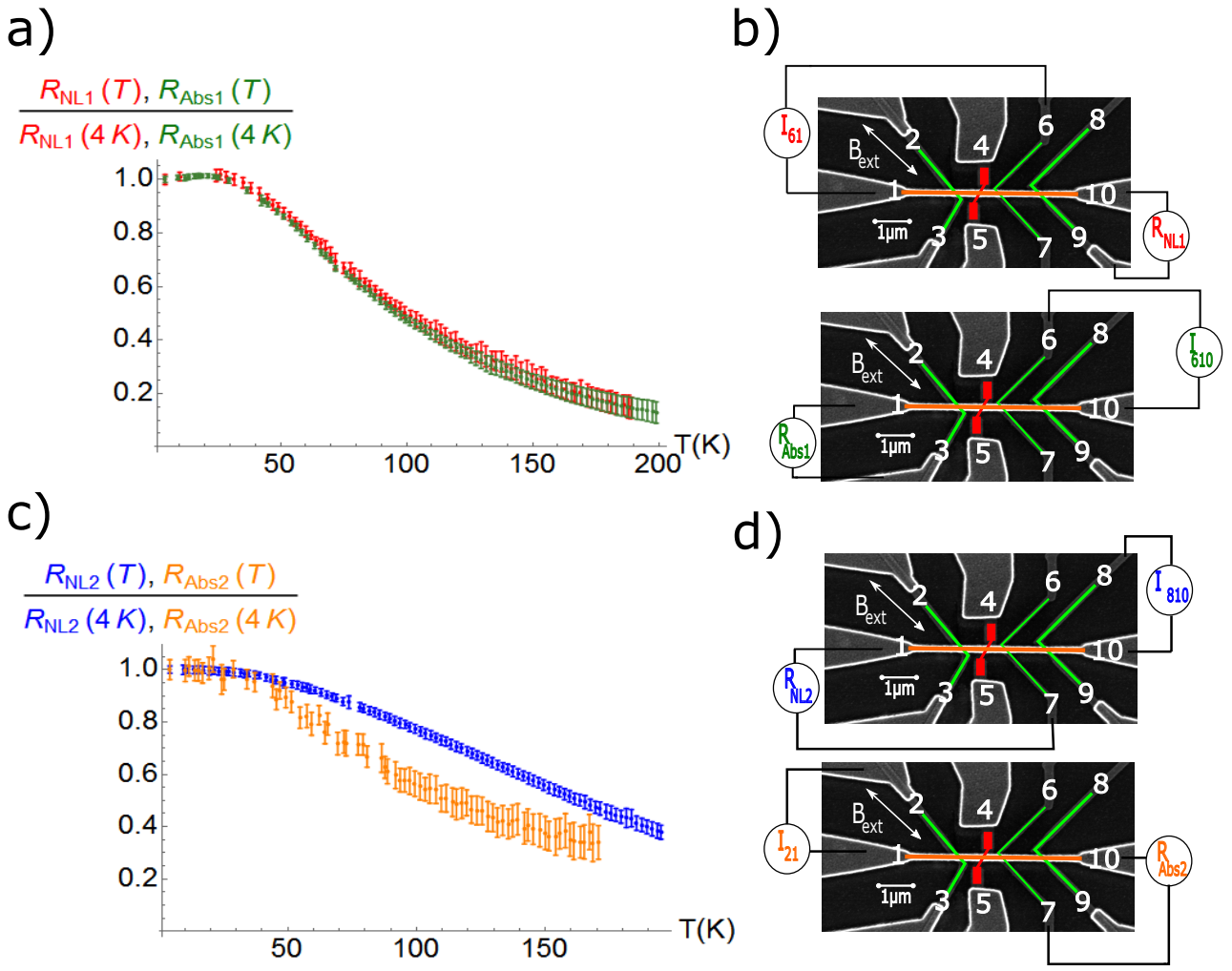

Fig. 5.5. Temperature dependence of the normalized conventional non-local and spin absorption signal for the samples based on the different recipes.
a) Temperature dependence of the conventional non-local signal (red curve) and the spin absorption signal (green curve) for the sample based on recipe 1. Within the error bars, the two curves are equivalent.
b) Probe configuration of the two studied signals for the sample based on recipe 1.
c) Temperature dependence of the conventional non-local signal (blue curve) and the spin absorption signal (orange curve) for the sample fabricated by recipe 2. In the temperature range between 50 K and 200 K we find a stronger decrease of the spin absorption signal with increasing temperature.
d) Probe configuration of the two studied signals for the sample fabricated by recipe 2.

5.3.4. Direct imaging of the buried Pt/Cu and Py/Cu interfaces

In this subsection, images of the buried Pt/Cu and Py/Cu interfaces are shown in Figure 5.6, which allow for a direct comparison of the size of the obtained spin signals with the interface quality for samples based on the different recipes. While we did not image the exact same samples used for the spin transport experiments, samples with nominally identical conditions grown on the same chip have been imaged. Given the good reproducibility of the transport results for samples fabricated with the different recipes, the results will be representative.

Individual SEM images have been taken using different acceleration voltages which are selected based on the results of a "CASINO" electron trajectory simulation [265]. The selected voltages for analysing the Cu/Py interface are 4.8 keV and 5.1 keV, while for analysing the Cu/Pt interface, voltages of 4.9 keV and 5.1 keV have been used. An upper electron detector has been used in order to maximize the back-

scattered electron signal, which provides depth information of the sample and material dependent contrast, as described in Section 2.1.2. The images, taken with different acceleration voltages, have been compared using a "MATLAB" script. In this manner, the contrast and the alignment of the images has been re-adjusted and a processed image is generated.

Within this thesis, representative images of the Pt/Cu and the central Py/Cu interfaces are shown, since the left and right Py/Cu interfaces show analogous results to the central one. As is evident in Figure 5.6a) and Figure 5.6b), significantly less inhomogeneities are observed for the sample fabricated by recipe 1 compared to the sample based on recipe 2, which can be quantified via the "effective defect free interface area" EA. These effective areas, marked by red boxes, can be understood as the area without significant detectable inhomogeneities, divided by the total area. It is emphasized that the effective areas should not be mistaken with the contact area of the interfaces, since the non-local signal scales reciprocally with the contact area [266] which is not the case for the described EA. Rather the EA corresponds to interface regions where efficient spin transport is expected. Within a clean area, single defects are marked as green circles. The areas marked in yellow are related to the varying thickness of the Pt and Py wires, caused by the in-situ milling procedure which decreases the thickness of the previously exposed parts of the Pt stripe and the Py wires prior to the Cu bridge deposition.

For the sample based on recipe 1 much more homogeneous Pt/Cu and Py/Cu interfaces are observed, resulting in an effective area of 73 % for the Pt/Cu and 70 % for the central Py/Cu interface. In particular for the sample fabricated by recipe 2, we observe a shadow region at the top edge of the Pt/Cu and the Py/Cu interface which are marked as blue boxes in the plots. This shadow region is also observed for the left and the right Py/Cu interface. Due to these shadow regions, the EA is significantly reduced down to 60 % for the Pt/Cu and 50 % for the central Py/Cu interface. As a result, significantly more spin relaxation at the interfaces may be expected to occur for samples based on recipe 2. This is consistent with the spin transport results where both a lower (i)SHE signal and a larger reduction of the non-local signal is found, compared to samples fabricated by recipe 1 which have better interfaces.

The worse interface quality in general for samples fabricated by recipe 2 compared to samples based on recipe 1 is further supported by EDX measurements, as shown in Figure 5.6c). While for samples fabricated by recipe 1 the EDX results are as expected based on the sample design, we find for samples based on recipe 2 some additional Cu content at the Py/Cu and the Pt/Cu edges, which is marked with yellow ellipses in the plot. As a result, recipe 2 leads to Cu content at undesired positions, which is consistent with the lower quality of the interfaces for samples based on recipe 2.

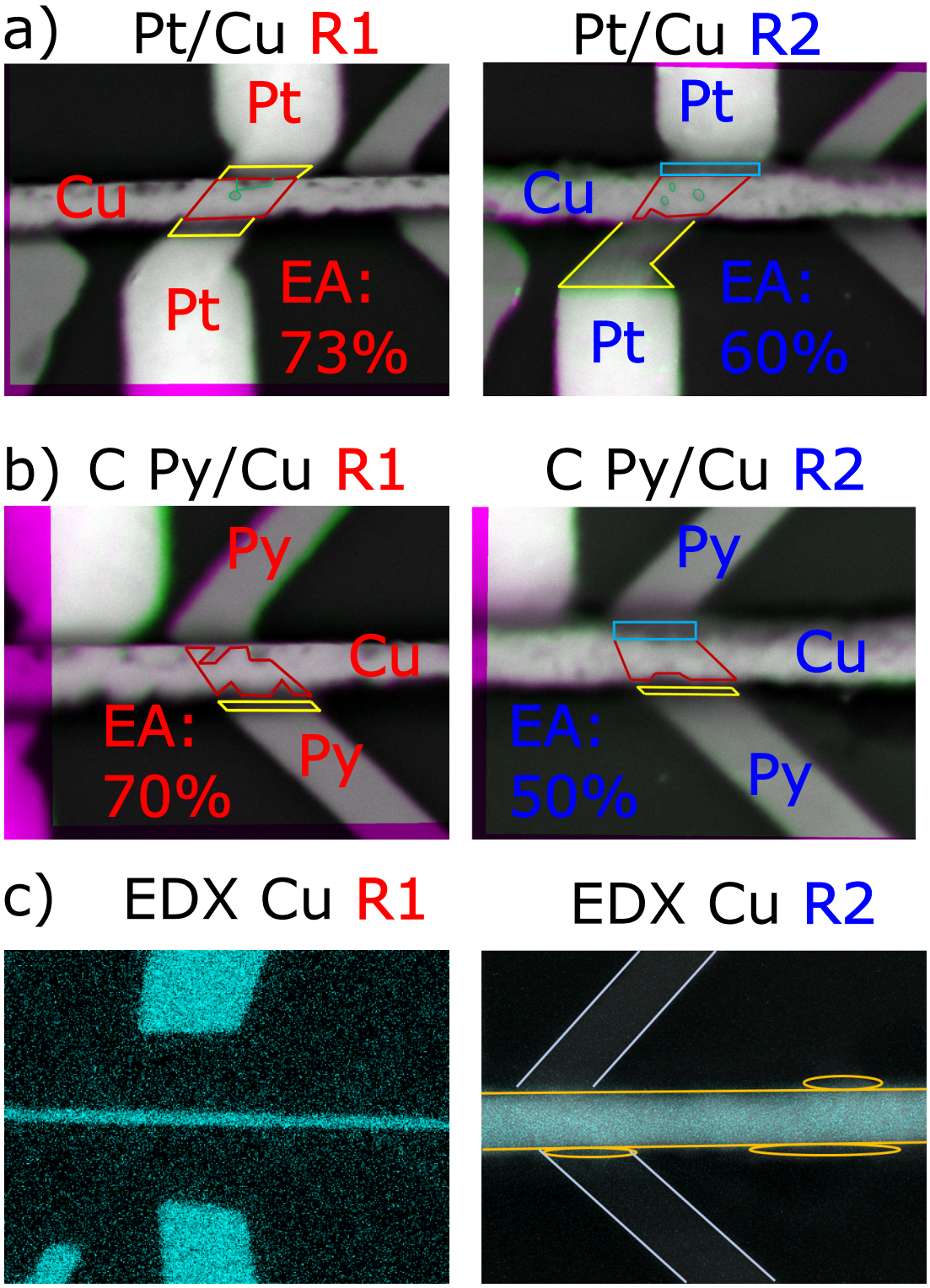

Fig. 5.6. a), b) Imaging of buried Pt/Cu and Py/Cu interfaces of samples based on the two different recipes. Regions marked by the red boxes indicate an effective area with a low amount of defects. Single defects within the red areas are marked by green circles. We find for samples based on recipe 2 shadow regions (marked by the blue boxes) at the top edge of the Cu/Pt and the Cu/Py interfaces, reducing significantly the effective defect free interface area EA. The yellow marked areas indicate the variation of the thickness of the Pt stripe and the Py wires, caused by the in-situ milling procedure. c) Performed EDX measurements for the Cu content of the samples based on the different recipes. For samples based on recipe 2, additional Cu content at the edges of the Cu wire is found (marked by the yellow ellipses), consistent with the lower quality of the interfaces of samples based on recipe 2 compared to samples fabricated by recipe 1.

5.4. Analysis And Discussion

As explained in Section 2.3, double-layer resists are usually employed to ease the lift-off procedure for thick deposited films. However, the work presented in this chapter clearly demonstrates that the device performance depends significantly on the used patterning process and deposition conditions since they lead to different interface qualities. These different interface qualities are neither detectable by charge transport measurements of the devices nor by conventional SEM imaging. However, these results have direct consequences for the determination of key transport parameters such as θ_{SH} and λ_{HM}. This is evident by the different estimates of both parameters for the different samples. In order to firstly determine λ_{HM}, we use the formula for $\Delta R_{\mathrm{abs}}/\Delta R_{\mathrm{NL}}$, which is given by [104]

$$\frac{\Delta R_{\mathrm{abs}}}{\Delta R_{\mathrm{NL}}} = \frac{2Q_{\mathrm{Pt}}\left[s(a) + 2Q_{\mathrm{Py}}e^{a} + 2Q_{\mathrm{Py}}^{2}e^{a}\right]}{c(a) - c\left(\frac{L-2d}{\lambda_{\mathrm{Cu}}}\right) + 2Q_{\mathrm{Py}}\cdot s(a)\cdot e^{\left(\frac{L-d}{\lambda_{\mathrm{Cu}}}\right)} + 2Q_{\mathrm{Pt}}\cdot s(a) + 4Q_{\mathrm{Py}}Q_{\mathrm{Pt}}e^{a} + 2Q_{\mathrm{Py}}e^{a}\cdot s\left(\frac{L-d}{\lambda_{\mathrm{Cu}}}\right) + 2Q_{\mathrm{Py}}^{2}e^{a} + 4Q_{\mathrm{Py}}^{2}Q_{\mathrm{Pt}}e^{a}} \tag{5.2}$$

with $a =: L/\lambda_{\mathrm{Cu}}$, $c =: \cosh$ and $s =: \sinh$. We furthermore define

$$Q_{\mathrm{Py}} = \frac{R_{\mathrm{Py}}}{R_{\mathrm{Cu}}} \qquad Q_{\mathrm{Pt}} = \frac{R_{\mathrm{Pt}}}{R_{\mathrm{Cu}}} \tag{5.3}$$

with R_{Py}, R_{Pt} and R_{Cu} as the spin resistances, defined as

$$R_{\mathrm{Cu}} = \frac{\lambda_{\mathrm{Cu}}\rho_{\mathrm{Cu}}}{w_{\mathrm{Cu}}t_{\mathrm{Cu}}}, \qquad R_{\mathrm{Py}} = \frac{\lambda_{\mathrm{Py}}\rho_{\mathrm{Py}}}{w_{\mathrm{Py}}w_{\mathrm{Cu}}(1-P_{\mathrm{Py}}^{2})} \qquad R_{\mathrm{Pt}} = \frac{\lambda_{\mathrm{Pt}}\rho_{\mathrm{Pt}}}{w_{\mathrm{Pt}}w_{\mathrm{Cu}}\tanh\left(\frac{t_{\mathrm{Pt}}}{\lambda_{\mathrm{Pt}}}\right)} \tag{5.4}$$

$\rho_{\mathrm{Cu,Py,Pt}}$, $\lambda_{\mathrm{Cu,Py,Pt}}$, $w_{\mathrm{Cu,Py,Pt}}$ and $t_{\mathrm{Cu,Pt}}$ are the resistivities, spin diffusion lengths, widths and thicknesses of the materials. P_{Py} is the spin polarisation of Py, L is the distance between the Py electrodes while d is the distance between the Py electrode and the Pt stripe. Assuming λ_{Cu} to be 900 nm, λ_{Py} to be 5 nm and P_{Py} to be 0.35 at 4.2 K the spin diffusion length of Pt, λ_{Pt}, is the only free parameter and thus can be determined for the samples based on two recipes. We determine (assuming $\Delta R_{\mathrm{abs}}/\Delta R_{\mathrm{NL}} = 0.8$) λ_{Pt1} to be 19 nm for the sample based on recipe 1, while for the sample fabricated by recipe 2 we determine λ_{Pt2} to be 3 nm. Analogously we use [254]

$$\frac{\overline{I_s}}{I_c} = \frac{\lambda_{\mathrm{Pt}}\left(1-e^{\left(-\frac{t_{\mathrm{Pt}}}{\lambda_{\mathrm{Pt}}}\right)}\right)^{2}}{t_{\mathrm{Pt}}\left(1-e^{\left(-2\frac{t_{\mathrm{Pt}}}{\lambda_{\mathrm{Pt}}}\right)}\right)} \times \frac{2P_{\mathrm{Py}}\left[Q_{\mathrm{Py}}s\left(\frac{L-d}{\lambda_{\mathrm{Cu}}}\right) + 2Q_{\mathrm{Py}}^{2}e^{\left(\frac{L-d}{\lambda_{\mathrm{Cu}}}\right)}\right]}{c(a) - c\left(\frac{L-2d}{\lambda_{\mathrm{Cu}}}\right) + 2Q_{\mathrm{Py}}\cdot s(a)e^{\left(\frac{L-d}{\lambda_{\mathrm{Cu}}}\right)} + 2Q_{\mathrm{Pt}}\cdot s(a) + 4Q_{\mathrm{Py}}Q_{\mathrm{Pt}}e^{a} + 2Q_{\mathrm{Py}}e^{a}\cdot s\left(\frac{L-d}{\lambda_{\mathrm{Cu}}}\right) + 2Q_{\mathrm{Py}}^{2}e^{a} + 4Q_{\mathrm{Py}}^{2}Q_{\mathrm{Pt}}e^{a}} \tag{5.5}$$

in order to determine the spin Hall angle θ_{SH} of Pt. In Equation 5.5 $\overline{I_s}$ is the effective spin current contributing to the iSHE in Pt. The spin Hall conductivity σ_{SH} is then given as [267]

$$\sigma_{\mathrm{SH}} = \sigma_{\mathrm{Pt}}\frac{w_{\mathrm{Pt}}}{x_{\mathrm{Pt}}}\left(\frac{\overline{I_s}}{I_c}\right)\Delta R_{\mathrm{iSHE}} \tag{5.6}$$

with $2\Delta R_{\mathrm{iSHE}}$ as the observed iSHE signal and x_{Pt} the shunting factor which has been described in Chapter 4. x_{Pt} takes into account the shunting of the generated charge current in the Pt by the highly conductive Cu. The shunting factor x_{Pt} is assumed to be 0.36 since the present situation is very similar to the situation described in [252] where the shunting factor has been determined to be 0.36±0.08 . By the determination of σ_{SH}, we are able to calculate the spin Hall angle θ_{SH} as follows

$$\theta_{\mathrm{SH}} = \frac{\sigma_{\mathrm{SH}}}{\sigma_{\mathrm{Pt}}} \tag{5.7}$$

and determine θ_{SH1} to be 1.6 % for the sample based on recipe 1 and θ_{SH2} to be 0.16 % for the sample fabricated by recipe 2. Hence again depending on the interface quality, there is an order of magnitude

difference in the determined key transport parameters, similar to the spread seen in the reports from different groups in the literature [103, 123, 268].

To explain the strong reduction of the spin absorption signal together with the low (i)SHE signal measured in the sample based on recipe 2, we consider different possible contributions. One possibility is that residual resist is present at the interface and the contamination and associated disorder in those regions (which are marked by the blue boxes) lead to enhanced spin flip scattering, leading to spin memory loss. Furthermore the structural disorder could modify the bond-modelling and related spin transparency of the interface.

However, the situation is different for the sample based on recipe 1. For recipe 1, we find that the interfaces are of significantly higher quality and additionally, no differences in the temperature behaviour of between the conventional non-local and the spin absorption signal have been seen. These results reveal strong differences depending on the interface homogeneity. As a result, spin transparency and spin memory loss must be taken into account to explain the surprising high (i)SHE signal and the surprising low spin absorption. The results suggest that there is little spin memory loss at the Pt/Cu interface for the samples based on recipe 1. Consequently, there is no significant reduction of the spin absorption signal compared to the conventional non-local signal, in contrast to the sample based on recipe 2. However, it is emphasized that little spin memory loss does not necessarily lead to a large (i)SHE signal, which additionally crucially depends on the transparency of the interface. As evident, due to the finite spin diffusion length in Pt, only the spin accumulation that has passed across the Pt/Cu interface and is not reduced by spin memory loss can be scattered and consequently contribute to the (i)SHE.

As evident from the strong variation of the effective transport parameters, the spin absorption method faces challenges due to its strong sensitivity to the different interfaces, which crucially depend on the fabrication method. As a result, strong variations of the determined spin transport parameters are possible. Experimental methods which are based on thin films and do not require a multi-step lift-off process, e.g. spin pumping [258, 260, 268], spin torque ferromagnetic resonance [123] or spin orbit torque measurements [262] might be more suitable for an accurate spin transport parameter determination. While also in these measurements contributions such as spin transparency and spin memory loss need to be considered, possible problems with residual resist and other fabrication related inhomogeneities at the interfaces are less relevant.

We can furthermore conclude that in addition to the intrinsic properties of Pt (θ_{SH} and λ_{Pt}), which are relevant to explain the device behaviour, interface contributions such as spin transparency and spin memory loss play a decisive role. For a proper characterization of the interfaces, both temperature dependent spin transport and buried interface characterization are necessary, since the subtitle differences leading to very interface different spin transport properties are not revealed by charge transport measurements or by conventional imaging. Especially the correlation between the fabrication method and the resulting interfaces characterized by buried interface imaging and spin transport measurements provides invaluable insights into the device performance. In particular it reveals the strong sensitivity of the spin transport properties to the fabrication recipe. In order to maximize the spin signals, in addition to a careful tailoring of the relevant interfaces, material combinations with minimized spin memory loss and maximized spin transparency, e.g. by suitable band structure matching [269] are promising.

5.5. Motivation For Further Experiments

Up to now in this chapter of the thesis, multi terminal Pt-Py-Cu lateral spin valves have been studied which allow for a comparison of the (inverse) spin Hall effect signal with the size of the spin absorption signal for two fabrication recipes of the Cu bridge. Samples based on the different fabrication recipes show very similar interface charge transport properties. However, very different spin absorption and (i)SHE are found for samples based on the different recipes.

For the sample based on the first recipe (single PMMA layer), a large (i)SHE signal is determined

but no significant spin absorption is found. Within the error bars, the temperature dependence of the conventional non-local signal and the spin absorption signal is equivalent.
For the sample based on the second recipe (dual MMA/PMMA layer), a low (i)SHE signal is found but a reduction of the spin signal of 76±3 % is observed. Significant differences in the temperature dependence of the conventional non-local and the spin absorption signal are found, with a much stronger reduction of the spin absorption signal with increasing temperature.

These large differences of the signals are explained by interface spin memory loss and spin relaxation at the Pt/Cu interface due to the varying interface quality. By performing direct imaging of the buried Pt/Cu and Py/Cu interfaces, we observe significantly higher quality interfaces for samples based on recipe 1 compared to recipe 2. Thus we are able to directly link the obtained spin signal with the imaged structural interface quality, which in-turn is determined by the fabrication method.

The results clearly demonstrate that for a full understanding of spin transport through interfaces, not only the electric charge transport properties but additionally the interface spin transport properties are crucial. One prominent example in the work presented in this chapter is the fact that strongly varying effective transport parameters are determined depending on the sample and thus on the fabrication method. While for recipe 1 the spin Hall angle θ_{SH1} is determined to be 1.6 %, for recipe 2 the spin Hall angle is determined to be θ_{SH2} =0.16 %. For the spin diffusion length, λ_{Pt}, values of 19 nm (for the sample based on recipe 1) and 3 nm (for the sample based on recipe 2) are determined. It is concluded that the widely used spin absorption method is not robust due to its strong sensitivity to the interface quality, which is not revealed in conventional imaging or by electrical interface characterization.

In order to check the extent to which our results are valid for different systems, in particular the correlation between the size of the signals and the absence or presence of spin absorption by a FM/HM absorber and the used fabrication method, we have performed additional spin absorption measurements in CoFe-Cu lateral spin valves, as presented in the next sections.

5.6. CoFe-Cu Lateral Spin Valves

5.6.1. Measured signals at 4.2 K in samples fabricated by different EHT and Cu bridge recipes

In the fabricated CoFe-Cu samples, we have varied the EHT for the CoFe patterning (10 kV, 20 kV and 30 kV) but the same 200 nm thick PMMA resist has been used. For each value of the EHT for the CoFe patterning, the two different recipes for the Cu bridge have been used. A SEM image of the studied devices is shown in Figure 5.7. We note here that the two 30 kV EHT samples (with 36 nm thick CoFe wires) have been patterned on the same chip, while the other four samples have been patterned on a second chip (with 25 nm thick CoFe wires). However, all important process parameters such as development time, in-situ etching time, sample position in the deposition chamber etc. have been chosen to be the same as far as possible in order to minimize their potential influence. Details of the fabrication processes for both the Pt-Py-Cu samples and the CoFe-Cu samples can be found in Appendix A.1.

The different widths for the different recipes are presented in Table 5.1. Variations of approximately 10 % in the widths of the different samples are determined, since both the CoFe and the Cu bridge exposure doses have been varied in order to achieve low ohmic CoFe/Cu interface resistances. We note here that the required exposure dose to fabricate a low ohmic CoFe/Cu interface resistance is significantly higher than that necessary to pattern a low ohmic Py/Cu interface resistance. For recipe 1, the required dose to pattern the Cu bridge on the Py nanowires is 580 μC/cm^2. Patterning of the same Cu bridge onto the CoFe nanowires requires an electron dose of 860 μC/cm^2 to achieve low ohmic interfaces. This can be explained by the different secondary electron yield for the two materials, leading to changes in the required dose to fully develop the Cu bridge. Interestingly, the Cu bridge is intact for much lower doses. However, if the exposure dose has been chosen too low, the interface resistance can be as high as 1000 Ω or higher, which demonstrates that the optimization of the charge

transport properties is a necessary but not sufficient criterion in order to fabricate high quality lateral spin valves.

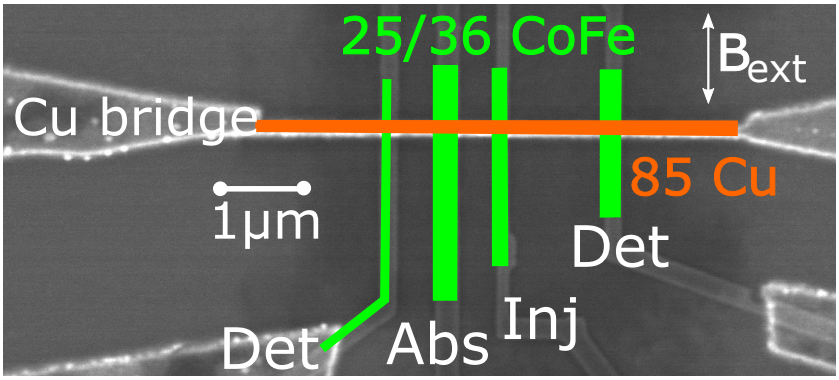

Fig. 5.7. SEM image of one of the fabricated CoFe-Cu spin valves. The CoFe wires are 36 nm thick for 30 kV EHT and 25 nm thick for 10 kV and 20 kV EHT. The Cu bridge is for all six combinations 85 nm thick. The third wire (approximately 200 nm in width) is used as the injector, while the first and fourth wire are approximately 250 nm wide and are used as detectors. The second wire acts as absorber and is approximately 300 nm wide.

EHT CoFe	**Cu Rec.**	**inj. w. [nm]**	**det. w. [nm]**	**abs. w. [nm]**	**Cu br. w. [nm]**
30 kV	1	150	220	280	180
30 kV	2	180	220	270	160
20 kV	1	200	260	340	160
20 kV	2	210	260	330	210
10 kV	1	200	250	300	200
10 kV	2	180	220	330	220

Tab. 5.1. Overview of the different injector widths (**inj. w. [nm]**), detector widths (**det. w. [nm]**), absorber widths (**abs. w. [nm]**) and Cu bridge widths (**Cu br. w. [nm]**) for the different CoFe EHT (**EHT CoFe**) and Cu bridge recipes (**Cu Rec.**).

The plots of the different signals at a temperature of 4.2 K for the samples based on the different EHT combinations and recipes are shown in Figure 5.8. The results are summarized in Table 5.2. Compared to the previous Pt-Py-Cu samples, where variations of the signal of approximately 25 % for the different injector/detector configurations have been observed, we find very low variations (less than 5 %) of the signals for the CoFe-Cu samples. As a result, we only show the signals for one probe configuration to keep the plots clear.

As evident, we find for all samples for a given EHT for the patterning of the CoFe Wires higher spin signals (both R_{sd} and R_{NL}) if the Cu bridge has been patterned with recipe 1 compared to samples fabricated by recipe 2. As before, we explain these results on the fabrication induced lower quality of the interfaces by recipe 2.

Secondly, we find very different reductions of the signals by spin absorption for the different samples, depending on the EHT of the CoFe wires and the fabrication recipe of the Cu bridge. As before, these variations cannot be explained by the small variations of the wire widths. Similar to the Pt-Py-Cu samples, we find the counter-intuitive relation between the spin signals (R_{Sd} and R_{NL}) and spin absorption, i.e. that for high spin signals there is a relatively low spin absorption (meaning a high spin absorption signal R_{Abs}), while for low spin signals there is much stronger spin absorption. Hence as before, different fabrication methods lead to different interface qualities. These results support our previous findings that for a proper determination of spin absorption by HM electrodes or by FM

electrodes, not only the intrinsic properties of CoFe (λ_{CoFe} and P_{CoFe}) are relevant to describe the spin transport, but additionally contributions such as interface spin memory loss and spin transparency are crucial and need to be taken into account.

In contrast to the previous measurements, some spin absorption by the CoFe is also seen for the high quality interfaces, which can be connected to the very wide CoFe absorption wire. From the measurements of the high quality interfaces, which show the smallest reduction, we can give an upper boundary for the contribution of the intrinsic spin absorption by the absorber CoFe electrode. If the high quality interfaces would be perfect, in particular showing no interface spin memory loss and maximum spin transparency, all reduction of the spin current would be caused by the intrinsic spin absorption. This means that for the samples with low quality interfaces, the majority of the spin current loss is not caused by the intrinsic properties of the CoFe absorber electrode but rather by the interface properties, demonstrating again that contributions such as interface spin memory loss and spin transparency are crucial for an understanding of the device performance.

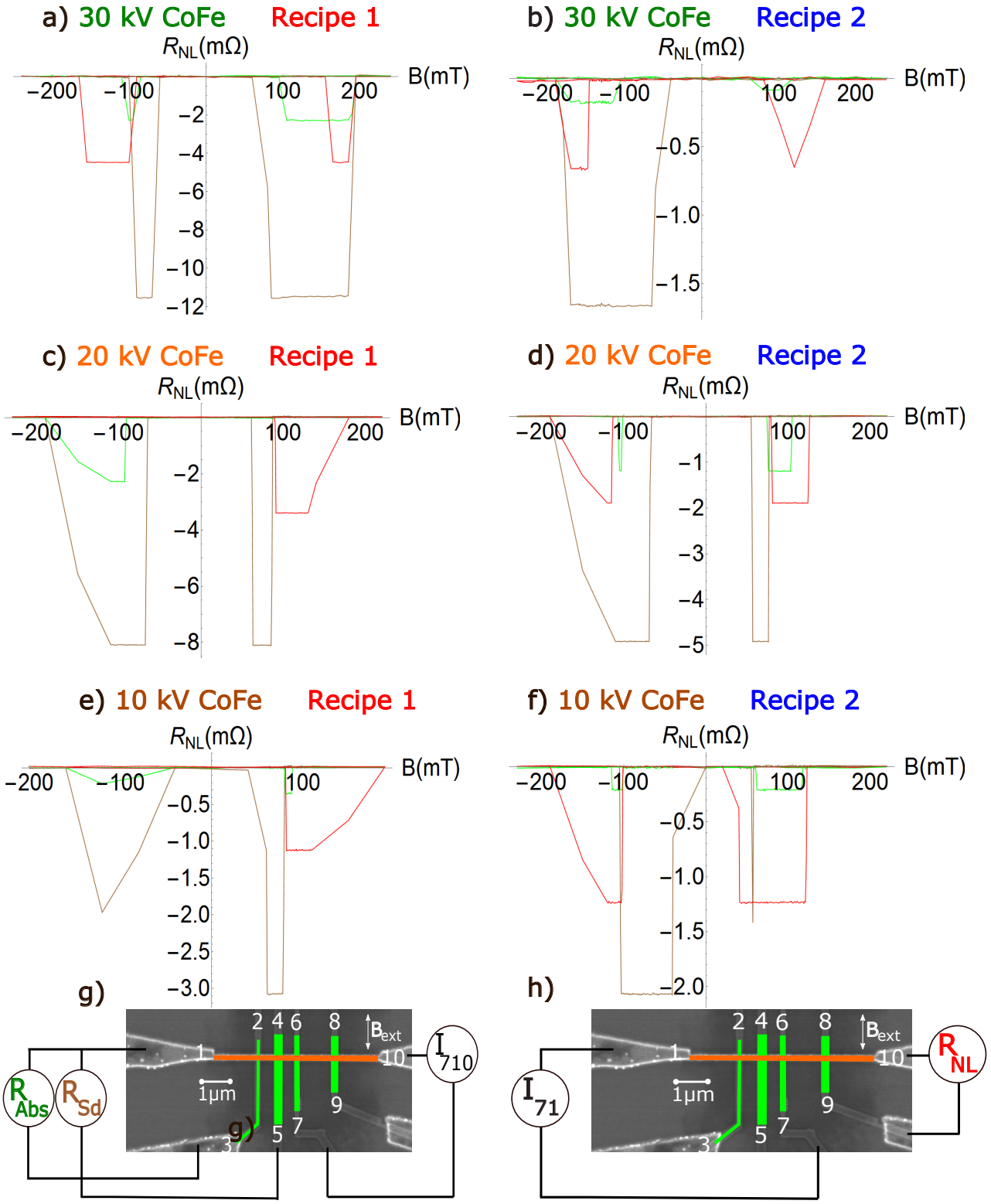

Fig. 5.8. Measured spin signals at 4.2 K in samples based on the different CoFe EHT and Cu bridge recipe combinations. The brown curves in the plots are termed short distance signals R_{Sd}. The red curves in the plots are termed non-local signals R_{NL}, while the green curves are termed spin absorption signals R_{Abs}. The probe configuration for the different signals is shown in g) and h).

EHT CoFe	Cu Rec.	R_{Sd} [mΩ]	R_{NL} [$m\Omega$]	R_{Abs} [mΩ]	1-(R_{NL}/R_{Abs}) [%]
30 kV	1	12.0	4.8	2.4	50
30 kV	2	1.6	0.6	0.2	67
20 kV	1	8.0	3.4	2.3	32
20 kV	2	5.0	1.9	1.2	37
10 kV	1	3.0	1.2	0.35	68
10 kV	2	2.0	1.2	0.2	83

Tab. 5.2. Overview of the three different signals (short distance signal R_{Sd}, conventional non-local signal R_{NL} and spin absorption signal R_{Abs}) measured in samples which are fabricated by different EHT for the CoFe wires (**EHT CoFe**) and different recipes for the Cu bridge (**Cu Rec.**).

5.6.2. Temperature dependence of conventional non-local and spin absorption signals of CoFe-Cu samples

Motivated by our previous results measured in Pt-Py-Cu samples, where significant differences in the temperature behaviour have been observed for the samples based on the different recipes, also the CoFe-Cu samples have been measured at varying temperatures. We note here that, as for the Pt-Py-Cu samples, for those combinations which have shown a very low signal, current injection and voltage detection have been switched in order to apply higher currents.

We compare the normalized non-local signal R_{NL} (red curves in the plots) and the spin absorption signal R_{Abs} (green curves in the plots) for the samples based on the different CoFe EHT and Cu bridge recipes, as shown in Figure 5.9. As is evident, we observe a clear correlation between the size of the absorption and differences in the temperature behaviour. For those EHT and Cu bridge recipes, which lead to high quality interfaces, resulting in low spin absorption (30 kV and recipe 1; 20 kV and recipe 1; 20 kV and recipe 2), we find hardly any differences between the normalized non-local signals and the spin absorption signals and the curves largely overlap within the error bars.

On the other hand, those fabrication recipes which lead to low quality interface and consequently show large spin absorption also show large differences in the temperature behaviour (30 kV and recipe 2; 10 kV and recipe 1; 10 kV and recipe 2;). As a result, the temperature behaviour directly reflects the signal behaviour and interface quality and our previous findings concerning the Pt-Py-Cu samples are strongly supported. For high quality interfaces, even a 300 nm wide CoFe absorption wire leads to relatively low spin absorption (between 32 % and 50 % at 4.2 K) and the absorption is (nearly) temperature independent. These results indicate that the spin polarization P_{CoFe} is (nearly) temperature independent in this temperature range. Furthermore we conclude that the spin diffusion length λ_{CoFe} is either (nearly) temperature independent or so short that within the thickness of the CoFe wires (25/36 nm), any possible temperature dependence does not play any role.

We now study those curves where significant differences in the temperature behaviour are observed. As for the previous measurements, we observe that if a significant reduction of the spin signal is present, always the spin absorption signal to decrease stronger with increasing temperature. Usually the Elliot-Yafet theory is sufficient to describe the temperature behaviour for Cu based spin valves between 50 K and room temperature. In these measurements, the additional CoFe/Cu interface needs to be taken into account to explain the temperature behaviour.

In order to explain the maximum of the signal and the subsequent decrease of the signal with decreasing temperature, different explanations such as the Kondo effect and increased surface scattering have been proposed in the literature [145, 148, 243, 246, 255]. In our measurements, we find for samples based on some EHT/recipe configurations an explicit maximum in both signals at 50 K while for some configurations, no explicit maximum of the signal but rather a constant signal between 50 K and 4.2 K is observed. Our results suggest that the maximum of the signal can be suppressed if low quality CoFe/Cu interfaces are present (both signals for 30 kV EHT and recipe 2; the spin absorption signal for 10 kV EHT and recipe 2).

As a result, the appearance of an explicit maximum in the non-local signal contains valuable information concerning the interface quality. In this particular system (CoFe-Cu samples fabricated by a two step lift-off process), only for high quality interfaces, contributions such as the Kondo effect need to be taken into account to explain the maximum of the signals. For low quality interfaces, possibly residual resist and other inhomogeneities, which are present at the interface, suppress the interdiffusion of the magnetic impurities into the conduit. Consequently the Kondo effect is suppressed and no explicit maximum of the spin signal is determined. Previously it could be demonstrated that the strength of the Kondo effect crucially depends on the purity of the material to grow the NM bridge [246] and on the growth mode, i.e. if shadow mask evaporation or a two step lift-off process has been used [270]. Our work implies that additionally for a given purity of the material to grow the NM and for a given growth mode, additionally the patterning process and consequently the homogeneity of the interfaces plays a decisive role if the Kondo effect is present, leading to an explicit maximum of the spin signal at a certain temperature and a consequent downturn of the signal by further decrease of the temperature.

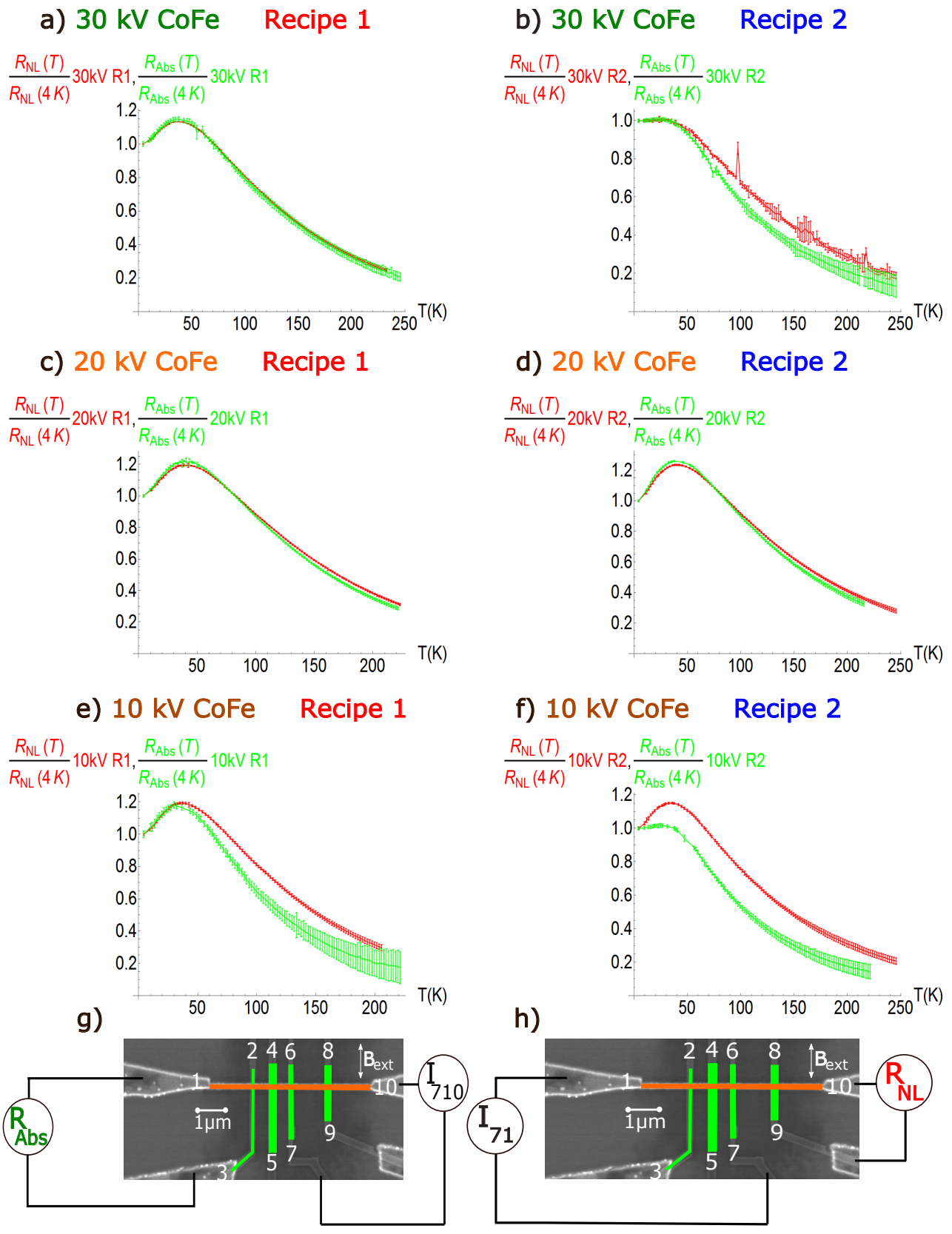

Fig. 5.9. Temperature dependent normalized conventional non-local and spin absorption signals measured in samples fabricated by the different EHT and Cu bridge recipe combinations. For samples with high quality interfaces (30 kV EHT and recipe 1; 20 kV and recipe 1; 20 kV and recipe 2), hardly any differences between the two signals for varying temperatures are observed. If samples with low quality interfaces are measured (30 kV EHT and recipe 2; 10 kV and recipe 1; 10 kV and recipe 2), the spin absorption signal decreases significantly faster with increasing temperature than the conventional non-local signal. The probe configuration for the different signals is shown in g) and h).

5.7. Summary Of The Chapter

In summary, we have studied the impact of different fabrication methods on the spin transport across HM/NM and FM/NM interfaces in Pt-Py-Cu and CoFe-Cu lateral spin valves.

For the Pt-Py-Cu samples, we have compared the (i)SHE signals and the spin absorption signals for samples based on two different recipes for the Cu bridge fabrication. For the sample fabricated by the first recipe (based on a single PMMA layer), a large (i)SHE signal but no significant spin absorption has been determined. For the sample fabricated by the second recipe (based on a dual MMA/PMMA layer) spin absorption of 76±3 % but a low (i)SHE signal is determined. These counter-intuitive results are explained by the varying quality of the interfaces which is neither evident from the charge transport properties of the interfaces nor from conventional imaging. By direct buried interface imaging, we find significant differences for the interfaces of the samples based on the different recipes, in full agreement with the temperature dependent spin transport measurements. In particular the role of contributions such as spin transparency and interface spin memory loss, leading to a loss of spin accumulation without contributing to the (i)SHE, is emphasized, which is in conventional analysis often disregarded. Our results clearly indicate that the widely used spin absorption technique is not robust due to its strong sensitivity to the interfaces which is also mimicked in the strong variation of the determination of the effective transport parameters for samples based on the different recipes.

In order to check the correlation between fabrication process and strength of the spin absorption for different systems, additional temperature dependent measurements in CoFe-Cu lateral spin valves with a very wide CoFe absorber have been performed. Also in these samples, using the first recipe for the Cu bridge fabrication leads to significantly higher quality interfaces compared to samples based on the second recipe and thus to high spin signals and low spin absorption. In contrast to the Pt-Py-Cu samples, due to the very wide absorption wire and the low variations of the signal for different injector/detector configurations, we are able to estimate the intrinsic contributions of the CoFe absorber wire and compare it to the interface contributions such as spin transparency and spin memory loss. While for samples with expected high quality interfaces, spin absorption between 30 % and 50 % is found, the spin absorption increases significantly to values between 70 % and 80 % for samples with expected low quality interfaces. While the reduction of spin current for high interface quality samples is mainly based on the intrinsic properties of the absorber wire, contributions such as spin transparency and interface spin memory loss are the major contributions for samples with lower quality interfaces.

The significance of the quality of the interfaces also plays a decisive role for the temperature dependence. While the normalized non-local and spin absorption signals measured in samples with high quality interfaces show no differences in the temperature behaviour within the error bars, a significantly stronger reduction of the spin absorption signal is found for increasing temperature in samples with low quality interfaces. As a result, we link these changes in the temperature behaviour to the properties of the additional CoFe/Cu interface. We conclude that the strength of the Kondo effect depends on the fabrication, in addition to the purity of the material to grow the NM and the deposition method, which have been previously studied. In particular we assume that by residual resist or other inhomogeneities present at the interface, the interdiffusion of nonmagnetic and ferromagnetic atoms is sufficiently suppressed.

Finally, the work presented in this chapter suggests new possible spin valve systems, which could be studied. As emphasized, our work clearly demonstrated that spin memory loss and spin transparency play a very important role in order to optimize spin transport across interfaces. Recently, Lidig. et al. could demonstrate by spin transport measurements that in Co_2MnSi/Ag interfaces, highly spin polarized surface states are present [269]. These highly spin polarised surface states could lead to a significant increase of the possible injected spin polarization into Ag compared into materials such as Cu. This can be understood by the Co_2MnSi/Ag interface (which can be grown epitaxially) having a higher spin transparency than the Co_2MnSi/Cu interface. This is in particular interesting, since Co_2MnSi itself is a highly spin polarized material [182], however if its intrinsic high spin polarisation is not preserved across the FM/NM interface, there is only limited use for potential devices. The next chapter is about the fabrication of Co_2MnSi-Cu and Co_2MnSi-Ag lateral spin valves. While

unfortunately no spin signal could be detected in the particular batch of samples as discussed later, nevertheless significant progress concerning improving the homogeneity of the etched wires and the electric interface resistance could be achieved.

Chapter VI

Fabrication of Co_2MnSi Based Spin Valves

In this chapter, the fabrication of Co_2MnSi based lateral spin valves is presented. Unfortunately, no spin signal has been seen for these samples. Nevertheless, a motivation for the fabrication of these devices is provided and furthermore, the fabrication for samples based on thin films has been significantly improved and opens a route to potentially produce lateral spin valves with high spin signals based on the findings and improvements. Additionally, ideas for an optimized stack are presented. More details of the fabrication, especially all parameters for the process steps including spin coating, EBL, development, IBE and residual resist removal are presented in detail in Appendix A.2.

6.1. Motivation

As explained in Chapter 5, lateral spin valves are ideally suited to study spin transport across HM/NM and FM/NM interfaces, which is a key component of many device concepts but currently poorly understood. As demonstrated in Chapter 5, in particular contributions such as spin transparency and interface spin memory loss, which are often disregarded in lateral spin valves and similar devices, play a decisive role and need to be understood and optimized in order to optimize the device performance.

One attractive possibility to maximize spin signals is to use Co_2MnSi as ferromagnetic material due to its extremely high spin polarization at the Fermi-energy even at room temperature [182]. Co_2MnSi is furthermore promising since it could be shown by spin transport measurements that by an epitaxial growth of a Co_2MnSi/Ag interface, a very high spin polarisation injected into the Ag is possible, which is ideal for devices [269]. In a previous work, we could demonstrate that in Co_2MnSi-Cu lateral spin valves, the effective spin polarization injected in the Cu is significantly higher than for lateral spin valves which are based on conventional 3*d*-ferromagnets [247]. However the injected spin polarisation was not very large which is caused by a relatively high interface resistance in the order of 5 Ω and additionally not optimized band-structure matching. We therefore expect that by an optimization of the fabrication conditions, in particular the removal of the residual resist, a significant enhancement of the spin signal is possible due to a lower interface resistance. Furthermore we expect that by suitable band structure matching, i.e. an epitaxial grown Co_2MnSi/Ag interface and the resulting higher spin transparency, significant improvements of the spin signals are possible since the injected spin polarisation in the Ag can be significantly higher compared to the injected spin polarisation in Cu.

6.2. Characterization Of The Fabricated Samples

In total, samples based on a 30Co_2MnSi/20Cu/2Ta/4Pt and on a 30Co_2MnSi/30Ag/2Ta/4Pt thin film have been patterned. The numbers are the thicknesses of the certain layers in nm. After developing a suitable recipe for the patterning and development and finding a suitable etching sequence, a lot of effort has been invested to remove the residual resist without attacking the wires. Many different organic removers including AR 300.76 and AR 300.70 have been tested [271]. However, for all organic solvents, a perfect removal of the resist, resulting in high quality low ohmic metallic interfaces could never be achieved. Even worse, it has been observed that these organic solvents reduce the thickness of nanowires (although not of marker crosses) and therefore only acetone is recommended as the organic solvent. For acetone it has been checked that no reduction of the thickness of the wires occurs, even when the sample is in acetone for several days. To remove the residual resist without damaging the nanowires, the treatment by oxygen plasma has been optimized. It is emphasized here that several different parameters for the oxygen plasma have been tested. The best results have been found for a power of 300 W and an oxygen pressure of 1.2 Torr. After determining optimal ashing conditions, the different stacks, especially with Ta and Pt as possible capping layers have been checked and the results are shown in Figure 6.1.

In Figure 6.1a), the XRR measurement of a 14 nm Ta thin film is shown in green while the same film, treated by oxygen plasma is shown in orange. Significant differences between the two films are observed. More evidence that Ta is not a suitable capping layer for oxygen plasma treated samples is shown in Figure 6.1b), where the XRR measurement of an as grown 30 CoFeB/20Cu/2Ta film is shown in brown while the same film treated by oxygen plasma is shown in purple. Significant differences between the two curves are determined.

However, as shown in Figure 6.1c), the situation is different when Pt is used as a capping layer. The XRR measurement of an as grown 30 CoFeB/20Cu/2Ta/4Pt thin film is shown in green while the same film treated by oxygen plasma at a very high position within the asher for 30 (60) seconds is shown in red (blue). Hardly any differences in the thickness of the stack are observed. Only the roughness is slightly increased, indicating that Pt is a suitable capping layer.

Further strong evidence that Pt is a suitable capping layer for oxygen plasma treated samples is

presented in Figure 6.1d). Here, the XRR measurement of a formerly 14 nm Pt film, etched via the in-situ argon gun in the UHV thermal evaporation chamber for 60 minutes is shown in blue. A reduction of the film thickness to approximately 8.5 nm is found. The XRR measurement of the same film which has been fully processed (spin coated, baking of the resist, etched via IBE, resist removal via acetone and the full oxygen plasma treatment) is shown after the final in-situ etching in the UHV thermal evaporation chamber. By the treatment, the Pt film becomes slightly rougher but does not change thickness nor resistivity. Due to the results of these measurements, 4 nm of Pt have been deposited on the Co_2MnSi films, which have been previously just capped with 2 nm of Ta.

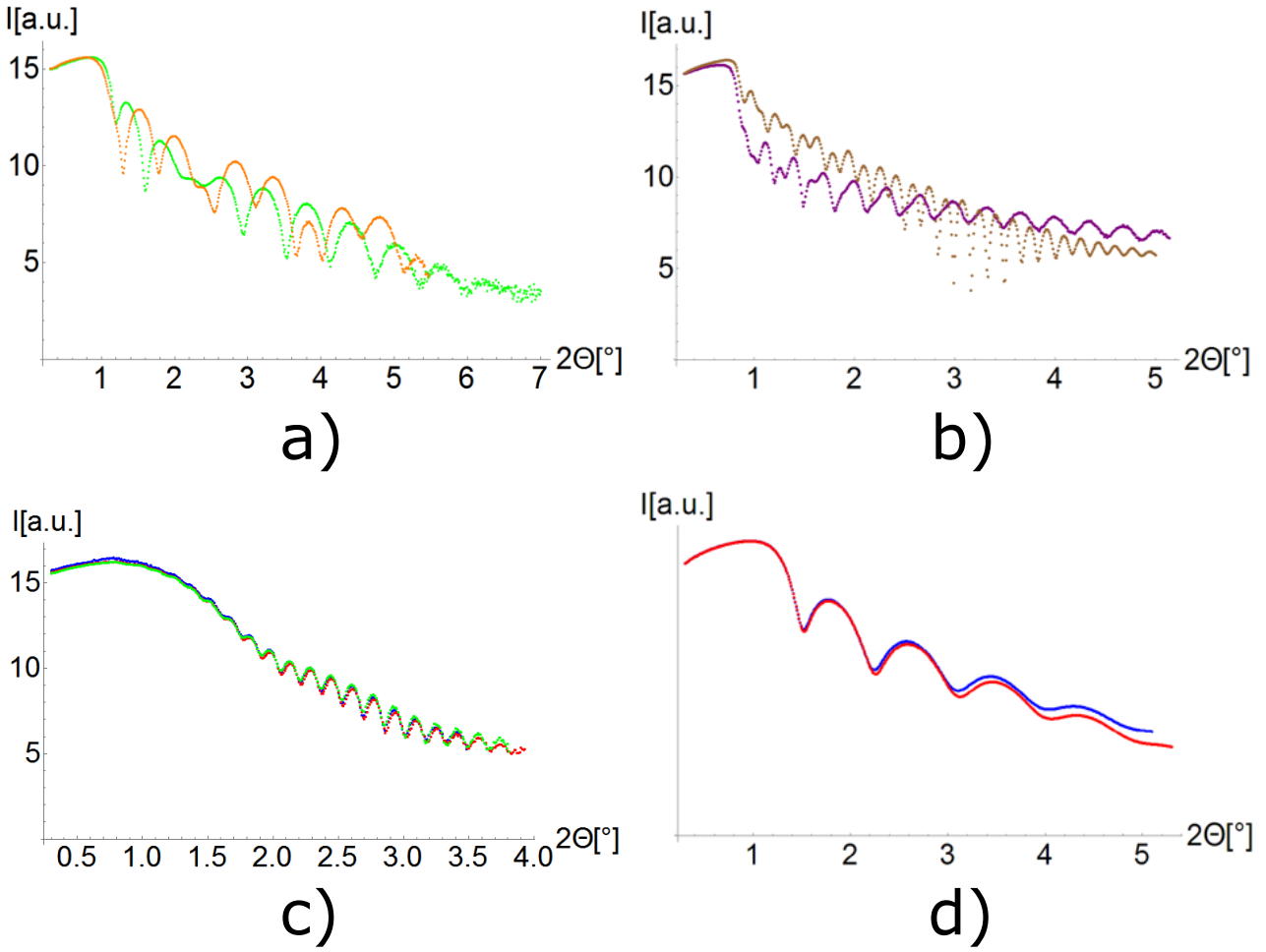

Fig. 6.1. XRR measurements of either Pt or Ta thin films or films with either Pt or Ta as a capping layer.
a) XRR measurement of an as grown 14 nm Ta film shown in green and the same film treated by oxygen plasma shown in orange. Differences between the two curves are observed, indicating a change of the thickness and of the roughness of the Ta film by the oxygen plasma treatment.
b) XRR measurement of an as grown 30CoFeB/20Cu/2Ta film shown in brown and the same film treated by oxygen plasma shown in purple. As in a), differences are observed for the two curves, indicating that Ta is not a suitable capping layer for oxygen plasma treated samples.
c) XRR measurement of an as grown 30CoFeB/20Cu/2Ta/4Pt film shown in green, 30 seconds oxygen plasma treated film shown in red and 60 seconds oxygen plasma treated film shown in blue. Hardly any differences of the XRR measurements are observed, indicating that Pt is a suitable capping layer for oxygen plasma treated samples.
d) XRR measurement of an as grown 14 nm Pt film etched for 60 minutes in the UHV thermal evaporation chamber shown in blue and the same film completely processed (spin coated, baking of the resist, IBE, acetone removal and oxygen plasma treatment) and etched at the same time shown in red. No differences in the thickness and only slight differences in the roughness are observed by the processing of the film.

As explained in detail in Appendix A.2, it is expected that the 2 nm Ta capping layer (of the film) leads to an increase of the thickness of the nanowires by 8 nm. Analogously, it is expected that the 4 nm Pt of the capping layer (of the film) lead to an increase of the thickness of the nanowires by 8 nm.

Consequently the fabricated and resist free Co_2MnSi wires have been etched via IBE in order to decrease the thickness of the capping layer. This step is necessary since the idea is to deposit the Cu via UHV thermal evaporation onto the in-situ grown Ag/Cu. If the capping is too thick (and especially Ta has a very low etching rate), the Cu would have been deposited onto the Ta and not on the Ag/Cu. Therefore, the two samples have been etched under an angle of incidence of 90 ° for 70 seconds to completely remove the Pt and to have 2.5 nm of Ta left, followed by the standard procedure to pattern the Cu bridge based on recipe 1, as explained in detail in Appendix A.1. After the complete fabrication, the samples have been finally etched via IBE for additional 70 seconds to make sure that the applied current flows in the highly resistive Co_2MnSi and is not shunted by the low resistive Ag/Cu. The different expected thicknesses and the different material compositions for the different process steps are schematically shown for the Cu based sample in Figure 6.3.

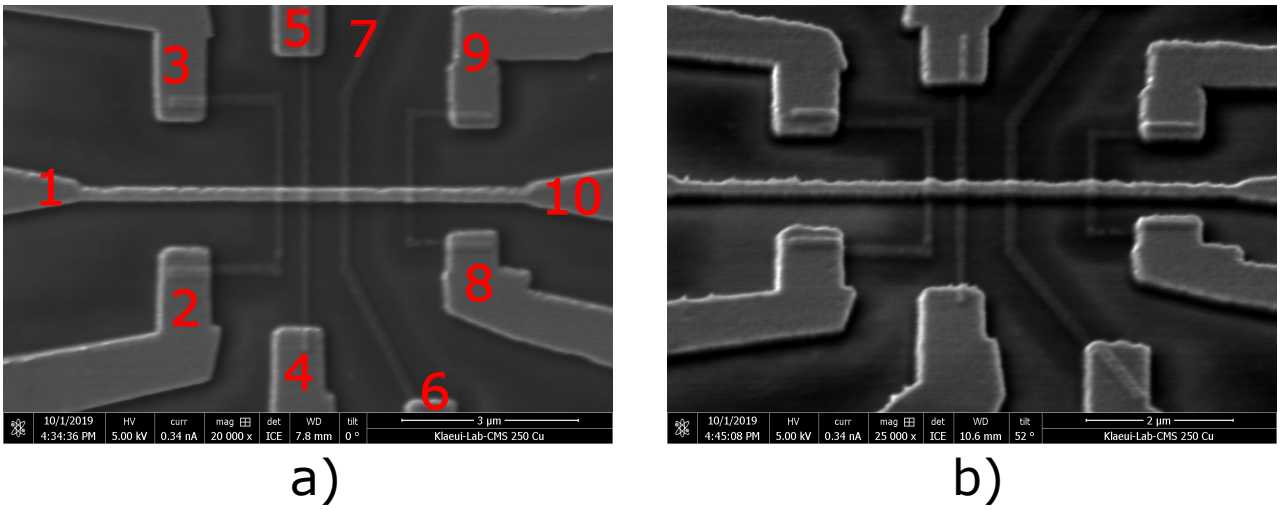

Fig. 6.2. SEM images of the fabricated Co_2MnSi nanowires, bridged by a Cu bridge.
a) SEM image with a tilting angle of 0 °.
b) SEM image with a tilting angle of 52 °.

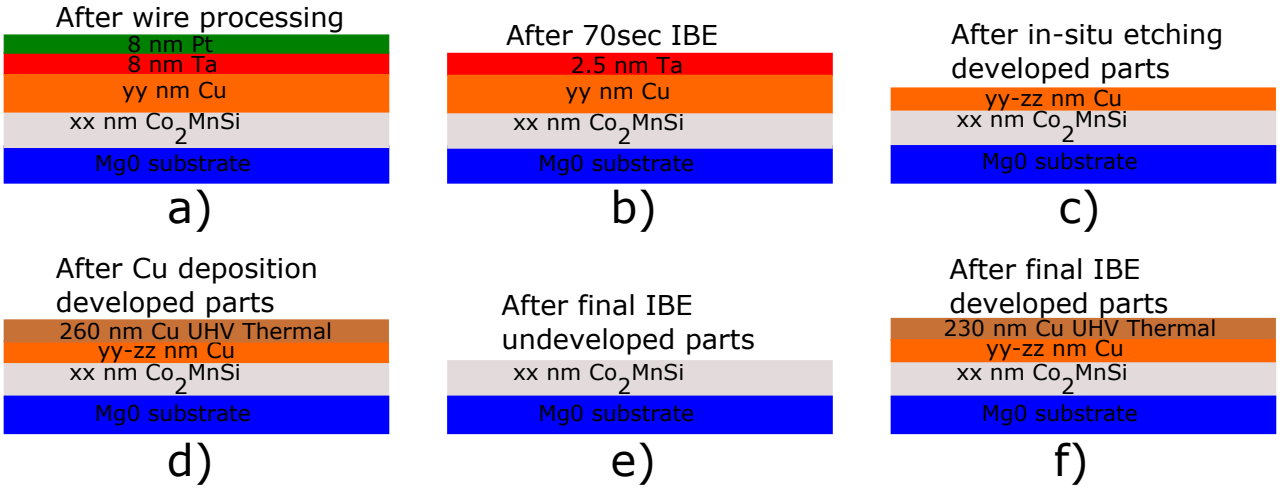

Fig. 6.3. Schematic illustration of the different expected thicknesses and material compositions of the fabricated Cu based Co_2MnSi nanowires. Further details concerning the fabrication can be found in detail in Appendix A.2.
a) By the nanowire processing, the 2 nm of the original Ta stack lead to an increase of the thickness of the nanowires by 8 nm. Analogously, the 4 nm Pt of the original stack lead to an increase of the thickness of the nanowires by 8 nm.
b) After 70 seconds of IBE under standard conditions, the 8 nm of the Pt are completely removed and the thickness of the Ta is reduced to approximately 2.5 nm.
c) By the in-situ etching procedure of the developed parts, the Ta is completely removed. The in-situ etching procedure stops in the Cu layer.
d) 260 nm of Cu are grown via UHV thermal evaporation and deposited onto the developed parts.
e) By a final IBE step, the residual Cu and the residual Ta of the undeveloped parts onto the Co_2MnSi wires are removed in order that the current flows in the Co_2MnSi and is not shunted in the Cu/Ag.
f) By the final IBE step, the thickness of the Cu bridge and the contacts grown by UHV thermal evaporation is reduced from 260 nm to approximately 230 nm.

The resistances of the different wires together with the interface resistances are summarized in Table 6.1. The resistance R_{IF} of e.g. the very left Co_2MnSi/Cu interface is measured by applying a current between contact 3 and contact 10 while measuring the voltage between contact 2 and contact 1. It is mentioned that after the oxygen plasma treatment, the Ag based samples looked "corny" which could be easily detected by the optical microscope. By leaving the sample in acetone overnight and using ultrasound for several minutes the next day, these "corns" could be significantly decreased and it has been possible to contact the Ag based wires. However, in comparison to the Cu based samples, not all wires showed electrical contact, yet those which were successfully contacted showed interface resistances comparable to the Cu based samples. Furthermore the two point resistances are significantly higher for the Ag based nanowires. It is noted that by comparing the two-point resistances, approximately 20 Ω need to be subtracted due to the resistance of the measurement wires.

Stack	Contacts	R[Ω]	R_{IF} [mΩ]
Co_2MnSi/Ag	1-4	5445	
Co_2MnSi/Ag	1-5	6599	
Co_2MnSi/Ag	4-5	12023	140
Co_2MnSi/Ag	1-6	5224	
Co_2MnSi/Ag	1-7	6158	
Co_2MnSi/Ag	6-7	11364	240
Co_2MnSi/Cu	1-2	1027	
Co_2MnSi/Cu	1-3	1333	
Co_2MnSi/Cu	2-3	2334	190
Co_2MnSi/Cu	1-4	1406	
Co_2MnSi/Cu	1-5	1288	
Co_2MnSi/Cu	4-5	2668	220
Co_2MnSi/Cu	1-6	1364	
Co_2MnSi/Cu	1-7	1772	
Co_2MnSi/Cu	6-7	3107	260
Co_2MnSi/Cu	1-8	728	
Co_2MnSi/Cu	1-9	1198	
Co_2MnSi/Cu	8-9	1898	70

Tab. 6.1. Overview of the two-point and interface resistances of the Cu based and Ag based Co_2MnSi samples. While the Ag based wires have significantly higher resistances, the interface resistances are very similar.

6.2.1. Possible reasons for the lack of spin signals

Since no spin signals for both samples could be detected above the noise level, possible reasons for the low signal are discussed in this subsection. A first possible reason is the worse interface quality compared to the previous measured lift-off based samples. In lift-off samples, the interface resistances are typically in the 1-10 mΩ range while here interface resistances in the 100 mΩ range are determined. However, since in a previous work relatively large spin signals have been seen with similar lateral dimensions and an interface resistance of approximately 5 Ω [247], it is unlikely that no spin signal at all is present just due to the higher electric interface resistance.

A second reason could be that due to the etching process, the wires are inhomogeneous in height. Since the etching times are chosen assuming a homogeneous thickness, a significant part of the wires has been etched either too short, which means that Cu has been deposited on Ta instead of Cu (Ag) for the Cu (Ag) based wires.

To check this, AFM measurements of the two samples have been performed, as shown in Figure 6.4. In Figure 6.4a) an overview AFM image of a Cu based sample with Cu contacts is shown while in Figure 6.4b) an overview AFM image of the Cu based Co_2MnSi nanowires is shown. Both images have been taken after the final IBE step. The corresponding line scans for the Cu based samples are shown in Figure 6.4c) and Figure 6.4d) in red while the line scans for a Ag based sample are shown in Figure 6.4e) and Figure 6.4f) in blue. As evident from Figure 6.4c) and Figure 6.4e), the thickness of the Cu contacts without any Co_2MnSi wire below is approximately 230 nm, as also described in Figure 6.3f. For both the Cu based and the Ag based sample, the thickness of the Co_2MnSi wire below the contact is approximately 50 nm, which fits well with our expectations since the UHV thermal evaporation grown Cu has been planned to be deposited onto the in-situ grown Cu/Ag. When we compare the thicknesses of the undeveloped parts of the Co_2MnSi wires as shown in Figure 6.4d) and Figure 6.4f), we find the Cu based sample to be approximately 35 nm thick while the Ag based sample is around 25 nm thick. This difference in the thickness can be explained due to the higher etching rate

of Ag compared to Cu. It additionally explains why the Ag based Co_2MnSi wires have a significantly higher resistance than the Cu based Co_2MnSi wires. As evident, the thickness of the wires is not uniform but varies by approximately 5 nm, which shows that parts of the wires could possibly contain Ta which in turn could lead to significant spin dependent scattering since Ta is a material with large spin orbit coupling.

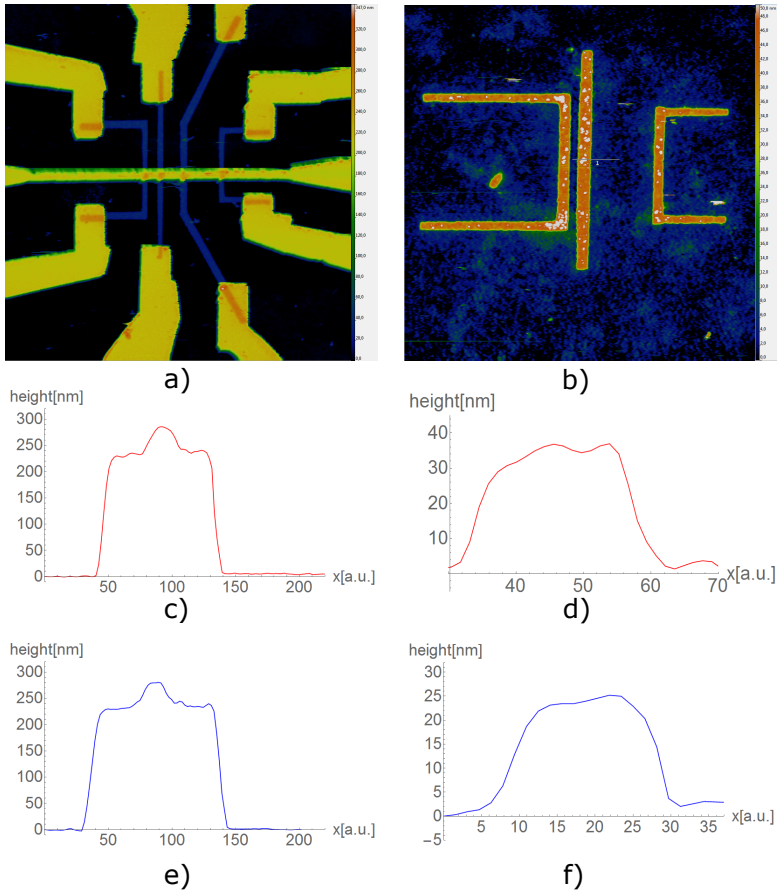

Fig. 6.4. AFM Images and line scans of the fabricated Co_2MnSi samples after the 70 seconds final IBE Step.
a) AFM image of a Cu based Co_2MnSi sample, together with the Cu contacts grown via UHV thermal evaporation.
b) AFM image of a Cu based Co_2MnSi sample without contacts.
c) Line Scan across a Cu contact with a Cu based Co_2MnSi nanowire below. The thickness of the contact is determined to be 230 nm while the thickness of the nanowire is found to be approximately 50 nm.
d) Line Scan across a Cu based Co_2MnSi nanowire. A thickness of approximately 35 nm is determined.
e) Line Scan across a Cu contact with a Ag based Co_2MnSi nanowire below. As for c), the thickness of the contact is determined to be 230 nm while the thickness of the nanowire is found to be approximately 50 nm.
f) Line Scan across a Ag based Co_2MnSi nanowire. A thickness of approximately 25 nm is determined.

As a possible third reason, it is assumed that by the etching of the Pt and the Ta capping layer, Pt and Ta atoms are implanted into the stack of the wire, leading to impurities which could be the source of a lot of spin flip events. To check this, EDX measurements have been performed by Anja Dion in our group, with the results shown in Figure 6.5. In Figure 6.5a), the EDX spectrum of the substrate is shown with the characteristic Mg and O peaks, while in Figure 6.5b) the spectrum of an alignment cross is shown. The Si, Co and Mn peaks are clearly visible, however neither Cu nor Ta

nor Pt is found. Finally the EDX scan of a Co_2MnSi nanowire with the Cu bridge on top is shown in Figure 6.5c). Here, none of the constituents (Co, Mn, Si) is identified which demonstrates that our EDX setup is not sensitive enough to detect them. Hence, there is little chance that the potential very low Pt or the very low Ta content could be identified.

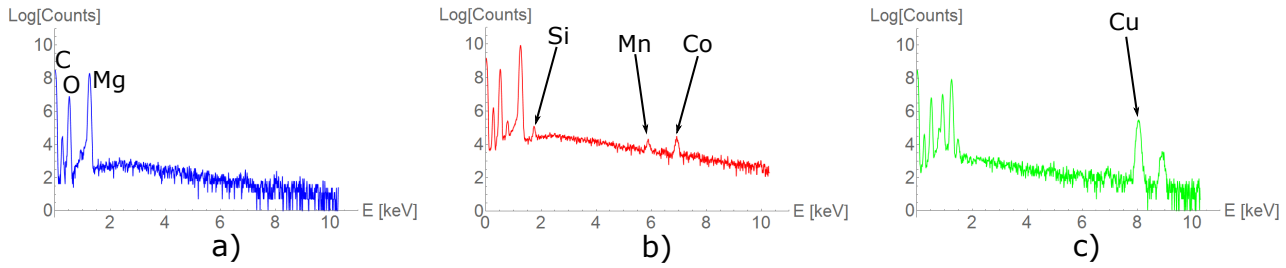

Fig. 6.5. a) EDX spectrum of the substrate which helps to identify the C, O and Mg peak.
b) EDX spectrum of a Co_2MnSi alignment cross. All three components are clearly identified.
c) EDX spectrum of a Co_2MnSi nanowire with the Cu bridge patterned onto the nanowire. It is no longer possible to identify the components of the nanowires.

6.2.2. Ideas for stack improvements

As a result of the analysis of the lack of the spin signal, possible improvements of the stack, based on the improvement of the etching and residual resist procedure achieved in this thesis, are proposed.

The original reason for choosing Ta (and later Pt) was that it is known that capping layers such as AlO_x are attacked by organic solvents such as AR 300.70. However, within the framework of this thesis, a procedure could be established which allows for high quality low ohmic metallic interfaces using just acetone as the organic solvent and an oxygen plasma treatment. Therefore, it is suggested to change the capping layer to AlO_x as a material with very low spin orbit coupling. This would also minimize the influence of the varying thickness of the wires which is difficult to avoid. The future steps would be the following:

a) Find out how thick the AlO_x capping layer must be in order to avoid changes in the XRR measurement of the original stack and to avoid changes of the resistivity of the stack by the oxygen plasma treatment. Typical, the AlO_x capping layer thickness is approximately 2 nm. It should, however, be checked whether this is sufficient to avoid any changes of the stack by the oxygen plasma treatment. For the next points, it is assumed that AlO_x is a suitable capping layer.

b) Do not use silver paste to glue the sample to the holder for the deposition but rather use PMMA. As shown in the AFM image, there are relatively many particles on the substrates which is either due to the cutting of the substrate or due to the silver paste. Also, directly deposit the stack on $5{\cdot}10\,mm^2$ substrates.

c) Deposit $30Co_2MnSi/40Cu/xAlO_x$ for the Cu based and $30Co_2MnSi/5Ag/40Cu/xAlO_x$ for the Ag based samples. By the use of these stacks, it is expected that after the AlO_x removal by the in-situ sputter gun, the UHV thermal evaporation grown Cu is deposited for both chips on the in-situ grown Cu. Differences in the spin signal can then directly be attributed to the differences of the Co_2MnSi/Cu and the Co_2MnSi/Ag interface.

Chapter VII

Summary And Outlook

In summary, we have studied both the fundamental properties of lateral spin valves including pure spin transport across metallic interfaces and the performance of an optimized device geometry, which allows for the study of spin current assisted magnetization switching of small magnetic elements.

To exploit lateral spin valves as possible devices for efficient magnetization manipulation by spin currents, we have studied the spin current assisted switching of a Py disc as a function of the applied charge current amplitude and polarity for different external field angles. For different field angles, different switching paths have been observed, which indicate a dominant influence of inhomogeneities, which strongly affect the switching behaviour. For some applied field angles, we observe direct mono-domain to mono-domain state transitions while for other field angles, switching paths with the vortex as an intermediate state are present. From the size of the occurring jumps of the non-local signal, the chirality of the vortex state can be identified. In order to study of the influence of the spin transfer torque on the device, the indirect mono-domain to mono-domain state switching via an intermediate vortex state has been studied in particular for a field sweep angle of 171/351 °. For this particular field angle, additional first order reversal curve measurements have been performed indicating the stability of the four different magnetic states at zero external field and maximum applied current pulses.

Although Joule heating is significant, thanks to our optimized geometry which allows for the synchronous application of current pulses in both injectors, we are able to observe a statistically significant effect of the spin transfer torque in assisting the switching via current polarity and amplitude dependent measurements.

To study the fundamental properties of lateral spin valves, i.e. the pure spin transport across HM/NM and FM/NM interfaces, Pt-Py-Cu based devices with a special kinked geometry have been investigated. By the geometry that was pioneered here, we are able to connect the switching of the magnetization of the Py wires with the (inverse) spin Hall effect signal and the conventional non-local signal in one single device. For the iSHE and the SHE, a signal is determined which depends on the probe configuration, which can be explained by significant shunting of the charge current in the Cu bridge. These signals depend crucially on the used probe configuration which indicates that the device behaviour is strongly dependent on the different interfaces. By the study of the temperature behaviour, differences of the normalized conventional non-local and the inverse spin Hall effect are found, which demonstrate that for a full description of the device spin current injection and detection and not only spin current transport need to be considered, as previously claimed.

Since no significant spin current absorption in these devices is found, in contradiction to most literature reports, optimized Pt-Py-Cu and CoFe-Cu lateral spin valves are fabricated, which allow a study of the spin transport across HM/NM and FM/NM together with the spin absorption by either Pt or CoFe. For the Pt-Py-Cu samples, the (i)SHE signal and the spin absorption signal are compared for samples based on different recipes for the Cu bridge fabrication. For the first recipe, which is based on a single PMMA layer, a large (i)SHE is determined but no large spin absorption is found. For the sample fabricated by the second recipe, very large spin absorption of 76 % is determined but only a low (i)SHE signal is determined. We explain these counter-intuitive results by the fabrication induced varying quality of the different interfaces, which is neither evident from the charge transport properties of the devices nor form structural imaging using conventional techniques. Rather we employ buried interface imaging and find significant differences for the interfaces of the samples based on the different recipes. These significant differences of the interfaces are also seen in the strongly varying temperature behaviour for the samples based on the different recipes. In particular the role of contributions such as spin transparency and interface spin memory loss, leading to an absorption of spin accumulation

from the Cu at the interface to Pt but at the same time not leading to a large spin current in the Pt because the spin information is largely lost when going across the interface. This mechanism that reduces the spin current in the Cu without contributing significantly to the (i)SHE is emphasized, which is in conventional analysis often disregarded. Our results indicate that the widely used spin absorption technique is not robust due to its strong sensitivity to the quality of the interfaces. This is also mimicked in the strong variation of the determination of the effective transport parameters of Pt for samples based on the different recipes.

In order to check the correlation between the fabrication induced quality of the interfaces and the strength of the spin absorption, additional temperature dependent measurements in CoFe-Cu lateral spin valves with a very wide CoFe absorber have been performed. As for the Pt-Py-Cu samples, also here we observe significant larger spin signals for samples based on the first recipe compared to samples based on the second recipe. Due to the very wide absorption wire and the low variations of the signal for the different injector/detector configurations, we are able to estimate the intrinsic contributions of the CoFe absorber wire and compare it to interface contributions such as spin transparency and interface spin memory loss. While in samples with high quality interfaces a low spin absorption between 30 % and 50 % is determined, we calculate values for the spin absorption between 70 % and 80 % for samples with low interface quality. These results indicate that for high quality interfaces the spin absorption is mainly based on the intrinsic properties of the absorber electrode. Contributions such as spin transparency and interface spin memory loss are in particular important for samples with low quality interfaces.

The significance of the fabrication induced quality of the interfaces also plays a decisive role for the temperature dependence. For samples with expected high quality of the interfaces, the normalised temperature dependence of the conventional non-local and the spin absorption signal are equivalent within the error bars. For the samples with low expected quality of the interfaces, a significantly stronger reduction of the spin absorption signal with increasing temperature is seen. These results suggest that the temperature dependence is governed, in addition to the spin current injection/detection and spin current transport mechanisms, also by the interface properties. This becomes in particular evident for the presence of the maximum spin signal at a certain temperature, which is seen for samples with high expected interface quality. Conversely, no maximum spin signal is seen for samples with low expected interface quality. We assume that in addition to the purity of the material to grow the NM and the deposition method, additionally the fabrication induced interface quality plays a decisive role for the strength of the Kondo effect, which is the recently put forward explanation for the presence of a maximum signal at a certain temperature due to the varying concentration of impurity atoms, suppressing the interdiffusion of magnetic and nonmagnetic atoms in the conduit.

For an outlook we first refer to the work presented in Chapter 6, where significant advances in the fabrication of lateral spin valves based on a prior grown metallic thin film are presented and explained. Since materials with interesting properties such as Heusler materials with exceptionally high intrinsic spin polarization are typically grown epitaxially with annealing steps, a reproducible recipe to achieve homogeneous, residual resist free nanowires is of great importance and could be established. As discussed in detail, as the next step one could try to try the presented procedure with an optimized stack geometry and check if a spin signal can be determined and if differences between a Co_2MnSi/Ag and a Co_2MnSi/Cu interface can be observed. If this would be successful, it would be possible to go one step ahead and try a full Heusler based stack, i.e. also use a nonmagnetic Heusler as the spin conduit to achieve even a better band structure matching, resulting in a higher spin transparency of the interface and consequently higher spin signals. In particular the effect of the spin transparency of the interface, which, together with interface spin memory loss, has often been disregarded could be determined in such devices. Furthermore, the interfaces could be studied via buried interface imaging, which would potentially allows one to disentangle fabrication induced inhomogeneities such as residual resist and intrinsic interface properties such as the spin transparency of the interface. However, since lateral spin valves are attractive geometries for the study of spin transport across of either metallic

interfaces or across tunnel barriers, many fascinating experiments could be realised in these devices.

A.Appendix

Sample Fabrication Parameters

In this part of the appendix, all relevant information for the fabrication of the nanowires produced in this thesis is provided, including the treatment of the substrates, the patterning of the nanostructures via EBL, the material deposition via sputter deposition or UHV thermal evaporation, the in-situ etching conditions prior to the deposition of the Cu bridge and the etching of nanowires and alignment crosses out of a thin film via IBE. Furthermore, all known and relevant etching rates both for the in-situ etching procedure and for the IBE are provided.

A.1. Fabrication Of The Pt-Py-Cu Samples and CoFe-Cu Samples

In the first step, the 10·10 mm^2 sapphire substrate is cleaned and spin coated as described below, in preparation for the EBL patterning for the Pt stripes and the alignment markers, the Py wires and the CoFe wires. For the patterning of the Cu bridge, two different recipes have been used, as explained in the main part of the thesis.

a) **Recipe 1:** The same procedure as written in Table A.1 has been used, the only difference is the rotation speed for the PMMA spin coating which has been chosen to be 3000 rpm for 60 seconds with an acceleration of 3000 .

b) **Recipe 2:** For this recipe, instead of directly spin coating PMMA firstly a 150 nm thick MMA EL6 layer has been spun onto the substrate with the same settings as for recipe 1. After spin coating, there is a 300 seconds long pause and then the sample is baked at 180 ° for 90 seconds, followed by a 300 seconds pause and then the PMMA A4 950 K is spun as for recipe 1.

The PMMA 950K A4 used is a mixture obtained from either Stefan Kauschke or Tobias Reimer based on PMMA 950K A11 (which is obtained commercially) diluted in anisole and therefore the exact PMMA concentrations can vary be a few ‰. However, the thicknesses claimed here are based on [272]. The MMA EL6 is obtained commercially. The used spin coater is "Süss MicroTec's LabSpin Platform" [273].

Step	Equipment	Time [seconds]	Remark
1: Acetone	Wet Bench	60	
2: Isopropanol	Wet Bench	60	
3: H_20	Wet Bench	60	
4: N_2 Blow Dry	Wet Bench	10	
5: Water Removal	Hot Plate	60	Minimum 120 $°C$
6: Pause	Wet Bench	60	
7: Pre Spin PMMA	Spin Coater	2	500 rpm; 500 Acc
8: Spin Coat PMMA	Spin Coater	60	4000 rpm; 4000 Acc;
9: Pause	Wet Bench	300	
10: PMMA Bake	Hot Plate	90	180 $°C$
11: Pause	Wet Bench	300	
12: Spin Coat AR PC 5090.02	Spin Coater	2	500 rpm; 500 Acc
13: Spin Coat AR PC 5090.02	Spin Coater	60	3000 rpm; 3000 Acc;
14: Pause	Wet Bench	120	
15: AR PC 5090.02 Bake	Hot Plate	120	90 $°C$

Tab. A.1. Different steps for the cleaning and spin coating procedure for PMMA on an insulating substrate such as MgO and Al_20_3.

Next, all relevant parameters for the electron beam lithography (EBL) are presented. The used system is the commercial "Pioneer" EBL system from "Raith", which is explained in detail in the main part of the thesis. The dose to deposit the Cu bridge onto the Pt stripe is the same as for the deposition of the Cu bridge onto the Py wires. The exact doses vary depending on the speed of dropping the resist and starting the spin coater. Typically the dose used is approximately 5-10 % higher than the required minimum dose. It is emphasized that a significantly higher exposure dose is required to achieve high quality low ohmic CoFe/Cu interfaces compared to the required dose to achieve high quality low ohmic Pt/Cu and Py/Cu interfaces. For all exposures, the working distance has been chosen to be approximately 8.5 mm. For the patterning of all nanostructures and alignment crosses, the chosen

aperture is 15 μm while for the patterning of the contacts, either the 60 μm or the 120 μm aperture has been used. All structures have been patterned via the "Meander" mode.

Material	EHT [kV]	Step Size [nm]	Exposure Dose [μC/cm^2]
Pt stripes	30	10	450
CoFe wires 30 kV	30	10	450
CoFe Wires 20 kV	20	10	350
CoFe Wires 10 kV	10	10	250
Py wires 20 kV	20	10	350
Py wires 10 kV	10	10	250
Cu bridge Recipe 1 on Pt	20	2	580
Cu bridge Recipe 2 on Pt	10	10	300
Cu bridge Recipe 1 on CoFe	20	2	860
Cu bridge Recipe 2 on CoFe	10	10	540
Cu contacts	20	37.5	200

Tab. A.2. Relevant parameters for the EBL patterning for the different material and recipes.

For all PMMA based nanostructures, the development has been performed as follows:

a) AR PC 5090.02 is washed away by dipping the substrate in H_2O for 45 seconds.

b) The resist is developed for 45 seconds in one part of MIBK diluted in three parts of IPA.

c) The development is stopped by dipping the substrate for 30 seconds in IPA.

d) The IPA is washed away by dipping the substrate for 15 seconds in H_2O.

Next the mounting of the samples for the in-situ argon milling procedure is shown in Figure A.1a). The samples are always mounted on the same position on the sample holder with the same orientation with respect to the in-situ argon gun. The samples are grounded via the screws touching the resist covered substrate. During the in-situ etching procedure, also the deposition chamber is grounded. ϕ_0=0 ° is defined with the orientation of the "nose" of the sample holder pointing towards the window of the chamber. The argon beam is parallel to the exposure of the nonmagnetic Cu bridge. During the in-situ etching, the position of the sample holder is as follows:

- **z:** 322 mm
- **y:** 5 mm
- **x:** 20 mm
- $\phi_{\mathbf{etch}}$: 85 °

The parameters of the in-situ argon gun are chosen to be:

- $\mathbf{p_{etch}}$: 6-7 $\cdot$ 10^{-5}mbar
- $\mathbf{I_{fil}}$: 10 mA
- $\mathbf{U_B}$: 1000 V

With these parameters the emission current is approximately 15 μA and the rates of several materials are as follows, determined via XRR measurements:

- **Py:** 3.5 nm/h

- **CoFe** 2.5 nm/h
- **Pt:** 5.5 nm/h
- **Ta:** 2 nm/h
- **Cu:** 9 nm/h
- **Ag:** 17 nm/h

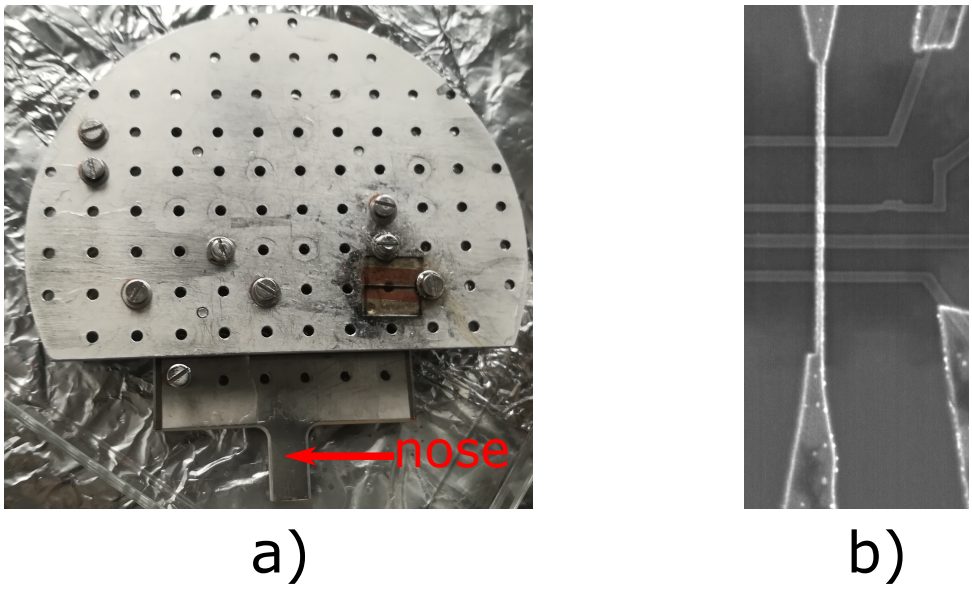

Fig. A.1. a) Photograph of the sample holder with the mounted samples, which are orientated such that the exposure of the Cu bridge is parallel to the "nose" of the sample holder. During the in-situ etching procedure the sample is orientated such that the argon beam is parallel to the nose of the holder and therefore parallel to the exposure of the Cu bridge.
b) SEM image of a patterned sample indicating the orientation of the Cu bridge during the in-situ milling procedure and the subsequent Cu deposition.

The Py-Pt-Cu samples have been etched in-situ for 60 minutes prior to the Cu deposition, while the CoFe-Cu samples have been etched in-situ for 90 minutes prior to the Cu deposition.

Next, the growth parameters of the different materials are presented in Table A.3. In Table A.3, p_b is the base pressure of the chamber while p_{dep} is the pressure during deposition. The chamber termed "Small Sputter" is the sputter chamber in room 423 of the Institute of Physics building. The chamber termed "Singulus" is the commercial sputter chamber from Singulus housed in the basement of the same building. The Pt deposition from the "Singulus" has been done with a rotation of the substrate of 60 rpm. while all other materials have been deposited without any rotations of the substrate. The chamber termed "UHV Thermal" is the UHV thermal evaporation chamber in room 123, also in the Institute of Physics building.

Material	Chamber	p_b [mbar]	p_{dep} [mbar]	rate [nm/min]
Pt	Small Sputter	$2{\cdot}10^{-9}$	0.01	4.5
Pt	Singulus	$3{\cdot}10^{-8}$	$6{\cdot}10^{-3}$	5.3
Py	UHV Thermal	$3{\cdot}10^{-9}$	$5{\cdot}10^{-9}$	0.25
CoFe	UHV Thermal	$3{\cdot}10^{-9}$	$5{\cdot}10^{-9}$	0.25
Cu	UHV Thermal	$3{\cdot}10^{-8}$	$5{\cdot}10^{-8}$	1.5

Tab. A.3. Overview of the deposition parameters of the different materials grown via UHV thermal evaporation or via sputter deposition.

It is recommended to cut the substrate, if this is necessary due to e.g. limitations of the sample holder size of the measurement setup, prior to the Cu patterning. Cutting Al_2O_3 substrates after the Cu deposition has led to destruction of the Cu bridges. Therefore all substrates have been cut in $10{\cdot}5\,mm^2$ pieces before the Cu patterning.

It is emphasized that the lift-off works fine by leaving the substrate in acetone for approximately 120 minutes and then using ultrasound for a few minutes. No other organic solvents expect acetone, IPA and H_20 are recommended. It is further recommended to spin coat a thin PMMA A2 layer prior to the AR PC 5090.2 layer when samples patterned on insulating substrates will be imaged via SEM. Some materials, e.g. CoFe, are attacked by the conductive AR PC 5090.2 layer. However, protecting the structures with a thin PMMA A2 layer does not significantly decrease the image quality but protects nanowires based on all materials which have been grown within the framework of this thesis.

A.2. Fabrication Of The Co_2MnSi-Cu And The Co_2MnSi-Ag Samples

The fabricated Co_2MnSi-Cu and Co_2MnSi-Ag samples have been processed from thin films via ion beam etching with the recipe as described in Table A.4. For these samples, the substrates have been directly cut in two $10{\cdot}5\,mm^2$ pieces prior to any processing. It is strongly recommended that only acetone (and IPA and H_2O) should be used to remove the residual resist after etching. Other organic solvents may attack the wires and reduce the thickness, even with Ta or Pt as a capping layer. The used recipe leads to a thickness of the photoresist of approximately 130 nm [181]. The etching rate of the resist under standard conditions and a 90 ° angle of incidence is around 5 nm/min, so for very thick material stacks a thicker resist might be required. Since the photoresist is a mixed match resist and therefore also sensitive to ultraviolet radiation, it is recommended to store the sample with the spun resist should on top in a black box. Furthermore, it is recommended to turn all screens off during the transfer in the different UHV chambers.

Step	Equipment	Time [seconds]	Remark
1: Acetone	Wet Bench	60	
2: Isopropanol	Wet Bench	60	
3: H_20	Wet Bench	60	
4: N_2 Blow Dry	Wet Bench	10	
5: Water Removal	Hot Plate	60	Minimum 120 °C
6: Pause	Wet Bench	60	
7: Pre Spin ARN 7520.073	Spin Coater	2	500 rpm; 500 Acc
8: Spin Coat ARN 7520.073	Spin Coater	60	3000 rpm; 3000 Acc;
9: Pause	Wet Bench	300	
10: Resist Bake	Hot Plate	60	85 °C

Tab. A.4. Different steps for the cleaning and spin coating procedure for ARN 7520.073 as a negative resist.

Next all relevant parameters for the electron beam lithography for the negative resist are presented. For all structures, the used aperture is 10 μm with 30 kV EHT and the step size is chosen to be 4 nm. As before, the working distance is approximately 8.5 mm. The exposure dose for the alignment markers is 170 $\mu C/cm^2$ while the dose of the patterning of the nanowires is 280 $\mu C/cm^2$ for the wide nanowire and 360 $\mu C/cm^2$ for the narrow nanowires. The Cu bridge on top of the etched wires is patterned as explained before using recipe 1.

The development of the ARN 7520.073 resist has been performed as described in the following, while emphasizing that the development time can be strongly changed by varying the ratio between the developer and H_20:

a) Four parts of AR 300.47, diluted in one part of H_2O, are dropped on the sample for 23 seconds.

b) The development is stopped by dropping H_20 on the substrate for 30 seconds.

To fabricate the wires and the crosses out of the thin film, the substrates have been etched in the commercial (reactive) ion beam etch system "IonSys500" from "Meyer Burger", as described in Section 2.4. The general etching parameters are chosen as described in detail in the main part of the thesis and are only repeated here. However, the recipe to reduce side wall-deposition is here presented in detail. In the last step, reactive IBE with a 3 sccm flow of oxygen has been used. To achieve stable conditions, the oxygen flow needs to be set for a short time to 5 sccm before etching for 15 seconds with an oxygen flow of 3 sccm under an angle of incidence of 80 °.

- **PBN:** argon flow of 4 sccm
- **IBS:** argon flow of 5 sccm
- **HBSC:** pressure of 2 mbar
- **MW-Power:** 250 W
- **V_B:** 300 V
- **V_{acc}:** 200 V
- **I_N:** 100 mA

These parameters lead to a beam current of approximately 55 mA and a beam current density of approximately 290 $\mu C/cm^2$. When an additional gas flow of 3 sccm oxygen is used, the current density is increased to around 360 $\mu C/cm^2$.

Step	Angle of incidence [°]	Time [s]	Remark
1: Load sample		900	Pressure in chamber $6{\cdot}10^{-8}$ mbar
2: Etch	80	20	
3: Close shutter			
4: Etch	10	20	Leave shutter open
5: Etch	10-80	12	Leave shutter open
6: Etch	80	20	
7: Close shutter			
8: Repeat the steps **2** to **7**	until etched under 80 °	for 200 s	
9: Etch	10	20	After etched for 200 s under 80 °
10: Close shutter			
11: Etch	80	15	Use additional 3 sccm oxygen

Tab. A.5. Argon etching procedure for the fabricated Co_2MnSi samples.

To remove the residual resist after IBE, the sample is processed as follows:

a) Leave the substrate in acetone overnight.

b) Put the sample the next day in acetone into the ultrasound bath for approximately 5 minutes.

c) Put the sample at the lowest possible position in the oxygen plasma in a Petri dish for 60 minutes. The power of the plasma is chosen to be 300 W and an oxygen pressure of 1.2 Torr is chosen. These parameters are highly recommended since with e.g. a lower oxygen pressure and a lower plasma power, significantly worse results are achieved.

d) Put the sample at a very high position in the asher (height of the 1000 ml beaker glass and the height of the smallest Petri dish) and use the same oxygen plasma conditions as before for two times 30 seconds. Do a pause of approximately 60 seconds between the two ashing procedures.

To check if the treatments, especially the etching and the argon ashing procedure, do not change the attributes of the stack, XRR measurements have been performed, as shown in Figure A.2. In Figure A.2a) the XRR measurement of an as grown 14 nm Ta thin film is shown in green, while the same thin film processed in the oxygen plasma is shown in orange. As clearly visible, the thickness of the film is reduced (and the resistivity has changed), making Ta an unfavourable capping layer for samples which are treated by oxygen ashing. This becomes also evident in Figure A.2b) where the XRR measurement of an as grown 30CoFeB/20Cu/2Ta film is shown in brown, while the oxygen plasma treated thin film is shown in purple. Clear differences in the XRR measurements are observed, indicating again that Ta is not suited to be a capping layer material.

This is different for the case shown in Figure A.2c). Here the XRR measurement of a 30CoFeB/20Cu/2Ta/4Pt film is presented. Hardly any differences between the as grown film (green curve), the film which has been ashed for 30 seconds at the top position in the oxygen plasma (red curve) and the film which has been ashed for 60 seconds (blue curve) are found. Further strong evidence that Pt is an excellent capping layer for oxygen plasma treated samples is presented in Figure A.2d). The blue curve shows the XRR measurement of a formerly 14 nm Pt film, etched via the in-situ argon gun in the UHV thermal evaporation chamber for 60 minutes. A reduction of the film thickness to approximately 8.5 nm is found. The red curve shows a formerly 14 nm Pt film, which has been fully processed (spin coated, baking of the resist, etched via IBE, resist removal via acetone and the full oxygen plasma treatment) and finally etched in the UHV thermal evaporation chamber with the same conditions. By the treatment, the Pt film becomes slightly rougher but does not change thickness or resistivity, indicating that Pt is a perfectly suited capping layer. Due to these measurements, 4 nm of Pt have been deposited on the Co_2MnSi samples, which have been previously just capped with 2 nm of Ta.

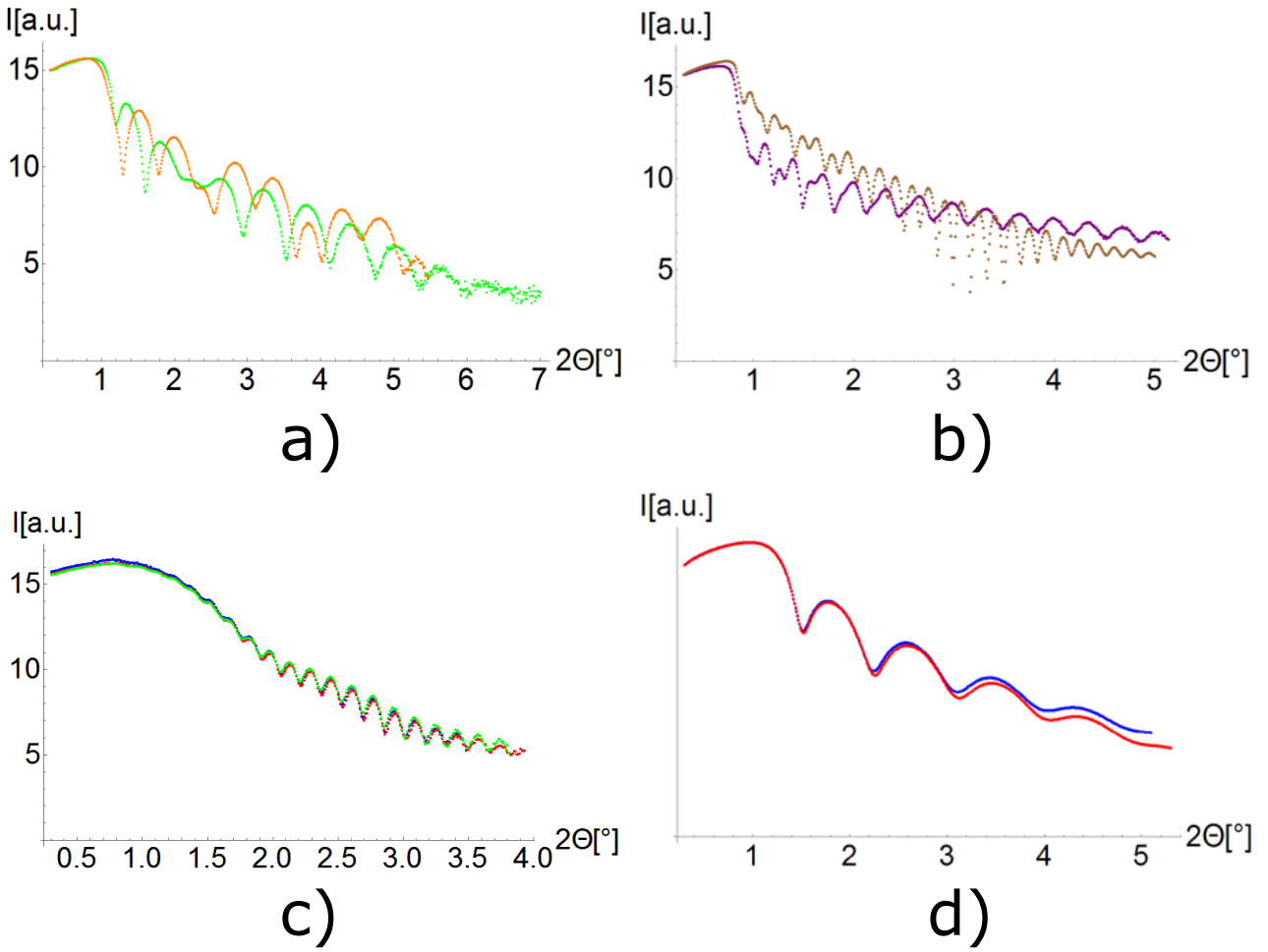

Fig. A.2. XRR measurements of either Pt/Ta films or films with either Pt or Ta as a capping layer.
a) XRR measurement of an as grown 14 nm Ta film shown in green and the same film treated by oxygen plasma shown in orange. Differences between the two curves are observed, indicating a change of the thickness and of the roughness of the Ta film by oxygen plasma treatment.
b) XRR measurement of an as grown 30CoFeB/20Cu/2Ta film shown in brown and the same film treated by oxygen plasma shown in purple. As in a), differences are observed for the two curves, indicating that Ta is not a suitable capping layer for oxygen plasma treated samples.
c) XRR measurement of an as grown 30CoFeB/20Cu/2Ta/4Pt film shown in green, 30 seconds oxygen plasma treated film shown in red and 60 seconds oxygen plasma treated film shown in blue. Hardly any differences of the XRR patterns are observed, indicating that Pt is a suitable capping layer for oxygen plasma treated samples.
d) XRR measurement of an as grown 14 nm Pt film etched for 60 minutes in the UHV thermal evaporation chamber shown in blue and the same film completely processed (spin coated, baking of the resist, IBE, acetone removal and oxygen plasma treatment) and etched at the same time shown in red. No differences in the thickness (8.5 nm) and only slight differences in the roughness are observed by the processing of the film.

Next, AFM line scans across certain nanowires based on the described etching recipe are shown in Figure A.3. Here the material stacks are varied in order to find out the increase of the thickness of the wires based on the original thickness of the Pt and the Ta in the grown stack. The three studied stacks with all numbers given in nm are:

a) Al_2O_3/30CoFeB/20Cu/2Ta/4Pt

b) Al_2O_3/30CoFeB/20Cu/2Ta/16Pt

c) Al_2O_3/30CoFeB/20Cu/10Ta/4Pt

For stack a), a thickness of 95 nm is determined while for stack b) ("Pt stack") a total thickness of 120 nm is observed. An increase of the thickness of the Pt in the stack of 12 nm leads to an increase in the thickness of the nanowires of 25 nm. Therefore the thickness of the wires based on the original stack is expected to be 8 nm Pt. For stack c) ("Ta stack") with 10 nm Ta, a total thickness of 130 nm is observed which means that an increase of the Ta thickness by 8 nm increases the thickness of the wires by 35 nm. As a result, the wires of the original stack are expected to have approximately 8 nm Ta.

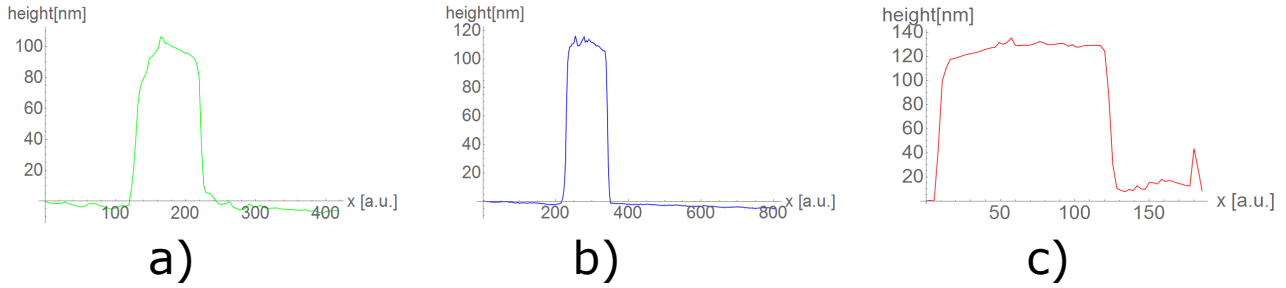

Fig. A.3. a) AFM line scan across a nanowire based on the original stack. The thickness is determined to be 95 nm.
b) AFM line scan across a nanowire based on a stack with additional 12 nm of Pt compared to the original stack ("Pt stack"). The thickness is determined to be 120 nm.
c) AFM line scan across a nanowire based on a stack with additional 8 nm of Ta compared to the original stack ("Ta stack"). The thickness is determined to be 130 nm.

In the next step, the wires have been etched via IBE for 120 seconds under an angle of incidence of 90 ° in order to compare the expected thicknesses with the measured thicknesses. The expected thicknesses are based on the etching rates of thin films, measured via endpoint detection or via XRR. For Pt, the rate is 16 nm/min, for Ta the rate is 8 nm/min and for Cu the rate is 24 nm/min. The results of the AFM measurements for the three types of wire are shown in Figure A.4. For the Pt stack, it is expected that the total thickness of the wires of 110 nm is comprised of a certain thickness of CoFeB and Cu with 8 nm of Ta and 32 nm of Pt. By etching for 120 seconds it is expected that the Pt is completely etched away and the resulting thickness should be approximately 88 nm. As shown in Figure A.4b) the thickness is determined to be 86 nm, in very good agreement with the expectations. For the Ta stack (Figure A.4c)), analogously a reduction of the thickness from previously 130 nm (a certain thickness of CoFeB and Cu with 32 nm of Ta and 8 nm of Pt) to 110 nm is expected since it takes 30 seconds to completely remove the 8 nm Pt and in 90 seconds, 12 nm of Ta are removed. As shown in Figure A.4c), also this measurement is in very good agreement with the expectations.

For the original stack (95 nm thick consisting of CoFeB and Cu with 8 nm Ta and 8 nm Pt) a resulting thickness of 67 nm is expected after 120 seconds of IBE under an angle of incidence of 90 °. The reduction of the thickness by 28 nm is based on the expectation that it takes 30 seconds to remove 8 nm of Pt and 60 seconds to remove 8 nm of Ta. Consequently 12 nm of Cu should be removed in 30 seconds. The measured thickness however is 38 nm and therefore significantly lower than expected.

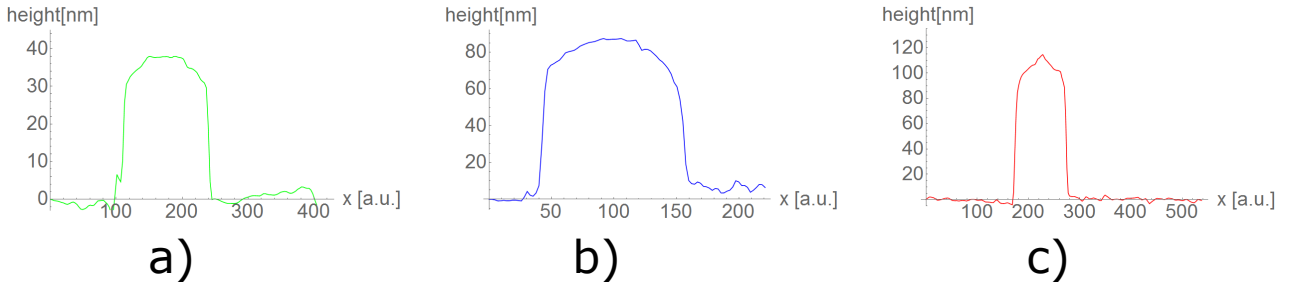

Fig. A.4. AFM line scans across nanowires etched out of the different material stacks after additional 120 seconds IBE with an angle of incidence of 90 °.
a) The thickness of the original stack, which was 95 nm before the etching, has been reduced to approximately 38 nm. A thickness of approximately 67 nm has been expected. The huge discrepancy between expected and measured thickness is not understood.
b) The thickness of the nanowires based on the Pt stack, which was 120 nm before the etching, has been reduced to approximately 86 nm. 16 nm of Pt in the stack lead to an increase of the thickness of 32 nm for the nanowires. As a result, a reduction of the thickness of 32 nm has been expected since Pt has a etching rate of 16 nm/min. The expected thickness is 88 nm while the measured thickness is 86 nm, resulting in a very good agreement.
c) The thickness of the nanowires based on the Ta stack, which was 130 nm before the etching, has been reduced to approximately 110 nm. 10 nm of Ta in the stack lead to an increase of the thickness of 40 nm, as a result a reduction of the thickness of 20 nm has been expected. To remove the 8 nm of Pt takes 30 seconds and in the remaining 90 seconds 12 nm of Ta are removed. As for the Pt stack very good agreement between the expected thickness and measured thickness is obtained.

In order to check if Cu has a significantly higher etching rate if nanowires are etched compared to thin films (which might explain the unexpected low thickness of wires based on the original stack), AFM measurements on old, already measured samples with Cu used for the nonmagnetic bridge and the contact pads, have been performed. The as grown Cu contacts are 130 nm thick while after 70 seconds IBE with an angle of incidence of 90 °, the thickness has been reduced to approximately 100 nm in full agreement with our expectations, since the etching rate of Cu is 24 nm/min.

In order to check the reliability of the significantly increased etching rate of Cu, once Ta and Pt are etched away, the previously 120 seconds Pt stack and the Ta stack has been etched for an additional 90 seconds. While the thickness of the nanowires based on the Ta stack has been reduced by approximately 12 nm, in full agreement with the expectations, and is therefore not shown, the thickness of the nanowires based on the Pt stack is reduced to approximately 35 nm, as shown in Figure A.5c).

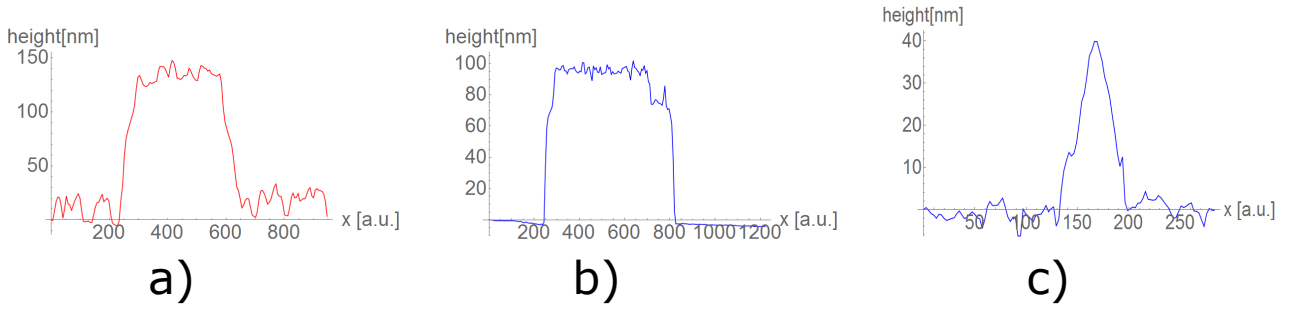

Fig. A.5. a) AFM line scan across a Cu contact. The thickness of the Cu contact is determined to be approximately 130 nm.
b) AFM line scan across a Cu contact after 70 seconds of IBE. As expected, the thickness of the Cu contact is reduced to approximately 100 nm.
c) AFM line scan across a nanowire of the Pt stack after additional 90 seconds of IBE under an angle of incidence of 90 °. The thickness of the nanowire is determined to be approximately 35 nm.

Bibliography

1. Binasch, G., Grünberg, P., Saurenbach, F. & Zinn, W. Enhanced magnetoresistance in layered magnetic structures with antiferromagnetic interlayer exchange. *Phys. Rev. B* **39,** 4828–4830 (1989).
2. Baibich, M. N. *et al.* Giant Magnetoresistance of (001)Fe/(001)Cr Magnetic Superlattices. *Phys. Rev. Lett.* **61,** 2472–2475 (1988).
3. IBM. *The Application of Spintronics* 2018. `https://www.ibm.com/ibm/history/ibm100/us/en/icons/spintronics/`.
4. Parkin, S. S. P., Hayashi, M. & Thomas, L. Magnetic Domain-Wall Racetrack Memory. *Science* **320,** 190–194 (2008).
5. Myers, E. B., Ralph, D. C., Katine, J. A., Louie, R. N. & Buhrman, R. A. Current induced switching of domains in magnetic multilayer devices. *Science* **285,** 867–870 (1999).
6. Ralph, D. & Stiles, M. Spin Transfer Torques. *J. Magn. Magn. Matter* **320,** 1190–1216 (2008).
7. Liu, L. *et al.* Spin-Torque Switching with the Giant Spin Hall Effect of Tantalum. *Science* **336,** 555–558 (2012).
8. Pai, C. F. *et al.* Spin transfer torque devices utilizing the giant spin Hall effect of tungsten. *Appl. Phys. Lett.* **101,** 122404 (2012).
9. Manchon, A. *et al.* Current-induced spin-orbit torques in ferromagnetic and antiferromagnetic systems. *Rev. Mod. Phys.* **91,** 035004 (2019).
10. Johnson, M. & Silsbee, R. H. Interfacial charge-spin coupling: Injection and detection of spin magnetization in metals. *Phys. Rev. Lett.* **55,** 1790–1793 (1985).
11. Jedema, F. J, Filip, A. T. & van Wees, B. J. Electrical spin injection and accumulation at room temperature in an all-metal mesoscopic spin valve. *Nature* **410,** 345–348 (2001).
12. Yang, T., Kimura, T. & Otani, Y. Giant spin-accumulation signal and pure spin-current-induced reversible magnetization switching. *Nat. Phys.* **4,** 851–854 (2008).
13. Ilgaz, D. *et al.* Domain-Wall Depinning Assisted by Pure Spin Currents. *Phys. Rev. Lett.* **105,** 076601 (2010).
14. Motzko, N. *et al.* Pure spin current-induced domain wall motion probed by localized spin signal detection. *Phys. Rev. B* **88,** 214405 (2013).
15. Pfeiffer, A. *et al.* Geometrical control of pure spin current induced domain wall depinning. *J. Phys.: Condens. Matter* **29,** 085802 (2017).
16. Behin-Aein, B., Datta, D., Salahuddin, S. & Datta, S. Proposal for an all-spin logic device with built-in memory. *Nat. Nanotechnol* **5,** 266–270 (2010).
17. Takahashi, Y. K., Kasai S. S. Hirayama, S. S., Mitani, S. & Hono, K. All-metallic lateral spin valves using Co_2Fe ($Ge_{0.5}Ga_{0.5}$) Heusler alloy with a large spin signal. *Appl. Phys. Lett.* **100,** 052405 (2012).
18. Yamada, M. *et al.* Scalability of Spin Accumulation Sensor. *IEEE T. Magn.* **49,** 713 (2012).
19. Eisberg, R. & Resnick, R. *Quantum Physics: Of Atoms, Molecules, Solids, Nuclei, and Particles* 2nd Edition (John Wiley & Sons Inc., 1985).
20. Schwabl, F. *Quantenmechanik* 7th edition (Springer, 2007).
21. Scheck, F. *Theoretische Physik 2* 3rd edition (Springer, 2013).
22. Coey, J. M. D. *Magnetism and Magnetic Materials* 1st Edition (Cambridge University Press, 2010).

23. Ashcroft, N. W. & Mermin, D. N. *Festkörperphysik* 4th Edition (De Gruyter Oldenbourg, 2012).
24. Lo Conte, R. *Magnetic nanostructures with structural inversion asymmetry* PhD thesis (Johannes Gutenberg-Universität Mainz, 2015).
25. Stoner, E. C. Collective Electron Ferromagnetism. II. Energy and Specific Heat. *Proceedings of the Royal Society A: Mathematical, Physical and Engineering Sciences* **169,** 339 (1939).
26. Ibach, H. & Lüth, H. *Festkörperphysik* 7th edition (Springer, 2009).
27. Stöhr, J. & Siegmann, H. C. *Magnetism* 1st edition (Springer, 2006).
28. Landau, L. D. & Lifshitz, E. M. On the Theory of the Dispersion of Magnetic Permeability in Ferromagnetic Bodies. *Phys. Zeitsch. Sow* **8,** 153–164 (1935).
29. Krüger, B. *Current-Driven Magnetization Dynamics: Analytical Modeling and Numerical Simulation* PhD thesis (Universität Hamburg, 2011).
30. Gilbert, T. L. A Lagrangian Formulation of the Gyromagnetic Equation of the Magnetization Field. *Phys.Rev.* **100,** 1243 (1955).
31. Heisenberg, W. Zur Theorie des Ferromagnetismus. *Z. Physik* **49,** 619–636 (1928).
32. Jackson, J. D. *Classical Electrodynamics* 3rd Edition (Wiley, 1998).
33. Honda, K., Kaya, S. & Masuyama, Y. On the Magnetic Properties of Single Crystals of Iron. *Nature* **117,** 753–754 (1926).
34. Rebouillat, J. P. High resolution automatic magnetometer using a superconducting magnet: Application to high field susceptibility measurements. *Trans. Magn.* **8,** 630–633 (1972).
35. Paige, D. M., Szpunar, B. & Tanner, B. K. The magnetocrystalline anisotropy of cobalt. *J. Magn. Magn. Mater.* **44,** 239–248 (1984).
36. Aharoni, A. *Introduction to the Theory of Ferromagnetism* 2nd Edition (Oxford University Press, 2000).
37. Blundell, S. *Magnetism in Condensed Matter* 2nd Edition (Oxford University Press, 2003).
38. Weiss, P. E. La variation du ferromagnétisme avec la temperature. *Comptes Rendus Acad. Sci* **143** (1906).
39. Weiss, P. E. and sur la théorie des propriétés magnétiques du fer au delà du point de transformation. *Comptes Rendus Acad. Sci* **144** (1906).
40. Hubert, A. & Schäfer, R. *Magnetic Domains* 3rd Edition (Springer, 2009).
41. Kläui, M. Head-to-head domain walls in magnetic nanostructures. *J. Phys. Condens. Matter* **20,** 313001 (2008).
42. Kronmüller, H. & Parkin, S. *Handbook of Magnetism and Advanced Magnetic Materials* 1st edition (Wiley, 2007).
43. McMichael, R. & Donahue, M. Head to head domain wall structures in thin magnetic strips. *IEEE Trans. Mag.* **33,** 4167–4169 (1997).
44. Nakatani, Y., Thiaville, A. & Miltat, J. Head-to-head domain walls in soft nano-strips: a refined phase diagram. *J. Magn. Magn. Mat.* **290,** 750–753 (2005).
45. Laufenberg, M. *et al.* Observation of thermally activated domain wall transformations. *Appl. Phys. Lett.* **88,** 052507 (2006).
46. Bryan, M. T., Bance, S., Dean, J., Schrefl, T. & Allwood, D. Transverse and vortex domain wall structure in magnetic nanowires with uniaxial in-plane anisotropy. *J. Phys.: Condens. Matter* **24,** 024205 (2012).
47. Krautscheid, P., Reeve, R. M., Lauf, M., Krüger, B. & Kläui, M. Domain wall spin structures in mesoscopic Fe rings probed by high resolution SEMPA. *J. Phys. D: Appl. Phys.* **49,** 425004 (2016).

48. Wilhelm, E. S., McGrouther, D., Heyne, L., Bisig, A. & Kläui, M. Vortex domain wall chirality rectification due to the interaction with end domain spin structures in permalloy nanowires. *Appl. Phys. Lett.* **95,** 252501 (2009).

49. Grollier, J. *et al.* Switching a spin valve back and forth by current-induced domain wall motion. *Appl. Phys. Lett.* **83,** 509 (2003).

50. Vernier, N., Allwood, D. A., Atkinson, D., Cooke, M. D. & Cowburn, R. P. Domain wall propagation in magnetic nanowires by spin-polarized current injection. *EPL* **65,** 526 (2003).

51. Tsoi, M., Fontana, R. E. & Parkin, S. S. P. Magnetic domain wall motion triggered by an electric current. *Appl. Phys. Lett.* **83,** 2617–2619 (2003).

52. Hayashi, M. *et al.* Influence of Current on Field-Driven Domain Wall Motion in Permalloy Nanowires from Time Resolved Measurements of Anisotropic Magnetoresistance. *Phys. Rev. Lett.* **96,** 197207 (2006).

53. Meier, G. *et al.* Direct Imaging of Stochastic Domain-Wall Motion Driven by Nanosecond Current Pulses. *Phys. Rev. Lett.* **98,** 187202 (2007).

54. Yang, S. & Erskine, J. L. Spin-transfer-torque-driven domin-wall dynamics in Permalloy nanowires. *Phys. Rev. B* **75,** 220403 (2007).

55. Kunz, A. Field induced domain wall collisions in thin magnetic nanowires. *Appl. Phys. Lett.* **94,** 132502 (2009).

56. Malinowski, G., Boulle, O. & Kläui, M. Current-induced domain wall motion in nanoscale ferromagnetic elements. *J. Phys. D: Appl. Phys.* **44,** 384005 (2011).

57. Zhang, S. & Li, Z. Roles of Nonequilibrium Conduction Electrons on the Magnetization Dynamics of Ferromagnets. *Phys. Rev. Lett.* **93,** 127204 (2004).

58. Berger, L. Exchange interaction between ferromagnetic domain wall and electric current in very thin metallic films. *J. Appl. Phys.* **55,** 1954 (1984).

59. Hayashi, M. *et al.* Current Driven Domain Wall Velocities Exceeding the Spin Angular Momentum Transfer Rate in Permalloy Nanowires. *Phys. Rev. Lett.* **98,** 037204 (2007).

60. Gilmore, K., Garate, I., MacDonald, A. H. & Stiles, M. D. First-principles calculation of the nonadiabatic spin transfer torque in Ni and Fe. *Phys. Rev. B* **84,** 224412 (2011).

61. Eltschka, M. *et al.* Nonadiabatic Spin Torque Investigated Using Thermally Activated Magnetic Domain Wall Dynamics. *Phys. Rev. Lett.* **105,** 056601 (2010).

62. Boulle, O. *et al.* Nonadiabatic Spin Transfer Torque in High Anisotropy Magnetic Nanowires with Narrow Domain Walls. *Phys. Rev. Lett.* **101,** 216601 (2008).

63. Garate, I., Gilmore, K., Stiles, M. D. & MacDonald, A. H. Nonadiabatic spin-transfer torque in real materials. *Phys. Rev. B* **79,** 104416 (2009).

64. Burrowes, C. *et al.* Non-adiabatic spin-torques in narrow magnetic domain walls. *Nat. Phys.* **6,** 17–21 (2010).

65. Heyne, L. *et al.* Direct Determination of Large Spin-Torque Nonadiabaticity in Vortex Core Dynamics. *Phys. Rev. Lett.* **105,** 187203 (2010).

66. Rößler, S. *et al.* Nonadiabatic spin-transfer torque of magnetic vortex structures in a permalloy square. *Phys. Rev. B* **89,** 174426 (2014).

67. Chiba, D. *et al.* Control of Multiple Magnetic Domain Walls by Current in a Co/Ni Nano-Wire. *Appl. Phys. Express* **3,** 073004 (2010).

68. Petit, D. *et al.* Mechanism for domain wall pinning and potential landscape modification by artificially patterned traps in ferromagnetic nanowires. *Phys. Rev. B* **79,** 214405 (2009).

69. Kim, J. S. *et al.* Synchronous precessional motion of multiple domain walls in a ferromagnetic nanowire by perpendicular field pulses. *Nature Commun.* **5,** 3429 (2014).

70. N. L. Schryer, N. L. & Walker, L. R. The motion of 180 degree domain walls in uniform dc magnetic fields. *J. Appl. Phys.* **45,** 5406 (1974).

71. Li, Z. & Zhang, S. Domain-wall dynamics driven by adiabatic spin-transfer torques. *Phys. Rev. B* **70,** 024417 (2004).

72. Schieback, C., Hinzke, D., Kläui, M., Nowak, U. & Nielaba, P. Temperature dependence of the current-induced domain wall motion from a modified Landau-Lifshitz-Bloch equation. *Phys. Rev. B* **80,** 214403 (2009).

73. Koyama, T. *et al.* Observation of the intrinsic pinning of a magnetic domain wall in a ferromagnetic nanowire. *Nat. Mater.* **10,** 194–197 (2011).

74. Althammer, M. Pure spin currents in magnetically ordered insulator/normal metal heterostructures. *J. Phys. D: Appl. Phys.* **51,** 313001 (2018).

75. Hoffmann, A. Spin Hall Effects in Metals. *IEEE Trans. Magn.* **49,** 5172–5193 (2013).

76. Karplus, R. & Luttinger, J. M. Hall effect in ferromagnetics. *Phys. Rev.* **95,** 1154 (1954).

77. Smit, J. The spontaneous Hall effect in ferromagnetics ii. *Physica* **24,** 39 (1958).

78. Berger, L. Side-jump mechanism for the Hall effect in ferromagnets. *Phys. Rev. B.* **2,** 4559 (1970).

79. Hall, E. H. On a new action of the magnet on electric currents. *Am. J. Math.* **2,** 287 (1879).

80. Hall, E. H. On the "rotational coefficient" in nickel and cobalt. *Philos. Mag.* **12,** 157 (1881).

81. Ando, T., Matsumoto, Y. & Uemura, Y. Theory of Hall effect in a two-dimensional electron system. *Phys. Soc. Jpn.* **39,** 279–288 (1975).

82. Klitzing, K. v., Dorda, G. & Pepper, M. New Method for High-Accuracy Determination of the Fine-Structure Constant Based on Quantized Hall Resistance. *Phys. Rev. Lett.* **45,** 494–497 (1980).

83. Tsui, D. C., Stormer, H. L. & Gossard, A. C. Two-Dimensional Magnetotransport in the Extreme Quantum Limit. *Phys. Rev. Lett.* **48,** 1559–1562 (1982).

84. Laughlin, R. B. Anomalous Quantum Hall Effect: An Incompressible Quantum Fluid with Fractionally Charged Excitations. *Phys. Rev. Lett.* **50,** 1395–1398 (1983).

85. Kundt, A. Das Hallsche Phänomen in Eisen, Kobalt und Nickel. *Wied. Ann.* **49,** 257–271 (1893).

86. Pugh, E. M. Hall Effect and the Magnetic Properties of Some Ferromagnetic Materials. *Phys. Rev.* **36,** 1503–1511 (1930).

87. Pugh, E. M. & Lippert, T. W. Hall e.m.f. and Intensity of Magnetization. *Phys. Rev.* **42,** 709–713 (1932).

88. Nagaosa, N., Sinova, J., Onoda, S., MacDonald, A. H. & Ong, N. P. Anomalous Hall effect. *Rev. Mod. Phys.* **82,** 1539–1592 (2010).

89. Chang, M.-C. & Niu, Q. Berry phase, hyperorbits, and the Hofstadter spectrum: Semiclassical dynamics in magnetic Bloch bands. *Phys. Rev. B* **53,** 7010–7023 (1996).

90. Sundaram, G. & Niu, Q. Wave-packet dynamics in slowly perturbed crystals: Gradient corrections and Berry-phase effects. *Phys. Rev. B* **59,** 14915–14925 (1999).

91. Berry, M. V. Quantal phase factors accompanying adiabatic changes. *Proc. R. Soc. London* **392,** 45 (1984).

92. Kubo, R. Statistical-Mechanical Theory of Irreversible Processes. I. General Theory and Simple Applications to Magnetic and Conduction Problems. *J. Phys. Soc. Jpn.* **12,** 570–586 (1957).

93. Haldane, F. D. M. Berry Curvature on the Fermi Surface: Anomalous Hall Effect as a Topological Fermi-Liquid Property. *Phys. Rev. Lett.* **93,** 206602 (2004).

94. Yao, Y. *et al.* First Principles Calculation of Anomalous Hall Conductivity in Ferromagnetic bcc Fe. *Phys. Rev. Lett.* **92,** 037204 (2004).

95. Wang, X., Yates, J. R., Souza, I. & Vanderbilt, D. Ab initio calculation of the anomalous Hall conductivity by Wannier interpolation. *Phys. Rev. B* **74,** 195118 (2006).

96. Wang, X., Vanderbilt, D., Yates, J. R. & Souza, I. Fermi-surface calculation of the anomalous Hall conductivity. *Phys. Rev. B* **76,** 195109 (2007).

97. Berger, L. Influence of spin-orbit interaction on the transport processes in ferromagnetic nickel alloys, in the presence of a degeneracy of the 3d band. *Physica (Amsterdam)* **30,** 1141–1159 (1964).

98. Sinitsyn, N. A. Semiclassical theories of the anomalous Hall effect. *J. Phys. Condens. Matter* **20,** 023201 (2007).

99. Nozières, P. & Lewiner, C. A simple theory of the anomalous hall effect in semiconductors. *J. Phys. France* **34,** 901–915 (1973).

100. Sinitsyn, N. A., MacDonald, A. H., Jungwirth, T., Dugaev, V. K. & Sinova, J. Anomalous Hall effect in a two-dimensional Dirac band: The link between the Kubo-Streda formula and the semiclassical Boltzmann equation approach. *Phys. Rev. B* **75,** 045315 (2007).

101. Keldysh, L. V. Diagram Technique for Nonequilibrium Processes. *Sov. Phys. JETP* **47,** 1515 (1964).

102. Kato, Y. K., Myers, R. C., Gossard, A. C. & Awschalom, D. D. Observation of the spin Hall effect in semiconductors. *Science* **306,** 1910 (2004).

103. Nguyen, M.-H., Ralph, D. C. & Buhrman, R. A. Spin Torque Study of the Spin Hall Conductivity and Spin Diffusion Length in Platinum Thin Films with Varying Resistivity. *Phys. Rev. Lett.* **116,** 126601 (2016).

104. Sagasta, E. *et al.* Tuning the spin Hall effect of Pt from the moderately dirty to the superclean regime. *Phys. Rev. B* **94,** 060412 (2016).

105. Hao, Q., Chen, W. & Xiao, G. Beta tungsten thin films: Structure, electron transport, and giant spin Hall effect. *Appl. Phys. Lett.* **106,** 182403 (2015).

106. Niimi, Y. *et al.* Giant Spin Hall Effect Induced by Skew Scattering from Bismuth Impurities inside Thin Film CuBi Alloys. *Phys. Rev. Lett.* **109,** 156602 (2012).

107. Niimi, Y. *et al.* Extrinsic spin Hall effects measured with lateral spin valve structures. *Phys. Rev. B* **89,** 054401 (2014).

108. Cramer, J. *et al.* Complex Terahertz and Direct Current Inverse Spin Hall Effect in YIG/Cu1–xIrx Bilayers Across a Wide Concentration Range. *Nano Lett.* **18,** 1064–1069 (2018).

109. Laczkowski, P. *et al.* Large enhancement of the spin Hall effect in Au by side-jump scattering on Ta impurities. *Phys. Rev. B* **96,** 140405 (2017).

110. Gradhand, M., Fedorov, D. V., Zahn, P. & Mertig, I. Spin Hall angle versus spin diffusion length: Tailored by impurities. *Phys. Rev. B* **81,** 245109 (2010).

111. Gradhand, M., Fedorov, D. V., Zahn, P. & Mertig, I. Extrinsic Spin Hall Effect from First Principles. *Phys. Rev. Lett.* **104,** 186403 (2010).

112. Seki, T. *et al.* Giant spin Hall effect in perpendicularly spin-polarized FePt/Au devices. *Nat. Mater.* **7,** 125–129 (2008).

113. Mihajlovic, G., Pearson, J. E., Garcia, M. A., Bader, S. D. & Hoffmann, A. Negative Nonlocal Resistance in Mesoscopic Gold Hall Bars: Absence of the Giant Spin Hall Effect. *Phys. Rev. Lett.* **103,** 166601 (2009).

114. Chen, C., Tian, D., Zhou, H., Hou, D. & Jin, X. Generation and Detection of Pure Spin Current in an H-Shaped Structure of a Single Metal. *Phys. Rev. Lett.* **122,** 016804 (2019).

115. Dyakonov, M. I. & Perel, V. I. Possibilty of orienting electron spins with current. *Sov. Phys. JETP Lett.* **13,** 467 (1971).

116. Hirsch, J. E. Spin Hall Effect. *Phys. Rev. Lett.* **83,** 1834 (1999).

117. Niimi Otani, Y. Reciprocal spin Hall effects in conductors with strong spin–orbit coupling: a review. *Rep. Prog. Phys.* **78,** 124501 (2015).

118. Dyakonov, M. I & Kheatskii, A. V. *Spin Physics in Semiconductors* 1st Edition (Springer, 2008).

119. Dyakonov, M. I. Magnetoresistance due to Edge Spin Accumulation. *Phys. Rev. Lett.* **99,** 126601 (2007).

120. Wang, H. L. *et al.* Scaling of Spin Hall Angle in 3d, 4d, and 5d Metals from $Y_3Fe_5O_{12}$/Metal Spin Pumping. *Phys. Rev. Lett.* **112,** 197201 (2014).

121. Tanaka, T. *et al.* Intrinsic spin Hall effect and orbital Hall effect in 4*d* and 5*d* transition metals. *Phys. Rev. B* **77,** 165117 (2008).

122. Wang, Y., Deorani, P., Qiu, X., Kwon, J. H. & Yanga, H. Large spin-orbit torques in Pt/Co-Ni/W heterostructures. *Appl. Phys. Lett.* **105,** 152412 (2014).

123. Zhang, W., Han, W., Jiang, X., Yang, S.-H. & Parkin, S. S. P. Role of transparency of platinum-ferromagnet interface in determining intrinsic magnitude of spin Hall effect. *Nat. Phys.* **11,** 496–502 (2015).

124. Edelstein V, M. Spin polarization of conduction electrons induced by electric current in two-dimensional asymmetric electron systems. *Solid State Commun.* **73,** 233–235 (1990).

125. Gambardella, P. & Mihai, M. I. Current-induced spin–orbit torques. *Phil. Trans. R. Soc. A* **369** (2011).

126. Winkler, R. *Spin–orbit coupling effects in two-dimensional electron and hole systems* 1st Edition (Springer Berlin, 2003).

127. Properties of semiconductors with an extremum loop. I. Cyclotron and combinational resonance in a magnetic field perpendicular to the plane of the loop. *Sov. Phys. Solid State* **2,** 1109–1122 (1960).

128. Casella, R. C. Toroidal Energy Surfaces in Crystals with Wurtzite Symmetry. *Phys. Rev. Lett.* **5,** 371–373 (1960).

129. Vasko, F. T. Spin splitting in the spectrum of two-dimensional electrons due to surface potential. *JETP Lett.* 541–544 (1979).

130. Bychkov, Y. & Rashba, E. Oscillatory effects and the magnetic susceptibility of carriers in inversion layers. *J. Phys. C* **17,** 6039–6045 (1984).

131. Cartoixà, X., Wang, L.-W., Ting, D.-Y. & Chang, Y.-C. Higher-order contributions to Rashba and Dresselhaus effects. *Phys. Rev. B* **73,** 205341 (2006).

132. LaShell, S., McDougall, B. A. & Jensen, E. Spin Splitting of an Au(111) Surface State Band Observed with Angle Resolved Photoelectron Spectroscopy. *Phys. Rev. Lett.* **77,** 3419–3422 (1996).

133. Reinert, F., Nicolay, G., Schmidt, S., Ehm, D. & Hüfner, S. Direct measurements of the L-gap surface states on the (111) face of noble metals by photoelectron spectroscopy. *Phys. Rev. B* **63,** 115415 (2001).

134. Krupin, O. *et al.* Rashba effect at magnetic metal surfaces. *Phys. Rev. B* **71,** 201403 (2005).

135. Engel, H.-A., Rashba, E. I. & Halperin, B. I. Out-of-Plane Spin Polarization from In-Plane Electric and Magnetic Fields. *Phys. Rev. Lett.* **98,** 036602 (2007).

136. Saarikoski, H. & Bauer, G. E. W. Spin Accumulation with Spin-Orbit Interaction. *Phys. Rev. Lett.* **102,** 097204 (2009).

137. Mugarza, A. *et al.* Lateral quantum wells at vicinal Au(111) studied with angle-resolved photoemission. *Phys. Rev. B* **66,** 245419 (2002).

138. Petersen, L & Hedegard, P. A simple tight-binding model of spin–orbit splitting of sp-derived surface states. *Surf. Sci.* **459,** 49–56 (2000).

139. Inoue, J.-i., Bauer, G. E. W. & Molenkamp, L. W. Diffuse transport and spin accumulation in a Rashba two-dimensional electron gas. *Phys. Rev. B* **67,** 033104 (2003).

140. Stern, N. P. *et al.* Current-Induced Polarization and the Spin Hall Effect at Room Temperature. *Phys. Rev. Lett.* **97,** 126603 (2006).

141. Silov, A. Y. *et al.* Current-induced spin polarization at a single heterojunction. *Appl. Phys. Lett.* **85,** 5929–5931 (2004).

142. Silsbee, R. H. Theory of the detection of current-induced spin polarization in a two-dimensional electron gas. *Phys. Rev. B* **63,** 155305 (2001).

143. Johnson, M. & Silsbee, R. H. Ferromagnet-Nonferromagnet Interface Resistance. *Phys. Rev. Lett.* **60,** 377–377 (1988).

144. Kimura, T., Hamrle, J. & Otani, Y. Estimation of spin-diffusion length from the magnitude of spin-current absorption: Multiterminal ferromagnetic/nonferromagnetic hybrid structures. *Phys. Rev. B* **72,** 014461 (2005).

145. Kimura, T., Sato, T. & Otani, Y. Temperature Evolution of Spin Relaxation in a NiFe/Cu Lateral Spin Valve. *Phys. Rev. Lett.* **100,** 066602 (2008).

146. Godfrey, R. & Johnson, M. Spin Injection in Mesoscopic Silver Wires: Experimental Test of Resistance Mismatch. *Phys. Rev. Lett.* **96,** 136601 (2006).

147. Motzko, N. *et al.* Spin relaxation in Cu and Al spin conduits. *physica status solidi (a)* **211,** 986–990 (2014).

148. O'Brien, L. *et al.* Kondo physics in non-local metallic spin transport devices. *Nat. Comm.* **5,** 3927 (2014).

149. Yan, W. *et al.* Large room temperature spin-to-charge conversion signals in a few-layer graphene/Pt lateral heterostructure. *Nat. Comm.* **8,** 661 (2017).

150. Ji, Y., Hoffmann, A., Jiang, J. S., Pearson, J. E. & Bader, S. D. Non-local spin injection in lateral spin valves. *J. Phys. D: Appl. Phys.* **40,** 1280 (2007).

151. Takahashi, S. & Maekawa, S. Spin injection and detection in magnetic nanostructures. *Phys. Rev. B* **67,** 052409 (2003).

152. Dubois, S. *et al.* Evidence for a short spin diffusion length in permalloy from the giant magnetoresistance of multilayered nanowires. *Phys. Rev. B* **60,** 477–484 (1999).

153. Sagasta, E. *et al.* Spin diffusion length of Permalloy using spin absorption in lateral spin valves. *Appl. Phys. Lett.* **111,** 082407 (2017).

154. Zahnd, G. *et al.* Spin diffusion length and polarization of ferromagnetic metals measured by the spin-absorption technique in lateral spin valves. *Phys. Rev. B* **98,** 174414 (2018).

155. Jedema, F. J, Heersche, H. B., Filip, A. T., Baselmans, J. J. & van Wees, B. J. Electrical detection of spin precession in a metallic mesoscopic spin valve. *Nature* **416,** 713 (2002).

156. Slachter, A., Bakker, F. L., Adam, J.-P. & van Wees, B. J. Thermally driven spin injection from a ferromagnet into a non-magnetic metal. *Nat. Phys.* **6,** 879–882 (2010).

157. Erekhinsky, M., Casanova, F., Schuller, I. K. & Sharoni, A. Spin-dependent Seebeck effect in non-local spin valve devices. *Appl. Phys. Lett.* **100,** 212401 (2012).

158. Hu, S., Itoh, H. & Kimura, T. Efficient thermal spin injection using CoFeAl nanowire. *NPG Asia Materials* **6,** e127 (2014).

159. Van Son, P. C., van Kempen, H. & Wyder, P. Boundary Resistance of the Ferromagnetic-Nonferromagnetic Metal Interface. *Phys. Rev. Lett.* **58,** 2271–2273 (1987).

160. Kiselev, S. *et al.* Microwave oscillations of a nanomagnet driven by a spin-polarized current. *Nature* **425,** 380–383 (2003).

161. Xu, Y., Xia, K. & Ma, Z. Spin transfer torques in the nonlocal lateral spin valve. *Nanotechnology* **19,** 235404 (2008).

162. Slonczweski, J. C. Current-driven excitation of magnetic multilayers. *J. Magn. Magn. Mater.* **159,** L1–L7 (1996).

163. Brataas, A., Bauer, G. E. W. & Kelly, P. J. Non-collinear magnetoelectronics. *Phys. Rep.* **427,** 157–255 (2006).

164. Stiles, M. D. & Zangwill, A. Anatomy of spin-transfer torque. *Phys. Rev. B* **66,** 014407 (2002).

165. Hershfield, S. & Zhao, H. L. Charge and spin transport through a metallic ferromagnetic-paramagnetic-ferromagnetic junction. *Phys. Rev. B* **56,** 3296–3305 (1997).

166. Brataas, A., Nazarov, Y. V. & Bauer, G. E. W. Finite-Element Theory of Transport in Ferromagnet–Normal Metal Systems. *Phys. Rev. Lett.* **84,** 2481–2484 (2000).

167. Sun, J. *IBM J. Res. Dev.* **50,** 81 (2006).

168. Steren, L. B. *et al.* Angular dependence of the giant magnetoresistance effect. *Phys. Rev. B* **51,** 292–296 (1995).

169. Nanofabrication, R. *Pioneer Two, Multi Technique Electron Beam Lithography* `https://www.raith.com/products/pioneer.html`.

170. Zeiss. *ZEISS GeminiSEM – Field Emission Scanning Electron Microscope* `https://www.zeiss.com/microscopy/int/products/scanning-electron-microscopes/geminisem.html`.

171. Reimer, L. & Pfefferkorn, G. *Rasterelektronenmikroskopie* 1st Edition (Springer-Verlag, Berlin, 1977).

172. Zhou, W. & W., Z. L. *Scanning Microscopy for Nanotechnology* 1st Edition (Springer Science and Business Media, 2007).

173. Van Zyl, W. *How to spot astigmatism in Scanning Electron Microscopy (SEM) images* `https://blog.phenom-world.com/astigmatism-electron-microscopy`.

174. Everhart, T. E. & Thornley, R. F. M. Wide-band detector for micro-microampere low-energy electron currents. *Rev. Sci. Instrum.* **37,** 246–248 (1960).

175. Bernhards, F. private communication. 2019.

176. Meitner, L. Über die Entstehung der beta-Strahl-Spektren radioaktiver Substanzen. *Z. Phys.* **9,** 131–144 (1922).

177. Auger, P. Sur les rayons beta secondaires produits dans un gaz par des rayons X. *C.R.A.S.* **177,** 169–171 (1923).

178. Goldstein, J. *Scanning Electron Microscopy and X-Ray Microanalysis* 3rd Edition (Springer US, 2003).

179. Seiler, H. Secondary electron emission in the scanning electron microscope. *J. Appl. Phys.* **54,** R1–R18 (1983).

180. McMullan, D. SEM-Past, Present and Future. *Journal of Microscopy* **155,** 373–392 (1989).

181. AllResist. *Negative E-Beam Resists AR-N 7520* 2019. `https://www.allresist.com/wp-content/uploads/sites/2/2016/12/allresist_produktinfos_ar-n7520_englisch.pdf`.

182. Jourdan, M. *et al.* Direct observation of half-metallicity in the Heusler compound Co2MnSi. *Nat. Comm.* **5,** 3974 (2014).

183. MeyerBurger. *IonSys - Model 500 - Ion Beam Deposition System- Brochure* https://www.energy-xprt.com/downloads/ionsys-model-500-ion-beam-deposition-system-brochure-656413.

184. Chen, F. F. *Introduction to Plasma Physics and Controlled Fusion* 1–51 (Plenum Press, New York, 1984).

185. Buchholz, B. *Physics of ion beam sources* http://citeseerx.ist.psu.edu/viewdoc/download;jsessionid=EB3294164DBEB9EF231B6C57EC4D7E33?doi=10.1.1.521.8140&rep=rep1&type=pdf.

186. Purswani, J. M., Spila, T. & Gall, D. Growth of epitaxial Cu on MgO(001) by magnetron sputter deposition. *Thin Solid Films* **515,** 1166–1170 (2006).

187. Aleman, A., Li, C. & Zaid, H. Ultrahigh vacuum dc magnetron sputter-deposition of epitaxial Pd(111)/Al2O3(0001) thin films. *J. Vac. Sci. Technol. A* **36,** 030602 (2018).

188. Seshan, K. *Handbook of Thin Film Deposition, Process and Technologies* 3rd Edition (William Andrew, 2012).

189. Wasa, K., Kanno, I. & Kotera, H. *Handbook of Sputter Deposition Technology* 2nd Edition (William Andrew, 2012).

190. Kehlberger, A. *Origin of the spin Seebeck effect* PhD thesis (Johannes Gutenberg-Universität Mainz, 2015).

191. Henini, M. *Molecular Beam Epitaxy-From Research to Mass Production* 2nd Edition (Elsevier, 2018).

192. Inficon2019. *SQM-160 Thin Film Deposition Monitor* https://products.inficon.com/en-us/nav-products/product/detail/sqm-160/.

193. Vacuum, P. *Mean free path* https://www.pfeiffer-vacuum.com/en/know-how/introduction-to-vacuum-technology/fundamentals/mean-free-path/.

194. Group, S. *IQE 11/35:Exractor type ion source optimized for sample cleaning* https://www.specs-group.com/nc/specs/products/detail/iqe-1135/.

195. Birkholz, M. *Thin Film Analysis by X-Ray Scattering* 1st Edition (WILEY-VCH, 2005).

196. Parratt, L. G. Surface Studies of Solids by Total Reflection of X-Rays. *Phys. Rev.* **95,** 359 (1954).

197. Eaton, P. & West, P. *Atomic force microscopy* 1st Edition (Oxford University Press, 2010).

198. Bruker. *Sharp Nitride Lever Probes* https://www.brukerafmprobes.com/p-3693-snl-10.aspx.

199. Lennard-Jones, J. E. On the determination of molecular fields.-II. From the equation of state of a gas. *Proc. Royal Soc. A* **106,** 463–477 (1924).

200. Nečas, D. & Klapetek, P. Gwyddion: an open-source software for SPM data analysis. *Cent. Eur. J. Phys.* **10,** 181–188 (2012).

201. Schnitzspan, L. *Charge Transport in Two Dimensional Carbon Heterostructures* MA thesis (Johannes Gutenberg Universität Mainz, 2019).

202. Amethek. *Data Sheet 7225 Dual Phase DSP Lock-In Amplifier* https://www.ameteksi.com/products/lock-in-amplifiers/7225-dual-phase-dsp-lock-in-amplifier.

203. Systems, S. R. *Manual SR830 Lock-In Amplifier* https://www.thinksrs.com/downloads/pdfs/manuals/SR830m.pdf.

204. Oswald. *Oswald-Power to move* https://www.oswald.de/en/.

205. Kepco. *Series BOP-MG 1KW High Power Models* https://www.kepcopower.com/bophimod.htm.

206. Cryotronics, L. S. *Cernox Cryogenic Temperature Sensors* https://www.lakeshore.com/products/categories/overview/temperature-products/cryogenic-temperature-sensors/cernox.

207. Cowburn, R. P., Koltsov, D. K., Adeyeye, A. O., Welland, M. E. & Tricker, D. M. Single-Domain Circular Nanomagnets. *Phys. Rev. Lett.* **83,** 1042–1045 (1999).

208. Shinjo, T., Okuno, T., Hassdorf, R., Shigeto, K. & Ono, T. Magnetic Vortex Core Observation in Circular Dots of Permalloy. *Science* **289,** 930–932 (2000).

209. Choe, S. B. *et al.* Vortex Core-Driven Magnetization Dynamics. *Science* **304,** 420–422 (2004).

210. Van Waeyenberge, B. *et al.* Magnetic vortex core reversal by excitation with short bursts of an alternating field. *Nature* **444,** 461–464 (2006).

211. Xiao, Q. F., Rudge, J., Girgis, E., Kolthammer, J. & Choia, B. C. Dynamics of magnetic vortex core switching in Fe nanodisks by applying in-plane magnetic field pulse. *Appl. Phys. Lett.* **102,** 103904 (2007).

212. Curcic, M. *et al.* Polarization Selective Magnetic Vortex Dynamics and Core Reversal in Rotating Magnetic Fields. *Phys. Rev. Lett.* **101,** 197204 (2008).

213. Yamada, K. *et al.* Electrical switching of the vortex core in a magnetic disk. *Nat. Mater.* **6,** 270–273 (2007).

214. Bedau, D. *et al.* Detection of Current-Induced Resonance of Geometrically Confined Domain Walls. *Phys. Rev. Lett.* **99,** 146601 (2007).

215. Yamada, K., Kasai, S., Nakatani, Y., Kobayashi, K. & Ono, T. Switching magnetic vortex core by a single nanosecond current pulse. *Appl. Phys. Lett.* **93,** 152502 (2008).

216. Kammerer, M. *et al.* Magnetic vortex core reversal by excitation of spin waves. *Nat. Commun.* **2,** 279 (2011).

217. Fu, X. *et al.* Optical manipulation of magnetic vortices visualized in situ by Lorentz electron microscopy. *Sci. Adv.* **4,** 3077 (2018).

218. Krüger, B. *et al.* Proposal of a Robust Measurement Scheme for the Nonadiabatic Spin Torque Using the Displacement of Magnetic Vortices. *Phys. Rev. Lett.* **104,** 077201 (2010).

219. Pollard, S. D., Huang, L., Buchanan, K. S., Arena, D. A. & Zhu, Y. Direct dynamic imaging of non-adiabatic spin torque effects. *Nat. Commun.* **3,** 1028 (2012).

220. Rößler, S. *et al.* Nonadiabatic spin-transfer torque of magnetic vortex structures in a permalloy square. *Phys. Rev. B* **89,** 174426 (2014).

221. Krautscheid, P. *et al.* Direct observation of spin diffusion enhanced nonadiabatic spin torque effects in rare-earth-doped permalloy. *Phys. Rev. B* **98,** 214406 (2018).

222. Scholz, W. *et al.* Transition from single-domain to vortex state in soft magnetic cylindrical nanodots. *J. Magn. Magn. Mater* **266,** 155–163 (2003).

223. Goiriena-Goikoetxea, M. *et al.* Magnetization reversal in circular vortex dots of small radius. *Nanoscale* **9,** 11269–11278 (2017).

224. Stoll, H. private communication. 2019.

225. Kimura, T., Otani, Y. & Levy, P. M. Electrical Control of the Direction of Spin Accumulation. *Phys. Rev. Lett.* **99,** 166601 (2007).

226. Yakata, S., Ando, Y. & Kimura, T. *Optimization of interface condition for efficient spin injection in Permalloy/Cu lateral spin valve* in *TENCON 2010 - 2010 IEEE Region 10 Conference* (Nov. 2010), 126–128.

227. Zahnd, G *et al.* Comparison of the use of NiFe and CoFe as electrodes for metallic lateral spin valves. *Nanotechnology* **27,** 035201 (2015).

228. Briones, J. *et al.* Stochastic and complex depinning dynamics of magnetic domain walls. *Phys. Rev. B* **83,** 060401 (2011).

229. Mayergoyz, I. D. Mathematical models of hysteresis. *IEEE Trans. Magn* **MAG-22,** 603 (1986).

230. Pike, C. R., Roberts, A. P. & Verosub, K. L. Characterizing interactions in fine magnetic particle systems using first order reversal curves. *J. Appl. Phys* **85,** 6660 (1999).

231. Chung, S.-H., McMichael, R. D., Pierce, D. T. & Unguris, J. Phase diagram of magnetic nanodisks measured by scanning electron microscopy with polarization analysis. *Phys. Rev. B* **81,** 024410 (2010).

232. M. Bode, M *et al.* Chiral magnetic order at surfaces driven by inversion asymmetry. *Nature* **447,** 190–193 (2007).

233. Im, M. Y. *et al.* Symmetry breaking in the formation of magnetic vortex states in a permalloy nanodisk. *Nat. Commun.* **3,** 983 (2012).

234. Vanatka, M. *et al.* Magnetic vortex nucleation modes in static magnetic fields. *AIP Adv.* **7,** 105103 (2017).

235. Schneider, M., Hoffmann, H. & Zweck, J. Lorentz microscopy of circular ferromagnetic permalloy nanodisks. *Appl. Phys. Lett.* **77,** 2909 (2000).

236. Zhong, Z. *et al.* Vortex chirality control in magnetic submicron dots with asymmetrical magnetic properties in lateral direction. *J. Magn. Magn. Mater.* **321,** 2345–2349 (2009).

237. Attané, J. P., Ravelosona, D., Marty, A., Samson, Y. & Chappert, C. Thermally Activated Depinning of a Narrow Domain Wall from a Single Defect. *Phys. Rev. Lett.* **96,** 147204 (2006).

238. Uhl, V. *et al.* Current-induced motion and pinning of domain walls in spin-valve nanowires studied by XMCD-PEEM. *Phys. Rev. B* **81,** 224418 (2010).

239. Hayward, T. J. & Omari, K. A. Beyond the quasi-particle: stochastic domain wall dynamics in soft ferromagnetic nanowires. *J. Phys. D: Appl. Phys.* **50,** 084006 (2017).

240. Wernsdorfer, W. *et al.* Experimental Evidence of the Néel-Brown Model of Magnetization Reversal. *Phys. Rev. Lett.* **78,** 1791–1794 (1997).

241. Garg, A. Escape-field distribution for escape from a metastable potential well subject to a steadily increasing bias field. *Phys. Rev. B* **51,** 15592–15595 (1995).

242. Pfeiffer, A., Reeve, R. M. & Kläui, M. Importance of spin current generation and detection by spin injection and the spin Hall effect for lateral spin valve performance. *J. Phys.: Condens. Matter* **30,** 465802 (2018).

243. Villamor, E., Isasa, M., Hueso, L. E. & Casanova, F. Contribution of defects to the spin relaxation in copper nanowires. *Phys. Rev. B* **87,** 094417 (2013).

244. Elliott, R. J. Theory of the Effect of Spin-Orbit Coupling on Magnetic Resonance in Some Semiconductors. *Phys. Rev.* **96,** 266–279 (1954).

245. Yafet, Y. g-factors and spin-lattice relaxation of conduction electrons. *Sol. St. Phys.* **14,** 1–98 (1963).

246. Batley, J. T. *et al.* Spin relaxation through Kondo scattering in Cu/Py lateral spin valves. *Phys. Rev. B* **92,** 220420 (2015).

247. Pfeiffer A. Hu, S. *et al.* Spin currents injected electrically and thermally from highly spin polarized Co2MnSi. *Appl. Phys. Lett.* **107,** 082401 (2015).

248. Kimura, T., Otani, Y., Sato, T., Takahashi, S. & Maekawa, S. Room-Temperature Reversible Spin Hall Effect. *Phys. Rev. Lett.* **98,** 156601 (2007).

249. Vila, L., Kimura, T. & Otani, Y. Evolution of the Spin Hall Effect in Pt Nanowires: Size and Temperature Effects. *Phys. Rev. Lett.* **99,** 226604 (2007).

250. Jacquod, P., Whitney, R. S., Meair, J. & Büttiker, M. Onsager relations in coupled electric, thermoelectric, and spin transport: The tenfold way. *Phys. Rev. B* **86,** 155118 (2012).

251. Van der Pauw, L. J. A method of measuring specific resistivity and Hall effect of discs of arbitrary shape. *Philips Res. Rep.* **13,** 1–9 (1958).

252. Niimi, Y. *et al.* Extrinsic Spin Hall Effect Induced by Iridium Impurities in Copper. *Phys. Rev. Lett.* **106** (2011).

253. Marmion, S. R., Ali, M., McLaren, M., Williams, D. A. & Hickey, B. J. Temperature dependence of spin Hall magnetoresistance in thin YIG/Pt films. *Phys. Rev. B* **89,** 220404 (2014).

254. Isasa, M., Villamor, E., Hueso, L. E., Gradhand, M. & Casanova, F. Temperature dependence of spin diffusion length and spin Hall angle in Au and Pt. *Phys. Rev. B* **91,** 024402 (2015).

255. Kim, K.-W., O'Brien, L., Crowell, P. A., Leighton, C. & Stiles, M. D. Theory of Kondo suppression of spin polarization in nonlocal spin valves. *Phys. Rev. B* **95,** 104404 (2017).

256. Hirohata, A., Yamamoto, Y., Murphy, B. A. & Vick, A. J. Non-destructive imaging of buried electronic interfaces using a decelerated scanning electron beam. *Nat. Commun.* **7,** 12701 (2016).

257. Jackson, E., Sun, M., Kubota, T., Takanashi, K. & Hirohata, A. Chemical and structural analysis on magnetic tunnel junctions using a decelerated scanning electron beam. *Sci. Rep.* **8,** 1785 (2018).

258. Ando, K. *et al.* Inverse spin-Hall effect induced by spin pumping in metallic system. *J. Appl. Phys.* **109,** 103913 (2011).

259. Zhang, W. *et al.* Determination of the Pt spin diffusion length by spin-pumping and spin Hall effect. *Appl. Phys. Lett.* **103,** 242414 (2013).

260. Tao, X. *et al.* Self-consistent determination of spin Hall angle and spin diffusion length in Pt and Pd: The role of the interface spin loss. *Sci. Adv.* **4,** eaat1670 (2018).

261. Nakayama, H. *et al.* Spin Hall Magnetoresistance Induced by a Nonequilibrium Proximity Effect. *Phys. Rev. Lett.* **110,** 206601 (2013).

262. Berger, A. J. *et al.* Determination of the spin Hall effect and the spin diffusion length of Pt from self-consistent fitting of damping enhancement and inverse spin-orbit torque measurements. *Phys. Rev. B* **98,** 024402 (2018).

263. Rojas-Sánchez, J.-C. *et al.* Spin Pumping and Inverse Spin Hall Effect in Platinum: The Essential Role of Spin-Memory Loss at Metallic Interfaces. *Phys. Rev. Lett.* **112,** 106602 (2014).

264. Dolui, K. Spin-memory loss due to spin-orbit coupling at ferromagnet/heavy-metal interfaces: Ab initio spin-density matrix approach. *Phys. Rev. B* **96,** 220403 (2017).

265. Drouin, D. *et al.* CASINO V2.42-A Fast and easy-to-use Modeling Tool for Scanning Electron Microscopy and Microanalysis Users. *Scanning* **29,** 92 (2007).

266. Kimura, T., Otani, Y. & Hamrle, J. Enhancement of spin accumulation in a nonmagnetic layer by reducing junction size. *Phys. Rev. B* **73,** 132405 (2006).

267. Morota, M. *et al.* Indication of intrinsic spin Hall effect in 4*d* and 5*d* transition metals. *Phys. Rev. B* **83,** 174405 (2011).

268. Wang, Y., Deorani, P., Qiu, X., Kwon, J. H. & Yang, H. Determination of intrinsic spin Hall angle in Pt. *Appl. Phys. Lett.* **105,** 152412 (2014).

269. Lidig, C. *et al.* Unidirectional Spin Hall Magnetoresistance as a Tool for Probing the Interfacial Spin Polarization of Co_2MnSi. *Phys. Rev. Applied* **11,** 044039 (2019).

270. Villamor, E., Isasa, M., Hueso, L. E. & Casanova, F. Temperature dependence of spin polarization in ferromagnetic metals using lateral spin valves. *Phys. Rev. B* **88,** 184411 (2013).

271. AllResist. *Remover for AR Resists* 2019. https://www.allresist.com/wp-content/uploads/sites/2/2018/01/allresist_produktinfos_ar600-70-71_300-76-70-72-73_englisch.pdf.

272. Chem, M. *Nano PMMA and Copolymer* http://microchem.com/pdf/PMMA_Data_Sheet.pdf.

273. MicroTec, S. *Süss MicroTec's LabSpin Platform* https://www.suss.com/en/products-solutions/coater-developer/labspin6-labspin8.

Publications List

- **A. Pfeiffer**, S. Hu, R. M. Reeve, A. Kronenberg, M. Jourdan, T. Kimura and M. Kläui Spin currents injected electrically and thermally from high spin polarized Co2MnSi. *Appl. Phys. Lett.* **107**, 082401 (2015)
- **A. Pfeiffer**, R. M. Reeve, M. Voto, W. Savero-Torres, N. Richter, L. Vila, J. P. Attané, L. Lopez-Diaz and M. Kläui Geometrical control of pure spin current induced domain wall depinning. *J. Phys.: Condens. Matter* **29**, 085802 (2017)
- **A. Pfeiffer**, R. M. Reeve and M. Kläui Importance of spin current generation and detection by spin injection and the spin Hall effect for lateral spin valve performance. *J. Phys.: Condens. Matter* **30**, 465802 (2018)
- **A. Pfeiffer**, R. M. Reeve, K. Elphick, A. Hirohata and M. Kläui Revealing the importance of interfaces for pure spin current transport. (submitted)

Danksagung

Removed in the electronic version of this thesis due to data protection regulations.
In der elektronischen Version entfernt aufgrund datenschutzrechtlicher Bestimmungen.

Curriculum Vitae

Removed in the electronic version of this thesis due to data protection regulations.
In der elektronischen Version entfernt aufgrund datenschutzrechtlicher Bestimmungen.